Optically and electrically driven nanoantennas
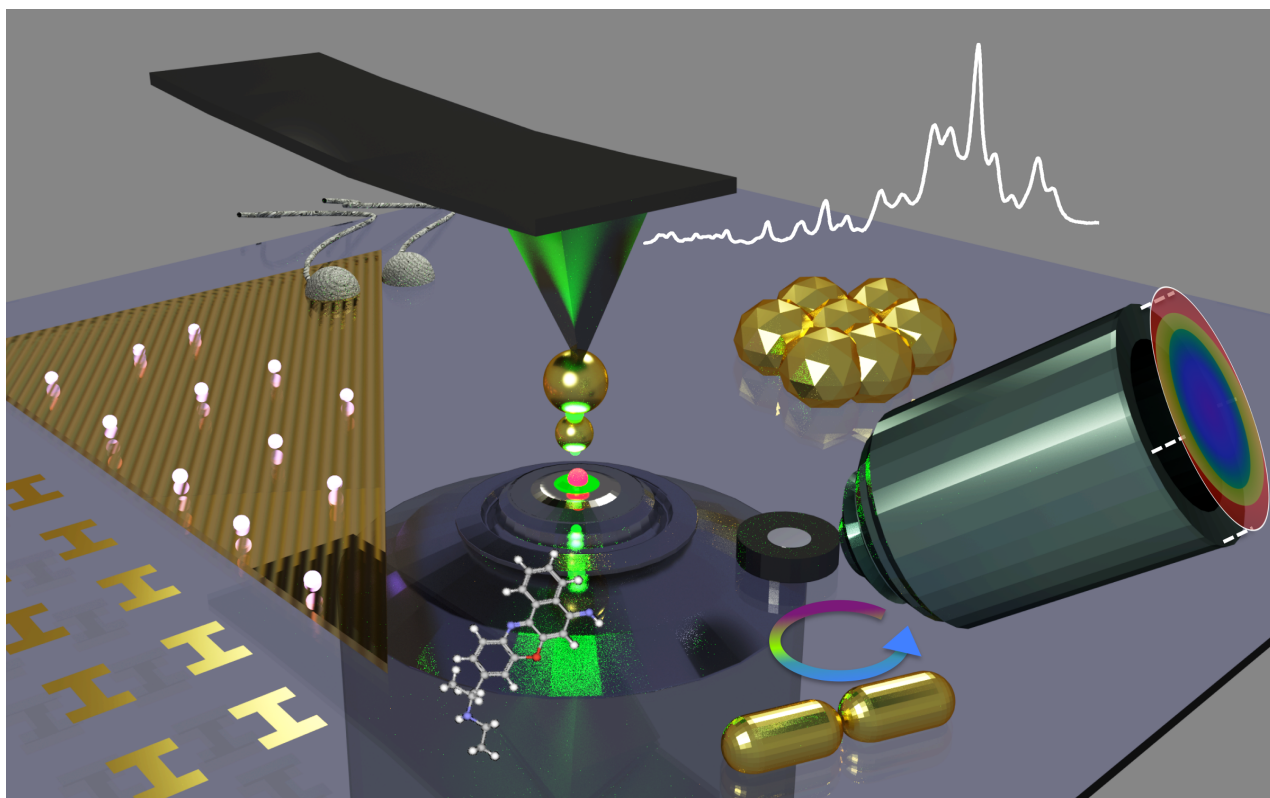
Edited by Alfred J. Meixner, Dai Zhang
and Monika Fleischer

Imprint

Optically and electrically driven nanoantennas

Monika Fleischer[*1], Dai Zhang[*2] and Alfred J. Meixner[*2]

Editorial

Address:
[1]Institute for Applied Physics and Center LISA+, University of
Tübingen, Auf der Morgenstelle 10, 72076 Tübingen, Germany and
[2]Institute of Physical and Theoretical Chemistry and Center LISA+,
University of Tübingen, Auf der Morgenstelle 18, 72076 Tübingen,
Germany

Email:
Monika Fleischer* - monika.fleischer@uni-tuebingen.de;
Dai Zhang* - dai.zhang@uni-tuebingen.de;
Alfred J. Meixner* - alfred.meixner@uni-tuebingen.de

* Corresponding author

Editorial

Optical antennas [+] serve to confine the energy of photons transported by a light wave to a tiny volume much smaller than the wavelength; or reversely, to convert the energy of an evanescent field that oscillates at optical frequencies to a traveling electromagnetic wave that can be observed in the far field. Optical antennas are key elements in nano-optics, bridging the gap between the dimension of an optical wavelength (several hundreds of nanometers) and the size of elementary quantum emitters such as single atoms, molecules, etc. (a few nanometers to below 1 nm). Nanoantennas have been under examination for the past few decades in view of their attractive fundamental properties, while the rapid development of nanofabrication techniques has opened up possibilities to create more and more sophisticated shapes and configurations with increasing control over their optical performance [1-4]. The strong local near-field enhancement by plasmonic nanoantennas is being harnessed for high sensitivity, high-resolution optical nanospec-troscopy techniques [5], such as surface-enhanced or tip-enhanced Raman spectroscopy (SERS or TERS) [6-15], as well as for (bio-)sensing applications [16-18]. The integration of nanoantennas can lead to enhanced functionality for optoelectronic devices, nano-light sources, light amplification, or hybrid systems in combination with nanoemitters or two-dimensional materials [19]. Under excitation with state-of-the-art lasers, ultrafast effects can be observed as well as a plethora of nonlinear characteristics [20]. Recently, also electrically driven nanoantennas have been demonstrated [21-25], which are an important milestone towards on-chip integration, device-to-device communication, and bilateral transduction between electrons and photons [26].

An optical gap antenna typically consists of two nanostructures with a nanometer gap in between. Optical excitation induces a coupled plasmon oscillation along the two antenna parts, which

can lead to large surface charge oscillations on the opposite surfaces confining the gap, and a field in the gap that is enhanced by several orders of magnitude with respect to the incident field [27]. The gap field is particularly strong when the particle plasmons are in resonance. The enhanced local field and the enhanced optical mode density can, for example, enhance the excitation and/or the emission rate of a quantum system that is positioned in this near-field region [28].

Both the enhanced local field and optical mode density are of great practical use for local spectroscopy with extremely high spatial resolution. They enable boosting the intrinsically low optical signal of a very small number of molecules by orders of magnitude with respect to any surrounding molecules, which can be the source of an overwhelming background signal. This principle applies to virtually any kind of optical spectroscopy. Prominent examples are SERS and TERS, where the intrinsically small Raman scattering cross-section is enhanced by several orders of magnitude, making single-molecule spectroscopy feasible. These spectroscopic techniques have shown tremendous progress in the last two decades [29-32].

Under high-power excitation of nanoantennas, higher order contributions to the particle polarization are no longer negligible, and nonlinear effects become apparent. Due to their inherent symmetry breaking, nanoantennas can act as local sources of second harmonic generation (SHG) with attractive applications in low-background medical imaging or nanolasers [33].

Electrically driven optical antennas emit light when a bias voltage is applied to the contacted antenna arms that are forming a tunnel junction. Inelastic electron tunneling through the gap excites gap–plasmon oscillations leading to the emission of photons as a consequence of radiative plasmon relaxation [34-36]. The relaxation depends on how the gap modes couple and can hence be controlled by the design of the antenna. The combination of an electrically driven antenna with optical excitation is a very promising but not yet well explored subject. Energy-level engineering in the gap by introducing molecules into the tunnel junction provides an additional handle to modulate photon emission from an electrically controlled optical antenna. Light emission by tunneling through a single molecule opens the door to combine electronics and quantum optics for a new class of quantum devices [37].

The concept, realization and prospective applications of such optically and electrically driven antennas are explored in the *Beilstein Journal of Nanotechnology* Thematic Issue, "Optically and electrically driven nanoantennas".

In most applications for ultrahigh sensitivity sensing the central feature for tightly confining and enhancing the optical near-field is a narrow gap between two metallic nanoparticles or tips. Creating such gaps to obtain a controlled distribution of hotspots, for example, on a chip, is no trivial task. This has been pursued using top-down approaches such as thin film deposition and nanopatterning, as well as bottom-up approaches such as chemical synthesis and self-assembly [38]. Gap sizes may range from a few tens of nanometers down to sub-nanometer tunnel junctions, where the classical description of the plasmonic behavior breaks down [39,40]. Here, several approaches to create low-cost, large-area SERS substrates that exhibit homogeneous Raman intensity enhancement are introduced. The substrates are based on quasi-hexagonally ordered gold particles prepared by block-copolymer micellar nanolithography and electroless deposition [41], or on dense silver island films created by pulsed laser deposition [42] or physical vapor deposition [43]. In [44], individual plasmonic nanotags are prepared by coating gold nanoparticle clusters with Raman reporters. This work explores the minimum number of tags required for obtaining a SERS signal under operation conditions. Moving further towards the (near-) infrared regime, different antennas are employed in a surface-enhanced infrared absorption (SEIRA) configuration [45]. Here the aim is to detect low concentrations of semiconductor nanocrystals through maximum local enhancement of their optical phonon response. High local field enhancement is likewise required in TERS experiments, where a tip with a hotspot located at its apex is scanned across a sample surface. The performance of a TERS measurement is closely related to the quality of the tip [46]. Therefore, researchers are on the lookout for nanotips that can be prepared fast and with reproducible properties, and at the same time, aim for ever higher field enhancement and localization to improve the sensitivity and spatial resolution of the TERS information. In [47], an earlier protocol for etching thin gold wires to a sharp tip is refined to a two-step procedure with high throughput. A self-assembly approach to create a dumbbell antenna consisting of a 40 nm and an 80 nm Au nanoparticle at a scanning tip is shown in [48] and applied for single molecule sensitivity imaging. The advantage of applying TERS for revealing local structural properties is illustrated in [49], where crystalline and amorphous regions within core–shell silicon nanowires are discerned with an optical resolution of a few nanometers. This study further demonstrates that it is possible to combine polarization angle-resolved experiments with a TERS setup, which has been rarely pursued so far.

In the hot topic area of active plasmonics, reversible changes in the refractive index of the environment of a plasmonic system, for example, by liquid crystals or thermosensitive polymers, allow for actively switching the plasmonic properties

[50,51]. A recent example of the strong coupling between silver nanorods and photochromic molecules is demonstrated in [52].

Due to the high local field intensity in the gap of a nanodimer, strong polarization of the particle, and consequently, strong SHG from the particle surface, may be expected. However, owing to the polarization and far-field interference, a silencing of the SHG is observed for decreasing gap sizes [53]. This effect is further studied in [54] using the surface integral equation method. On the other hand, the generation of higher harmonics by a dielectric nanostructure can be boosted by forming a hybrid antenna. In the case of [55] an AlGaAs nanopillar, which has an anapole mode resonant with the pump wavelength, is encompassed by a gold ring. The field enhancement by the plasmonic structure is shown to lead to almost two orders of magnitude improvement of the SHG and a sizeable third-harmonic generation from the pillar. The fact that nonlinear effects can already be observed in the absorption and scattering of single gold nanoparticles at much lower laser intensities is demonstrated in [56]. Using the so-called *x*-scan technique, a nanoparticle is scanned through a confocal laser spot, and power-dependent modifications are observed in the resulting point-spread function profile.

Last but not least, the electrically driven generation of photons is explored in [26] and [57]. In [26] the emission of light from electromigrated in-plane tunnel junctions is observed, where the feed-gap is shown to couple to propagating modes in waveguides with up to 30% efficiency. Making use of propagating surface plasmon polaritons (SPPs), directional light beams are created in [57]. The SPPs are excited by inelastic tunneling from a scanning probe. The probe is positioned in the focus of an elliptical structure, which is formed by a slit in a gold film. By defining the dimensions of the ellipse, it becomes possible to control the directionality of the emitted light beam.

The contributions collected in this Thematic Issue thus highlight current and emerging directions in the fast-moving field of optically and electrically driven nanoantennas. In the current age of photonics, such elements may prove essential in further expanding the functionality of electrical devices by integration with photonic functionalities. We sincerely thank all colleagues who contributed to this Thematic Issue with their time and research results.

Monika Fleischer, Dai Zhang and Alfred J. Meixner

Tübingen, September 2020

ORCID® iDs

Monika Fleischer - https://orcid.org/0000-0001-5625-5975
Dai Zhang - https://orcid.org/0000-0001-8190-3030
Alfred J. Meixner - https://orcid.org/0000-0002-0187-2906

References

1. Crozier, K. B.; Sundaramurthy, A.; Kino, G. S.; Quate, C. F. *J. Appl. Phys.* **2003,** *94,* 4632. doi:10.1063/1.1602956
2. Bharadwaj, P.; Deutsch, B.; Novotny, L. *Adv. Opt. Photonics* **2009,** *1,* 438–483. doi:10.1364/aop.1.000438
3. Park, Q.-H. *Contemp. Phys.* **2009,** *50,* 407–423. doi:10.1080/00107510902745611
4. Novotny, L.; van Hulst, N. *Nat. Photonics* **2011,** *5,* 83–90. doi:10.1038/nphoton.2010.237
5. Kern, A. M.; Zhang, D.; Brecht, M.; Chizhik, A. I.; Failla, A. V.; Wackenhut, F.; Meixner, A. J. *Chem. Soc. Rev.* **2014,** *43,* 1263–1286. doi:10.1039/c3cs60357a
6. Kneipp, K.; Kneipp, H.; Itzkan, I.; Dasari, R. R.; Feld, M. S. *Chem. Rev.* **1999,** *99,* 2957–2976. doi:10.1021/cr980133r
7. Knoll, B.; Keilmann, F. *Nature* **1999,** *399,* 134–137. doi:10.1038/20154
8. Stöckle, R. M.; Suh, Y. D.; Deckert, V.; Zenobi, R. *Chem. Phys. Lett.* **2000,** *318,* 131–136. doi:10.1016/s0009-2614(99)01451-7
9. Xie, W.; Schlücker, S. *Rep. Prog. Phys.* **2014,** *77,* 116502. doi:10.1088/0034-4885/77/11/116502
10. Mauser, N.; Hartschuh, A. *Chem. Soc. Rev.* **2014,** *43,* 1248–1262. doi:10.1039/c3cs60258c
11. Zhang, Z.; Sheng, S.; Wang, R.; Sun, M. *Anal. Chem. (Washington, DC, U. S.)* **2016,** *88,* 9328–9346. doi:10.1021/acs.analchem.6b02093
12. Ding, S.-Y.; You, E.-M.; Tian, Z.-Q.; Moskovits, M. *Chem. Soc. Rev.* **2017,** *46,* 4042–4076. doi:10.1039/c7cs00238f
13. Kawata, S.; Ichimura, T.; Taguchi, A.; Kumamoto, Y. *Chem. Rev.* **2017,** *117,* 4983–5001. doi:10.1021/acs.chemrev.6b00560
14. Deckert-Gaudig, T.; Taguchi, A.; Kawata, S.; Deckert, V. *Chem. Soc. Rev.* **2017,** *46,* 4077–4110. doi:10.1039/c7cs00209b
15. Langer, J.; et al. *ACS Nano* **2020,** *14,* 28–117. doi:10.1021/acsnano.9b04224
16. Willets, K. A.; Van Duyne, R. P. *Annu. Rev. Phys. Chem.* **2007,** *58,* 267–297. doi:10.1146/annurev.physchem.58.032806.104607
17. Stockman, M. I. *Science* **2015,** *348,* 287–288. doi:10.1126/science.aaa6805
18. Di Fabrizio, E.; Schlücker, S.; Wenger, J.; Regmi, R.; Rigneault, H.; Calafiore, G.; West, M.; Cabrini, S.; Fleischer, M.; van Hulst, N. F.; Garcia-Parajo, M. F.; Pucci, A.; Cojoc, D.; Hauser, C. A. E.; Ni, M. *J. Opt. (Bristol, U. K.)* **2016,** *18,* 063003. doi:10.1088/2040-8978/18/6/063003
19. Stockmann, M. I. *Phys. Today* **2011,** *64* (2), 39–44. doi:10.1063/1.3554315
20. Kauranen, M.; Zayats, A. V. *Nat. Photonics* **2012,** *6,* 737–748. doi:10.1038/nphoton.2012.244
21. Kern, J.; Kullock, R.; Prangsma, J.; Emmerling, M.; Kamp, M.; Hecht, B. *Nat. Photonics* **2015,** *9,* 582–586. doi:10.1038/nphoton.2015.141
22. Parzefall, M.; Bharadwaj, P.; Jain, A.; Taniguchi, T.; Watanabe, K.; Novotny, L. *Nat. Nanotechnol.* **2015,** *10,* 1058–1063. doi:10.1038/nnano.2015.203
23. Dathe, A.; Ziegler, M.; Hübner, U.; Fritzsche, W.; Stranik, O. *Nano Lett.* **2016,** *16,* 5728–5736. doi:10.1021/acs.nanolett.6b02414

24. Gurunarayanan, S. P.; Verellen, N.; Zharinov, V. S.; Shirley, F. J.; Moshchalkov, V. V.; Heyns, M.; Van de Vondel, J.; Radu, I. P.; Van Dope, P. *Nano Lett.* **2017,** *17,* 7433–7439. doi:10.1021/acs.nanolett.7b03312

25. Kullock, R.; Ochs, M.; Grimm, P.; Emmerling, M.; Hecht, B. *Nat. Commun.* **2020,** *11,* 115. doi:10.1038/s41467-019-14011-6

26. Dasgupta, A.; Buret, M.; Cazier, N.; Mennemanteuil, M.-M.; Chacon, R.; Hammani, K.; Weeber, J.-C.; Arocas, J.; Markey, L.; Colas des Francs, G.; Uskov, A.; Smetanin, I.; Bouhelier, A. *Beilstein J. Nanotechnol.* **2018,** *9,* 1964–1976. doi:10.3762/bjnano.9.187

27. Mühlschlegel, P.; Eisler, H.-J.; Martin, O. J. F.; Hecht, B.; Pohl, D. W. *Science* **2005,** *308,* 1607–1609. doi:10.1126/science.1111886

28. Kühn, S.; Håkanson, U.; Rogobete, L.; Sandoghdar, V. *Phys. Rev. Lett.* **2006,** *97,* 017402. doi:10.1103/physrevlett.97.017402

29. Cialla, D.; März, A.; Böhme, R.; Theil, F.; Weber, K.; Schmitt, M.; Popp, J. *Anal. Bioanal. Chem.* **2012,** *403,* 27–54. doi:10.1007/s00216-011-5631-x

30. Hartschuh, A.; Qian, H.; Meixner, A. J.; Anderson, N.; Novotny, L. *Surf. Interface Anal.* **2006,** *38,* 1472–1480. doi:10.1002/sia.2351

31. Lee, J.; Crampton, K. T.; Tallarida, N.; Apkarian, V. A. *Nature* **2019,** *568,* 78–82. doi:10.1038/s41586-019-1059-9

32. Yang, B.; Chen, G.; Ghafoor, A.; Zhang, Y.; Zhang, Y.; Zhang, Y.; Luo, Y.; Yang, J.; Sandoghdar, V.; Aizpurua, J.; Dong, Z.; Hou, J. G. *Nat. Photonics* **2020**. doi:10.1038/s41566-020-0677-y

33. Butet, J.; Brevet, P.-F.; Martin, O. J. F. *ACS Nano* **2015,** *9,* 10545–10562. doi:10.1021/acsnano.5b04373

34. Braun, K.; Wang, X.; Kern, A. M.; Adler, H.; Peisert, H.; Chassé, T.; Zhang, D.; Meixner, A. J. *Beilstein J. Nanotechnol.* **2015,** *6,* 1100–1106. doi:10.3762/bjnano.6.111

35. Braun, K.; Laible, F.; Hauler, O.; Wang, X.; Pan, A.; Fleischer, M.; Meixner, A. J. *Nanophotonics* **2018,** *7,* 1503–1516. doi:10.1515/nanoph-2018-0080

36. Parzefall, M.; Novotny, L. *Rep. Prog. Phys.* **2019,** *82,* 112401. doi:10.1088/1361-6633/ab4239

37. Galperin, M.; Nitzan, A. *Phys. Chem. Chem. Phys.* **2012,** *14,* 9421–9438. doi:10.1039/c2cp40636e

38. Yang, Y.; Gu, C.; Li, J. *Small* **2019,** *15,* 1804177. doi:10.1002/smll.201804177

39. Esteban, R.; Borisov, A. G.; Nordlander, P.; Aizpurua, J. *Nat. Commun.* **2012,** *3,* 825. doi:10.1038/ncomms1806

40. Savage, K. J.; Hawkeye, M. M.; Esteban, R.; Borisov, A. G.; Aizpurua, J.; Baumberg, J. J. *Nature* **2012,** *491,* 574–577. doi:10.1038/nature11653

41. Gürdal, E.; Dickreuter, S.; Noureddine, F.; Bieschke, P.; Kern, D. P.; Fleischer, M. *Beilstein J. Nanotechnol.* **2018,** *9,* 1977–1985. doi:10.3762/bjnano.9.188

42. Budner, B.; Kuźma, M.; Nasiłowska, B.; Bartosewicz, B.; Liszewska, M.; Jankiewicz, B. J. *Beilstein J. Nanotechnol.* **2019,** *10,* 882–893. doi:10.3762/bjnano.10.89

43. Liszewska, M.; Budner, B.; Norek, M.; Jankiewicz, B. J.; Nyga, P. *Beilstein J. Nanotechnol.* **2019,** *10,* 1048–1055. doi:10.3762/bjnano.10.105

44. Amendola, V. *Beilstein J. Nanotechnol.* **2019,** *10,* 1016–1023. doi:10.3762/bjnano.10.102

45. Milekhin, A. G.; Kuznetsov, S. A.; Milekhin, I. A.; Sveshnikova, L. L.; Duda, T. A.; Rodyakina, E. E.; Latyshev, A. V.; Dzhagan, V. M.; Zahn, D. R. T. *Beilstein J. Nanotechnol.* **2018,** *9,* 2646–2656. doi:10.3762/bjnano.9.246

46. Fleischer, M. *Nanotechnol. Rev.* **2012,** *1,* 313–338. doi:10.1515/ntrev-2012-0027

47. Foti, A.; Barreca, F.; Fazio, E.; D'Andrea, C.; Matteini, P.; Maragò, O. M.; Gucciardi, P. G. *Beilstein J. Nanotechnol.* **2018,** *9,* 2718–2729. doi:10.3762/bjnano.9.254

48. Herrmann, J. F.; Höppener, C. *Beilstein J. Nanotechnol.* **2018,** *9,* 2188–2197. doi:10.3762/bjnano.9.205

49. Van den Berg, M.; Moeinian, A.; Kobald, A.; Chen, Y.-T.; Horneber, A.; Strehle, S.; Meixner, A. J.; Zhang, D. *Beilstein J. Nanotechnol.* **2020,** *11,* 1147–1156. doi:10.3762/bjnano.11.99

50. Si, G.; Zhao, Y.; Leong, E. S. P.; Liu, Y. J. *Materials* **2014,** *7,* 1296–1317. doi:10.3390/ma7021296

51. Jiang, N.; Zhuo, X.; Wang, J. *Chem. Rev.* **2018,** *118,* 3054–3099. doi:10.1021/acs.chemrev.7b00252

52. Lamri, G.; Veltri, A.; Aubard, J.; Adam, P.-M.; Felidj, N.; Baudrion, A.-L. *Beilstein J. Nanotechnol.* **2018,** *9,* 2657–2664. doi:10.3762/bjnano.9.247

53. Berthelot, J.; Bachelier, G.; Song, M.; Rai, P.; Colas des Francs, G.; Dereux, A.; Bouhelier, A. *Opt. Express* **2012,** *20,* 10498–10508. doi:10.1364/oe.20.010498

54. Butet, J.; Bernasconi, G. D.; Martin, O. J. F. *Beilstein J. Nanotechnol.* **2018,** *9,* 2674–2683. doi:10.3762/bjnano.9.250

55. Gili, V. F.; Ghirardini, L.; Rocco, D.; Marino, G.; Favero, I.; Roland, I.; Pellegrini, G.; Duò, L.; Finazzi, M.; Carletti, L.; Locatelli, A.; Lemaître, A.; Neshev, D.; De Angelis, C.; Leo, G.; Celebrano, M. *Beilstein J. Nanotechnol.* **2018,** *9,* 2306–2314. doi:10.3762/bjnano.9.215

56. Jagadale, T. C.; Murali, D. S.; Chu, S.-W. *Beilstein J. Nanotechnol.* **2019,** *10,* 2182–2191. doi:10.3762/bjnano.10.211

57. Cao, S.; Le Moal, E.; Jiang, Q.; Drezet, A.; Huant, S.; Hugonin, J.-P.; Dujardin, G.; Boer-Duchemin, E. *Beilstein J. Nanotechnol.* **2018,** *9,* 2361–2371. doi:10.3762/bjnano.9.221

Electromigrated electrical optical antennas for transducing electrons and photons at the nanoscale

Arindam Dasgupta[1], Mickaël Buret[1], Nicolas Cazier[1], Marie-Maxime Mennemanteuil[1], Reinaldo Chacon[1], Kamal Hammani[1], Jean-Claude Weeber[1], Juan Arocas[1], Laurent Markey[1], Gérard Colas des Francs[1], Alexander Uskov[2,3], Igor Smetanin[2] and Alexandre Bouhelier[*1]

Abstract

Background: Electrically controlled optical metal antennas are an emerging class of nanodevices enabling a bilateral transduction between electrons and photons. At the heart of the device is a tunnel junction that may either emit light upon injection of electrons or generate an electrical current when excited by a light wave. The current study explores a technological route for producing these functional units based upon the electromigration of metal constrictions.

Results: We combine multiple nanofabrication steps to realize in-plane tunneling junctions made of two gold electrodes, separated by a sub-nanometer gap acting as the feedgap of an optical antenna. We electrically characterize the transport properties of the junctions in the light of the Fowler–Nordheim representation and the Simmons model for electron tunneling. We demonstrate light emission from the feedgap upon electron injection and show examples of how this nanoscale light source can be coupled to waveguiding structures.

Conclusion: Electromigrated in-plane tunneling optical antennas feature interesting properties with their unique functionality enabling interfacing electrons and photons at the atomic scale and with the same device. This technology may open new routes for device-to-device communication and for interconnecting an electronic control layer to a photonic architecture.

Introduction

The constant evolution of information technologies requires the integration and development of complex processing functionalities. The fast increasing demand of connectivity between devices necessitates the deployment of new data-transfer strategies. Optical fiber input/output pigtail-wiring connections are the key technology enabling fast and reliable data transfer down to on-card system level. However, the need for parallel processing and the physical size of these optical buses prevent their deployment as a sustainable technology for short-range on-chip interconnects. Alternative propagation supports are being developed to meet integration requirements. Silicon-based photonics for instance is offering a cost-effective strategy to merge microelectronics and photonics [1,2] and address the next generation of interchip and intrachip optical interconnects. Optical and electrical cross talk between vertical interconnect accesses, thermal envelope, footprint, wafer-bonding requirements, and the drastic increase of power consumption with the number of links are limiting factors for using this platform at the nanoscale. In parallel, the integration of alternative chip-scale routing networks is being developed [3]. For instance wireless radio-frequency (RF) data transmission between distant nodes is emerging as an alternative for wired physical wave-guiding channels [4]. This approach is enabled by the availability of complementary metal-oxide semiconductor (CMOS)-compatible transceivers [5] and may offer cost-effective robust interconnects operating with a large bandwidth [6]. Yet, the implementation of hardware components for wireless network-on-chip (WNoC) is constrained by the physical size of the transmitting antennas. For instance, ultra wide-band RF interconnects and millimeter-wave traffic are relying on device sizes comparable to dimension of the chip itself (millimeters). A new paradigm is thus required to develop miniature antennas enabling future WNoC to operate with sub-micrometer transmitting units [7].

In this context, optical antennas are offering an interesting technological route to meet this integration requirement. Optical antennas are devices operating at frequencies from visible light to infrared [8]. They were primarily developed to enhance light–matter near-field interactions [9] via the excitation of surface plasmons for metal-based devices [10] or Mie resonances for dielectric antennas [11,12]. Interestingly, optical antennas have radiating properties bearing similarities with traditional RF antennas [13-16] but have a nanometer-scale footprint offering thus unsurpassed integration capability. However, the deployment of such components for interconnects has not been a viable solution so far as optical antennas are typically used as wave-vector converters to manipulate optical fields. Recent developments showed that a novel generation of optical antennas can be electrically connected [17]. These devices are operating based upon the unique properties of tunnel junctions. In particular, they can be deployed as electro-optical transceivers because they may either emit light upon injection of electrons [18-21] or optically rectify an incident electromagnetic wave [22-27]. Additionally atomic-scale gaps provide a unique test bed to identify the rules governing the physics of electron interaction with surface plasmons and photons: quantum effects were shown to challenge the classical plasmonic description [28-30] and the fluctuations of the electronic current impart a rich photon statistics [31,32].

In this work, we present a strategy to realize electrically connected optical antennas by employing the electromigration of metal nano-constrictions. The atomic-scale gap acts as an active feedgap operating a transduction between an electrical signal and an optical radiation. We electrically characterize the device and deduce the relevant properties using the standard description of tunneling transport. We demonstrate light generation from the feedgap and discuss different emission mechanisms based on the radiated spectrum and activation voltage.

Results and Discussion
Nanofabrication of electrically connected optical antennas

The starting geometry for realizing an electrically connected optical antenna is a Au constriction formed between two fan-out electrodes laying on a glass cover slip. We use electron-beam lithography and standard physical vapor deposition to produce gold constrictions and the proximity electrodes. The thickness of the Au layer is typically 50 nm, and we use a 2 nm thick Cr or Ti adhesion layer to improve gold adhesion on the glass substrate. A scanning electron micrograph of a pristine 150 nm wide Au constriction formed between two bow-tie leads is exemplified in Figure 1a. The electrical connections of the constriction to outside control electronics is obtained in a second step of fabrication by ultraviolet (UV) photolithography. An image of a typical sample, constituted of 24 constrictions and their associated macroscopic electrodes, is illustrated in Figure 1b. The red and blue regions are realized by electron-beam lithography and UV lithography, respectively. Each electrode is connected to a common ground (centered square) and can be individually addressed by a set of peripheral electrodes.

To create a tunnel junction that will eventually form the active feedgap of an optical antenna, we perform an operator-controlled electromigration of the constriction. Electromigration is, in a broad sense, the transport of mass due to an electric current passing through a metal. The phenomenon depends on several variables, such as current density, temperature, composition, stresses in the solid, and grain structure [33]. We adapted and
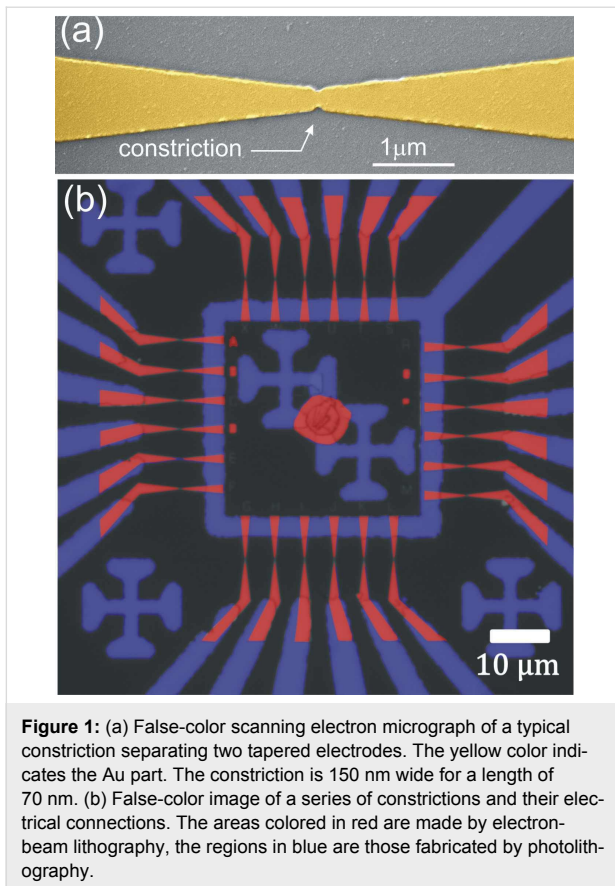
Figure 1: (a) False-color scanning electron micrograph of a typical constriction separating two tapered electrodes. The yellow color indicates the Au part. The constriction is 150 nm wide for a length of 70 nm. (b) False-color image of a series of constrictions and their electrical connections. The areas colored in red are made by electron-beam lithography, the regions in blue are those fabricated by photolithography.

tested different strategies available from the literature ranging from the simple ramping of an applied voltage until breakdown to approaches relying on feedback mechanisms [34]. We finally settled on a method where the applied bias is manually adjusted to control the time evolution of the conductance of the constriction. The procedure is as follows: An ac voltage applied across the constriction with an amplitude V_{ac} = 20 mV and a frequency F = 12.6 kHz is summed to an adjustable direct current (dc) bias V_{dc}. F is used as an external reference for a lock-in amplifier. A current-to-voltage amplifier converts the current flowing through the device to a voltage output read by the lock-in amplifier. The output of the lock-in is proportional to the amplitude of the modulated current oscillating at F. The conductance of the constriction G is then estimated by dividing the lock-in signal by V_{ac}. The conductance of the devices before electromigration is in the range of 1 to 4 mS, and includes the contribution from leads and contacts. V_{dc} is then incremented by steps of 100 mV. We monitor $G(t)$ during each step and the entire electromigration process may be divided into phases.

During the first few V_{dc} steps, $G(t)$ is fairly constant because Joule dissipation is not yet affecting the temperature-dependent resistivity of gold. On increasing V_{dc}, the temperature of the constriction grows and the conductance starts to fluctuate. The

general trend is that $G(t)$ decreases when stepping up V_{dc}. We also consistently observe a momentary rise of the conductance, which we attribute to the desorption of surface contaminants as well as a temperature annealing of the constriction due to dissipation of the electrical power in this area. This effect can be traced in Figure 2a at around t = 150 s. An example of another temperature effect is illustrated at t = 200 s in Figure 2a. The applied bias is constant, but $G(t)$ decays towards a stable value. This is understood from the temperature-dependent resistivity of the material: For a given V_{dc} the current flowing in the constriction dissipates heat and affects in return the temperature-dependent resistivity [35]. These conductance fluctuations are typically observed for $V_{dc} \leq 1.7$ V and corresponds to the end of the first phase of voltage increments.

When applying higher voltages, $G(t)$ generally drops with a rate rapidly increasing with time. The process is entering a second phase. This behavior is the signature of the onset of electromigration of the device, and will rapidly lead to the failure of the constriction if the applied bias is maintained. In order to control the electromigration process, we reduce V_{dc} by 100 mV when the dropping rate of $G(t)$ exceeds 5 µS·s^{-1}. This usually stops the runaway momentarily. An example of the procedure is illustrated at t = 420 s in Figure 2a. After a few seconds, the conductance drop resumes and V_{dc} is again adjusted to control the decrease of the conductance. When $G(t)$ stays constant, the electromigration is hindered because the temperature of the constriction is too low to thermally assist the process [36]. V_{dc} is consequently increased by a few increments to trigger the process again. The constriction will eventually break for bias voltages V_{dc} of around 500 mV. We sometimes observe quantized conductance steps indicating the change of transport regime from diffusive to ballistic as illustrated in Figure 2b. The conductance is normalized by the quantum of conductance $G_0 = 2e^2/h$ = 77 µS, where e is the electron charge and h is Planck's constant. The passage to the tunneling regime when $G < G_0$ ends the electromigration process. In the inset of Figure 2b, we show a statistics of the final conductance values measured after the electromigration of a series of 24 constrictions. About 17% of the devices feature large conductances approaching G_0.

A scanning electron image (SEM) of an electromigrated constriction is displayed in Figure 2c. Electron imaging is made possible by sputtering a thin conductive Au layer. Different information can be deduced from the image. To begin with, the tunneling gap is not situated at the location of the constriction, but is displaced towards the source electrode as already reported in the past [37]. There are two reasons why the formation of the gap is not occurring at the constriction. First, the dissipation of electrical power during the process takes place at
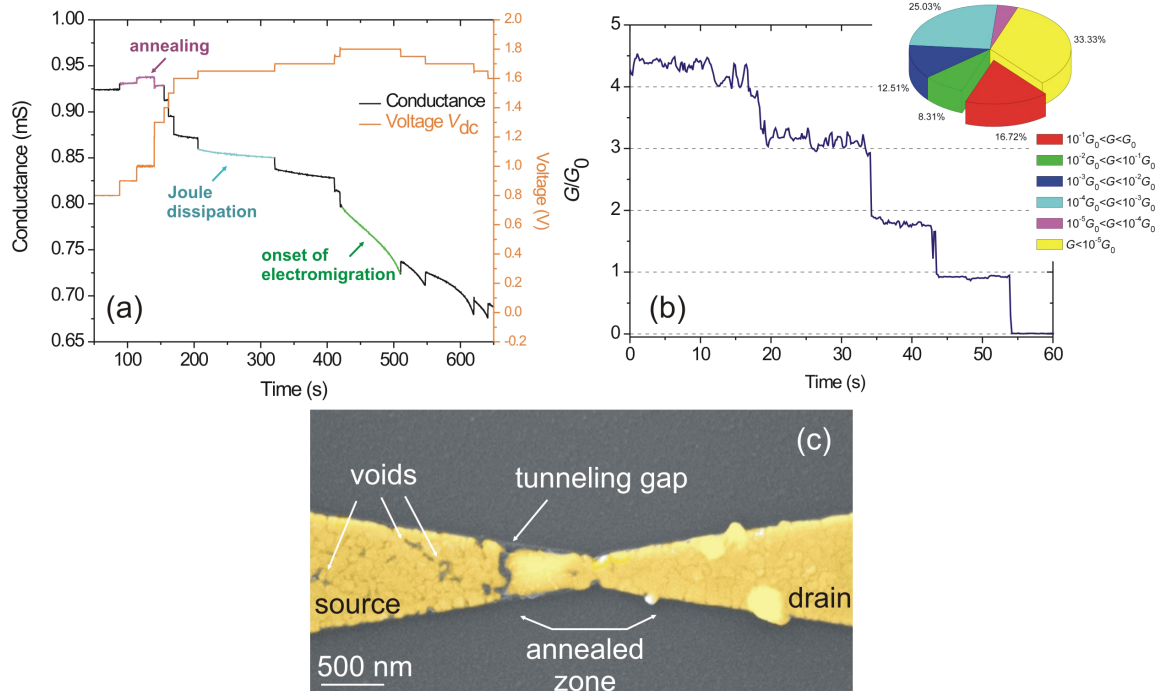
Figure 2: (a) Temporal extract of the electromigration sequence featuring the effect of partial annealing, Joule heating and onset of electromigration on the evolution of the condutance with bias increments. (b) Time trace of the conductance $G(t)$ during the last moments of the electromigration process. The conductance is quantized in units of G_0, the quantum of conductance. Inset: statistics on the final conductance for a series of 24 electromigrated constrictions. (c) False-color scanning electron micrograph of the device after electromigration. The tunneling junction forms on the source electrode. The zone corresponding to the constriction has been annealed by Joule dissipation during the process, reducing the number of grain boundaries available to trigger electromigration. Voids resulting from Au migration are also observed on the source electrode. The image is obtained by sputtering a thin conductive Au layer on the post mortem device.

the constriction, i.e., at the region of highest resistance [38]. The evaporated Au layer can thus be partially annealed through Joule heating. We substantiate this hypothesis by the temporary improvement of the conductance at $t = 150$ s before the onset of electromigration discussed in Figure 2a. The SEM image of Figure 2c is also providing additional confirmation of a partial annealing of the constriction. In the area marked "annealed zone" in the image, the concentration of triple points considerably reduces and the dimensions of grain sizes increase. The constriction is thus less susceptible to failure because diffusion of atoms is facilitated by these polycristalline structural defects [39]. Secondly, the gap is occurring at the source electrode because charge carriers here first collide with grain boundaries to initiate atom diffusion as it can be seen by number of voids present in this electrode (Figure 2c).

Electrical characterization

The electrical characterization of the tunneling feedgap forming the active area of the optical antenna primarily consists of measuring the current-to-voltage characteristics $I_T(V_{dc})$. An example is illustrated in Figure 3a. In this graph, the current density ($J_T = I_T/A$) is displayed for an arbitrary tunneling junction area A, chosen at 100 nm^2.

For a tunneling barrier subject to a small applied bias, the transport may be described by Simmons' equation of tunneling electrons [40]:

$$J_T \left(eV \ll \Phi \right) = \frac{I_T}{A} = \frac{e^2}{h^2} \frac{\sqrt{2m\phi}}{d} V_{dc} \exp\left[-B\sqrt{\phi} \right], \quad (1)$$

where $B = 4\pi d h^{-1}\sqrt{2m}$, A and d are the effective area and width of the junction, m is the electron mass, and h is Planck's constant. The average barrier height ϕ includes the presence of an image potential that reduces the barrier height. Considering that the work function of gold is ca. 5.4 eV, Equation 1 is usually valid for applied bias voltages up to a few volts.

The shape of the tunneling characteristics of $I_T(V_{dc})$ essentially depends on the parameters d and ϕ with minor corrections from the effective area A [41]. These parameters can be extracted by fitting the experimental characteristics. Generally, the current-to-voltage plots measured from electromigrated gaps are not symmetrical with respect to the applied bias. The irregularities of the gap, such as protrusions, affect the two sides of the

Figure 3: (a) Current density J_T plotted versus applied bias V_{dc}. The black circles are experimental data points and the solid red line is the best fit to the data using Simmons' model of tunneling transport. (b) The fitting parameters ϕ, $\Delta\phi$, and *d* as functions of the junction area *A*. The yellow frame represents a parameter space consistent with respect to the experimental measurements.
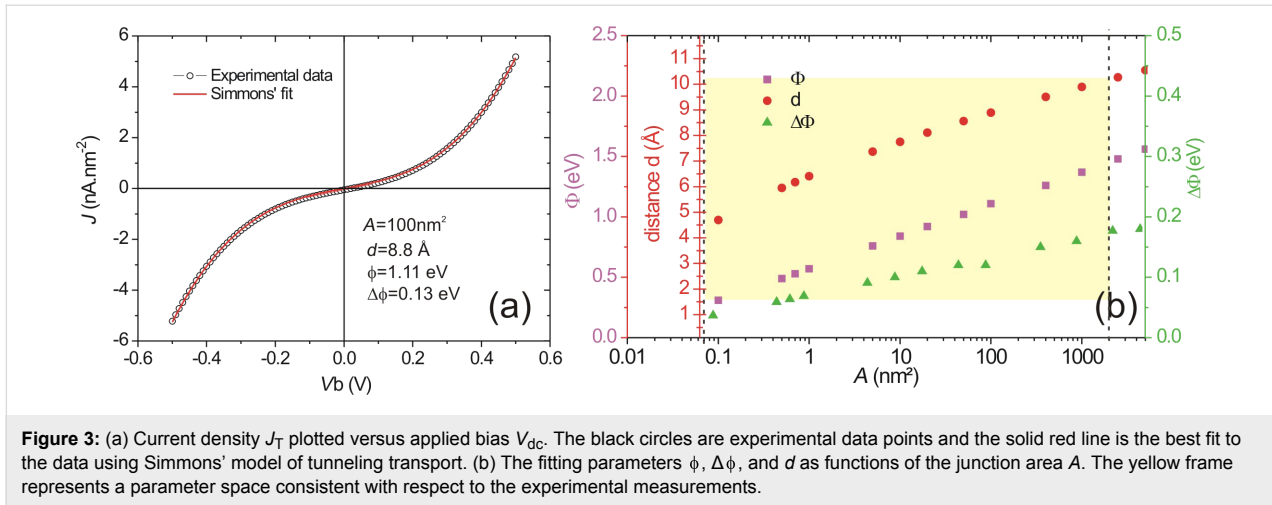
energy barrier, ϕ_1 and ϕ_2, differently [42] leading to asymmetric output characteristics. Electron tunneling through an asymmetrical trapezoidal barrier is described following Brinkman's formalism [43]:

$$G\left(V_{dc}\right) = G_{\left(V_{dc}=0\right)}\left(1 - \frac{A_0 \Delta\phi}{32\phi^{3/2}} V_{dc} + \frac{3 A_0^2}{128\phi} V_{dc}^2\right), \quad (2)$$

with $A_0 = 4\sqrt{2md}/(3\hbar)$ and $\Delta\phi = \phi_1 - \phi_2$. $G_{\left(V_{dc}=0\right)}$ is the zero-bias conductance:

$$G_{\left(V_{dc}=0\right)} = A \cdot 10^{-18} \frac{e^2}{h^2} \frac{\sqrt{2m\phi e}}{d \times 10^{-10}} \exp\left[-\frac{4\pi d \times 10^{-10}}{h}\sqrt{2m\phi e}\right]$$

$$= A \cdot 3.16 \cdot 10^{-4} \frac{\sqrt{\phi}}{d} \exp\left[-1.025 d\sqrt{\phi}\right]. \quad (3)$$

d is here in angstroms, *A* is in square nanometers, *e* is in coulombs and ϕ is in electronvolts. Combining Equation 2 and Equation 3, the current density $J_T(V_{dc})$ is

$$J_T\left(V_{dc}\right) = \int_0^{V_{dc}} G\left(V_{dc}\right) dV_{dc}$$

$$= \left(V_{dc} - \frac{A_0 \Delta\phi}{32\phi^{3/2}} V_{dc}^2 + \frac{3 A_0}{128} V_{dc}^3\right)$$

$$\cdot 3.16 \cdot 10^{-4} \frac{\sqrt{\phi}}{d} \exp\left[-1.025 d\sqrt{\phi}\right] \quad (4)$$

$$= \left(\frac{3.16 \times 10^{-4} \sqrt{\phi}}{d} V_{dc} - \frac{2.7 \times 10^{-5} \Delta\phi}{\phi} V_{dc}^2\right.$$

$$\left. + \frac{5.5 \times 10^{-5} d\sqrt{\phi}}{\phi} V_{dc}^3\right) \exp\left[-1.025 d\sqrt{\phi}\right].$$

The set of parameters [*d*, ϕ and $\Delta\phi$] is determined by conducting a fit to the experimental data as shown by the red curve in Figure 3a. We arbitrarily set the effective area to $A = 100$ nm^2 because we cannot obtain a precise experimental determination of the active area in which the electrons tunnel from the complex morphology of electromigrated gaps. In Figure 3b, we explore the dependence of *d*, ϕ and $\Delta\phi$ on the area *A*. The yellow region in the graph shows the boundaries of the parameter space, limited on one side by half of the area occupied by a gold atom, and on the other side, by the cross-sectional area of the constriction. Even with a variation of *A* by four orders of magnitude, the estimated gap size remains at *d* < 1 nm. Such a small distance between two electrodes is the key characteristics for developing the novel generation of electro-optical antennas discussed here.

It is interesting to display the characteristics of $J_T(V_{dc})$ using the so-called Fowler–Nordheim representation to understand the physical meaning of the average barrier height ϕ, which is in the region considered in Figure 3b considerably lower than the work function of gold. The Fowler–Nordheim plot, $\ln(J_T/V_{dc}^2)$ as a function of $1/V_{dc}$, is commonly used to distinguish the transition between direct tunneling at low V_{dc} and a high-bias regime where the energy barrier is drastically reduced and electrons are tunneling by field emission [44]. Thus, the representation isolates two extreme cases of bias polarization: $\left|eV_{dc}\right| \ll \phi$ and $\left|eV_{dc}\right| \gg \phi$ separated by a minimum in the plot indicating the cross-over between the transport regimes. The effective barrier height of the electrodes may be directly inferred from this minimum, commonly referred to as the transition voltage V_t.

The Fowler–Nordheim plot of the $J_T(V_{dc})$ characteristics discussed in Figure 3 is displayed in Figure 4a. Two clear minima are identified with respect to bias polarity at nearly symmetric

values $1/V_t^- = -3.51 \pm 0.16$ V^{-1} and $1/V_t^+ = 3.5 \pm 0.09$ V^{-1}, corresponding to an average transition voltage $|V_t| = 0.28$ V. It is immediately obvious here that the transition voltage inferred from the Fowler–Nordheim plot differs significantly from the average barrier height resulting from Simmons' model ($\phi = 1.11$ eV). However, such a low value of ϕ is consistently reported in Au tunnel junctions [19,26,41,45] and is tentatively attributed to surface states on the electrodes [41,46], the effect of image charges [47], the presence of protruding atoms [48] or a Schottky contact [45]. Despite this body of work, the interpretation of the Fowler–Nordheim plot and the transition voltage has been debated in the past. Huisman et al. [49] followed by Vilan et al. [50] argued that the inflection in the Fowler–Nordheim plot is a generic property of the nonlinear characteristics and takes place when the third-order term in Equation 2 becomes important. By recasting Equation 2 in the Fowler–Nordheim form, we find an analytical expression for V_t by searching the minimum of the function:

$$V_t = \frac{2\hbar}{\sqrt{m}} \cdot \frac{\sqrt{3\phi}}{d},\qquad(5)$$

where $\hbar$ is in electronvolts and d is in angstroms. Equation 5 shows that the transition voltage does not depend on the barrier height ϕ but on the ratio between the square root of the average barrier height and the barrier width, $\sqrt{\phi}/d$. Huisman derived a similar expression [49] using Stratton's tunneling formalism with a dependence on $\sqrt{2\phi}/d$. Inserting the values of ϕ and d deduced from Simmons' fit to Equation 5 leads to $V_t = 0.28$ V, which is exactly the value inferred from the Fowler–Nordheim plot. To reinforce this interpretation of the transition voltage,

we plot in Figure 4b the $\sqrt{\phi}/d$-dependence of the transition voltages measured on either side of the Fowler–Nordheims plot for a series of 15 electromigrated junctions. The solid black curve is $|V_t|$ calculated using Equation 5 and the parameters ϕ and d extracted from fitting the experimental data of $J_T(V_{dc})$ with Equation 4. The dependence of the transition voltage on $\sqrt{\phi}/d$ is clearly revealed from the graph, demonstrating that V_t cannot be an estimate of the tunneling barrier height.

Even if the Fowler–Nordheim plot of the device shown in Figure 4a feature a symmetric transition voltage with respect to the bias polarities, electromigrated junctions may have asymmetric current-to-voltage characteristics; the data points representing $\left|V_t^-\right|$ and V_t^+ in Figure 4b do not generally coincide. This is expected from the irregular morphology of the junction and its influence onto the barrier height [51].

Light-emitting electron-fed optical antennas

The electromigrated planar junctions discussed above may serve as light-emitting optical antennas when electrons are injected in the tunnel barrier formed between the two metal leads. The junction acts as the antenna feed because radiation is emitted from this driven element [52].

Light emitted from tunnel junctions has been heavily investigated since the pionner work of Lambe and McCarthy [53] and is generally attributed to inelastic scattering of tunneling electrons into radiative surface plasmon modes. Generally, spectra detected from electrically-driven on-chip optical antennas are in agreement with this picture [19-21,27,54]. However, some authors reported an over-bias emission from atomic contacts where the emitted spectra are no longer limited by the kinetic
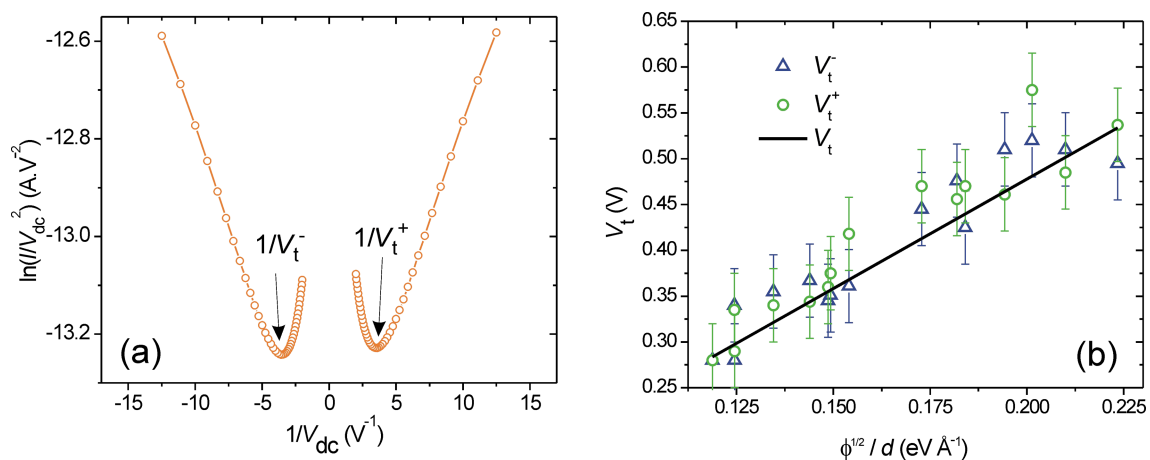
Figure 4: (a) Fowler–Nordheim representation of the $J_T(V_{dc})$ data shown in Figure 3a. The transition voltages V_t^- and V_t^+ are determined from the inflection points of the representation. (b) $\left|V_t^-\right|$ and V_t^+ as functions of $\sqrt{\phi}/d$ for 15 electromigrated junctions. The solid line is the transition voltage V_t calculated with Equation 5 and the parameters ϕ and d deduced from Simmons' fit of the electrical characteristics.

energy of the electrons given by the applied bias [18,55,56]. In these devices, the emission is described by thermal radiation of an out-of-equilibrium heated electron distribution, which is promoted by the electron–electron interaction dynamics. Both light-emission mechanisms may be observed in the electromigrated junctions discussed in the previous section as illustrated in Figure 5. Prevalence of inelastic scattering in the barrier over electronic heating essentially depends on the conductance of the device and the current density flowing through the contact. Typically, the quantum cutoff $h\nu < eV_{dc}$ is violated when $0.1G_0 < G < G_0$, where ν is the frequency of the photon.

In the left column of Figure 5, we show an example of emission from a hot distribution of carriers for an electromigrated junction biased at $V_{dc} = 1.1$ V. The light generated by the tunnel junction upon electrical biasing and emitting in the substrate is collected using an inverted optical microscope (Nikon, Eclipse) equipped with a 100×, 1.49 numerical aperture (N.A.) objective and a charge-coupled device (CCD) camera recording the object plane of the microscope (Andor, Luca EM S 658M). The resolution of the microscope is about 300 nm at 800 nm emission wavelength. The optical activity in Figure 5b is restricted to the location of the gap (not distinguishable in the optical transmission image of Figure 5a). The electrical characteristics (Figure 5c) feature a value of $G_{(V_{dc}=0)} = 69$ µS $= 0.9G_0$. Figure 5d shows the emission spectrum of the device taken at $V_{dc} = 900$ mV. In the framework of inelastic electron tunneling, no light should be detected in the sensitivity window of Si-based devices because at $V_{dc} = 900$ mV, the wavelength at the quantum cutoff is 1300 nm to which the Si detectors are

Figure 5: (a) Transmission optical image showing a series of electromigrated constrictions. (b) Optical image of the light emission when the centered junction is biased at 1.1 V. (c) Corresponding current-to-voltage characteristics where the black and red curves are the forward and backward voltage sweep, respectively. (d) Emission spectrum recorded for $V_{dc} = 0.9$ V. The entire spectrum violates the quantum cutoff since $h\nu > eV_{dc}$. (e) and (f) are images of another series of electromigrated gaps showing the respective layout of the structure and the optical activity when the center junction is biased at 4.0 V. (g) Corresponding current-to-voltage characteristics. (h) Electroluminescent spectrum of the light-emitting device obtained at $V_{dc} = 4$ V. The emission is characteristic of inelastic electron tunneling events with $h\nu < eV_{dc}$. The spectra are corrected for the quantum efficiency of the CCD camera and the transmission of the microscope.

blind. Clearly, the spectrum is violating this quantum cutoff. Here, this overbias response is understood from the spontaneous emission of hot carriers, accelerated by the electric field present at the junction, and colliding with the boundary of the gap [18]. The detected spectrum is thus the visible tail of a thermal peak located in the infrared. The position of peak is not directly related to the bias via the quantum relation cited above, but to the electronic temperature of the hot electrons responsible for the emission. In our previous report on analogous devices [18], electron temperatures exceeding 1000 K were measured for similar operating conditions, which pushes the thermal peak roughly between 2 and 3 µm.

The column on the right of Figure 5 illustrates an example of electromigrated junction operating in a different emission regime. Here the device is biased at $V_{dc} = 4.0$ V. Very much like the thermal glow of Figure 5b, the active region is restricted to the tunnel gap, but the electrical characteristic (Figure 5g) gives $G_{(V_{dc}=0)} = 5.6 \cdot 10^{-8}$ µS $= 7 \cdot 10^{-4}$ G_0. The spectrum emitted by the optical tunneling gap antenna is consistent with the quantum cutoff; the energy of the detected photons is smaller than the kinetic energy of the tunnel electrons. The substantial drop of intensity below 600 nm is due to the onset of interband transitions in the material. For this device, the emission is probably resulting from the radiative decay of surface plasmons populated by inelastic tunnel electrons [19-21].

In the following section we show examples of devices where light emission from tunneling electron-fed optical antennas is not simply radiated in free-space but partially coupled to waveguiding architectures. Here, the objective is to implement a first technological step to integrate compact transducing tunnel optical antennas directly at the input port of photonic links to provide for an electronically driven optical transmission line with broadband spectral characteristics. This asset may help at increasing the bandwidth via wavelength-division multiplexing. Integrated broadband sources are also utilized in photonic sensing chips [57] or to command non-classical secondary photon sources [58]. There is thus a demand for versatile and low-cost integrated light sources, and optical tunneling gap antennas may provide an alternative technology to solid-state light emitting diodes or quantum dots. Coupling of such a junction have been recently demonstrated in plasmonic strips [27,59] and we extend the concept to dielectric TiO_2 waveguides and slot geometry.

Electrically connected optical antennas on TiO_2 waveguides

Because the emission spans the visible part of the spectrum, and, depending on the underlying mechanism, extends to near-infrared wavelengths, standard silicon-based platforms are not adapted to collect and guide photons emitted by the junctions. For the operation at visible wavelengths waveguiding structures composed of TiO_2 feature interesting material properties [60,61] such as broadband transparency, high refractive index, compatibility with complementary metal-oxide semiconductors and ease of processing.

We realize the implementation of tunneling antennas on a TiO_2 waveguide through a multi-step process. First, a 85 to 110 nm thick titanium dioxide layer is deposited by physical vapor deposition on a clean glass substrate. Then, the Au backbone that will subsequently define the electrically connected tunneling optical antennas is fabricated by electron-beam lithography, Au evaporation and lift-off process. The structures consist of either a gold nanowire of 1.1 µm length and 130 nm width or a constriction as discussed above. For both types, the structures are connected to a set of electrodes. The thickness of the nanowire and electrodes is 50 nm, including a 5 nm Ti adhesion layer. The third step is the dry etching of the TiO_2 layer. For that, we first create an etching mask by electron-beam lithography, thermal deposition of a 30 nm thick nickel layer and lift-off. Reactive ion etching is then used to remove the TiO_2 layer and to define the waveguides. More details about this etching process can be found in [62]. A last optical lithography step is carried out to define the macroscopic leads that are connected to the microscopic electrodes. The process is subsequently terminated by electromigrating in situ the nanowire to create the optical tunneling gap antenna. Figure 6a,c,e illustrates the experiment with different waveguide geometries and gap orientations. In Figure 6a, the TiO_2 waveguide is 85 nm thick and 1.5 µm wide, and the SEM image was taken before the electromigration of the nanowire. In Figure 6c and Figure 6e the waveguides have a cross section of 500 nm × 110 nm and both images were taken after creating the optical tunneling gap antennas. Note that in Figure 6e, the displacement of the junction towards the source electrode has been taken into account to place the tunneling gap at the center of the waveguide.

Figure 6b,d,f shows false-color CCD images showing the distribution of the light radiated in the substrate when the tunneling junctions are biased by V_{dc}. The electrical operating conditions are reported in the images. In all these devices, light is most likely emitted by inelastic tunneling because the detected spectral range is below the bias energy: $h\nu < eV_{dc}$. The zero-bias conductance values are all about $10^{-2}G_0$.

In the set of images in Figure 6, the strongest signal detected through the glass slide originates from the junction itself. However, the images show also that light emerges from the distal end of the TiO_2 stripes indicating that a portion of the power emitted by the electron-fed antennas is coupled to the dielectric
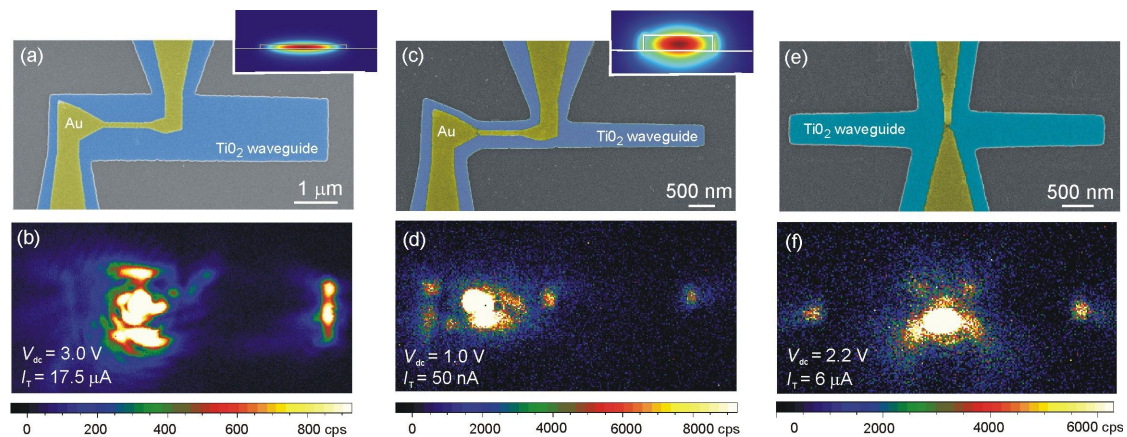
Figure 6: (a, c, e) Colorized scanning electron micrographs of the electron-fed optical antennas integrated in various waveguiding geometries. The yellow and blue hues show the Au and TiO_2 materials, respectively, and the glass substrate appears in gray. The TiO_2 waveguides are 1.5 µm wide in (a) and 500 nm wide in (c) and (e). The Au electrodes are parallel to the waveguide axis in (a) and (c) while in (e), the orientation of the electrodes is perpendicular to the two symmetrical TiO_2 stripes. Insets: Calculated modal distribution of the electric field norm in the waveguides evaluated at 800 nm. (b, d, f) False-color CCD images of the distribution of light in the structure upon electrical biasing of the tunnel junction. The electrical conditions are given in the images and the integration time is 30 s for all frames. The color scale is saturated to enhance the contrast.
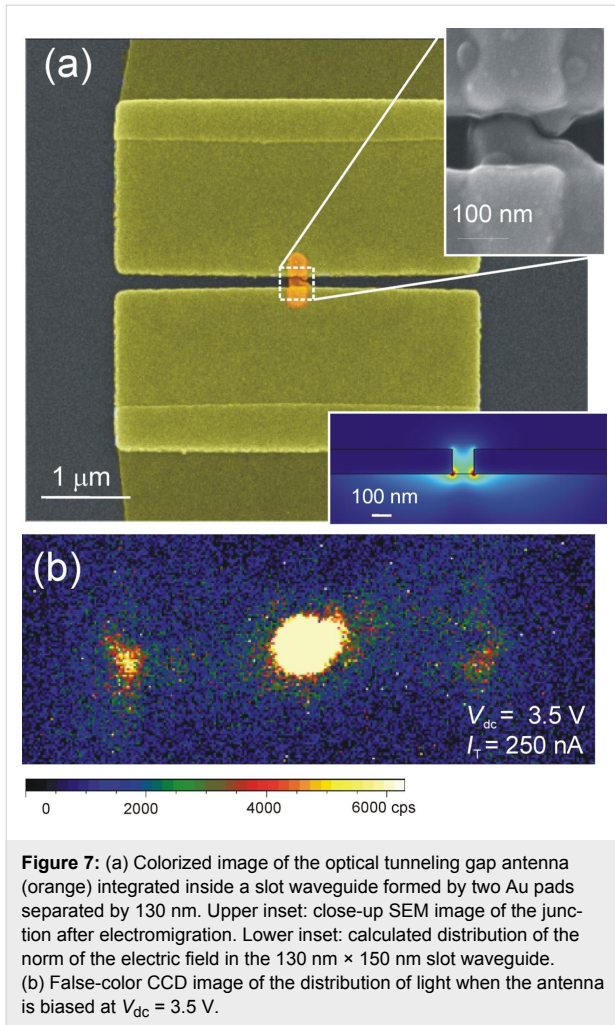
structure and is transmitted away from the radiating feedgap. The optical tunneling gap antenna may therefore be used as an electrically activated local source of light. An absolute coupling efficiency is difficult to estimate since only the light emitted in the substrate is collected here. Nonetheless, we may qualitatively evaluate an effective coupling yield and compare devices. We numerically assess the characteristics of the mode supported by the TiO_2 waveguides by a two-dimensional finite element calculation (Comsol software) using published values of the refractive index of TiO_2[63]. The insets of Figure 6a and Figure 6c display cross-sectional views of the norm of the electric field existing in the waveguides at a wavelength of 800 nm. At the operating voltage, the emission of the electron-fed antenna is typically spanning the visible and near-infrared spectral region. For the TiO_2 geometries discussed here, the confinement loss is calculated to be about 10^{-2} dB for a 10 µm long waveguide. We may therefore neglect propagation losses in the TiO_2 while estimating the coupling ratio. In Figure 6b, the light collected at the waveguide termination is about 12% of the total signal received on the detector. Optimizing the amount of power emitted by the local source and transferred to the waveguided modes requires to shape the wavevector distribution radiated by the antenna and to reduce the influence of the electrode. This may be achieved by introducing multi-element antennas [16,64]. The electromigrated gap features the characteristic of a dipolar source [18] despite the marked nanometer-scale irregularities of the gap itself. Structuring the immediate environment of the junction, i.e., the feed of the antenna, with elements acting as a reflector and directors may help in shaping the broadband-emission diagram emitted in the dielectric and improve the overlap with photonic modes. There are also

reports of efficient coupling by engineering a cladding material surrounding the active emitting area [65], by a heterogeneous integration of the source in a structured waveguide [66,67], or by using extreme modal confinement [68].

We have tried simple steps to increase the apparent coupling yield to the modes sustained by the geometries without relying on directivity-enhanced designs or more complex engineering. As it can be observed in Figure 6b and Figure 6d, scattering takes place at the edges of the waveguide right above and below the location of the junction as well as on the Au electrodes. Thus, losses imparted by the electrodes at the top of the waveguide are present and contribute to attenuating the mode in this part of the waveguide. These scattering information further suggest that the antenna radiates also in a direction perpendicular to the main axis of the waveguide. To decrease these scattering points, we introduce the geometry of Figure 6e, where the waveguides are oriented perpendicular to the electrodes. While the amount of signal emerging from the distal ends remains modest (8% on the left port and 6% on the right port), scattering and attenuation by the electrical circuit is reduced.

Electrically connected optical antennas emitting in slot waveguides

Figure 7 shows another example of the integration of optical tunneling gap antennas. In this configuration, the electromigrated junction is located between two 130 nm thick large metallic pads forming a slot waveguide. Slot waveguides are characterized by deep modal confinement while maintaining micrometer-range propagation [69]. Excitation of the mode from free-space radiation is usually insured by the mediation of

Figure 7: (a) Colorized image of the optical tunneling gap antenna (orange) integrated inside a slot waveguide formed by two Au pads separated by 130 nm. Upper inset: close-up SEM image of the junction after electromigration. Lower inset: calculated distribution of the norm of the electric field in the 130 nm × 150 nm slot waveguide. (b) False-color CCD image of the distribution of light when the antenna is biased at V_{dc} = 3.5 V.

passive antenna couplers [70]. In the example shown in Figure 7, the 130 nm wide slot is directly excited in situ by the emission of the electron-fed antenna, providing thereby a simultaneous excitation and coupling strategy of the modal landscape with a self-content ultracompact device. As in the case of the TiO$_2$ waveguide, the strongest detected signal originates from the junction itself. However, light is also observed at the two outputs of the slot demonstrating that confined modes can be electrically excited by the junction.

The percentage of light scattered at the slot termination represents about 10% of the total collected signal. If we take into account the attenuation of the mode, the percentage effectively coupled to the mode at the location of the source is likely to be higher. We also estimated the propagation length of the slot mode using finite-element simulations. A cross-sectional view of the norm of the electric field is shown in the inset of Figure 7 for a mode existing at 800 nm. The field is mostly located in the slot and the calculated propagation length is L_{spp} = 6.2 μm. If we take this attenuation into account, the percentage of the light

coupled to the waveguide can be evaluated in the following manner. Starting from the intensities measured at both ends of the slot waveguide I_{end}^{left} and I_{end}^{right}, we first calculate the intensity coupled to the waveguide mode I_{mod} at the location of the feed:

$$I_{mod} = \left(I_{end}^{left} + I_{end}^{right} \right) \exp\left(2\mu m / L_{spp} \right).$$

We then calculate the coupling coefficient Γ by normalizing I_{mod} with the total intensity collected by the CCD camera including the intensity effectively recorded at the position of the antenna I_{feed} and the estimated intensity delivered to the waveguided mode I_{mod}:

$$\Gamma = \frac{I_{mod}}{I_{feed} + I_{mod}} \approx 30\%. \tag{6}$$

The somewhat larger coupling ratio of the antenna emission to the slot mode can be understood from the increased modal confinement compared to dielectric TiO$_2$ waveguides. Because the emission is radiated from the nanometer-scale feedgap of the electromigrated junction, the emitted wavevector distribution matches better the momentum of the mode confined between the two metal electrodes.

Conclusion

We argue in this work the potential of electromigrated in-plane tunnel junctions to act as electron-fed light-emitting optical antennas. Starting from an electrically connected gold constriction, we describe the electromigration process by a constant monitoring of the electrical conductance. We analyze the different signatures leading to the formation of the gap including the occurrence of quantized conductance steps characteristic of a ballistic transport of electrons. We detail the balanced contribution of the thermal dissipation, which is on one hand required to assist the electromigration but is, on the other hand, preventing the formation of the gap at the constriction. The electrical nonlinear properties of the tunnel junction are investigated with a standard model of electron tunneling enabling to extract crucial parameters such as the gap size and the effective barrier height. We discuss the interpretation of the Fowler–Nordheim representation and show that the transition voltage deduced from this representation not only depends on the energy barrier height as commonly reported, but also on the barrier width. We show that upon injection of electrons, the electromigrated tunnel junctions are emitting light. The emission mechanism depends on the zero-bias conductance G of the tunnel junction. Roughly speaking, light is generated by inelastic tunneling events when G is much smaller than the quantum of conductance G_0 in accordance with the standard description of electromagnetic ra-

diation produced in metal–insulator–metal devices. However, when the gap is small (few angstroms) and G approaches G_0, the energy of the photons exceeds the energy of the electrons provided by the bias, and the emission originates from the glowing radiation of a hot electron gas. We finally demonstrate that these electron-fed optical antennas produced by electromigration can be integrated into more complex device architectures. In particular, we show that the emission released by the feedgap can be coupled to propagating modes with the efficiency approaching 30% for slot waveguides. Additional efforts are required to optimize the coupling yield, notably by developing strategies to shape the momentum and the energy of emitted photons. The devices discussed in this report may also be used for the reverse transduction whereby an incoming electromagnetic radiation is rectified to produce an electrical current flowing in the circuitry [23,26]. The interfacing of electron-fed optical antenna with an optical rectenna may thus open a new era for on-chip communication between distant nanometer-scale emitters and receivers [71].

Acknowledgements

ORCID® iDs

Kamal Hammani - https://orcid.org/0000-0003-4271-7539
Alexander Uskov - https://orcid.org/0000-0001-8816-4103
Igor Smetanin - https://orcid.org/0000-0002-0303-4543

References

1. Roelkens, G.; Liu, L.; Liang, D.; Jones, R.; Fang, A.; Koch, B.; Bowers, J. *Laser Photonics Rev.* **2010,** *4,* 751–779. doi:10.1002/lpor.200900033
2. Liu, L.; Roelkens, G.; van Campenhout, J.; Brouckaert, J.; van Thourhout, D.; Baets, R. *J. Nanosci. Nanotechnol.* **2010,** *10,* 1461–1472. doi:10.1166/jnn.2010.2032
3. Carloni, L. P.; Pande, P.; Xie, Y. Networks-on-chip in emerging interconnect paradigms: Advantages and challenges. In *2009 3rd ACM/IEEE International Symposium on Networks-on-Chip,* 2009; pp 93–102.
4. Deb, S.; Ganguly, A.; Pande, P. P.; Belzer, B.; Heo, D. *IEEE J. Emerging Sel. Top. Circuits Syst.* **2012,** *2,* 228–239. doi:10.1109/jetcas.2012.2193835
5. Matolak, D. W.; Kodi, A.; Kaya, S.; Ditomaso, D.; Laha, S.; Rayess, W. *IEEE Wireless Commun.* **2012,** *19,* 58–65. doi:10.1109/mwc.2012.6339473
6. Kaya, S.; Laha, S.; Kodi, A.; Ditomaso, D.; Matolak, D.; Rayess, W. On ultra-short wireless interconnects for NoCs and SoCs: Bridging the 'THz Gap'. In *2013 IEEE 56th International Midwest Symposium on Circuits and Systems (MWSCAS),* 2013; pp 804–808.
7. Alù, A.; Engheta, N. *Phys. Rev. Lett.* **2010,** *104,* 213902. doi:10.1103/physrevlett.104.213902
8. Bharadwaj, P.; Deutsch, B.; Novotny, L. *Adv. Opt. Photonics* **2009,** *1,* 438–483. doi:10.1364/aop.1.000438
9. Novotny, L.; van Hulst, N. *Nat. Photonics* **2011,** *5,* 83–90. doi:10.1038/nphoton.2010.237
10. Mühlschlegel, P.; Eisler, H.-J.; Martin, O. J. F.; Hecht, B.; Pohl, D. W. *Science* **2005,** *308,* 1607–1609. doi:10.1126/science.1111886
11. Gérard, D.; Wenger, J.; Devilez, A.; Gachet, D.; Stout, B.; Bonod, N.; Popov, E.; Rigneault, H. *Opt. Express* **2008,** *16,* 15297–15303. doi:10.1364/oe.16.015297
12. Schuller, J. A.; Brongersma, M. L. *Opt. Express* **2009,** *17,* 24084–24095. doi:10.1364/oe.17.024084
13. Alù, A.; Engheta, N. *Phys. Rev. Lett.* **2008,** *101,* 43901. doi:10.1103/PhysRevLett.101.043901
14. Huang, C.; Bouhelier, A.; Colas des Francs, G.; Bruyant, A.; Guenot, A.; Finot, E.; Weeber, J.-C.; Dereux, A. *Phys. Rev. B* **2008,** *78,* 155407. doi:10.1103/physrevb.78.155407
15. Curto, A. G.; Volpe, G.; Taminiau, T. H.; Kreuzer, M. P.; Quidant, R.; van Hulst, N. F. *Science* **2010,** *329,* 930–933. doi:10.1126/science.1191922
16. Pavlov, R. S.; Curto, A. G.; van Hulst, N. F. *Opt. Commun.* **2012,** *285,* 3334–3340. doi:10.1016/j.optcom.2012.04.010
17. Prangsma, J. C.; Kern, J.; Knapp, A. G.; Grossmann, S.; Emmerling, M.; Kamp, M.; Hecht, B. *Nano Lett.* **2012,** *12,* 3915–3919. doi:10.1021/nl3007374
18. Buret, M.; Uskov, A. V.; Dellinger, J.; Cazier, N.; Mennemanteuil, M.-M.; Berthelot, J.; Smetanin, I. V.; Protsenko, I. E.; Colas-des-Francs, G.; Bouhelier, A. *Nano Lett.* **2015,** *15,* 5811–5818. doi:10.1021/acs.nanolett.5b01861
19. Kern, J.; Kullock, R.; Prangsma, J.; Emmerling, M.; Kamp, M.; Hecht, B. *Nat. Photonics* **2015,** *9,* 582–586. doi:10.1038/nphoton.2015.141
20. Parzefall, M.; Bharadwaj, P.; Jain, A.; Taniguchi, T.; Watanabe, K.; Novotny, L. *Nat. Nanotechnol.* **2015,** *10,* 1058–1063. doi:10.1038/nnano.2015.203
21. Gurunarayanan, S. P.; Verellen, N.; Zharinov, V. S.; James Shirley, F.; Moshchalkov, V. V.; Heyns, M.; Van de Vondel, J.; Radu, I. P.; Van Dorpe, P. *Nano Lett.* **2017,** *17,* 7433–7439. doi:10.1021/acs.nanolett.7b03312
22. Guhr, D. C.; Rettinger, D.; Boneberg, J.; Erbe, A.; Leiderer, P.; Scheer, E. *Phys. Rev. Lett.* **2007,** *99,* 086801. doi:10.1103/physrevlett.99.086801
23. Ward, D. R.; Hüser, F.; Pauly, F.; Cuevas, J. C.; Natelson, D. *Nat. Nanotechnol.* **2010,** *5,* 732–736. doi:10.1038/nnano.2010.176
24. Arielly, R.; Ofarim, A.; Noy, G.; Selzer, Y. *Nano Lett.* **2011,** *11,* 2968–2972. doi:10.1021/nl201517k
25. Miskovsky, N. M.; Cutler, P. H.; Mayer, A.; Weiss, B. L.; Willis, B.; Sullivan, T. E.; Lerner, P. B. *J. Nanotechnol.* **2012,** *2012,* 19. doi:10.1155/2012/512379
26. Stolz, A.; Berthelot, J.; Mennemanteuil, M.-M.; Colas des Francs, G.; Markey, L.; Meunier, V.; Bouhelier, A. *Nano Lett.* **2014,** *14,* 2330–2338. doi:10.1021/nl404707t
27. Du, W.; Wang, T.; Chu, H.-S.; Nijhuis, C. A. *Nat. Photonics* **2017,** *11,* 623–627. doi:10.1038/s41566-017-0003-5

28. Savage, K. J.; Hawkeye, M. M.; Esteban, R.; Borisov, A. G.; Aizpurua, J.; Baumberg, J. J. *Nature* **2012,** *491,* 574–577. doi:10.1038/nature11653

29. Sanders, A.; Bowman, R. W.; Baumberg, J. J. *Sci. Rep.* **2016,** *6,* 32988. doi:10.1038/srep32988

30. Zhu, W.; Esteban, R.; Borisov, A. G.; Baumberg, J. J.; Nordlander, P.; Lezec, H. J.; Aizpurua, J.; Crozier, K. B. *Nat. Commun.* **2016,** *7,* 11495. doi:10.1038/ncomms11495

31. Beenakker, C. W. J.; Schomerus, H. *Phys. Rev. Lett.* **2004,** *93,* 096801. doi:10.1103/physrevlett.93.096801

32. Zakka-Bajjani, E.; Dufouleur, J.; Coulombel, N.; Roche, P.; Glattli, D. C.; Portier, F. *Phys. Rev. Lett.* **2010,** *104,* 206802. doi:10.1103/physrevlett.104.206802

33. Pierce, D.; Brusius, P. *Microelectron. Reliab.* **1997,** *37,* 1053–1072. doi:10.1016/s0026-2714(96)00268-5

34. Strachan, D. R.; Smith, D. E.; Johnston, D. E.; Park, T.-H.; Therien, M. J.; Bonnell, D. A.; Johnson, A. T. *Appl. Phys. Lett.* **2005,** *86,* 043109. doi:10.1063/1.1857095

35. Mennemanteuil, M.-M.; Buret, M.; Cazier, N.; Colas des Francs, G.; Bouhelier, A.; Besbes, M.; Ben-Abdallah, P. *Phys. Rev. B* **2016,** *94,* 035413. doi:10.1103/physrevb.94.035413

36. Esen, G.; Fuhrer, M. S. *Appl. Phys. Lett.* **2005,** *87,* 263101. doi:10.1063/1.2149174

37. Shi, S.-F.; Xu, X.; Ralph, D. C.; McEuen, P. L. *Nano Lett.* **2011,** *11,* 1814–1818. doi:10.1021/nl200522t

38. Ward, D. R.; Halas, N. J.; Natelson, D. *Appl. Phys. Lett.* **2008,** *93,* 213108. doi:10.1063/1.3039060

39. Cho, J.; Thompson, C. V. *Appl. Phys. Lett.* **1989,** *54,* 2577–2579. doi:10.1063/1.101054

40. Simmons, J. G. *J. Appl. Phys.* **1963,** *34,* 1793–1803. doi:10.1063/1.1702682

41. Mangin, A.; Anthore, A.; Della Rocca, M. L.; Boulat, E.; Lafarge, P. *Phys. Rev. B* **2009,** *80,* 235432. doi:10.1103/physrevb.80.235432

42. Mayer, A.; Chung, M. S.; Lerner, P. B.; Weiss, B. L.; Miskovsky, N. M.; Cutler, P. H. *J. Vac. Sci. Technol., B: Nanotechnol. Microelectron.: Mater., Process., Meas., Phenom.* **2011,** *29,* 041802. doi:10.1116/1.3599756

43. Brinkman, W. F.; Dynes, R. C.; Rowell, J. M. *J. Appl. Phys.* **1970,** *41,* 1915–1921. doi:10.1063/1.1659141

44. Beebe, J. M.; Kim, B.; Gadzuk, J. W.; Daniel Frisbie, C.; Kushmerick, J. G. *Phys. Rev. Lett.* **2006,** *97,* 026801. doi:10.1103/physrevlett.97.026801

45. Frimmer, M.; Puebla-Hellmann, G.; Wallraff, A.; Novotny, L. *Appl. Phys. Lett.* **2014,** *105,* 221118. doi:10.1063/1.4903748

46. Bâldea, I. *EPL* **2012,** *98,* 17010. doi:10.1209/0295-5075/98/17010

47. Sotthewes, K.; Hellenthal, C.; Kumar, A.; Zandvliet, H. J. W. *RSC Adv.* **2014,** *4,* 32438–32442. doi:10.1039/c4ra04651j

48. Wu, K.; Bai, M.; Sanvito, S.; Hou, S. *Nanotechnology* **2013,** *24,* 025203. doi:10.1088/0957-4484/24/2/025203

49. Huisman, E. H.; Guédon, C. M.; van Wees, B. J.; van der Molen, S. J. *Nano Lett.* **2009,** *9,* 3909–3913. doi:10.1021/nl9021094

50. Vilan, A.; Cahen, D.; Kraisler, E. *ACS Nano* **2013,** *7,* 695–706. doi:10.1021/nn3049686

51. Miskovsky, N. M.; Shepherd, S. J.; Cutler, P. H.; Sullivan, T. E.; Lucas, A. A. *Appl. Phys. Lett.* **1979,** *35,* 560–562. doi:10.1063/1.91179

52. Parzefall, M.; Bharadwaj, P.; Novotny, L. Antenna-Coupled Tunnel Junctions. In *Quantum Plasmonics;* Bozhevolnyi, S. I.; Martin-Moreno, L.; Garcia-Vidal, F., Eds.; Springer: Berlin, Germany, 2017; pp 211–236.

53. Lambe, J.; McCarthy, S. L. *Phys. Rev. Lett.* **1976,** *37,* 923–925. doi:10.1103/PhysRevLett.37.923

54. Vardi, Y.; Cohen-Hoshen, E.; Shalem, G.; Bar-Joseph, I. *Nano Lett.* **2016,** *16,* 748–752. doi:10.1021/acs.nanolett.5b04622

55. Malinowski, T.; Klein, H. R.; Iazykov, M.; Dumas, P. *EPL* **2016,** *114,* 57002. doi:10.1209/0295-5075/114/57002

56. Kalathingal, V.; Dawson, P.; Mitra, J. *Sci. Rep.* **2017,** *7,* 3530. doi:10.1038/s41598-017-03766-x

57. Sun, Y.; Fan, X. *Anal. Bioanal. Chem.* **2011,** *399,* 205–211. doi:10.1007/s00216-010-4237-z

58. Lee, J. P.; Murray, E.; Bennett, A. J.; Ellis, D. J. P.; Dangel, C.; Farrer, I.; Spencer, P.; Ritchie, D. A.; Shields, A. J. *Appl. Phys. Lett.* **2017,** *110,* 071102. doi:10.1063/1.4976197

59. Cazier, N.; Buret, M.; Uskov, A. V.; Markey, L.; Arocas, J.; Colas des Francs, G.; Bouhelier, A. *Opt. Express* **2016,** *24,* 3873–3884. doi:10.1364/oe.24.003873

60. Kischkat, J.; Peters, S.; Gruska, B.; Semtsiv, M.; Chashnikova, M.; Klinkmüller, M.; Fedosenko, O.; Machulik, S.; Aleksandrova, A.; Monastyrskyi, G.; Flores, Y.; Masselink, W. T. *Appl. Opt.* **2012,** *51,* 6789–6798. doi:10.1364/ao.51.006789

61. Choy, J. T.; Bradley, J. D. B.; Deotare, P. B.; Burgess, I. B.; Evans, C. C.; Mazur, E.; Lončar, M. *Opt. Lett.* **2012,** *37,* 539–541. doi:10.1364/ol.37.000539

62. Weeber, J.-C.; Hammani, K.; Colas des Francs, G.; Bouhelier, A.; Arocas, J.; Kumar, A.; Eloi, F.; Buil, S.; Quélin, X.; Hermier, J.-P.; Nasilowski, M.; Dubertret, B. *ACS Photonics* **2016,** *3,* 844–852. doi:10.1021/acsphotonics.6b00054

63. Guan, X.; Hu, H.; Oxenløwe, L. K.; Frandsen, L. H. *Opt. Express* **2018,** *26,* 1055–1063. doi:10.1364/oe.26.001055

64. Bernal Arango, F.; Kwadrin, A.; Koenderink, A. F. *ACS Nano* **2012,** *6,* 10156–10167. doi:10.1021/nn303907r

65. Kim, M.-K.; Li, Z.; Huang, K.; Going, R.; Wu, M. C.; Choo, H. *Opt. Express* **2013,** *21,* 25796–25804. doi:10.1364/oe.21.025796

66. Crosnier, G.; Sanchez, D.; Bouchoule, S.; Monnier, P.; Beaudoin, G.; Sagnes, I.; Raj, R.; Raineri, F. *Nat. Photonics* **2017,** *11,* 297–300. doi:10.1038/nphoton.2017.56

67. Daveau, R. S.; Balram, K. C.; Pregnolato, T.; Liu, J.; Lee, E. H.; Song, J. D.; Verma, V.; Mirin, R.; Nam, S. W.; Midolo, L.; Stobbe, S.; Srinivasan, K.; Lodahl, P. *Optica* **2017,** *4,* 178–184. doi:10.1364/optica.4.000178

68. Barthes, J.; Bouhelier, A.; Dereux, A.; Colas des Francs, G. *Sci. Rep.* **2013,** *3,* 2734. doi:10.1038/srep02734

69. Dionne, J. A.; Sweatlock, L. A.; Atwater, H. A.; Polman, A. *Phys. Rev. B* **2006,** *73,* 035407. doi:10.1103/physrevb.73.035407

70. Andryieuski, A.; Zenin, V. A.; Malureanu, R.; Volkov, V. S.; Bozhevolnyi, S. I.; Lavrinenko, A. V. *Nano Lett.* **2014,** *14,* 3925–3929. doi:10.1021/nl501207u

71. Dasgupta, A.; Mennemanteuil, M.-M.; Buret, M.; Cazier, N.; Colas des Francs, G.; Bouhelier, A. *Nat. Commun.* **2018,** *9,* 1992. doi:10.1038/s41467-018-04382-7

Self-assembled quasi-hexagonal arrays of gold nanoparticles with small gaps for surface-enhanced Raman spectroscopy

Emre Gürdal[*1,2], Simon Dickreuter[1,2], Fatima Noureddine[1,2], Pascal Bieschke[1,2], Dieter P. Kern[1,2] and Monika Fleischer[*1,2]

Address:
1Institute for Applied Physics, Eberhard Karls University of Tübingen, Auf der Morgenstelle 10, 72076 Tübingen, Germany and 2Center for Light-Matter-Interaction, Sensors and Analytics (LISA+), Eberhard Karls University of Tübingen, Auf der Morgenstelle 15, 72076 Tübingen, Germany

Email:
Emre Gürdal* - emre.guerdal@gmail.com; Monika Fleischer* - monika.fleischer@uni-tuebingen.de

* Corresponding author

Abstract

The fabrication and optical characterization of self-assembled arrangements of rough gold nanoparticles with a high area coverage and narrow gaps for surface-enhanced Raman spectroscopy (SERS) are reported. A combination of micellar nanolithography and electroless deposition (ED) enables the tuning of the spacing and size of the noble metal nanoparticles. Long-range ordered quasi-hexagonal arrays of gold nanoparticles on silicon substrates with a variation of the particle sizes from about 20 nm to 120 nm are demonstrated. By increasing the particle sizes for the homogeneously spaced particles, a large number of narrow gaps is created, which together with the rough surface of the particles induces a high density of intense hotspots. This makes the surfaces interesting for future applications in near-field-enhanced bio-analytics of molecules. SERS was demonstrated by measuring Raman spectra of 4-MBA on the gold nanoparticles. It was verified that a smaller inter-particle distance leads to an increased SERS signal.

Introduction

Over the last decades self-assembled layers of gold nanoparticles have taken an important role in emerging nanotechnologies. Noble metal nanoparticles show localized surface plasmon polariton resonances (LSPRs) in the visible and infrared spectral range and exhibit a very strong near-field in their close vicinity [1]. The plasmonic resonances of gold nanoparticles can be varied by changes in size, shape and geometrical arrangement [2,3]. A high density of intense hotspots can be induced by narrow gap sizes and rough surfaces [4,5]. These remarkable optical properties make them attractive for applications in biosensing, biomedical science and as optical antennas [6-8]. In particular, metal nanoparticles can be employed to

strongly enhance the signal intensity in chemically specific Raman sensing [9]. This technique is known as surface enhanced Raman spectroscopy (SERS) [10]. Ordered arrays of such particles can be fabricated by different methods. Electron-beam lithography for example is a top-down method which provides good control, but is time consuming and costly. In contrast, the self-assembly of block-copolymers is a bottom-up method, which enables the parallel processing of large areas. A cost-effective photochemical method is block copolymer micelle lithography (BCML), which can be used to create templates on the surfaces of substrates [10-12]. To use the templates for further patterning of the substrate with nanodots, different techniques such as reactive ion etching, thermal evaporation and atomic layer deposition can be used in combination with BCML [13-15]. Here it is important to choose the optimum chain length of the diblock copolymers for obtaining the desired inter-particle spacing [16,17]. It is thus feasible to obtain quasi-hexagonally ordered regular arrays of gold nanoparticles over large areas by simple means. For the fabrication of gold nanoparticles gold salts can be used to load the micelle core, and the copolymer can be removed afterwards with an oxygen plasma treatment [18-20]. For tuning the size of the gold nanoparticles, a combination of micellar nanolithography and subsequent electroless deposition (ED) makes it possible to increase the size of the particles [18]. In this work, we follow the cost-effective and simple photochemical method outlined in [18], but in the present case pursue the goal to fabricate dense ordered arrays of gold nanoparticles with sizes up to >100 nm and single digit gaps on silicon. We first describe the synthesis of gold nanoparticles, which is based on micellar lithography. For tuning the size of the gold nanoparticles we use electroless deposition for different durations. Rough particles with sizes up to 120 nm in diameter are achieved in quasi-hexagonally ordered arrays, resulting in a high density of hotspots as has been shown for similar raspberry-like nanostructures [21,22].

Next, the optical properties of the samples are characterized by measuring the scattering spectra of selected gold nanoparticles. Finally, we demonstrate SERS enhancement by measuring Raman spectra of 4-mercaptobenzoic acid (4-MBA) molecules that are adsorbed to the gold nanoparticles.

Experimental
Block-copolymer micellar lithography
1×1 cm^2 silicon substrates were cleaned with acetone in an ultrasonic bath for two minutes. Then they were rinsed with isopropanol, and finally dried with nitrogen gas. A symmetric diblock copolymer (polystyrene-block-poly-2-vinylpyridine, PS(133000)-block-P2VP(132000), polymer source) was dissolved in toluene at a concentration of 1 mg/mL and stirred for

2 days. The micelles were loaded with chlorauric acid (HAuCl$_4$, loading parameter ($L = 0.5$), Sigma-Aldrich) and stirred again for 2 days. Spin-coating was applied to cover the substrate with a monolayer of the gold-loaded micelles (30 s at 2000 rpm).

Electroless deposition
A quartz glass slide was placed on top of the substrate after a drop of about 10 µL of water was applied. The assembly was then exposed for 4 min to deep UV light (254 nm, 85 W). After this step, the substrate was placed in an aqueous solution of enthanolamine (2 mM, Sigma-Aldrich) and potassium gold(III) chloride (KAuCl$_4$, 0.1 wt %, Sigma-Aldrich), to grow the gold precursor particles with the electroless deposition process. Reactive ion etching (Oxford Plasmalab 80 Plus) was used to remove the polymer with an oxygen plasma treatment with the following settings: process pressure 100 mTorr, power 100 W, temperature 20 °C and duration of the etching process 60 s. To measure the inter-particle spacing and sizes of the gold nanoparticles in this work we used a Scanning Electron Microscope (SEM) (Hitachi SU 8030).

Darkfield spectroscopy
The scattering spectra of gold nanoparticles were measured with a custom-built dark-field spectroscopy setup. A 50× objective (Mitutoyo BD Plan APO SL 50X) was used for imaging and taking the spectra. The samples were illuminated by a laser driven light source (Energetiq EQ-99-FC) at an incident angle of light of about 45°. The spectra were taken with an Andor Shamrock SR-303i spectrometer equipped with an iDus DU416A-LDC-DD detector.

Raman spectroscopy
The gold nanoparticles were incubated for 22 h with a 5 mM solution of 4-MBA (Sigma Aldrich) in ethanol. After this process, the substrate was rinsed with ethanol and dried with nitrogen gas. The Raman spectra were measured in a confocal Raman spectrometer (LabRam HR 800, Horia JobinYvon) using a 632.8 nm He–Ne-laser with a laser power of 50 mW and a 50× objective. The laser aperture was set to 1000 µm, the slit size to 200 µm and the grating had 1800 lines/mm, resulting in a spectral resolution of ≈2 cm^{-1}. For all measurements the exposure time was set to 60 s to reduce noise.

Results and Discussion
We use the bottom-up method of BCML combined with ED to fabricate tunable gold nanoparticles forming quasi-hexagonal arrays on a silicon substrate. The optical properties of the gold nanoparticles are investigated by dark-field spectroscopy. Finally we show that by tuning the size (and thus the inter-particle spacing) of the particles, a higher SERS signal intensity could be obtained.

The PS-b-P2VP diblock copolymer is dissolved in toluene, which is an apolar solvent. An apolar solvent dissolves preferentially the PS block [23]. The hydrophobic PS forms the shell, and the hydrophilic P2VP the core of the spherically shaped micelles [24]. Within their core gold salt can be assembled, which is bonded by protonization or complexation [25]. The loaded spherical micelles form a hexagonal array when being deposited on a substrate. Exposing them to an aqueous environment promotes a morphological change of the spherical micelles [18]. In the next step, the micelles are treated with UV irradiation, which causes the gold salt particles in the center to grow bigger by photochemical growth [18]. To enlarge the metal precursor particles even further in a controlled fashion, an electroless deposition step using potassium gold(III) chloride was performed [18,26]. To reduce the gold ions to elemental gold, a solution of ethanolamine as a reducing agent can be used [18]. The final size of the gold particles can be tuned by the duration of the process [18]. A schematic overview of the fabrication process is shown in Figure 1. In a first step a silicon substrate is coated with gold-loaded polymer micelles (Figure 1a) via spin-coating. In a second step the micelles are exposed to deep UV illumination while the substrate is covered with a quartz glass slide (Figure 1b). In a third step the nanoparticles are enlarged by electroless deposition (Figure 1c), and finally the polymer is removed by an oxygen plasma treatment (Figure 1d).

SEM images of the primary distribution of the gold precursor particles without any size increase by ED confirming that the micelles cover the entire silicon surface are shown in Figure 2a,b. The distribution is mostly regular, except for occasional defects, and shows a roughly hexagonal order. The center-to-center-spacing of the ordered particles amounts to 109 ± 20 nm. After deep UV illumination, electroless deposition and oxygen plasma treatment, SEM images are taken at two different magnifications, which are shown in Figure 2c–j. For a direct comparison between SERS platforms with large and small gaps, four substrates were fabricated, two each with identical parameters for process assessment.

In Figure 2c,d and 2e,f, representative images of gold nanoparticles after an electroless deposition step of 30 min are shown. The first substrate (A) (Figure 2c,d) exhibits an average nanoparticle size (nps) of 66 ± 25 nm and an average inter-particle distance from edge to edge (ipd) of 56 ± 9 nm. The second substrate (B) (Figure 2e,f) shows an nps of 73 ± 16 nm and an ipd of 33 ± 6 nm. Substrate A shows a lower degree of order than B. Two more samples were prepared with the same process steps, but with an electroless deposition of 90 min instead of 30 min. In Figure 2g,h sample C has an nps of 96 ± 12 nm and an ipd of 17 ± 6 nm. The second sample (D) in Figure 2i,j shows an nps of 97 ± 10 nm and an ipd of 14 ± 9 nm. The statistical ipd of 14 ± 9 nm indicates the presence of a considerable number of sub-10 nm gaps. Comparing the particle sizes, one finds a significant variation between the 30 min samples, while the 90 min samples exhibit very similar arrangements. The results are summarized in Table 1. The inter-particle distances were measured directly from the SEM images, and averaged
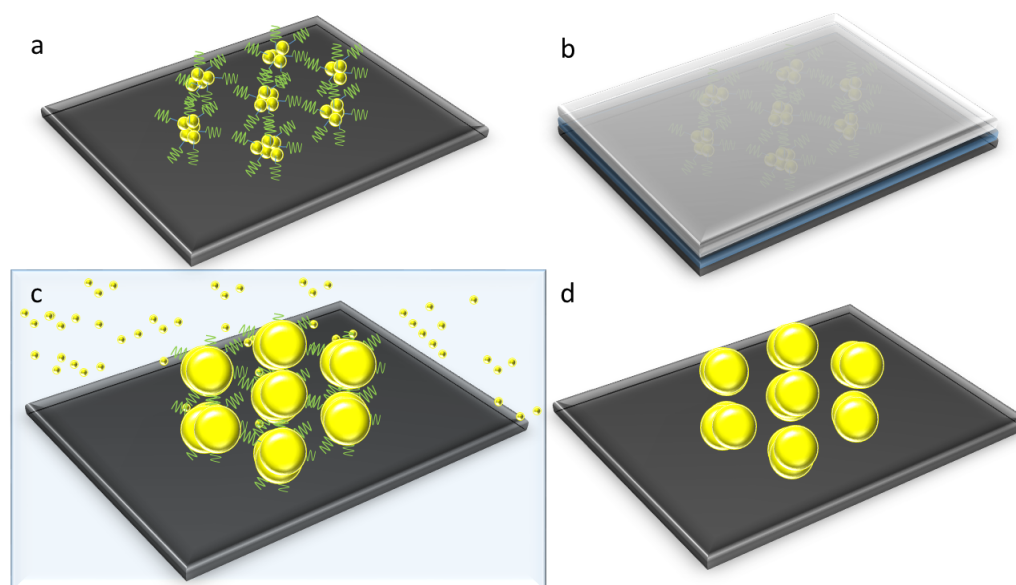

Figure 1: Schematic illustration of the preparation of variable-size gold nanoparticle arrays on top of a silicon substrate: (a) Gold nanoparticles with block copolymer micelles after spin-coating. (b) Deep UV illumination with water and a quartz glass on top of the substrate. (c) Electroless deposition. (d) Substrate after oxygen plasma, which removes the organic components.
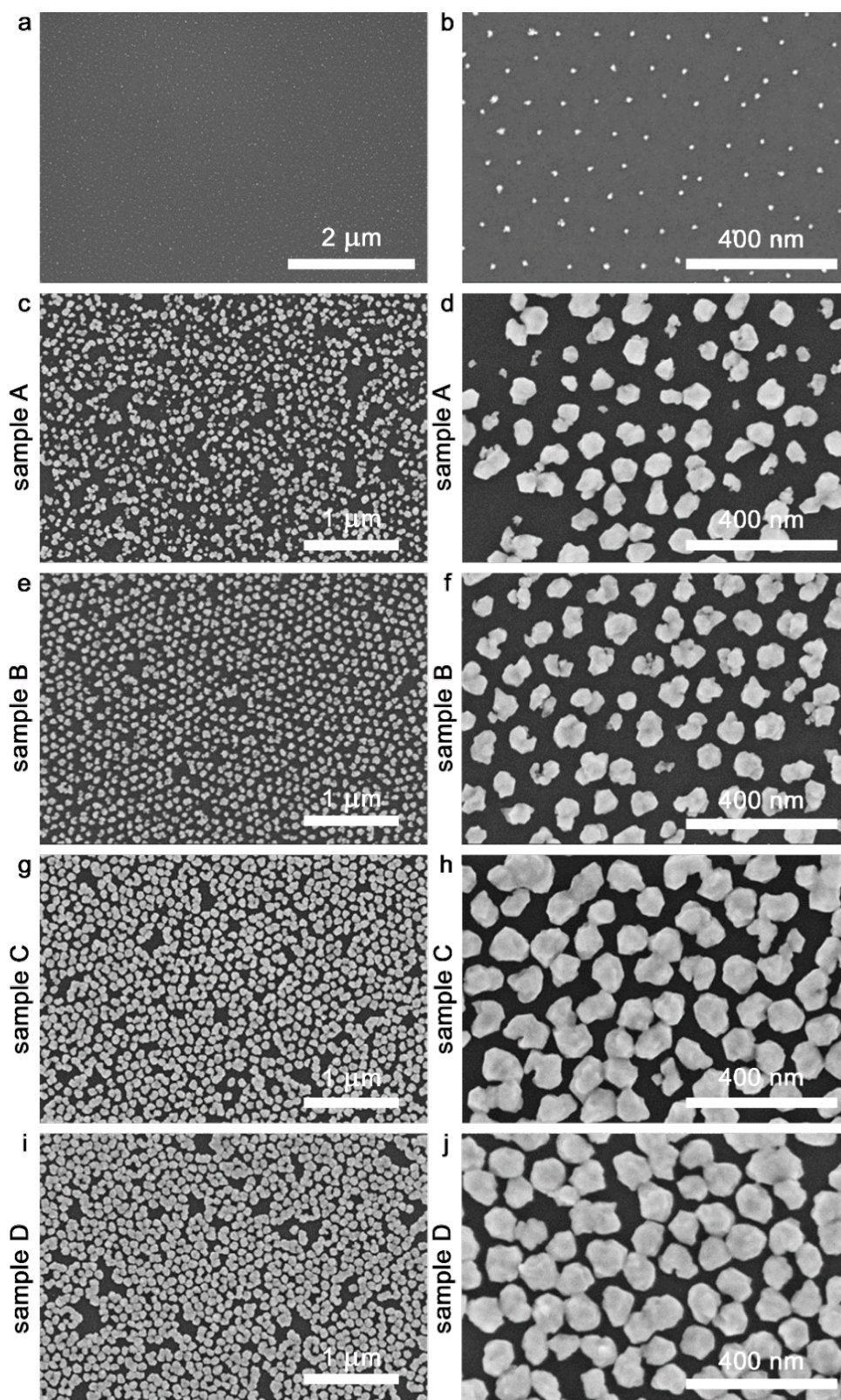
Figure 2: SEM images of the gold precursor particles after oxygen plasma treatment (a, b) and gold nanoparticles after electroless deposition and oxygen plasma treatment: (c, d) sample A with 30 min ED, (e, f) sample B with 30 min ED, (g, h) sample C with 90 min ED, (i, j) sample D with 90 min ED. Scale bars: (a) 2 µm; (c, e, g, i) 1 µm; (b, d, f, h, j) 400 nm.

Table 1: Measured average particle sizes and interparticle distances for the different samples.

Sample	ED duration	Avg. nanoparticle size	Avg. inter-particle distance
A	30 min	66 ± 25 nm	56 ± 9 nm
B	30 min	73 ± 16 nm	33 ± 6 nm
C	90 min	96 ± 12 nm	17 ± 6 nm
D	90 min	97 ± 10 nm	14 ± 9 nm

over ten measurements. The nanoparticle sizes for the samples A and B were evaluated by using the method described in the next paragraph. Because many of the particles in samples C and D touch each other, they could not be separately discerned by this method, and their nps had to be measured manually from the SEM images, also averaging over ten measurements.

In order to find the dependence of the gold particle diameter on the ED time, two additional series of samples with different time steps were fabricated. The preparation parameters were similar to the ones shown before, only the polymer concentration was reduced to 0.7 mg/mL and the loading parameter was set to $L = 1$. The results are summarized in Figure 3. The SEM images for each sample were evaluated using a python script that applies a threshold in order to generate binary images. Blob detection is used to find the particles in the binary images and to evaluate the pixel count for each individual particle. From this pixel count, the area coverage and thus the mean equivalent diameter of the particles is calculated, assuming perfectly round particles. A histogram of all the diameters is calculated and a Gaussian is fitted to this histogram. This allows us to extract the

mean equivalent diameter as well as the full-width-at-half-maximum (fwhm) of the diameter distribution, which is indicated by the error bars in Figure 3. Since in reality the particles are irregular and exhibit some surface roughness, the equivalent diameters underestimate the maximum outer diameter, and thus the minimum gap sizes to neighbouring particles may be even smaller than indicated by this evaluation. A general trend of increasing particle diameters with increasing ED times can be observed. The growth goes into saturation when the particle size approaches the interparticle spacing. Before ED, the gold-loaded micelles start with sizes around 10 nm to 20 nm. As the ED duration increases, their size increases up to about 100 nm to 120 nm. A systematic offset can be discerned between the separate test series, indicating that the process is highly sensitive to the exact preparation conditions during the fabrication process even when the same recipe is followed. In addition, the center-to-center spacing varies slightly from sample to sample.

To compare the SERS signal of smaller particles with larger gaps to that of larger particles with small gaps, the optical properties of the samples shown in Figure 2 were further analyzed using dark-field spectroscopy. For every sample, 25 measurements at different points were taken and averaged. The results are shown in Figure 4. The bigger particles (sample C and D) show an overall increase in the scattering intensity compared to the smaller ones (A and B), as one would expect for Rayleigh scattering. The curves exhibit very broad spectral features.

To measure the SERS signal, the gold nanoparticles were covered with a self-assembled monolayer of 4-MBA. Because the thiol-group of the 4-MBA molecules has a very high affinity
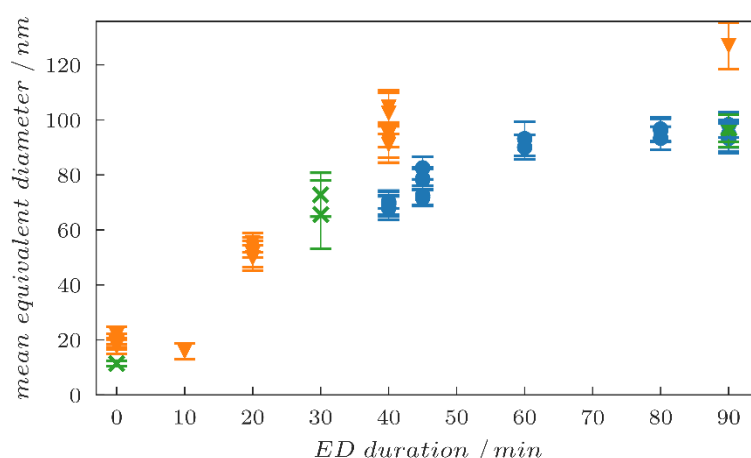

Figure 3: Dependence of the mean equivalent diameter of the gold particles on the ED duration. Three separate sets of samples were fabricated and evaluated. The series are color coded as orange triangles, blue circles and green crosses. Each marker represents the data from one SEM image. The error bars indicate the deviations of the mean equivalent diameter within the respective SEM images. The green crosses correspond to the samples that are shown in Figure 2. The values for the green crosses for an ED duration of 90 min were evaluated manually from the SEM images, all others were calculated by using the method described in the main text.
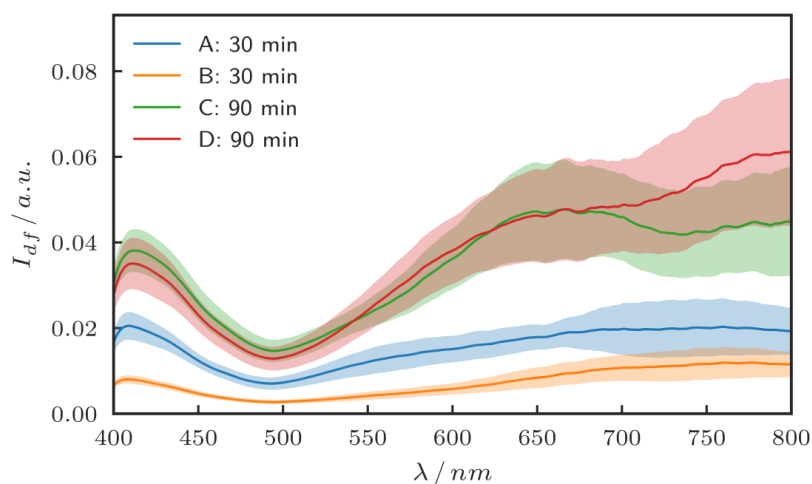
Figure 4: Mean dark-field spectra of the different samples. For each sample 25 spectra at different positions were taken and averaged. The shaded regions show the standard deviation of the average.

for gold [27], and the samples were rinsed thoroughly with ethanol to remove any unbound molecules, we can assume that mostly 4-MBA molecules are present on the gold surfaces and not on the substrate.

Raman spectra were recorded as described above at three different positions on every sample and averaged. For the excitation the laser wavelength of 632.8 nm was chosen, since according to Figure 4 it appears to have good spectral overlap with the plasmon resonances (maxima in the scattering intensity) of the larger gold particles, and is thus expected to excite strong hotspots in the gaps. The intensity of the characteristic Raman bands for 4-MBA at 1085 cm^{-1} and 1590 cm^{-1} were evaluated [28]. The background-corrected peak intensities are summarized in Table 2, denoted as "raw". By looking at the SEM images in Figure 2, it is obvious that the samples show a difference in the amount of gold that is present, which also means that for each sample a different amount of molecules attached to gold is present in the focal spot of the Raman laser. To approximately correct for the different amounts of molecules on the different samples one can use the filling factor (area coverage) of the samples: A threshold was applied to the SEM images, and the white pixels representing the presence of gold were counted.

The filling factor was then calculated by dividing the white pixel count by the number of pixels of the image. This represents a measure for the average particle size as well as for the density of the particles, and correspondingly it also provides a measure for the number of molecules on gold per unit area. The Raman intensities were then divided by this filling factor, which results in filling factor-corrected intensities. The resulting filling factors and corrected Raman intensities (denoted as "corrected") are shown in Table 2, while the raw background-corrected Raman intensities as measured are visualized in Figure 5.

By looking at the raw Raman spectra for the different samples one can see that the larger particles show higher Raman intensities than the smaller particles by more than a factor of 2. Of course, in this case the larger gold surface and thus the higher number of molecules was not taken into account. If the Raman intensities are corrected for the filling factor as explained above, the difference between the samples becomes smaller, but still the larger particles show an increased Raman signal, particularly for the peak at 1085 cm^{-1}. Figure 6 shows a comparison of the corrected Raman intensities for the different samples where this increase is clearly visible. This effect may be explained by the much shorter mean inter-particle distances between the

Table 2: Filling factor and measured Raman intensities (raw: background corrected raw data, corrected: Raw spectra normalized by filling factor) for all samples.

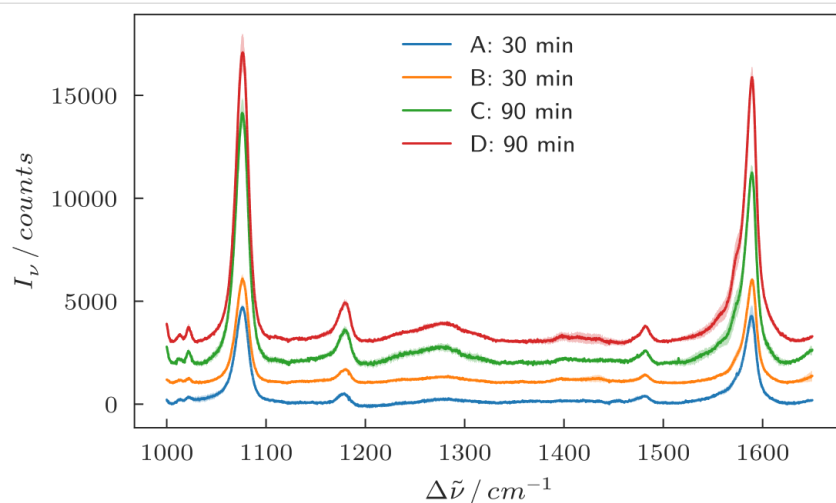| Sample	Filling factor	Raman int. at 1085 cm^{-1} [k counts]		Raman int. at 1590 cm^{-1} [k counts]	
		raw	corrected	raw	corrected
A	0.31	3.8 ± 0.1	12.2 ± 0.3	3.1 ± 0.4	10.1 ± 1.3
B	0.33	4.3 ± 0.2	13.1 ± 0.6	3.8 ± 0.1	11.5 ± 0.4
C	0.56	10.3 ± 0.5	18.6 ± 1.0	6.8 ± 0.2	12.2 ± 0.4
D	0.62	12.0 ± 0.8	19.5 ± 1.3	9.3 ± 0.3	15.0 ± 0.5

Figure 5: Background-corrected mean Raman spectra of the four different samples. For each sample three Raman spectra at three random positions on the samples were taken and averaged. The shaded regions show the standard deviation of the average. The spectra were offset vertically for clarity.
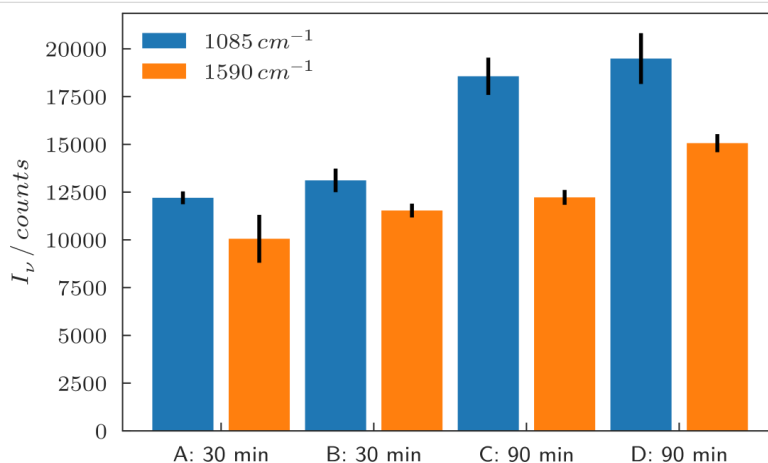

Figure 6: Filling factor-corrected Raman intensities of the different samples, for the two peaks at 1085 cm^{-1} and 1590 cm^{-1}. The average of 3 measurements for each sample is shown, the black bars denote the standard deviation.

larger nanoparticles, including some very narrow gaps due to the statistical variation, which causes an increased coupling between the particles and thus an increased near-field [29].

To estimate a lower boundary for the enhancement factor of the particles we compared the corrected Raman spectra of sample A to a measurement of 4-MBA on a smooth gold film with a thickness of 70 nm, also on a silicon substrate. Both samples were treated in exactly the same way. The spectra are shown in Figure 7. For the gold film no signal was observed, and thus we assume that the upper limit of the signal is the peak-to-peak noise in the measurement. By dividing the maximum corrected signal of the Raman mode at 1085 cm^{-1} by the peak-to-peak noise of the measurement on the gold film we obtain a lower limit of the enhancement factor of ≈300. This is a very conser-

vative lower limit, and compared to values commonly reported in literature it is significantly smaller, but we would like to stress that the estimation of SERS enhancement factors is inherently difficult and is still a much discussed topic within the community [30,31].

As can be seen in the SEM images for the samples with 90 min ED, the particles show average separation distances around 15 nm and individual separations down to only a few nanometers. This means that the method presented here allows for the fabrication of nano-particles that exhibit very small mode volumes and high near-fields. The fabrication is based on bottom-up processes and thus offers the possibility to scale it up to bigger substrates and higher throughput. The high near-fields and the ease of fabrication make these structures particularly
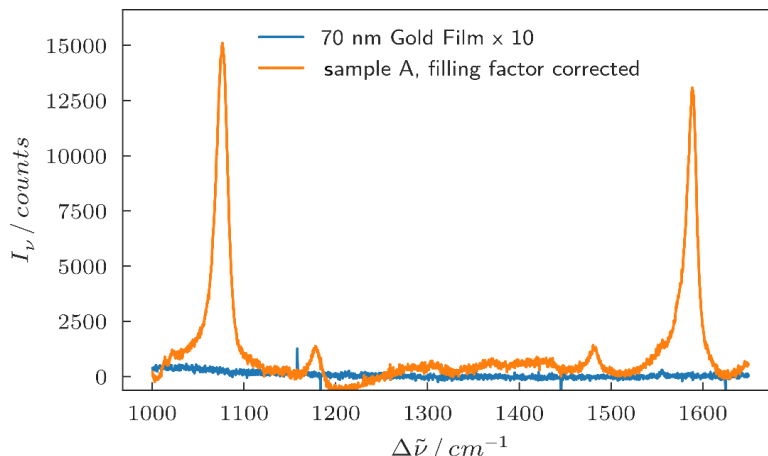
Figure 7: Filling factor-corrected Raman spectrum of sample A compared to a Raman spectrum on smooth gold film.

suitable for sensing applications, for example for SERS as it was shown here.

Conclusion

In conclusion, we describe a cost-effective, scalable, parallel method for the fabrication of quasi-hexagonally ordered arrays of nanoparticles with particle sizes up to 120 nm and gap sizes down to few nanometers, which are fabricated by block copolymer micellar nanolithography combined with electroless deposition. The resulting particle arrangements are compared for samples prepared with 30 min vs 90 min ED. The dark-field scattering intensity is compared for the different nanoparticle sizes. We demonstrate the SERS effect exhibited by these samples by measuring Raman spectra of 4-MBA that is adsorbed to the gold nanoparticles. The spectra show an increase in Raman intensity for larger particles and smaller gap sizes by a factor of >2. The surfaces with the narrower gap sizes result in higher intensities even when correcting for the different particle sizes and area coverage. This effect may be attributed to a stronger near-field coupling between the particles due to smaller interparticle distances.

Acknowledgements

References

1. Jain, P. K.; Lee, K. S.; El-Sayed, I. H.; El-Sayed, M. A.
   J. Phys. Chem. B **2006,** *110,* 7238–7248. doi:10.1021/jp057170o
2. Kelly, K. L.; Coronado, E.; Zhao, L. L.; Schatz, G. C. *J. Phys. Chem. B*
   2003, *107,* 668–677. doi:10.1021/jp026731y
3. Talley, C. E.; Jackson, J. B.; Oubre, C.; Grady, N. K.; Hollars, C. W.;
   Lane, S. M.; Halas, N. J. *Nano Lett.* **2005,** *5,* 1569–1574.
   doi:10.1021/nl050928v
4. Chen, G.; Wang, Y.; Yang, M.; Xu, J.; Goh, S. J.; Pan, M.; Chen, H.
   J. Am. Chem. Soc. **2010,** *132,* 3644–3645. doi:10.1021/ja9090885
5. Alexander, K. D.; Hampton, M. J.; Zhang, S.; Dhawan, A.; Xu, H.;
   Lopez, R. *J. Raman Spectrosc.* **2009,** *40,* 2171–2175.
   doi:10.1002/jrs.2392
6. Jin, Y. *Adv. Mater.* **2012,** *24,* 5153–5165.
   doi:10.1002/adma.201200622
7. Huang, X.; El-Sayed, I. H.; Qian, W.; El-Sayed, M. A.
   J. Am. Chem. Soc. **2006,** *128,* 2115–2120. doi:10.1021/ja057254a
8. Park, Q.-H. *Contemp. Phys.* **2009,** *50,* 407–423.
   doi:10.1080/00107510902745611
9. Horrer, A.; Schäfer, C.; Broch, K.; Gollmer, D. A.; Rogalski, J.;
   Fulmes, J.; Zhang, D.; Meixner, A. J.; Schreiber, F.; Kern, D. P.;
   Fleischer, M. *Small* **2013,** *9,* 3987–3992. doi:10.1002/smll.201300449
10. Moskovits, M. *Rev. Mod. Phys.* **1985,** *57,* 783.
    doi:10.1103/RevModPhys.57.783
11. Glass, R.; Möller, M.; Spatz, J. P. *Nanotechnology* **2003,** *14,* 1153.
    doi:10.1088/0957-4484/14/10/314
12. Kadem, L. F.; Lamprecht, C.; Purtov, J.; Selhuber-Unkel, C. *Langmuir*
    2015, *31,* 9261–9265. doi:10.1021/acs.langmuir.5b02168
13. Cheng, J. Y.; Ross, C. A.; Chan, V. Z.-H.; Thomas, E. L.;
    Lammertink, R. G. H.; Vancso, G. J. *Adv. Mater.* **2001,** *13,* 1174–1178.
    doi:10.1002/1521-4095(200108)13:15<1174::AID-ADMA1174>3.0.CO;
    2-Q
14. Lopes, W. A.; Jaeger, H. M. *Nature* **2001,** *414,* 735–738.
    doi:10.1038/414735a
15. Moon, H.-S.; Kim, J. Y.; Jin, H. M.; Lee, W. J.; Choi, H. J.; Mun, J. H.;
    Kim, S. O. *Adv. Funct. Mater.* **2014,** *24,* 4343–4348.
    doi:10.1002/adfm.201304248
16. Jeong, H.-H.; Mark, A. G.; Lee, T.-C.; Son, K.; Chen, W.;
    Alarcón-Correa, M.; Kim, I.; Schütz, G.; Fischer, P. *Adv. Sci.* **2015,** *2,*
    1500016. doi:10.1002/advs.201500016
17. Purwaningsih, L.; Schoen, T.; Wolfram, T.; Pacholski, C.; Spatz, J. P.
    Beilstein J. Nanotechnol. **2011,** *2,* 545–551. doi:10.3762/bjnano.2.58
18. Kundrat, F.; Baffou, G.; Polleux, J. *Nanoscale* **2015,** *7,* 15814–15821.
    doi:10.1039/C5NR04751J

19. Lu, J. Q.; Yi, S. S. *Langmuir* **2006,** *22,* 3951–3954.
    doi:10.1021/la053377x
20. Härtling, T.; Seidenstücker, A.; Olk, P.; Plettl, A.; Ziemann, P.;
    Eng, L. M. *Nanotechnology* **2010,** *21,* 145309.
    doi:10.1088/0957-4484/21/14/145309
21. Rong, Y.; Zhang, L.; Liu, Z.; Dai, L.; Huang, Y.; Chen, T.
    J. Nanosci. Nanotechnol. **2016,** *16,* 5683–5688.
    doi:10.1166/jnn.2016.11723
22. Kinoshita, T.; Nguyen, D. Q.; Nishino, T.; Nakao, H.; Shiigi, H.;
    Nagaoka, T. *Anal. Sci.* **2015,** *31,* 487–493. doi:10.2116/analsci.31.487
23. Haupt, M.; Miller, S.; Ladenburger, A.; Sauer, R.; Thonke, K.;
    Spatz, J. P.; Riethmüller, S.; Möller, M.; Banhart, F. *J. Appl. Phys.*
    2002, *91,* 6057–6059. doi:10.1063/1.1465117
24. Kästle, G.; Boyen, H.-G.; Weigl, F.; Lengl, G.; Herzog, T.; Ziemann, P.;
    Riethmüller, S.; Mayer, O.; Hartmann, C.; Spatz, J. P.; Möller, M.;
    Ozawa, M.; Banhart, F.; Garnier, M. G.; Oelhafen, P.
    Adv. Funct. Mater. **2003,** *13,* 853–861. doi:10.1002/adfm.200304332
25. Spatz, J. P.; Mössmer, S.; Hartmann, C.; Möller, M.; Herzog, T.;
    Krieger, M.; Kabius, B.; Boyen, H.-G.; Ziemann, P. *Langmuir* **2000,** *16,*
    407–415. doi:10.1021/la990070n
26. Kruss, S.; Srot, V.; van Aken, P. A.; Spatz, J. P. *Langmuir* **2012,** *28,*
    1562–1568. doi:10.1021/la204395d
27. Nuzzo, R. G.; Allara, D. L. *J. Am. Chem. Soc.* **1983,** *105,* 4481–4483.
    doi:10.1021/ja00351a063
28. Michota, A.; Bukowska, J. *J. Raman Spectrosc.* **2003,** *34,* 21–25.
    doi:10.1002/jrs.928
29. Gunnarsson, L.; Bjerneld, E. J.; Xu, H.; Petronis, S.; Kasemo, B.;
    Käll, M. *Appl. Phys. Lett.* **2001,** *78,* 802–804. doi:10.1063/1.1344225
30. Le Ru, E. C.; Blackie, E.; Meyer, M.; Etchegoin, P. G. *J. Phys. Chem. C*
    2007, *111,* 13794–13803. doi:10.1021/jp0687908
31. Le Ru, E. C.; Etchegoin, P. G. *MRS Bull.* **2013,** *38,* 631–640.
    doi:10.1557/mrs.2013.158

Dumbbell gold nanoparticle dimer antennas with advanced optical properties

Janning F. Herrmann[1] and Christiane Höppener[*2]

Abstract

Plasmonic nanoantennas have found broad applications in the fields of photovoltaics, electroluminescence, non-linear optics and for plasmon enhanced spectroscopy and microscopy. Of particular interest are fundamental limitations beyond the dipolar approximation limit. We introduce asymmetric gold nanoparticle antennas (AuNPs) with improved optical near-field properties based on the formation of sub-nanometer size gaps, which are suitable for studying matter with high-resolution and single molecule sensitivity. These dumbbell antennas are characterized in regard to their far-field and near-field properties and are compared to similar dimer and trimer antennas with larger gap sizes. The tailoring of the gap size down to sub-nanometer length scales is based on the integration of rigid macrocyclic cucurbituril molecules. Stable dimer antennas are formed with an improved ratio of the electromagnetic field enhancement and confinement. This ratio, taken as a measure of the performance of an antenna, can even exceed that exhibited by trimer AuNP antennas composed of comparable building blocks with larger gap sizes. Fluctuations in the far-field and near-field properties are observed, which are likely caused by distinct deviations of the gap geometry arising from the faceted structure of the applied colloidal AuNPs.

Introduction

The introduction of the antenna concept to the field of optics has opened up new routes to manipulate light on the nanometer scale [1-5]. For more than a decade, optical antennas have demonstrated a tremendous impact on a broad spectrum of applications [6-9]. A key function, in particular for sensing and imaging applications, is the ability of optical antennas to provide a high signal enhancement ratio and light confinement across the UV–vis–NIR spectral range. The development of new configurations has always come along with the question of fundamental limitations in regard to the obtainable electromagnetic field strength or the signal enhancement, and the achievable confinement of the light in plasmonic nanostructures [10-

14]. Furthermore, this stimulated the discussion of the onset of non-classical phenomena, such as, screening effects, non-localities and charge transfer in coupled plasmonic systems [11,15-20]. Phenomena governed by non-classical physical effects have been observed already at early stages after the introduction of the concept [15,17,21], but only recently a fundamental understanding of these effects became accessible based on detailed experimental [18,19,22] and theoretical studies [23,24]. In addition to these fundamental limits, the importance of the nanoscale morphology of antennas has been identified as a key parameter affecting their far-field and near-field optical properties [25-30]. The simplest antenna geometries, whose optical response is governed by plasmonic mode coupling, are symmetric dimers formed of spherical nanoparticles. Often these structures are used as a model system to understand the impact of hot spots in more complex systems [31,32]. However, the multiplicity of modes, and with that, the ability for tailoring the plasmon resonances and the electromagnetic field distribution in these structures, is much more versatile for asymmetric (dumbbell) antennas [33-37]. Introducing a defined asymmetry for these gap structures, e.g., converts dark anti-symmetric modes into bright modes [38] and also influences non-linear responses generated in these structures [39]. In addition, the asymmetry induces a cascade of the electromagnetic field enhancement towards the pointed end of the structure such that these structures are often discussed in terms of acting as a nanolens [10,40-43]. Although the local electromagnetic field is strongest in the gap, the electromagnetic field at the end point of the smallest nanoparticle of these structures can be also increased (see for Metallic Nanopaticle Boundary Element Method (MNPBEM)-simulation of the electromagnetic field

distribution [44], Figure 1A). Usually, this end point of the antenna is not considered in common SERS applications due to the one to two orders of magnitude lower electromagnetic field strength. As a consequence, the signal majorly stems from the interparticle locations. However, for applications of such dimers in TENOM or TERS, the optical response is primarily driven by the field at the end point of the probe. Theoretical investigations of the electromagnetic field distribution of these dimers at particular wavelengths demonstrate a tight connection of the optical response associated with the two particular locations, i.e., the gap and the end point [40]. Decreasing the interparticle gap size, therefore, leads to stronger electromagnetic fields at the gap and the end point locations. However, one has to keep in mind, that the reduction of the gap size also is accompanied by a shift of the plasmon resonance and the strongest electric field enhancement is observed for red-shifted excitation wavelengths.

Fabrication strategies of optical antennas, and in particular gap antennas with an optical response in the visible to NIR regime, are versatile and are often correlated with the final application schemes. Although top-down approaches, which rely on, e.g., electron-beam lithography, ion milling and other techniques, are widely used, often tailoring gap structures explores common limitations in regard to their obtainable resolution and non-invasiveness. In contrast, common bottom-up approaches often rely on the specific interaction of linker molecules, which may be used for a directed assembly of individual antenna parts. Besides of the general discussion on methodologies, the effect of the crystallinity of the employed noble metals has attracted attention [45]. The versatility of colloidal chemistry provides
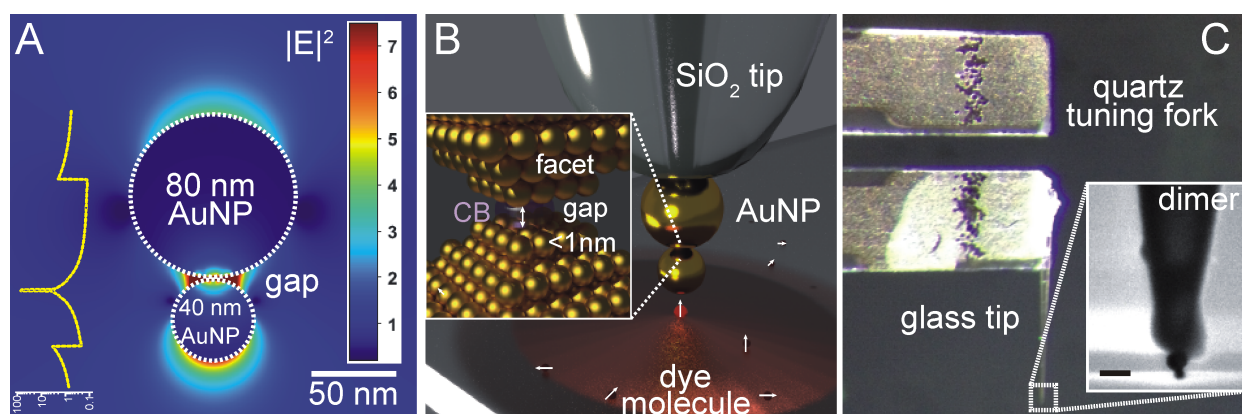
Figure 1: Tip-supported dumbbell antenna. (a) Calculated electromagnetic field distribution of a 80–40 nm AuNP dimer antenna with a gap size of 1 nm. (B) Schematic representation of a dimer antenna formed of spherical AuNPs attached to a sharply pointed glass tip. Inset: Magnification to the gap region showing the aligned CB[*n*]s on the NP surfaces, which results in a sub-nanometer gap distance. (C) Macroscale picture of a glass tip attached to a piezoelectric quartz tuning fork acting as a force sensor. Inset: SEM image of the CB[*n*] mediated dimer antenna attached to the pointed end of the glass tip. Scale bar: 100 nm.

nowadays a tool box of nanoparticles made of different materials, shapes and sizes. In addition, the crystallinity of these structures leads to the formation of facets, edges and corners. Using colloidal nanoparticles, their chemical assembly demands for certain properties of the specific linker molecules [46]. In particular mastering the formation of sub-nanometer gap sizes requires short, rigid molecules with high chemical selectivity. In addition, these linker molecules should not affect the optical response of the formed antenna. Although sub-nanometer gap dimers can be also formed artificially by the placement of nanoparticles on a mirror substrate using defined spacer layers [47,48], in general, this approach is non-transferrable to tip-supported antennas used, e.g., in TENOM and TERS. Another frequently considered approach utilizes DNA as scaffold for the alignment of the nanoparticles [41,49,50]. In particular, DNA origami-structures provide a high versatility of the formed structures, however, the gap sizes on the sub-nanometer scale are difficult to control. Recently, we succeeded in the formation of dumbbell dimer antennas by means of the electrostatic interaction of positively charged 40 nm AuNPs and negatively charged 80 nm AuNPs [28]. Positively charged AuNPs were formed through a ligand exchange reaction with cysteamin. Incubation of a mixture of both AuNP solutions leads to the formation of AuNP dimers with gap sizes on the order of 1.3 nm to 0.8 nm. Similarly, tip-supported AuNP dimer antennas were assembled by adding a dithiol to the shell of an 80 nm AuNP, which previously has been attached to the end of a sharply pointed glass tip [10]. Due to the molecular size of the dithiol, these dimer antennas exhibit relatively large gap sizes. Commonly, the gap size is found to be on the order of 1.5–2.0 nm. Utilizing the capabilities of an AFM to manipulate such structures with sub-nanometer precision in space enables to add a smaller 40 nm AuNP to the larger one. Even though, shorter linker thiol molecules could be used instead, in principle, the high mobility of these linker molecules on the AuNP surface limits its applicability [51,52].

Results and Discussion
Fabrication of dumbbell dimer antennas with sub-nanometer gap size

In this study, we modify the previously established protocol of the formation of tip-supported dimer and trimer antennas by replacing the dithiol linker molecules with a rigid macrocyclic molecule (scheme, Figure 1B). Cucurbiturils (CB[n]s) are cyclic methylene-bridged glycoluril oligomers forming a barrel-like structure with a hollow cavity. In particular due to their sub-nanometer height of ≈0.9 nm [53], CBs can be considered as ideal spacer molecules for the formation of dumbbell dimers. Furthermore, carbonyl groups at the top and bottom face of this barrel provide a high affinity to gold surfaces. Therefore, CBs bind in a flat configuration to gold surfaces, which drives a

dimer formation with well-defined gaps in terms of the gap size (inset, Figure 1B). In comparison with other linker molecules, such as dithiols, CB[n]-mediated dimer assembly enables to reduce the interparticle gap sizes down to the sub-nanometer regime. As a consequence, nanoparticle aggregates induced by interactions with CB[n]s have been shown to provide strong interparticle hot-spots, and thus, to be well-suited as SERS substrates [54,55]. The high reactivity of CB[n]s with Au surfaces may lead to the uncontrolled formation nanoparticle aggregates in solution, and often prevents a controlled self-assembly into dimers or small oligomer structures. However, using guided assembly by taking advantage of AFM manipulation methods, CB[n] is ideally suited to mediate sub-nanometer gap formation. For this, a sharply pointed glass tip is glued to a piezoelectric quartz tuning fork (Figure 1C), which enables to control the tip position with respect to AuNPs deposited on a glass surface with sub-nanometer precision in space. Briefly, the fabrication of tip-supported nanoparticle antennas includes at first the attachment of a single spherical AuNP to the pointed end of a glass tip. For this, the glass surface is functionalized with 3-aminopropoyl-trimethoxy silane (APTMS) by means of vapor deposition. Controlled interaction of the glass tip with loosely adhered Au nanoparticles on a glass surface leads to an attachment of the AuNP at the pointed end. This tip-supported AuNP is sequentially functionalized with the corresponding linker molecule, i.e., by dipping the tip-supported AuNP into an aqueous 0.5 μM CB[8] solution. After an incubation time of 5 min the tips are rinsed with milli-Q water (18 MΩ) to prevent an aggregation of CB[8] on the AuNP surface. The CB[8] modified AuNP tips are then used to attach a smaller AuNP to the tip by repeating the above described AFM-based manipulation procedure.

Approximation of the electromagnetic field enhancement by measuring the fluorescence of high-QY emitters

Tip-supported AuNP monomers and dimers are characterized for the provided electromagnetic field enhancement and light confinement capabilities by probing the fluorescence enhancement of quantum emitters with LSPR-matched absorption and emission spectra and high intrinsic quantum yields. The latter ensures that the probed fluorescence enhancement factor stems largely from the provided electromagnetic field enhancement [1,3,56]. Since the measurements are not carried out in the regime of strong coupling, this approach only provides an approximation of the electromagnetic field strength at the end point of the dimer, since at the same time, quenching of the fluorescence occurs. Despite of this, the method provides a straight forward means to compare modifications of the electromagnetic field induced by alterations of geometrical properties [10].

Figure 2 summarizes measurements conducted with different types of monomer and dimer antennas on a high QY emitter excitable at a wavelength of λ_{exc} = 633 nm and an excitation power P_{exc} of 50 to 100 nW. The examples depicted in Figure 2 are typical in regard of the obtained signal strength and the noise floor. Clearly, for all measurements individual dye molecules are identified. However, the signal contrast strongly deviates for each measurement. Apparently, the best signal-to-noise level is achieved with the CB[8]-mediated dimer antenna. For comparison Figure 2C shows a fluorescence image acquired with an 80 nm monomer AuNP antenna [57,58]. The signal intensity is clearly lower than for the dimer antennas. In order to qualitatively access the light confinement and signal enhancement capabilities of these different antennas, fluorescence intensity cross-sections measured from individual spots, which can be assigned to molecules with a longitudinal orientation of the transition dipole, are comparatively displayed in Figure 2D. In addition, data points are plotted from measurements acquired with a 40 nm monomer AuNP antenna and a 80–40–20 nm trimer antenna. From these line-profiles it is obvious that the provided light confinement is largely determined by the diameter of the foremost AuNP of the antenna. Considering the radius of curvature, the light confinement is slightly better than the diameter of this AuNP, i.e., 15 nm for the 20–40–80 nm AuNP

trimer antenna, ≈25 nm for the 40–80 nm AuNP dimer antennas and the 40 nm AuNP monomer antenna and 55 nm for the 80 nm AuNP monomer. Furthermore, the signal strength clearly increases with the size and number of AuNP added to the antenna structure. The latter is indicative for the expected cascade of the electromagnetic field towards the intermediate points of these gap structures. Figure 2D indicates that the CB[8] antenna provides similar light confinement capabilities than the thiol trimer. Most strikingly, the electromagnetic field enhancement of this dimer antenna reaches the same level as the more complex trimer antenna. This can be ascribed to the decreased gap size of the CB[8] dimer, which results in a stronger coupling efficiency across the gap, and thus, induces also a stronger electromagnetic field at the smallest AuNP of the dimer.

A quantitative evaluation of the fluorescence enhancement factor can be also accomplished by measuring the fluorescence emission of single dye molecule as a function of the antenna–sample separation. The corresponding approach curves account for two mechanisms occurring when the antenna is coupled to the dye molecule: 1.) the absorption enhancement due to the interaction of the molecule with the evanescent electromagnetic field of the antenna and 2.) quenching of the
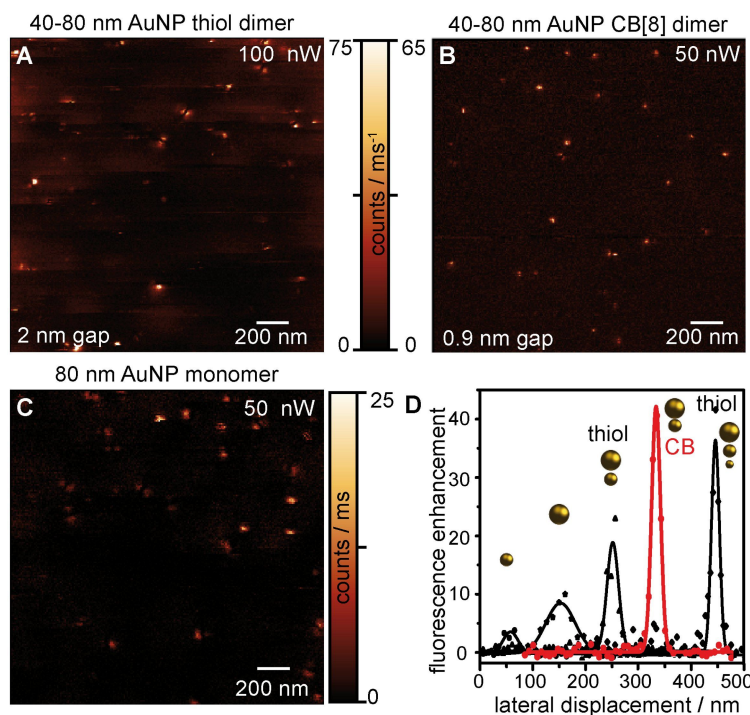

Figure 2: Antenna-enhanced fluorescence images of randomly distributed high-QY emitters on a glass surface imaged with dimer antennas with a gap size of 1.5 nm (A) and 1 nm (B), and a monomer antenna (C). (D) Line profiles taken from individual monomer- (40 nm and 80 nm AuNP), dimer- (40–80 nm thiol and CB[8] mediated) and trimer (20–40–80 nm thiol-mediated)-enhanced fluorescence spots normalized to the confocal background signal for comparison of the provided fluorescence enhancement and light confinement (FWHM).

excited state, i.e., the relaxation of the excited state by means of radiationless energy transfer to the metallic interface of the AuNP. Since the spontaneous emission rate equals the product of these contributions for an excitation far from the saturation limit, the corresponding approach curves exhibit a characteristic profile. Typical approach curves acquired with a monomer and a dimer antenna are displayed in Figure 3A. For antenna–sample distances larger than the corresponding diameter of the foremost AuNP, the optical response of the excited molecule corresponds to the pure confocal excitation, i.e., the evanescent field of the antenna is entirely faded out and quenching by the metallic interface of the antenna is negligible. For smaller distances at first the excitation enhancement and by reciprocity the emission enhancement are driven by the secondary field of the antenna. The exponential increase of the electromagnetic field strength with decreasing antenna–sample distance leads to a continuous increase of the emitted fluorescence signal. However, with decreasing distance, the influence of the electromagnetic field enhancement is counterbalanced by nonradiative transitions to electronic states of the metallic interface and sequential dissipation of the excited state energy. Therefore, for small AuNP-dye distances the spontaneous emission starts to decline. The onset for this decline differs clearly for the different antenna types, according to the relative distance dependence and strength of the two contributing mechanisms. Clearly, the maximum for the spontaneous emission rate mediated by the CB[8]-AuNP dimer is reached for increased distances to the molecule. Compared to the monomer antenna the onset is shifted by ≈2–2.5 nm. This offset is indicative for an increased quenching rate due to the larger total size of the dimer compared to the monomer. Despite of this increased quenching rate, the maximum electromagnetic field enhancement provided by a dimer antenna clearly exceeds the one of a simple monomer antenna with equal NP diameters. The displayed approach curves can be ideally used for determining the corresponding fluorescence enhancement factors. For this, the approach curves are corrected for the luminescence background of the antenna and the maximum spontaneous emission rate and the confocal background are evaluated. For the examples shown in Figure 3A the enhancement factor of the monomer antenna is 11 and for the CB[8]-dimer with an expected gap size of 0.9 nm the fluorescence enhancement factor yields a significantly increased value of ≈50. Taking into account that the fluorescence enhancement primarily stems from the electromagnetic field enhancement and an enhancement of the radiative rate is negligible, the decrease of the gap size clearly leads to a stronger electromagnetic field enhancement at the foremost end of the asymmetric dimer. In addition, the steep increase of the fluorescence rate within the sub-10 nm distance to the molecule demonstrates the stronger spatial light confinement provided by the dimer antenna. Taking into account this incline, it is obvious that the light confinement capabilities are dominated by the foremost, smallest AuNP of the antenna. However, a closer inspection of both approach curves also shows that for antenna-molecule separations beyond 10 nm the optical response stems largely from the 80 nm AuNP antenna.

Plasmon resonance spectra of CB[8]-mediated dimers

Figure 3B summarizes the determined fluorescence enhancement factors for several antennas of the same kind. On average, the fluorescence enhancement factor of the 80 nm AuNP monomer antenna is 10. Clearly, the spread in the obtained maximum and minimum enhancement factors and the corresponding vari-
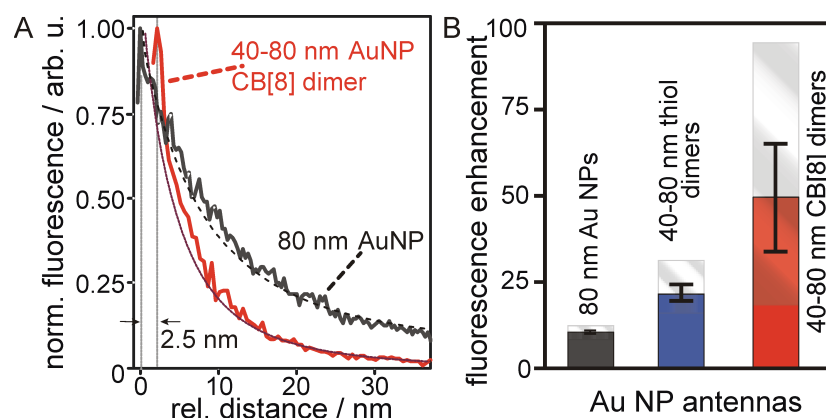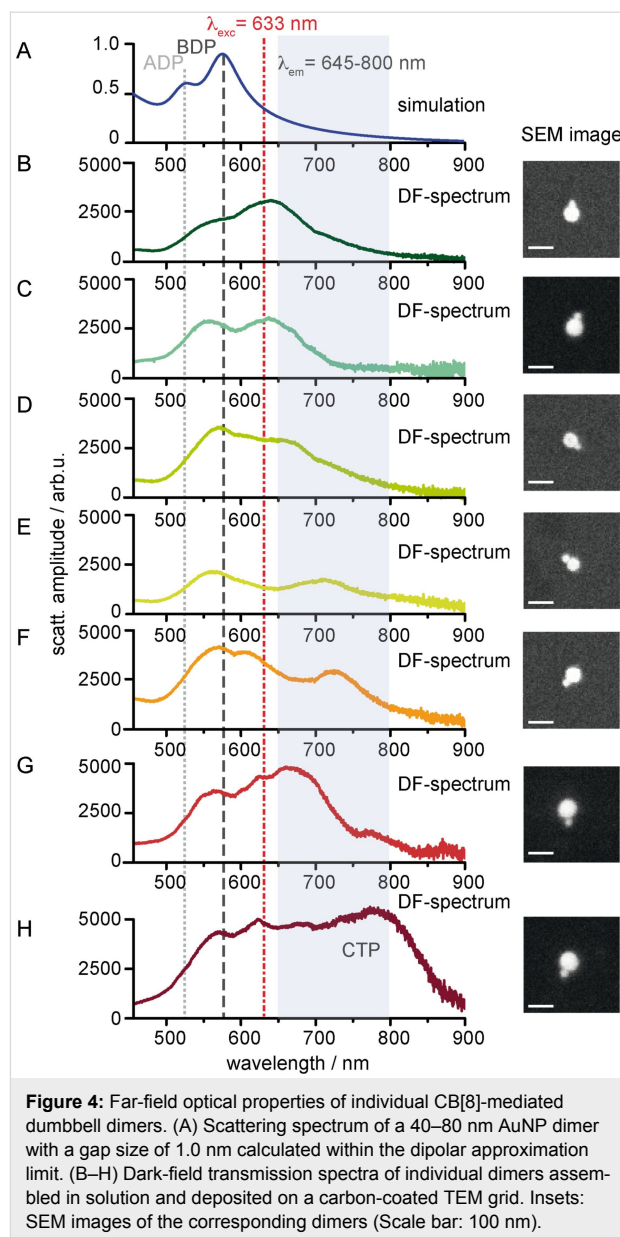

Figure 3: Antenna enhanced fluorescence of high QY emitters. (A) Normalized fluorescence emission rates as a function of the antenna-molecule distance for a CB[8]-mediated 40–80 nm AuNP dimer and a spherical 80 nm AuNP monomer antenna. The red, dotted and the black, dashed line correspond to the evaluation of the calculated electromagnetic field for these antennas. (B) Comparison of the absolute and averaged enhancement factors obtained for multiple 80 nm monomer antennas, thiol- and CB[8]-mediated 40–80 nm AuNP dimers.The error bars display the standard deviation.

ance is relatively low, indicating a high reproducibility of these antennas and a low influence of deviations from the sphere geometry on the enhancement factor. The enhancement factor is further increased by utilizing the gap mode. In this case the average fluorescence enhancement factor for the thiol-mediated gap antennas is determined to ≈22 whilst the CB[8]-mediated dimers enhance the fluorescence signal of a single *z*-aligned dye molecule on average by a factor ≈48. Apparently the reproducibility for the CB[8]-mediated dimers is lower than for the thiol-mediated dimers, although a high rigidity is expected for the CB[8]. The observed fluctuations in the fluorescence enhancement likely relate to variations in their far-field optical properties. Therefore, differences in the LSPR positions, width and the amplitude of the scattering-cross section may affect the near-field optical response. Due to the small gap size of CB[8]-mediated dumbbell dimers alterations in their far-field properties from the ideal dipolar model are expected to be more pronounced than for similar thiol-mediated dimers, which possess enlarged gap sizes. Entering the regime of sub-nanometer gaps the onset of quantum effects, such as, e.g., charge screening, are known to alter the plasmon coupling, and thus, the optical response. Furthermore, antennas with sub-nanometer gaps are more sensitive to deviations from the ideal sphere geometry, gap size fluctuations and morphological changes [27].

Therefore, dark-field spectra are recorded of individual CB[8]-mediated dimers, which are compared to the calculated scattering spectrum of an idealized dimer with a gap size of 1.0 nm (Figure 4). Clearly, the scattering spectrum calculated within the dipolar approximation limit reveals the dipolar bonding dimer plasmon (BDP) mode at 572 nm, and blue-shifted from the BDP, also the dipolar anti-bonding dimer plasmon (ADP) mode (Figure 4A), which is characteristic for the asymmetric dimer geometry. The experimentally recorded dark-field spectra displayed in Figure 4B–Figure 4H reflect this profile. However, the BDP and ADP peak positions are red-shifted and broadened in comparison to the calculated spectrum (Figure 4A). This can be largely explained by the different environmental conditions, i.e., the calculation does not account for the thin carbon substrate used for the measurements.

In addition to the dipolar mode structure, multiple spectra are characterized by a red-shift and a broadening of the BDP mode or even exhibit an additional peak (CTP-charge transfer plasmon mode) in the NIR region. The latter is indicative for the onset of charge transfer mechanisms. The origin for these deviations is not evident from the geometrical structure of the investigated dimers. Both, the size and the shape of the dimer-forming AuNPs appear relatively homogeneous from the additionally displayed SEM images (Figure 4). Furthermore, strong size variations can be also excluded for the tip-supported dimers

Figure 4: Far-field optical properties of individual CB[8]-mediated dumbbell dimers. (A) Scattering spectrum of a 40–80 nm AuNP dimer with a gap size of 1.0 nm calculated within the dipolar approximation limit. (B–H) Dark-field transmission spectra of individual dimers assembled in solution and deposited on a carbon-coated TEM grid. Insets: SEM images of the corresponding dimers (Scale bar: 100 nm).

based on the height information collected during the attachment process, the observed light confinement and the post-characterization by means of scanning electron microscopy imaging (SEM image, inset Figure 1C).

Since the spontaneous emission rate is taken as a measure for the electromagnetic field enhancement, the influence of the observed changes in the dark-field (DF) scattering spectra on the emission rate has to be considered. As outlined before, the spontaneous emission rate depends on the excitation/emission rate $\gamma_{exc/em}$ enhancement and on the quenching rate γ_{abs}. Despite of the origin of the observed spectral fluctuations of the individual dimers, these impose strong consequences on the fluorescence enhancement capabilities of a dimer antenna, since

the modification of the corresponding molecular transition rates is obeyed by different spectral dependencies. This usually finds evidence in the observation, that the fluorescence enhancement is strongest red-shifted from the LSPR peak. Taking into account the excitation wavelength of $\lambda_{exc} = 632.8$ nm used for the characterization of near-field optical properties of the dimers, the excitation rate enhancement is strongest for the dimers shown in Figure 4F–Figure 4H. For these dimers the scattering amplitude at λ_{exc} is approximately twice as strong as for the most regular spectra (Figure 4B and Figure 4C). Furthermore, these dimers possess also a strong scattering cross-section across the spectral emission region. Finally, the spectral resonance of the quenching rate has also to be taken into account additionally, which is usually blue-shifted from the LSPR. As a consequence of these dependencies, the effective local density of states (LDOS) varies.

The observed spectral variations for geometrically similar dimers are likely correlated to the spread in the fluorescence enhancement factor. In principle, these observed variations in the far-field and near-field optical properties may have different origins. Particularly, the particle size, particle geometry and gap capacitor properties, such as, the gap size, the gap conductivity and the gap morphology are the most intuitive parameters, which have been shown to affect the LSPR position, width and scattering cross-section [18,25,28,36,59,60]. As a first parameter, variations in the gap size have to be considered. Figure 5A

and Figure 5B display TEM images of a typical dumbbell dimer with a sub-nanometer gap size. In accordance with the used CB[8] linker molecule a gap size of 0.85 nm is found (lineprofile, Figure 5C). Overall, the observed gap sizes are in excellent agreement with the known height of CB[8] and only minor deviations occur.

Nanoscale morphology of the gap region

Furthermore, taking into account size variations of the dimer-forming AuNPs, these correlate well with the variations observed for the thiol-mediated dimers, which provide a relatively uniform enhancement factor. Therefore, minor geometric deviations are likely to be ruled out as a source for the wide spreading of enhancement factors found for the CB-mediated dimers. Therefore, dimers with sub-nanometer gaps are in addition characterized for their nanoscale structure in the gap region. High resolution TEM images of the formed dimers immediately reveal the faceted surface of the AuNPs. Therefore, these NPs do not match with the shape of a perfect sphere used frequently for the simulations. Recently, it has been shown that the uniformity and size of the facets has strong influence on the homogeneity of their LSPR spectra [28,30,60]. From the high-magnification TEM images of the gap region of the dimers displayed in Figure 6, it is obvious that the facet-nature of the AuNPs leads to multiple possible gap configurations. Large planar gaps are formed in the case that the two AuNPs assemble in a fashion that the gap-forming facets are aligned parallel to
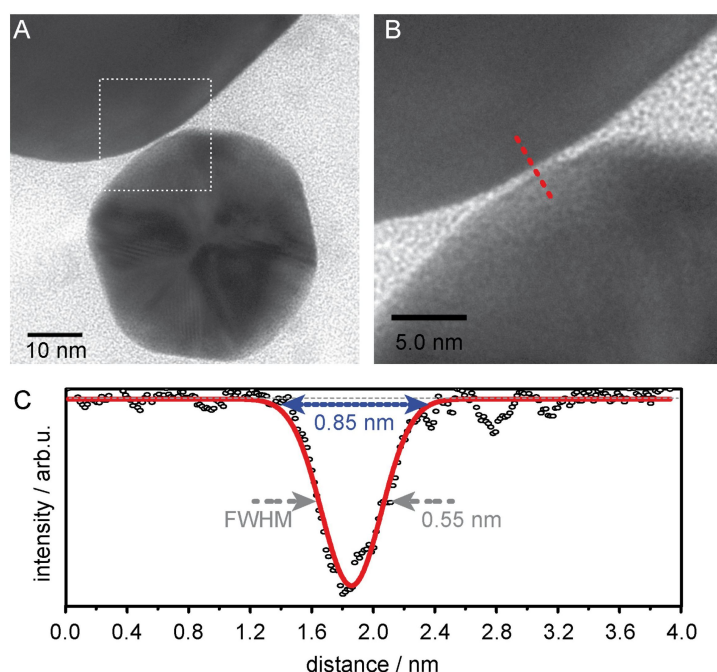

Figure 5: Gap size of CB[8] mediated 40–80 nm AuNP dimers. (A) TEM image of a dimer with sub-nanometer gap size. (B) High-magnification TEM image of the gap region. (C) Line-profile drawn across the gap (red dotted line in B).
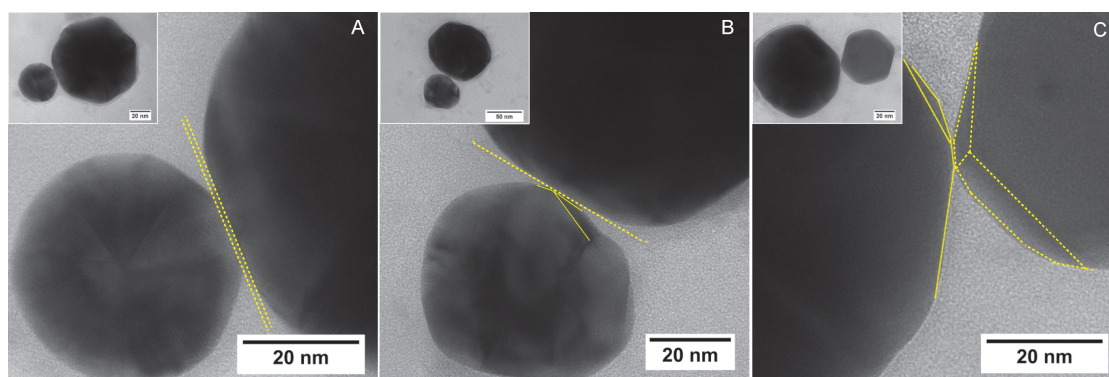
Figure 6: Morphologies of dumbbell dimers with sub-nanometer gap sizes. (A) Dimer with a planar gap. (B) Dimer with a gap formed by a large facet of the 80 nm AuNP and edge of the 40 nm AuNP. (C) Dimer with a pointed gap morphology formed by the interaction of the facet edges/corners of both contributing AuNPs.

each other (Figure 6A). However, the gap formation can include also facet edges (Figure 6B) or the corner of several facets merging in this point (Figure 6C). In this case the gap morphology changes from a larger planar gap into a smaller pointed gap, which modifies the mode volume, and thus, can lead to a stronger light concentration in the gap region, and thus, results in a higher electromagnetic field strength [61]. The facet edges, corners and atomic protrusion can be considered as points where the electromagnetic field is strongly confined, i.e., they can serve as hot spots of the electromagnetic field [14]. Therefore, the gap morphology of sub-nanometer size gaps has attracted high attention and recent investigations have shown a strong influence on the far-field properties of such gap antennas. For the CB[8]-mediated dimers with sub-nanometer gap sizes it is likely that different gap morphologies can alter the electromagnetic field confined to the end-point of the smallest sphere, especially if onsetting quantum effects lead to a redistribution of the electromagnetic near-field.

Conclusion

In conclusion, CB[8]-mediated dumbbell dimers formed of 40 nm and 80 nm AuNP dimers are shown to exhibit advanced properties in regard to the signal enhancement ratio and light confinement as compared to AuNP dimers with gap sizes of twice that of CB[8]-dimers. In particular, it is demonstrated that the enhancement of the electromagnetic field of the CB[8]-dimers is comparable to that of a similar trimer antenna composed of 20 nm, 40 nm and 80 nm AuNPs. In a few instances, even higher enhancement factors have been observed. Although the gap size reduction explains well the higher electromagnetic field strength at the end point of the dimer, the broad variation of enhancement factors assigned to multiple dumbbell dimers cannot be assigned to gap size fluctuations. The rigidity of CB[8] compared to alkane thiol linker molecules should lead to a high stability of the gap size. TEM

images reveal gap sizes of ≈0.85 nm. In addition to fluctuations in the electromagnetic field enhancement, strong variations in their far-field response are observed, which influence the near-field response in terms of the enhancement of the fluorescence emission of a single quantum emitter. The deviations are likely correlated to different gap configurations, which are easily identified in HR-TEM studies. The influence of the gap morphology on the optical properties turns out to be non-negligible. However, this effect becomes only significant for sub-nanometer size gaps. As such, the observed deviations are likely also to be governed by a modified onset of quantum size effects.

Methods
Fluorescence measurements

All optical measurements are acquired with an in-house built microscope, which combines a confocal microscope with an AFM setup for tip-enhanced fluorescence measurements. A detailed description of the microscope can be found in [62]. Briefly, the system uses a linearly polarized 15 mW HeNe laser (λ_{em} = 632.8 nm) as an excitation source for the fluorescence measurements. The laser beam is converted into a radially polarized beam by means of a liquid crystal mode converter (ArcOptics, Switzerland) which is coupled to an inverse microscope (Ti-U, Nikon, Japan) and is tightly focussed with a high NA objective (100× Plan APO, NA 1.49, Nikon, Japan) to the tip–sample region. The emitted fluorescence signal is collected with the same objective and is spectrally filtered for discrimination from the excitation light by means of a combination of dichroic mirrors and bandpass filters. The signal is detected by means of an Avalanche photodiode (SPCM-AQRH-TR, Excelitas, Canada). Images are recorded by scanning the sample through the laser focus using a piezoelectric scanner (Nano-H, Mad City Labs, USA). For each image pixel the emitted fluorescence signal is integrated for 5–10 ms. For the antenna-enhanced fluorescence emission, the antenna is precisely

aligned in the laser focus and the antenna–sample distance is maintained with sub-nanometer accuracy to 2–4 nm by means of a force feedback loop regulating on the frequency shift of the force sensor, which is excited at its resonance frequency. The fluorescence emission rate as a function of the antenna–sample distance is recorded with the feedback loop switched off, and retracting the antenna by 50 nm from the surface. The high quantum yield dyes Alexa633 and Alexa680 respectively, are applied for these measurements, which provide suitable absorption and emission properties in regard to the LSPR of the applied monomer and dimer AuNP antennas.

Dark-field spectroscopy

Dark-field spectra are acquired using a commercial dark-field condensor (TI-DF-NA 1.45-1.2, Nikon, Japan) for white light illumination. The scattered light is collected with a 100× objective with a variable numerical aperture, which is adjusted to ≈0.6, and spectrally resolved by means of a spectrograph with coupled CCD camera (Shamrock-303i-A/Newton EMCCD, Andor, Ireland). The recorded spectra are corrected for the background and for the spectrally varying detection efficiency of the CCD chip.

SEM/TEM investigations

SEM images are recorded with a Zeiss Gemini Crossbeam FIB/SEM with an acceleration voltage of 5 kV and the TEM investigations are carried out with a a FEI Technai $G^2$20 with an acceleration voltage of 200 kV, respectively, in brightfield mode. In order to access the correct gap size of the asymmetric dimers the TEM stage is tilted in 0.1° steps. TEM images with a high magnification used for the determination of the gap size are acquired for the tilt position providing the largest gap size.

Acknowledgements

ORCID® iDs

Christiane Höppener - https://orcid.org/0000-0002-4747-3951

References

1. Bharadwaj, P.; Deutsch, B.; Novotny, L. *Adv. Opt. Photonics* **2009,** *1,* 438–483. doi:10.1364/aop.1.000438
2. Schuller, J. A.; Barnard, E. S.; Cai, W.; Jun, Y. C.; White, J. S.; Brongersma, M. L. *Nat. Mater.* **2010,** *9,* 193–204. doi:10.1038/nmat2630
3. Höppener, C.; Novotny, L. *Q. Rev. Biophys.* **2012,** *45,* 209–255. doi:10.1017/s0033583512000042
4. Wang, T.; Nijhuis, C. A. *Appl. Mater. Today* **2016,** *3,* 73–86. doi:10.1016/j.apmt.2016.03.001
5. Bozhevolnyi, S. I.; Mortensen, N. A. *Nanophotonics* **2017,** *6,* 1185–1188. doi:10.1515/nanoph-2016-0179
6. Atwater, H. A.; Polman, A. *Nat. Mater.* **2010,** *9,* 205–213. doi:10.1038/nmat2629
7. Knight, M. W.; Sobhani, H.; Nordlander, P.; Halas, N. J. *Science* **2011,** *332,* 702–704. doi:10.1126/science.1203056
8. Kristensen, A.; Yang, J. K. W.; Bozhevolnyi, S. I.; Link, S.; Nordlander, P.; Halas, N. J.; Mortensen, N. A. *Nat. Rev. Mater.* **2016,** *2,* 16088. doi:10.1038/natrevmats.2016.88
9. Shi, X.; Coca-López, N.; Janik, J.; Hartschuh, A. *Chem. Rev.* **2017,** *117,* 4945–4960. doi:10.1021/acs.chemrev.6b00640
10. Höppener, C.; Lapin, Z. J.; Bharadwaj, P.; Novotny, L. *Phys. Rev. Lett.* **2012,** *109,* 017402. doi:10.1103/physrevlett.109.017402
11. Ciracì, C.; Hill, R. T.; Mock, J. J.; Urzhumov, Y.; Fernández-Domínguez, A. I.; Maier, S. A.; Pendry, J. B.; Chilkoti, A.; Smith, D. R. *Science* **2012,** *337,* 1072–1074. doi:10.1126/science.1224823
12. Chikkaraddy, R.; de Nijs, B.; Benz, F.; Barrow, S. J.; Scherman, O. A.; Rosta, E.; Demetriadou, A.; Fox, P.; Hess, O.; Baumberg, J. J. *Nature* **2016,** *535,* 127–130. doi:10.1038/nature17974
13. Richard-Lacroix, M.; Zhang, Y.; Dong, Z.; Deckert, V. *Chem. Soc. Rev.* **2017,** *46,* 3922–3944. doi:10.1039/c7cs00203c
14. Trautmann, S.; Aizpurua, J.; Götz, I.; Undisz, A.; Dellith, J.; Schneidewind, H.; Rettenmayr, M.; Deckert, V. *Nanoscale* **2017,** *9,* 391–401. doi:10.1039/c6nr07560f
15. Pack, A.; Hietschold, M.; Wannemacher, R. *Opt. Commun.* **2001,** *194,* 277–287. doi:10.1016/s0030-4018(01)01310-4
16. David, C.; García de Abajo, F. J. *J. Phys. Chem. C* **2011,** *115,* 19470–19475. doi:10.1021/jp204261u
17. Atay, T.; Song, J.-H.; Nurmikko, A. V. *Nano Lett.* **2004,** *4,* 1627–1631. doi:10.1021/nl049215n
18. Scholl, J. A.; García-Etxarri, A.; Koh, A. L.; Dionne, J. A. *Nano Lett.* **2013,** *13,* 564–569. doi:10.1021/nl304078v
19. Savage, K. J.; Hawkeye, M. M.; Esteban, R.; Borisov, A. G.; Aizpurua, J.; Baumberg, J. J. *Nature* **2012,** *491,* 574–577. doi:10.1038/nature11653
20. Jung, H.; Cha, H.; Lee, D.; Yoon, S. *ACS Nano* **2015,** *9,* 12292–12300. doi:10.1021/acsnano.5b05568
21. Danckwerts, M.; Novotny, L. *Phys. Rev. Lett.* **2007,** *98,* 026104. doi:10.1103/physrevlett.98.026104
22. Zhu, W.; Esteban, R.; Borisov, A. G.; Baumberg, J. J.; Nordlander, P.; Lezec, H. J.; Aizpurua, J.; Crozier, K. B. *Nat. Commun.* **2016,** *7,* 11495. doi:10.1038/ncomms11495
23. Esteban, R.; Borisov, A. G.; Nordlander, P.; Aizpurua, J. *Nat. Commun.* **2012,** *3,* 825. doi:10.1038/ncomms1806
24. Mortensen, N. A.; Raza, S.; Wubs, M.; Søndergaard, T.; Bozhevolnyi, S. I. *Nat. Commun.* **2014,** *5,* 3809. doi:10.1038/ncomms4809
25. Kern, J.; Großmann, S.; Tarakina, N. V.; Häckel, T.; Emmerling, M.; Kamp, M.; Huang, J.-S.; Biagioni, P.; Prangsma, J. C.; Hecht, B. *Nano Lett.* **2012,** *12,* 5504–5509. doi:10.1021/nl302315g
26. Gallinet, B.; Siegfried, T.; Sigg, H.; Nordlander, P.; Martin, O. J. F. *Nano Lett.* **2013,** *13,* 497–503. doi:10.1021/nl303896d
27. Esteban, R.; Aguirregabiria, G.; Borisov, A. G.; Wang, Y. M.; Nordlander, P.; Bryant, G. W.; Aizpurua, J. *ACS Photonics* **2015,** *2,* 295–305. doi:10.1021/ph5004016
28. Popp, P. S.; Herrmann, J. F.; Fritz, E.-C.; Ravoo, B. J.; Höppener, C. *Small* **2016,** *12,* 1667–1675. doi:10.1002/smll.201503536

29. Mertens, J.; Kleemann, M.-E.; Chikkaraddy, R.; Narang, P.;
Baumberg, J. J. *Nano Lett.* **2017,** *17,* 2568–2574.
doi:10.1021/acs.nanolett.7b00332

30. Huh, J.-H.; Lee, J.; Lee, S. *ACS Photonics* **2018,** *5,* 413–421.
doi:10.1021/acsphotonics.7b00856

31. Wang, Z. B.; Luk'yanchuk, B. S.; Guo, W.; Edwardson, S. P.;
Whitehead, D. J.; Li, L.; Liu, Z.; Watkins, K. G. *J. Chem. Phys.* **2008,**
128, 094705. doi:10.1063/1.2835598

32. Herrmann, J. F.; Kretschmer, F.; Hoeppener, S.; Höppener, C.;
Schubert, U. S. *Small* **2017,** *13,* 1701095. doi:10.1002/smll.201701095

33. Lee, H.; Kim, G.-H.; Lee, J.-H.; Kim, N. H.; Nam, J.-M.; Suh, Y. D.
Nano Lett. **2015,** *15,* 4628–4636. doi:10.1021/acs.nanolett.5b01322

34. Rechberger, W.; Hohenau, A.; Leitner, A.; Krenn, J.; Lamprecht, B.;
Aussenegg, F. *Opt. Commun.* **2003,** *220,* 137–141.
doi:10.1016/s0030-4018(03)01357-9

35. Nordlander, P.; Oubre, C.; Prodan, E.; Li, K.; Stockman, M. I.
Nano Lett. **2004,** *4,* 899–903. doi:10.1021/nl049681c

36. Brown, L. V.; Sobhani, H.; Lassiter, J. B.; Nordlander, P.; Halas, N. J.
ACS Nano **2010,** *4,* 819–832. doi:10.1021/nn9017312

37. Lee, J.-H.; Nam, J.-M.; Jeon, K.-S.; Lim, D.-K.; Kim, H.; Kwon, S.;
Lee, H.; Suh, Y. D. *ACS Nano* **2012,** *6,* 9574–9584.
doi:10.1021/nn3028216

38. Sheikholeslami, S.; Jun, Y.-w.; Jain, P. K.; Alivisatos, A. P. *Nano Lett.*
2010, *10,* 2655–2660. doi:10.1021/nl101380f

39. Horneber, A.; Baudrion, A.-L.; Adam, P.-M.; Meixner, A. J.; Zhang, D.
Phys. Chem. Chem. Phys. **2013,** *15,* 8031–8034.
doi:10.1039/c3cp43349h

40. Li, K.; Stockman, M. I.; Bergman, D. J. *Phys. Rev. Lett.* **2003,** *91,*
227402. doi:10.1103/physrevlett.91.227402

41. Bidault, S.; García de Abajo, F. J.; Polman, A. *J. Am. Chem. Soc.*
2008, *130,* 2750–2751. doi:10.1021/ja711074n

42. Kravets, V. G.; Zoriniants, G.; Burrows, C. P.; Schedin, F.;
Casiraghi, C.; Klar, P.; Geim, A. K.; Barnes, W. L.; Grigorenko, A. N.
Phys. Rev. Lett. **2010,** *105,* 246806.
doi:10.1103/physrevlett.105.246806

43. Gramotnev, D. K.; Bozhevolnyi, S. I. *Nat. Photonics* **2014,** *8,* 13–22.
doi:10.1038/nphoton.2013.232

44. Hohenester, U.; Trügler, A. *Comput. Phys. Commun.* **2012,** *183,*
370–381. doi:10.1016/j.cpc.2011.09.009

45. Kusar, P.; Gruber, C.; Hohenau, A.; Krenn, J. R. *Nano Lett.* **2012,** *12,*
661–665. doi:10.1021/nl203452d

46. Fruhnert, M.; Kretschmer, F.; Geiss, R.; Perevyazko, I.; Cialla-May, D.;
Steinert, M.; Janunts, N.; Sivun, D.; Hoeppener, S.; Hager, M. D.;
Pertsch, T.; Schubert, U. S.; Rockstuhl, C. *J. Phys. Chem. C* **2015,**
119, 17809–17817. doi:10.1021/acs.jpcc.5b04346

47. Mertens, J.; Eiden, A. L.; Sigle, D. O.; Huang, F.; Lombardo, A.;
Sun, Z.; Sundaram, R. S.; Colli, A.; Tserkezis, C.; Aizpurua, J.;
Milana, S.; Ferrari, A. C.; Baumberg, J. J. *Nano Lett.* **2013,** *13,*
5033–5038. doi:10.1021/nl4018463

48. Marshall, A. R. L.; Stokes, J.; Viscomi, F. N.; Proctor, J. E.;
Gierschner, J.; Bouillard, J.-S. G.; Adawi, A. M. *Nanoscale* **2017,** *9,*
17415–17421. doi:10.1039/c7nr05107g

49. Ding, B.; Deng, Z.; Yan, H.; Cabrini, S.; Zuckermann, R. N.; Bokor, J.
J. Am. Chem. Soc. **2010,** *132,* 3248–3249. doi:10.1021/ja9101198

50. Heck, C.; Prinz, J.; Dathe, A.; Merk, V.; Stranik, O.; Fritzsche, W.;
Kneipp, J.; Bald, I. *ACS Photonics* **2017,** *4,* 1123–1130.
doi:10.1021/acsphotonics.6b00946

51. Cossaro, A.; Mazzarello, R.; Rousseau, R.; Casalis, L.; Verdini, A.;
Kohlmeyer, A.; Floreano, L.; Scandolo, S.; Morgante, A.; Klein, M. L.;
Scoles, G. *Science* **2008,** *321,* 943–946. doi:10.1126/science.1158532

52. Smith, R. K.; Reed, S. M.; Lewis, P. A.; Monnell, J. D.; Clegg, R. S.;
Kelly, K. F.; Bumm, L. A.; Hutchison, J. E.; Weiss, P. S.
J. Phys. Chem. B **2001,** *105,* 1119–1122. doi:10.1021/jp0035129

53. Kim, J.; Jung, I.-S.; Kim, S.-Y.; Lee, E.; Kang, J.-K.; Sakamoto, S.;
Yamaguchi, K.; Kim, K. *J. Am. Chem. Soc.* **2000,** *122,* 540–541.
doi:10.1021/ja993376p

54. Taylor, R. W.; Lee, T.-C.; Scherman, O. A.; Esteban, R.; Aizpurua, J.;
Huang, F. M.; Baumberg, J. J.; Mahajan, S. *ACS Nano* **2011,** *5,*
3878–3887. doi:10.1021/nn200250v

55. de Nijs, B.; Kamp, M.; Szabó, I.; Barrow, S. J.; Benz, F.; Wu, G.;
Carnegie, C.; Chikkaraddy, R.; Wang, W.; Deacon, W. M.; Rosta, E.;
Baumberg, J. J.; Scherman, O. A. *Faraday Discuss.* **2017,** *205,*
505–515. doi:10.1039/c7fd00147a

56. Kern, A. M.; Zhang, D.; Brecht, M.; Chizhik, A. I.; Failla, A. V.;
Wackenhut, F.; Meixner, A. J. *Chem. Soc. Rev.* **2014,** *43,* 1263–1286.
doi:10.1039/c3cs60357a

57. Anger, P.; Bharadwaj, P.; Novotny, L. *Phys. Rev. Lett.* **2006,** *96,*
113002. doi:10.1103/physrevlett.96.113002

58. Kühn, S.; Håkanson, U.; Rogobete, L.; Sandoghdar, V. *Phys. Rev. Lett.*
2006, *97,* 017402. doi:10.1103/physrevlett.97.017402

59. Grillet, N.; Manchon, D.; Bertorelle, F.; Bonnet, C.; Broyer, M.;
Cottancin, E.; Lermé, J.; Hillenkamp, M.; Pellarin, M. *ACS Nano* **2011,**
5, 9450–9462. doi:10.1021/nn2041329

60. Yoon, J. H.; Selbach, F.; Langolf, L.; Schlücker, S. *Small* **2018,** *14,*
1702754. doi:10.1002/smll.201702754

61. Barbry, M.; Koval, P.; Marchesin, F.; Esteban, R.; Borisov, A. G.;
Aizpurua, J.; Sánchez-Portal, D. *Nano Lett.* **2015,** *15,* 3410–3419.
doi:10.1021/acs.nanolett.5b00759

62. Herrmann, J. F.; Popp, P. S.; Winter, A.; Schubert, U. S.; Höppener, C.
ACS Photonics **2016,** *3,* 1897–1906.
doi:10.1021/acsphotonics.6b00419

Metal–dielectric hybrid nanoantennas for efficient frequency conversion at the anapole mode

Valerio F. Gili[1], Lavinia Ghirardini[2], Davide Rocco[3], Giuseppe Marino[1], Ivan Favero[1], Iännis Roland[1], Giovanni Pellegrini[2], Lamberto Duò[2], Marco Finazzi[2], Luca Carletti[3], Andrea Locatelli[3], Aristide Lemaître[4], Dragomir Neshev[5], Costantino De Angelis[3], Giuseppe Leo[1] and Michele Celebrano[*2]

Abstract

Background: Dielectric nanoantennas have recently emerged as an alternative solution to plasmonics for nonlinear light manipulation at the nanoscale, thanks to the magnetic and electric resonances, the strong nonlinearities, and the low ohmic losses characterizing high refractive-index materials in the visible/near-infrared (NIR) region of the spectrum. In this frame, AlGaAs nanoantennas demonstrated to be extremely efficient sources of second harmonic radiation. In particular, the nonlinear polarization of an optical system pumped at the anapole mode can be potentially boosted, due to both the strong dip in the scattering spectrum and the near-field enhancement, which are characteristic of this mode. Plasmonic nanostructures, on the other hand, remain the most promising solution to achieve strong local field confinement, especially in the NIR, where metals such as gold display relatively low losses.

Results: We present a nonlinear hybrid antenna based on an AlGaAs nanopillar surrounded by a gold ring, which merges in a single platform the strong field confinement typically produced by plasmonic antennas with the high nonlinearity and low loss characteristics of dielectric nanoantennas. This platform allows enhancing the coupling of light to the nanopillar at coincidence with the

anapole mode, hence boosting both second- and third-harmonic generation conversion efficiencies. More than one order of magnitude enhancement factors are measured for both processes with respect to the isolated structure.

Conclusion: The present results reveal the possibility to achieve tuneable metamixers and higher resolution in nonlinear sensing and spectroscopy, by means of improved both pump coupling and emission efficiency due to the excitation of the anapole mode enhanced by the plasmonic nanoantenna.

Introduction

Second-harmonic generation (SHG) in bulk materials, first demonstrated by Franken and co-workers in 1961 [1], is nowadays successfully applied in a variety of disciplines. Besides its extended application in laser science for the realization of coherent light sources [2], SHG is a fundamental tool for the analysis and characterization of the crystal structure of solid materials [3-5]. The background-free character of SHG makes it an attractive tool for imaging biological tissues [6] and investigating structural and conformational properties of molecules at liquid–liquid interfaces [7]. The ability to downscale nonlinear optical processes, such as SHG, in extremely confined spatial regions opens many fascinating opportunities in light manipulation and multiplexing [8] as well as in optical sensing and spectroscopy [9,10]. Yet, to date, realizing nonlinear optical processes at the nanoscale remains a challenging task since phase-matching cannot be exploited as enhancement mechanism in systems confined below the wavelength of light. Exploiting the intense field enhancements stemming from plasmonic resonances in metallic nanoantennas is instead one of the most successful approaches to compensate for the lack of phase-matching and long interaction lengths at the nanoscale [11]. However, metals display large material losses in the visible range and limit the penetration depth of electric fields, thereby hindering the beneficial effects induced by the field enhancements. Moreover, centrosymmetry in metals results in extremely small efficiencies for second-order processes, a limitation that can be partly circumvented by designing individual nano-antennas [12] and extended array arrangements [13,14] featuring a lower degree of symmetry. Metal-less nanophotonics based on dielectrics of high refractive index and semiconductors recently emerged as a promising alternative to plasmonic nanostructures for linear and nonlinear nanophotonic applications due to the reduced losses at optical frequencies [15]. Since in high-index dielectric materials the electric field penetrates deeply into the volume [16], the exploitation of large bulk nonlinearities also enables enhanced nonlinear light–matter interactions at the nanoscale. Third-harmonic generation (THG) was the first nonlinear effect observed in nanoscale semiconductors with sizeable efficiency enhancement. First reported in individual silicon-on-insulator nanodisks [17] and soon after in a coupled nanodisk trimer configuration [18], the THG enhancement attained was up to 100 times higher than in a Si slab of the same thickness thanks to the exploitation of Mie-type resonances. Even higher THG efficiency enhancement has been recently achieved in germanium nanodisks thanks to the excitation of the so-called anapole mode (from the ancient Greek "without any pole") [19]. As the name suggests, the anapole mode consists in the superposition of a toroidal dipole (TD) and an electric dipole (ED) mode with a π-phase difference, which results in transparency at the anapole wavelength and a high energy stored inside the material [20,21]. The extremely confined fields in the resonator along with the relative weak coupling of the resonator to the external radiation allow for a boost of the quality factors in these Mie resonators. This peculiar feature holds great potential to further enhance light–matter interaction. For this reason, these systems are currently the subject of intense investigations and strategies to attain light absorption enhancement [21], nonlinear amplification [22] and enhanced Raman scattering [23] have been recently suggested.

In this framework, $Al_xGa_{1-x}As$, a III–V semiconductor, has become a popular material for nonlinear photonics thanks to its non-centrosymmetric structure and other important key assets including: i) a large band gap enabling TPA-free operation at 1.55 μm, ii) a high non-resonant quadratic susceptibility ($d_{14} \approx 100$ pm/V for GaAs in the near infrared), and iii) a broad spectral window of transparency in the mid-infrared (up to 17 μm), which allows for the generation of intense second-order nonlinear optical effects. Many results have already been achieved in integrated nonlinear optics [24], including SHG in quasi-phase-matched waveguides [25], efficient frequency-comb generation [25], and optical parametric oscillation [26]. Only very recently, thanks to the dramatic improvement of nanofabrication techniques, the integration of semiconducting materials has been pushed even further with the realization of nanoscale platforms featuring efficient second-order nonlinear processes. Recently, a nanoscale system based on AlGaAs nanodisks pumped in the telecom range (λ ≈ 1554 nm), at coincidence with the magnetic dipolar resonance, was theoretically proposed as an efficient system to enhance second-order nonlinear effects in nanoscale optics [27]. Soon after, three independent experiments validated these theoretical predictions [28-
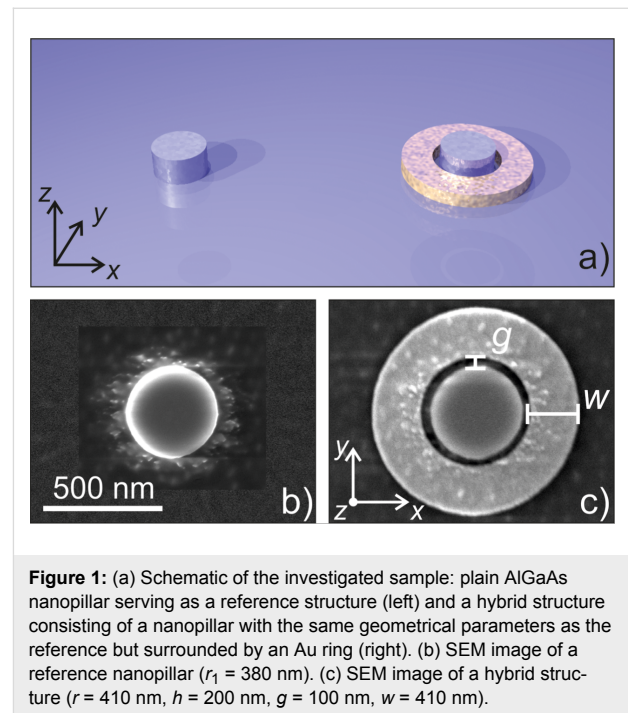
30]. The conversion efficiencies reported were higher than 10^{-5}, which is more than four orders of magnitude higher than in optimized plasmonic nanoantennas pumped at similar intensities [12]. Concurrently, promising studies on enhanced SHG at the nanoscale have also been performed on perovskite nanoparticles [31,32].

Several strategies that involve coupled nanosystems have been employed to enhance both second and third harmonic nonlinearities. For example, we recently reported enhanced SHG by closely coupling two AlGaAs nanopillars in a dimer configuration and by tuning the pump fundamental frequency to the anapole mode [33]. A further viable strategy involving coupled nanosystems, consists in placing a metal nanostructure in the proximity of the dielectric nanoantenna to manipulate the in- and out-coupling of light [34,35]. This hybrid integration was exploited to significantly boost the nonlinear conversion efficiency of nanosystems [32,36,37]. In particular, Maier and co-workers proposed a nanoantenna composed of a silicon disk core surrounded by an annular plasmonic antenna, which combines the energy-storage capabilities of the anapole mode with the enhanced efficiency of light-coupling in metal–dielectric systems. This allowed them to achieve a THG efficiency enhancement up to three orders of magnitude with respect to the bare disk [37]. In this work, we apply the same approach to obtain SHG enhancement in AlGaAs nanostructures [27,28,33] and investigate the properties of the emitted nonlinear optical signal. We find that the SHG yield at the anapole mode in these hybrid platforms is almost two orders of magnitude higher than in isolated nanopillars. We also find sizeable THG with an emission yield comparable to that of SHG, which is unexpected since third-order nonlinear processes are commonly negligible in these systems [28,38]. The polarization-dependent optical properties of this platform together with the SHG angular emission characteristics indicate an improvement in both pump coupling and emission efficiency. We hence obtain solid indications for the realization of a new class of nano-photonic platforms for nonlinear light manipulation at the nanoscale.

Results and Discussion

Our plasmonic-dielectric hybrid nanostructures consist of AlGaAs nanodisks surrounded by an Au ring (Figure 1). Individual nanodisks (Figure 1b) and Au rings with the same geometrical parameters are also fabricated as a reference. We consider two distinct geometries: type 1 features a nanopillar with nominal radius $r_1 = 410$ nm, height $h = 200$ nm and gap size $g_1 \approx 100$ nm as shown in Figure 1c, while type 2 features a nanopillar radius $r_2 = 380$ nm with the same height and a gap size $g_2 = 200$ nm (not shown). The geometrical parameters of the Au ring in both cases are $w = 410$ nm and $h = 80$ nm. At the fundamental wavelength the plasmonic ring produces a strong electric field at its center. This allows for an improved coupling to the toroidal dipole moment inside the disk, therefore providing a more efficient excitation of the anapole mode (i.e., ED and TD moments of equal magnitude and in phase opposition) at the fundamental wavelength ($\lambda = 1554$ nm).

Figure 1: (a) Schematic of the investigated sample: plain AlGaAs nanopillar serving as a reference structure (left) and a hybrid structure consisting of a nanopillar with the same geometrical parameters as the reference but surrounded by an Au ring (right). (b) SEM image of a reference nanopillar ($r_1 = 380$ nm). (c) SEM image of a hybrid structure ($r = 410$ nm, $h = 200$ nm, $g = 100$ nm, $w = 410$ nm).

We investigated the scattering characteristics of this structure at near-IR wavelengths by using finite element method (FEM) simulations in COMSOL. The incident light is a plane wave with a wave vector, **k**, parallel to the cylinder axis and the electric field, **E**$_0$, polarized along the y-axis with respect to the reference system of Figure 2a. For the dispersion of the refractive index of Al$_{0.18}$Ga$_{0.82}$As we used the analytical model proposed in [39]. In Figure 2b,c both the electric and magnetic field enhancements are depicted, respectively, which help identifying the typical anapole configuration. We have compared the linear behavior of the hybrid geometry against that of a bare nanodisk with its anapole mode at correspondence with the pump wavelength. To do so we focused on two key parameters: the total scattered power, calculated as the surface integral of the Poynting vector normal to an imaginary sphere enclosing the entire structure, and the internal energy defined as the volume integral of the squared electric field inside the cylinder.

To gain further insights into this behavior, in Figure 2d (2e) we show the contributions to the scattered power of the first five radiating multipole moments in the bare nanodisk (hybrid system) we computed the first five Cartesian multipole moments inside the cylinder using the expressions summarized
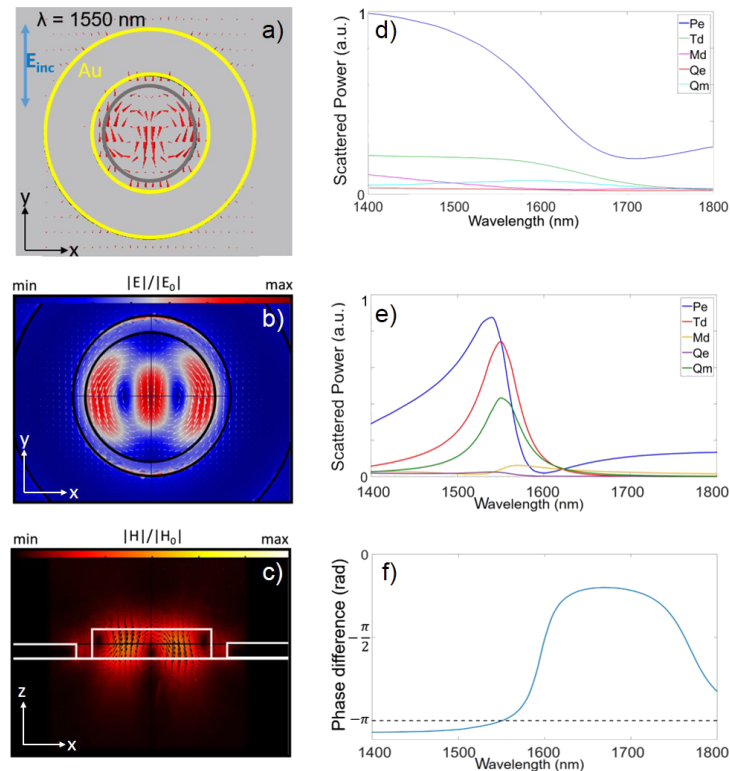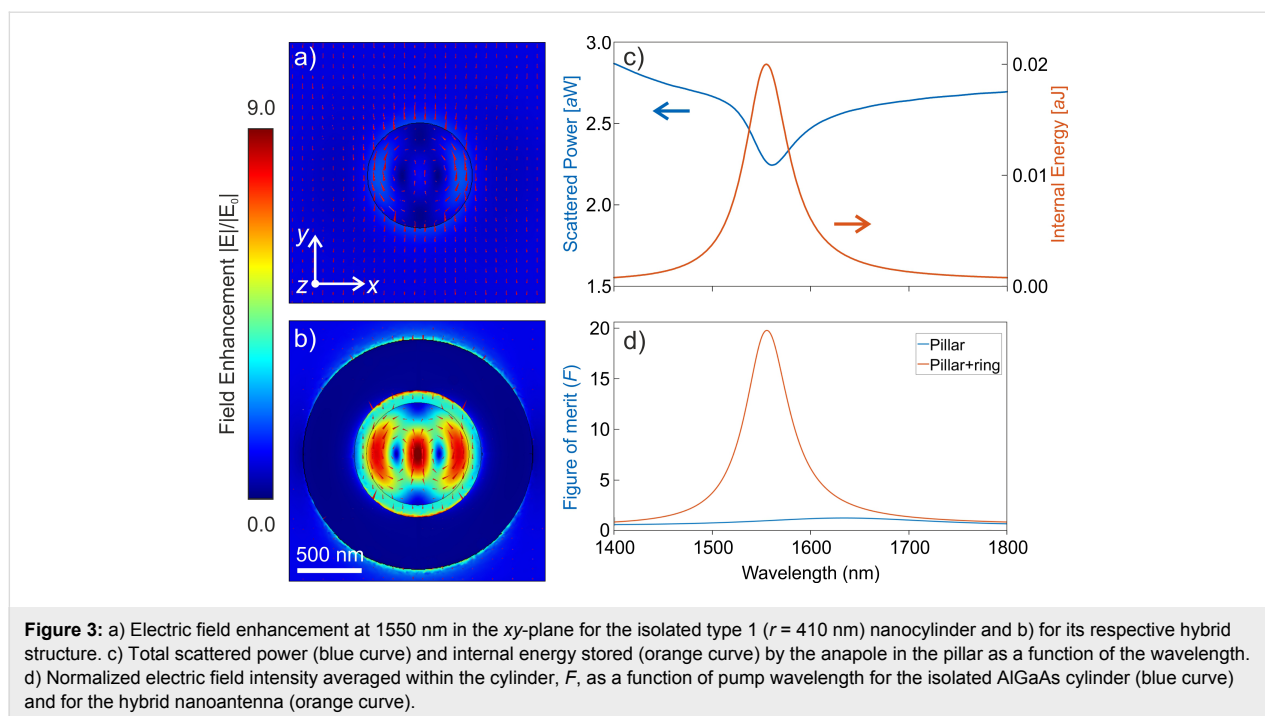
Figure 2: a) Electric field vector map at 1550 nm for the proposed structure. b) Electric and c) magnetic field distribution in the hybrid nanoantenna at 1550 nm. d) The full multipolar decomposition of the first five contributing multipole moments: electric dipole (Pe), magnetic dipole (Md), toroidal dipole (Td), electric quadrupole (Qe), magnetic quadrupole (Qm) for and isolated pillar and e) in the hybrid structure. f) Phase difference between Cartesian dipole moment Pe and toroidal moment Td of the induced current inside the cylinder in the hybrid structure.

in [40], where Pe, Md, Td, Qe and Qm indicate the electric dipole, magnetic dipole, toroidal dipole, electric quadrupole and magnetic quadrupole moments, respectively. The multipole decomposition reveals that, while the electric dipole is dominant in the bare nanodisk, both the electric and toroidal dipole components are dominant inside the cylinder when the gold ring is present. In particular, they have the same magnitude and a phase difference close to $-\pi$ (see Figure 2f) for $\lambda = 1550$ nm. Let us recall that, to get the exact anapole condition, the two abovementioned dipoles must be in phase opposition and exhibit the same magnitude while all the other contributions are zero. Unlike the ideal case, in our situation, there is a magnetic quadrupole contribution that slightly perturbs the anapole condition. Looking at the electric field inside the cylinder, it is possible to observe the typical anapole field distribution (see upper panel of Figure 2a) where almost the whole E-field amplitude circulates in the plane of the disk and is confined inside it. We also evaluated the electric field enhancement inside the cylinder, defined as the ratio between the total field E and the incident field E_0, as a figure of merit to assess the performance of the ring-assisted antenna. The maximum field enhancement is about six times higher in the hybrid structure than

in the isolated cylinder, as shown by the comparison between Figure 3a and Figure 3b. Figure 3c displays the wavelength-dependent total scattered power and internal energy stored in the structure, which confirm the anapole-like behavior at the pump wavelength. By engineering the geometrical parameters of dielectric nanoresonators working at the anapole mode, Wang and Dal Negro [21] demonstrated that light absorption can be enhanced. While this approach proved effective to finely tune the anapole condition, the pump light absorption and, therefore, the field enhancement inside the structure remains rather limited. In this work, by exploiting the plasmonic ring, we obtain a 20-fold increase in the field intensity enhancement averaged over the whole structure volume, F, as compared to the bare nanopillar (see Figure 3d), which is comparable to what was already reported in [37].

In this experiment we fully characterized the nonlinear emission from individual nanostructures, by using the nonlinear confocal setup described in the Experimental section (see also [28,33,38]). In brief, each individual nanoantenna is addressed with ultrashort pump pulses (140 fs) centered at 1554 nm and focused down to the diffraction limit by a 0.85 NA objective.

Figure 3: a) Electric field enhancement at 1550 nm in the *xy*-plane for the isolated type 1 (*r* = 410 nm) nanocylinder and b) for its respective hybrid structure. c) Total scattered power (blue curve) and internal energy stored (orange curve) by the anapole in the pillar as a function of the wavelength. d) Normalized electric field intensity averaged within the cylinder, *F*, as a function of pump wavelength for the isolated AlGaAs cylinder (blue curve) and for the hybrid nanoantenna (orange curve).

The pump peak intensity is kept below a few gigawatts per square centimeter. We measured 10 × 10 arrays of individual pillars, individual Au rings, and the hybrid structures, where the former two are used as references. Figure 4a shows the SHG maps recorded on portions of the arrays: from left to right are shown pillar, rings and hybrid antennas. A statistic of the emission within each array leads to the histogram shown in Figure 4b.

The type-1 configuration (*g* = 100 nm) yields a SHG enhancement factor up to 30 with respect to the corresponding individual pillar (*r* = 410 nm), while for the type-2 configuration (*g* = 200 nm) the signal enhancement is about one order of magnitude. The contribution of the Au ring to the overall SH emission is negligible (Figure 4b), and thus the signal enhancement is only the result of the better field confinement inside the dielectric material brought about by the hybrid configuration, as shown in Figure 3d. A log–log plot of the emission as a function of the power acquired from a type-2 platform using a narrowband filter at 775 nm (25 nm bandwidth) shows the quadratic behavior typical of two-photon processes (Figure 4c). Figure 4d shows the emission spectra collected around the SHG line from the different structures under study. It can be clearly seen that the emission within our window of interest is pure SHG and, along with Figure 3b, this set of measurements quantifies the nonlinear emission enhancement effect due to the hybrid-antenna configuration. Thus, compared to an all-dielectric structure with the same geometrical parameters, the hybrid configuration offers a sizeable nonlinear signal enhancement

when the anapole is excited at the fundamental wavelength. To better address this outcome, we have thoroughly analyzed the SHG dependence as a function of the incident polarization as well as the SHG emission patterns for both the hybrid structure and the reference isolated pillar.

Figure 5 shows the polar plots of the total collected SH intensity (i.e., without an analyzer in the collection path) as a function of the incident light polarization for both the reference elements (Figure 5a) and for the hybrid antennas (Figure 5b). This confirms that the gold ring improves the coupling of the pump light into the crystal by inducing an electric dipole inside the semiconductor that can be oriented parallel to the crystallographic axes for improved SHG. There is also an intensity difference of one order of magnitude between the two sets of polar plots, in agreement with the SHG enhancement factors extrapolated from Figure 4. The emission pattern recorded at the back focal plane for the reference elements (Figure 5c,e) and for the hybrid antennas (Figure 5d,f) confirm an improved collection efficiency for the hybrid configuration. Interestingly, the emission pattern is also strongly modified, moving from an isotropic emission in the reference structures to a dipole-like strongly directional emission in the presence of the plasmonic antenna element.

The highest conversion efficiency achieved by the type-2 hybrid structures is about 5×10^{-6}, at a pump intensity of about 1.6 GW·cm^{-2}. This value is comparable to that of nanopillars of the same material excited at correspondence with the magnetic
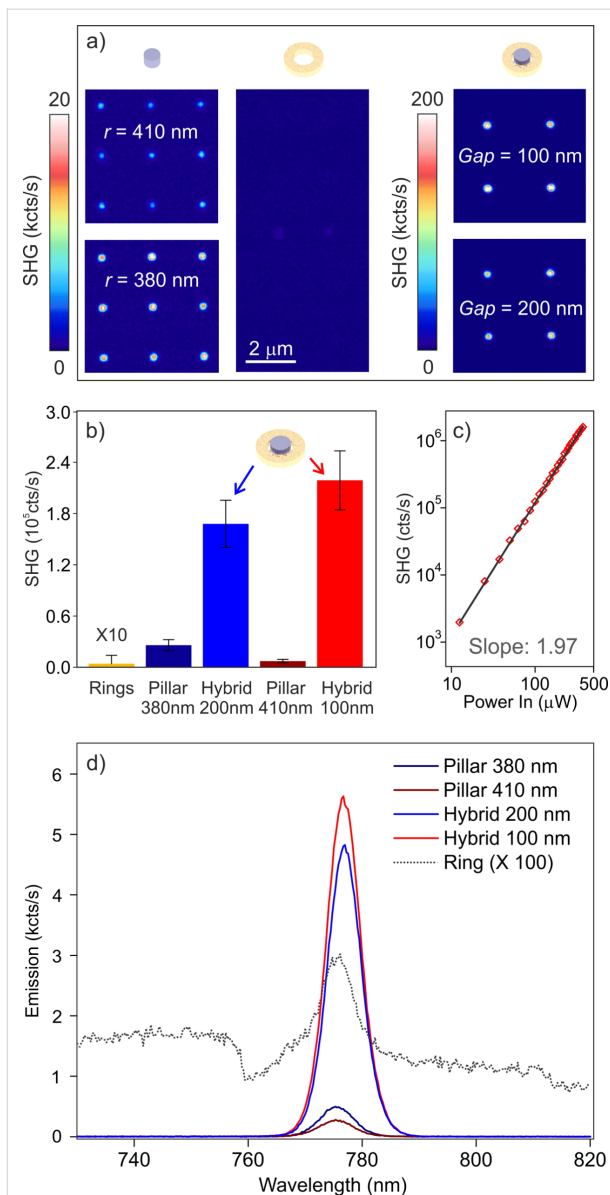
Figure 4: (a) SH nonlinear maps collected from the hybrid antennas and from the reference structures. From left to right: isolated pillars (3 × 3 sub-array), rings (2 × 4 sub array) and hybrid structures (2 × 2 sub-array). (b) Histogram showing the emission statistics for each array. (c) Log–log plot of the emission as a function of the power of structures with a gap of 200 nm, superimposed with a line of slope = 1.97. (d) Nonlinear emission spectra from the different elements under investigation obtained using the same incident pump intensity of 2 GW·cm^{-2}.

Figure 5: Polar plots of SHG emission from (a) the reference elements and (b) the hybrid antennas as a function of the incident polarization. Experimental emission pattern of the type-1 (c) and type-2 (e) isolated nanopillars used as reference and of their respective hybrid antennas (d) and (f). The white arrow in (c) indicates the polarization direction of the pump field for all the back focal plane maps.

dipole resonance at the fundamental wavelength, as measured in our previous works [38,41]. This experimental outcome, which is confirmed by our simulations, is the result of a trade-off situation. In fact, while the magnetic dipole resonance in the isolated dielectric nanostructures reported in our early work corresponds to a strong scattering regime, the anapole mode is weakly coupled to radiating modes, therefore it cannot be efficiently excited by far-field illumination. This results in a low
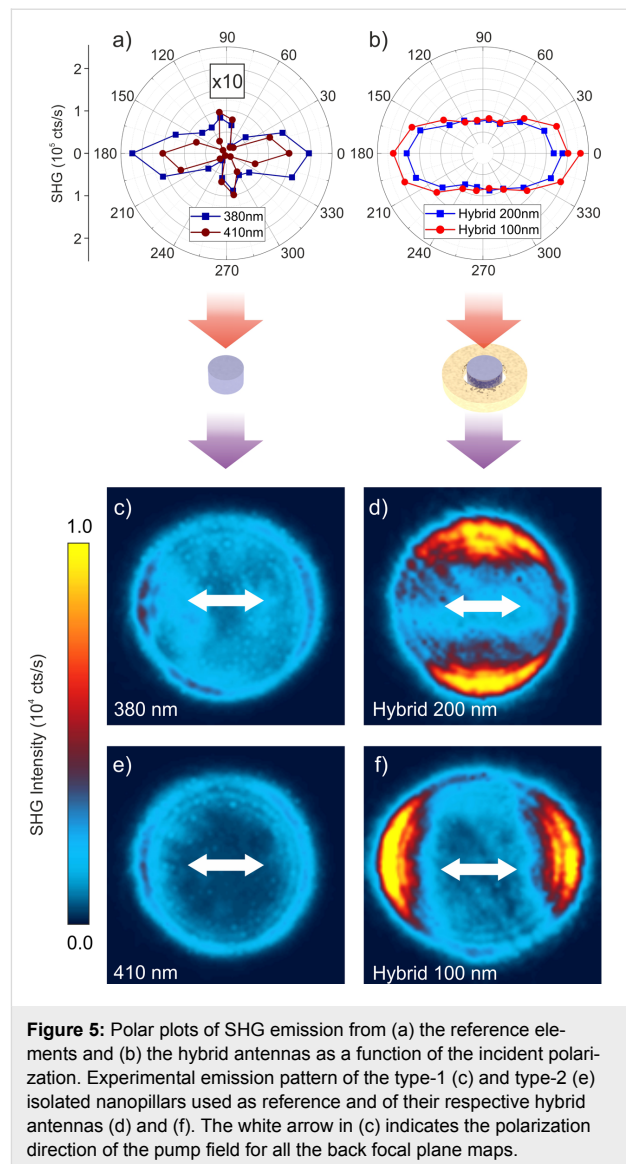
field enhancement averaged inside the structure, *F* (blue line in Figure 3d) and in a much higher SHG efficiency for the former platform compared to the nanodisk operating at the anapole condition. In this frame, opening a coupling channel for the light via the gold nanoring helps improving the field enhancement *F* inside the nanodisk, but it also weakens the anapole condition and reduces the quality factor because of increased radiation losses. As a result, while the *F* value in the hybrid antenna is enhanced by more than two orders of magnitude, the SHG yield is only increased by one order of magnitude (see Figure 5d,f). Furthermore, in the hybrid configuration, SHG still gets irradiated at high angles with respect to the antenna axis, hence the overall collection efficiency it not improved substantially. The development of optimized plasmonic nanoantennas for better light coupling and nonlinear emission directionality would allow one to further enhance this process.

A noteworthy feature of these hybrid nanoantennas, featuring a strong anapole mode-matching at the fundamental wavelength, is also the strong emission yield obtained in THG, which is unexpectedly high for this material, as confirmed by previous investigations [28]. Figure 6 shows the spectra collected from an individual type-2 pillar and its respective hybrid structure, acquired in the whole visible range. While a sizeable THG is already emitted by the reference pillar, the improved field confinement produced by the Au ring in the structure allows one to achieve more than one order of magnitude enhancement in the THG. This corresponds to emission yields comparable with SHG, when an average incident excitation power of about 1 mW is employed.
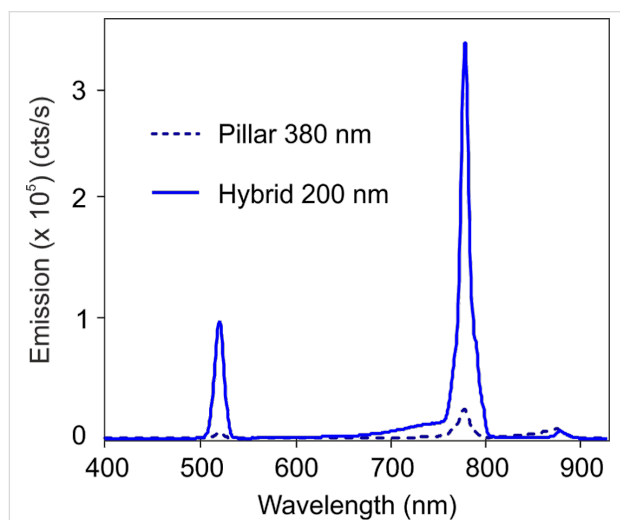

Figure 6: Emission spectrum of a type-2 pillar and its relative hybrid structure. The hybrid structure features more than one order of magnitude enhancement for the THG.

Conclusion

We thoroughly investigated a hybrid nanoantenna composed of an individual AlGaAs nanopillar, featuring an anapole mode resonant with the pump wavelength, surrounded by an Au ring designed to improve light coupling to the nanostructure anapole. This enables the improvement of both the second- and third-order nonlinear efficiencies, with measured enhancement factors of about 30 and 15 for the SHG and THG processes, respectively. The analysis of both SHG emission as a function of the pump polarization and angular emission of the SHG reveal that the plasmonic ring increases the pump in-coupling as well as the emission out-coupling. These results represent a step forward in the optimization of nonlinear light manipulation in dielectric nanostructures. The possibility to effectively enhance SHG using the anapole mode field distribution boosted by a plasmonic nanoantenna opens up new avenues for nonlinear sensing, spectroscopy as well as frequency down-conversion and nonlinear multiplexing at the nanoscale [8].

Experimental
Sample fabrication

The samples are grown by molecular beam epitaxy from a (100) non-intentionally doped GaAs substrate. At the end of the process, 400 nm of $Al_{0.18}Ga_{0.82}As$ rest on a 1 μm $Al_{0.98}Ga_{0.02}As$ sacrificial layer, which will be selectively oxidized at a later stage to achieve a low-index AlO_x substrate. 3 nm of SiO_x are deposited on the surface via plasma-enhanced chemical vapor deposition (PECVD) to later improve the adhesion of the negative-tone HSQ resist on the III–V layer. A first positive-tone lithography step with PMMA resist is performed to realize the alignment structures, followed by electron beam evaporation of 5 nm of Ti and 80 nm of Au. Finally, a standard lift-off procedure reveals the gold alignment structures. The choice of gold as a material at this stage is crucial to ensure the highest possible contrast and precision in the successive lithography step. HSQ resist is then spun and nanoantenna patterns are transferred on the resist with a second lithography step. Two non-selective etching processes are then performed: a first CHF_3-mediated reactive ion etching (RIE) removes the 3 nm SiO_x layer which is no longer needed, while the second inductively coupled plasma RIE with $SiCl_4/Ar$ gas treatment transfers the nanoantenna pattern on the $Al_{0.18}Ga_{0.82}As$ layer, revealing the Al-rich layer. The latter is immediately selectively oxidized at 390° for 30 min under a controlled water vapor flow with N_2H_2 carrier gas. Finally, a third positive-tone lithography process analogous to the first one, followed by electron beam evaporation and lift-off, defines the gold nanorings.

Optical setup

The nonlinear optical microscope employed in our experiment is depicted in Figure 7. The radiation from a 150 fs-laser centered at 1554 nm is sent to the sample through a high-NA
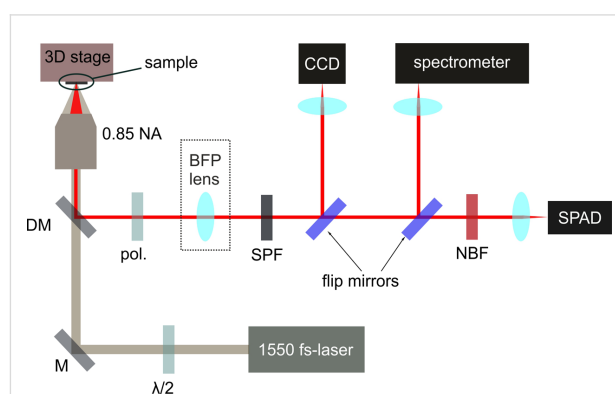

Figure 7: Sketch of the nonlinear setup employed for our measurements. The setup allows for the acquisition of nonlinear maps, nonlinear spectra and nonlinear back-focal-plane images of the pillars. DM, dichroic mirror; BFP lens, back focal plane lens; SPF, short-pass filter; NBF, narrow-band filter; SPAD, single photon avalanche detector.

(0.85) air objective, after setting the linear polarization direction with a half-wavelength plate. The nonlinear emission from the antennas is collected in reflection geometry and filtered before detection with a short-pass filter at 1000 nm and with a narrow-band filter at 775 nm to eliminate the residual pump signal and any TH and photoluminescence components. SH maps of the antennas are obtained by raster scanning the sample with a piezoelectric stage, and by recording the signal with a single-photon detector. Once a desired structure has been selected, instead, it is possible to image its SH radiation pattern in the Fourier space on a cooled-CCD camera by inserting a confocal lens focusing at the objective BFP. A flip-mirror can also be inserted in the detection path to send the unfiltered emission to a visible spectrometer for spectrum acquisition.

Acknowledgements

ORCID® iDs

Valerio F. Gili - https://orcid.org/0000-0001-8723-9986
Lavinia Ghirardini - https://orcid.org/0000-0003-4049-129X
Davide Rocco - https://orcid.org/0000-0002-5678-0531
Giuseppe Marino - https://orcid.org/0000-0001-8979-051X
Marco Finazzi - https://orcid.org/0000-0002-9197-3654
Aristide Lemaître - https://orcid.org/0000-0003-1892-9726
Dragomir Neshev - https://orcid.org/0000-0002-4508-8646
Costantino De Angelis - https://orcid.org/0000-0001-8029-179X
Michele Celebrano - https://orcid.org/0000-0003-3336-3580

References

1. Franken, P. A.; Hill, A. E.; Peters, C. W.; Weinreich, G. *Phys. Rev. Lett.* **1961,** *7,* 118–119. doi:10.1103/PhysRevLett.7.118
2. Cerullo, G.; De Silvestri, S. *Rev. Sci. Instrum.* **2003,** *74,* 1–18. doi:10.1063/1.1523642
3. Sipe, J. E.; Moss, D. J.; van Driel, H. M. *Phys. Rev. B* **1987,** *35,* 1129–1141. doi:10.1103/PhysRevB.35.1129
4. Petrocelli, G.; Pichini, E.; Scudieri, F.; Martellucci, S. *J. Opt. Soc. Am. B* **1993,** *10,* 918–923. doi:10.1364/JOSAB.10.000918
5. Bottomley, D. J.; Lüpke, G.; Mihaychuk, J. G.; van Driel, H. M. *J. Appl. Phys.* **1993,** *74,* 6072–6078. doi:10.1063/1.355223
6. Chen, X.; Nadiarynkh, O.; Plotnikov, S.; Campagnola, P. J. *Nat. Protoc.* **2012,** *7,* 654–669. doi:10.1038/nprot.2012.009
7. Steel, W. H.; Walker, R. A. *Nature* **2003,** *424,* 296–299. doi:10.1038/nature01791
8. Liu, S.; Vabishchevich, P. P.; Vaskin, A.; Reno, J. L.; Keeler, G. A.; Sinclair, M. B.; Staude, I.; Brener, I. *Nat. Commun.* **2018,** *9,* No. 2507. doi:10.1038/s41467-018-04944-9
9. Krasnok, A.; Tymchenko, M.; Alù, A. *Mater. Today* **2018,** *21,* 8–21. doi:10.1016/j.mattod.2017.06.007
10. Caldarola, M.; Albella, P.; Cortés, E.; Rahmani, M.; Roschuk, T.; Grinblat, G.; Oulton, R. F.; Bragas, A. V.; Maier, S. A. *Nat. Commun.* **2015,** *6,* No. 7915. doi:10.1038/ncomms8915
11. Kauranen, M.; Zayats, A. V. *Nat. Photonics* **2012,** *6,* 737–748. doi:10.1038/nphoton.2012.244
12. Celebrano, M.; Wu, X. F.; Baselli, M.; Grossmann, S.; Biagioni, P.; Locatelli, A.; De Angelis, C.; Cerullo, G.; Osellame, R.; Hecht, B.; Duò, L.; Ciccacci, F.; Finazzi, M. *Nat. Nanotechnol.* **2015,** *10,* 412–417. doi:10.1038/nnano.2015.69
13. Baselli, M.; Baudrion, A.-L.; Ghirardini, L.; Pellegrini, G.; Sakat, E.; Carletti, L.; Locatelli, A.; De Angelis, C.; Biagioni, P.; Duò, L.; Finazzi, M.; Adam, P.-M.; Celebrano, M. *Plasmonics* **2017,** *12,* 1595–1600. doi:10.1007/s11468-016-0423-y
14. Marino, G.; Segovia, P.; Krasavin, A. V.; Ginzburg, P.; Olivier, N.; Wurtz, G. A.; Zayats, A. V. *Laser Photonics Rev.* **2018,** *12,* 1700189. doi:10.1002/lpor.201700189
15. Kuznetsov, A. I.; Miroshnichenko, A. E.; Brongersma, M. L.; Kivshar, Y. S.; Luk'yanchuk, B. *Science* **2016,** *354,* aag2472. doi:10.1126/science.aag2472
16. Smirnova, D.; Kivshar, Y. S. *Optica* **2016,** *3,* 1241–1255. doi:10.1364/OPTICA.3.001241
17. Shcherbakov, M. R.; Neshev, D. N.; Hopkins, B.; Shorokhov, A. S.; Staude, I.; Melik-Gaykazyan, E. V.; Decker, M.; Ezhov, A. A.; Miroshnichenko, A. E.; Brener, I.; Fedyanin, A. A.; Kivshar, Y. S. *Nano Lett.* **2014,** *14,* 6488–6492. doi:10.1021/nl503029j
18. Shcherbakov, M. R.; Shorokhov, A. S.; Neshev, D. N.; Hopkins, B.; Staude, I.; Melik-Gaykazyan, E. V.; Ezhov, A. A.; Miroshnichenko, A. E.; Brener, I.; Fedyanin, A. A.; Kivshar, Y. S. *ACS Photonics* **2015,** *2,* 578–582. doi:10.1021/acsphotonics.5b00065
19. Grinblat, G.; Li, Y.; Nielsen, M. P.; Oulton, R. F.; Maier, S. A. *ACS Nano* **2017,** *11,* 953–960. doi:10.1021/acsnano.6b07568
20. Miroshnichenko, A. E.; Evlyukhin, A. B.; Yu, Y. F.; Bakker, R. M.; Chipouline, A.; Kuznetsov, A. I.; Luk'yanchuk, B.; Chichkov, B. N.; Kivshar, Y. S. *Nat. Commun.* **2015,** *6,* No. 8069. doi:10.1038/ncomms9069
21. Wang, R.; Dal Negro, L. *Opt. Express* **2016,** *24,* 19048–19062. doi:10.1364/OE.24.019048
22. Gongora, J. S. T.; Miroshnichenko, A. E.; Kivshar, Y. S.; Fratalocchi, A. *Nat. Commun.* **2017,** *8,* No. 15535. doi:10.1038/ncomms15535
23. Baranov, D. G.; Verre, R.; Karpinski, P.; Käll, M. *ACS Photonics* **2018,** *5,* 2730–2736. doi:10.1021/acsphotonics.8b00480
24. Pu, M.; Ottaviano, L.; Semenova, E.; Yvind, K. *Optica* **2016,** *3,* 823–826. doi:10.1364/OPTICA.3.000823
25. Morais, N.; Roland, I.; Ravaro, M.; Hease, W.; Lemaître, A.; Gomez, C.; Wabnitz, S.; De Rosa, M.; Favero, I.; Leo, G. *Opt. Lett.* **2017,** *42,* 4287–4290. doi:10.1364/OL.42.004287
26. Savanier, M.; Ozanam, C.; Lanco, L.; Lafosse, X.; Andronico, A.; Favero, I.; Ducci, S.; Leo, G. *Appl. Phys. Lett.* **2013,** *103,* 261105. doi:10.1063/1.4853595
27. Carletti, L.; Locatelli, A.; Stepanenko, O.; Leo, G.; De Angelis, C. *Opt. Express* **2015,** *23,* 26544–26550. doi:10.1364/OE.23.026544
28. Gili, V. F.; Carletti, L.; Locatelli, A.; Rocco, D.; Finazzi, M.; Ghirardini, L.; Favero, I.; Gomez, C.; Lemaître, A.; Celebrano, M.; De Angelis, C.; Leo, G. *Opt. Express* **2016,** *24,* 15965–15971. doi:10.1364/OE.24.015965

29. Camacho-Morales, R.; Rahmani, M.; Kruk, S.; Wang, L.; Xu, L.;
Smirnova, D. A.; Solntsev, A. S.; Miroshnichenko, A. A.; Tan, H. H.;
Karouta, F.; Naureen, S.; Vora, K.; Carletti, L.; De Angelis, C.;
Jagadish, C.; Kivshar, Y. S.; Neshev, D. N. *Nano Lett.* **2016,** *16,*
7191–7197. doi:10.1021/acs.nanolett.6b03525

30. Liu, S.; Vabishchevich, P. P.; Vaskin, A.; Reno, J. L.; Keeler, G. A.;
Sinclair, M. B.; Staude, I.; Brener, I. *arXiv* **2017,** 1711.

31. Timpu, F.; Sergeyev, A.; Hendricks, N. R.; Grange, R. *ACS Photonics*
2017, *4,* 76–84. doi:10.1021/acsphotonics.6b00570

32. Timpu, F.; Hendricks, N. R.; Petrov, M.; Ni, S.; Renaut, C.; Wolf, H.;
Isa, L.; Kivshar, Y.; Grange, R. *Nano Lett.* **2017,** *17,* 5381–5388.
doi:10.1021/acs.nanolett.7b01940

33. Rocco, D.; Gili, V. F.; Ghirardini, L.; Carletti, L.; Favero, I.; Locatelli, A.;
Marino, G.; Neshev, D. N.; Celebrano, M.; Finazzi, M.; Leo, G.;
De Angelis, C. *Photonics Res.* **2018,** *6,* B6–B12.
doi:10.1364/PRJ.6.0000B6

34. Guo, R.; Rusak, E.; Staude, I.; Dominguez, J.; Decker, M.;
Rockstuhl, C.; Brener, I.; Neshev, D. N.; Kivshar, Y. S. *ACS Photonics*
2016, *3,* 349–353. doi:10.1021/acsphotonics.6b00012

35. Decker, M.; Pertsch, T.; Staude, I. *Philos. Trans. R. Soc., A* **2017,** *375,*
20160312. doi:10.1098/rsta.2016.0312

36. Kruk, S.; Weismann, M.; Bykov, A. Y.; Mamonov, E. A.;
Kolmychek, I. A.; Murzina, T.; Panoiu, N. C.; Neshev, D. N.;
Kivshar, Y. S. *ACS Photonics* **2015,** *2,* 1007–1012.
doi:10.1021/acsphotonics.5b00215

37. Shibanuma, T.; Grinblat, G.; Albella, P.; Maier, S. A. *Nano Lett.* **2017,**
17, 2647–2651. doi:10.1021/acs.nanolett.7b00462

38. Ghirardini, L.; Carletti, L.; Gili, V.; Pellegrini, G.; Duò, L.; Finazzi, M.;
Rocco, D.; Locatelli, A.; De Angelis, C.; Favero, I.; Ravaro, M.; Leo, G.;
Lemaître, A.; Celebrano, M. *Opt. Lett.* **2017,** *42,* 559–562.
doi:10.1364/OL.42.000559

39. Carletti, L.; Rocco, D.; Locatelli, A.; De Angelis, C.; Gili, V. F.;
Ravaro, M.; Favero, I.; Leo, G.; Finazzi, M.; Ghirardini, L.;
Celebrano, M.; Marino, G.; Zayats, A. V. *Nanotechnology* **2017,** *28,*
114005. doi:10.1088/1361-6528/aa5645

40. Gehrsitz, S.; Reinhart, F. K.; Gourgon, C.; Herres, N.; Vonlanthen, A.;
Sigg, H. *J. Appl. Phys.* **2000,** *87,* 7825–7837. doi:10.1063/1.373462

41. Radescu, E. E.; Vaman, G. *Phys. Rev. E* **2002,** *65,* 046609.
doi:10.1103/PhysRevE.65.046609

License and Terms

Directional light beams by design from electrically driven elliptical slit antennas

Shuiyan Cao[1], Eric Le Moal[*1], Quanbo Jiang[2], Aurélien Drezet[2], Serge Huant[2], Jean-Paul Hugonin[3], Gérald Dujardin[1] and Elizabeth Boer-Duchemin[1]

Full Research Paper

Address:
[1]Institut des Sciences Moléculaires d'Orsay (ISMO), CNRS, Univ Paris Sud, Université Paris-Saclay, F-91405 Orsay, France, [2]Université Grenoble Alpes, Institut NEEL, F-38000 Grenoble, France and CNRS, Institut NEEL, F-38042 Grenoble, France and [3]Laboratoire Charles Fabry, Institut d'Optique, 91127 Palaiseau, France

Email:
Eric Le Moal[*] - eric.le-moal@u-psud.fr

* Corresponding author

Abstract

We report on the low-energy, electrical generation of light beams in specific directions from planar elliptical microstructures. The emission direction of the beam is determined by the microstructure eccentricity. A very simple, broadband, optical antenna design is used, which consists of a single elliptical slit etched into a gold film. The light beam source is driven by an electrical nanosource of surface plasmon polaritons (SPP) that is located at one focus of the ellipse. In this study, SPPs are generated through inelastic electron tunneling between a gold surface and the tip of a scanning tunneling microscope.

Introduction

With the ever-growing demand for higher information capacity and the diversification of applications, the integration of nanophotonics with nanoelectronics in microdevices has never been more relevant than now [1-9]. In this context, miniaturized electrical light sources are needed for chip-to-chip communication and optical interactions with the surrounding environment (e.g., for remote control, external communication or sensing applications). A number of electrically driven emitting optical antennas have been described in the recent literature [10-

19], where the emission of light is activated using low voltage (a few volts) and low current (nanoamperes to microamperes), compatible with integrated electronics. These antennas were based on plasmonic micro- or nanostructures of various geometries (Yagi–Uda, bull's-eye, nanoparticle dimer, or wire antennas), coupled in the near field (or incorporating in their design) an electrically driven nanosource of surface plasmon polaritons (SPPs, light waves coupled to electron density oscillations at a metal–dielectric interface). In particular, the electrical SPP

nanosource can be a nanoscale tunnel junction where the emission process relies on inelastic electron tunneling effects [20].
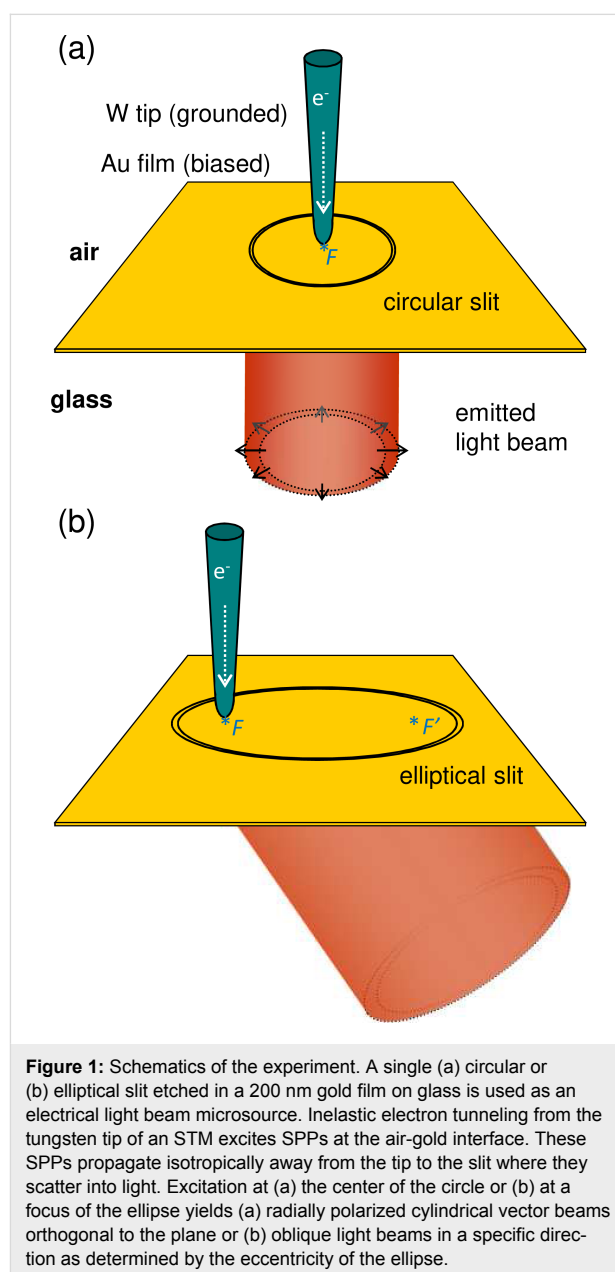
A central issue for miniaturized electrical light sources is the control of their emission direction, especially given that SPP excitation with electrons results in a broad power spectrum [21-24]. When based on a single plasmonic nanoparticle, these sources exhibit angularly broad emission patterns resembling that of an electric dipole, possibly with additional higher-order multipolar contributions [25-27]. Antenna designs based on the arrangement of several plasmonic nanoparticles (e.g., Yagi–Uda antennas [28]) yield more directional emission [29]. However, the light is most often emitted at the critical angle of the substrate–superstrate interface [30] or in directions that strongly vary depending on the optical frequency [31]. Light beams with an angular spread of only a few degrees [32,33] may be obtained from periodic microstructures (e.g., bull's-eye antennas [34,35]), yet again with a strong dependence on frequency. Foremost, planar antennas with cylindrical symmetry, such as bull's-eye [36] and patch antennas [37,38], invariably emit light in a beam or cone the axis of which is orthogonal to the surface plane. Thus, for all applications where light is emitted from electrically driven optical antennas and specific directions of emission are desired, a different antenna design has to be found [39].

Recently, we have demonstrated that the electrical excitation of SPPs in the center of a plasmonic lens consisting of a single circular slit etched in a gold film results in the emission of a spectrally broad cylindrical vector beam of light [40,41]. The resulting emission direction, which is invariably orthogonal to the surface plane on average, does not depend on the frequency and the angular spread of the resulting beam is determined by the ratio of the lens diameter to the emission wavelength. In addition, previous experiments carried out using a scanning electron microscope in vacuum have shown that oblique light beams may be produced from elliptical corrals etched in a single crystal of gold. In order to produce the oblique beam of light, the high-energy (30 keV) electron beam is focussed onto one of the two focal points of the structure [42]. The emission direction is determined by the eccentricity of the corral and could, in principle, be tailored by design. Inspired by this work, we investigate in the present paper the low-energy (below 3 eV) electrical excitation and the resulting light beams from single elliptical antennas consisting of an elliptical slit etched in a gold film. We theoretically and experimentally show that when the excitation takes place at one of the two focii, these elliptical slits act as highly directional antennas that convert electrically excited SPPs into light beams that are emitted in specific directions as determined by the ellipse eccentricity and the refractive index of the surrounding medium. The angular spread of the

emitted beam is inversely proportional to the length of the ellipse axes.

Results and Discussion

Figure 1 shows schematics of the experiment performed in this study. All experiments are carried out in air and at room temperature using a scanning tunneling microscope (STM) head mounted on top of an inverted optical microscope. The setup is described in detail in the Experimental section. Circular or elliptical slits are etched in an optically thick (200 nm) gold film deposited on a glass coverslip. The inelastic effects of the tunnel current between the STM tip and the surface of the gold film generate circular waves of surface plasmon polaritons,

Figure 1: Schematics of the experiment. A single (a) circular or (b) elliptical slit etched in a 200 nm gold film on glass is used as an electrical light beam microsource. Inelastic electron tunneling from the tungsten tip of an STM excites SPPs at the air-gold interface. These SPPs propagate isotropically away from the tip to the slit where they scatter into light. Excitation at (a) the center of the circle or (b) at a focus of the ellipse yields (a) radially polarized cylindrical vector beams orthogonal to the plane or (b) oblique light beams in a specific direction as determined by the eccentricity of the ellipse.

which propagate isotropically away from the tip along the air–gold interface [23]. The SPPs are scattered at the slit into photons in air (not shown) and in the glass. Only the light emitted in the glass is collected using a high numerical aperture (NA) microscope objective. The angular distribution of the emitted light is acquired from Fourier-space images [24,25].

The angular emission pattern results from the far-field interference of the light scattered from all along the slit. When the STM tip is positioned in the center of the disc formed by a circular slit (see Figure 1a), all points along the perimeter of the slit are equidistant from the SPP source. Thus, light is emitted in phase from all along the slit. As a result, a light beam is emitted in the direction orthogonal to the surface plane. Due to the cylindrical symmetry of the system, the emitted beam is a cylindrical vector beam with radial polarization [40].

When the tip is off-center, the emission from different positions along the circular slit is out-of-phase. As previously reported in [40], light beams tilted by up to 10° may be obtained in this way while maintaining a comparatively low angular spread. However, beyond this limit more intricate emission patterns are obtained. A lateral shift of the excitation source is not equivalent to an angular tilt of the emitted beam. Different geometries must be found in order to produce light beams in specific directions.

The working principle of an elliptical slit antenna

Figure 2 shows a planar surface illuminated by a plane wave light beam. If the incidence angle is $\theta = 0$, the optical field at the surface is in phase for the entire illuminated area. Otherwise, if $\theta \neq 0$ and the incidence plane is the **xz**-plane, the phase φ of the optical field at the surface varies with position, i.e., $\varphi(x) = kx\sin\theta + \varphi_0$, where k is the wavevector modulus of the incident light and φ_0 is a constant. In order to emit a beam of light in a specific direction, a light source at a planar surface must reproduce this spatial phase distribution. In the specific case of a slit that scatters surface waves (emitted from a point-like source) into light, the phase is the delay due to the propagation of the surface waves from the source to the slit. Thus, the distance d traveled must vary along the slit such that the phase of the scattered light is

$$\varphi(x) = kx\sin\theta + \varphi_0. \tag{1}$$

We assume that the propagation and scattering of these surface waves may be treated within the scalar approximation as in the case of plane waves in free space. This approximation has been shown to be correct for the case of SPPs [43]. Within this
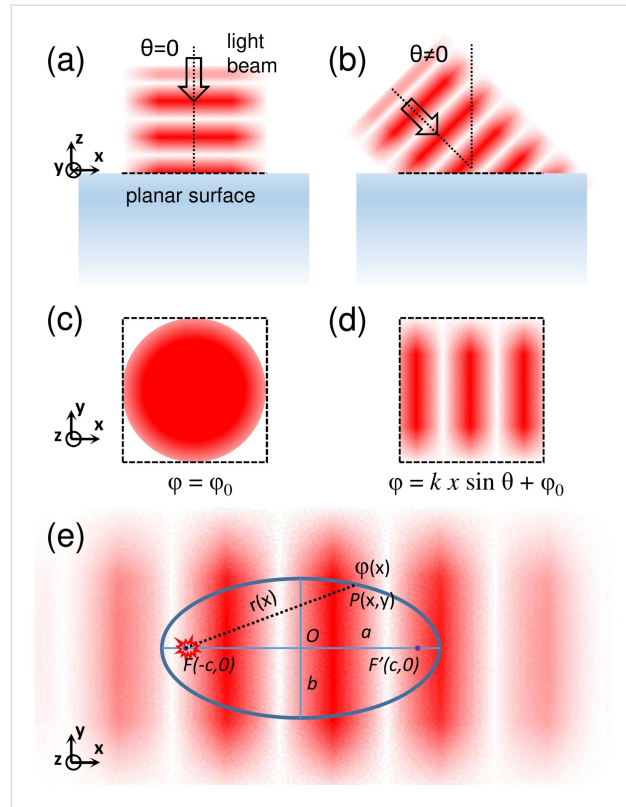

Figure 2: Working principle of an elliptical slit antenna: control of the phase. At a planar surface, the phase of the electric field of an incident light beam in (a,c) orthogonal or (b,d) oblique incidence is spatially (a,c) independent or (b,d) dependent, respectively. If this spatial phase distribution is reproduced on a planar surface, an extended planar light source can emit a beam of light in a particular direction out of the plane. (e) Such a light source is obtained when an elliptical slit antenna is fed by circular surface waves at one of its focii. The scattered light from the slit has the same spatial phase distribution at the surface as a light beam arriving at oblique incidence. The eccentricity of the ellipse determines the emission angle of the beam.

approximation, Equation 1 reads $\kappa d = kx\sin\theta + \varphi_0$, where κ is the wavevector modulus of the surface waves.

The only geometry that meets this condition is an ellipse with the surface wave source located at one of the focii. An ellipse is the ensemble of points $P(x,y)$ that satisfies the equation $(x^2)/(a^2) + (y^2)/(b^2) = 1$, where a and b are the semiaxes of the ellipse. If $a > b$ and the ellipse is centered at $(0,0)$, the focii are at $F(-c,0)$ and $F'(c,0)$, where $c^2 = a^2 - b^2$. The eccentricity of the ellipse is $e = c/a$. The distance from F to $P(x,y)$ is $r = ex + a$. As a result, when the source is at F, wave propagation to the slit introduces a phase shift of $\kappa(ex + a)$. Thus, a light beam emitted at an angle θ is expected where θ satisfies the equation

$$\kappa e = k\sin\theta. \tag{2}$$

In this way the emission angle may be tailored by varying the eccentricity of the ellipse. The available angular range is from

$\theta = 0$ to $\theta = \arcsin(\kappa e)/k$, with e chosen between 0 (i.e., a circle) and up to but not including 1 ($e = 1$ yields a parabola).

Figure 3a shows that the intersection of a cylinder with a plane yields an ellipse the eccentricity of which is precisely $e = \sin\theta$, where θ defines the tilt of the cylinder axis with respect to the
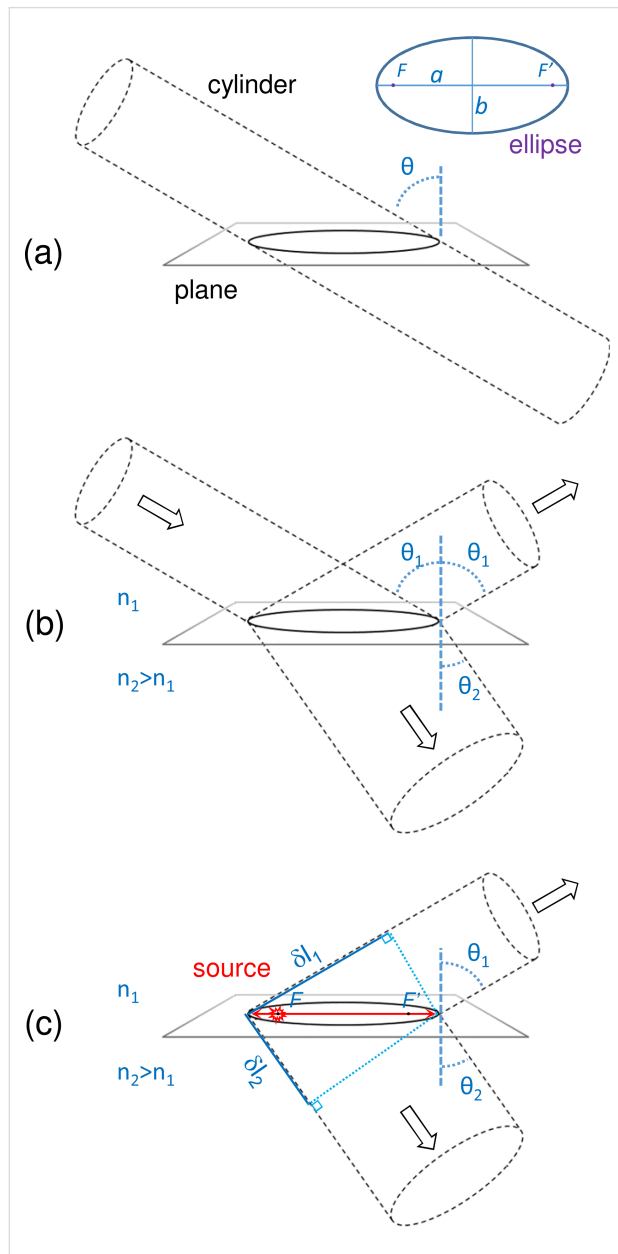

Figure 3: Working principle of an elliptical slit antenna: shape of the emitted beams. (a) The intersection of a cylinder and a plane is an ellipse. However, elliptical slit antennas do not necessarily emit cylindrical beams. (b) This is in analogy to a cylindrical beam with a circular section that becomes elliptical after refraction at the interface between two media with different refractive indices. (c) Similarly, due to different propagation speeds of light in the superstrate, of light in the substrate and of the surface waves at the interface, elliptical slit antennas emit non-cylindrical light beams at angles that depend on the refractive indices of the upper and lower media.

normal of the plane. Based on the similarity with Equation 2, one may expect that cylindrical beams can be emitted from elliptical slit antennas fed with surface wave sources at their focii. However, Equation 2 shows that this is only true if light and surface waves propagate at the same speed, i.e., $\kappa = k$. Figure 3b shows that the refraction of a cylindrical beam at a planar interface between two media does not yield a cylindrical beam if the two media do not have same index of refractive, since the shape of the beam changes as a result of the change in emission angle. In the case of reflection, since the medium and thus the emission angle remain the same, the beam remains cylindrical.

In order to have a beam of light, the phase due to the optical path difference of light in the medium (i.e., $k_0 n_1 \delta l_1$ or $k_0 n_2 \delta l_2$) must equal the phase due to the difference in propagation length from the source at a focus to the slit (i.e., $2\kappa c$). k_0 is the wavevector modulus of photons in vacuum. In other words, $2(\kappa/k_0)c = n_1\delta l_1 = n_2\delta l_2$. Air and glass have refractive indexes n_1 and n_2 of about 1 and 1.5, respectively, and the SPPs at the air–gold interface have an effective index close to 1. Our elliptical slit antennas are thus expected to emit quasi cylindrical beams on the air side, since the speed of photons in air, and of SPPs on an air–gold interface are similar. In contrast, the light beam emitted in glass must have an elliptical section. This is not directly visible in the Fourier-space images since they reveal the angular, and not the spatial distribution of the emitted light. Note that the model of a cylinder intersecting a plane introduced above yields similar results as the virtual parabola model proposed in [42] for the beaming of an elliptical cavity and provides a simple framework to describe the shape of the emitted beams.

We can produce beams of light emitting in the angular range from 0° to $\arcsin(k_{\text{SPP}}/n_i k_0)$, with $i = 1$ in air and $i = 2$ in glass. In principle, our elliptical slit antennas can thus emit light beams at all polar angles in air (i.e., 0° to about 90°) and from 0° to about 43° in glass (at $\lambda_0 = 700$ nm). Interestingly, light beams at virtually all polar angles in glass (i.e., up to 90°) could be obtained if the SPP nanosource were located at the glass–gold interface or if it excited a gold film sandwiched between two media of the same refractive index (e.g., a suspended gold membrane in air). The latter geometry (i.e., a prototypical insulator–metal–insulator waveguide) has the additional advantage that it supports long-range SPPs that have lower propagation losses [44].

Angular emission pattern

Figure 4 provides the experimental demonstration that light beams may be emitted in chosen directions from electrically driven elliptical slit antennas. The emission angle is determined
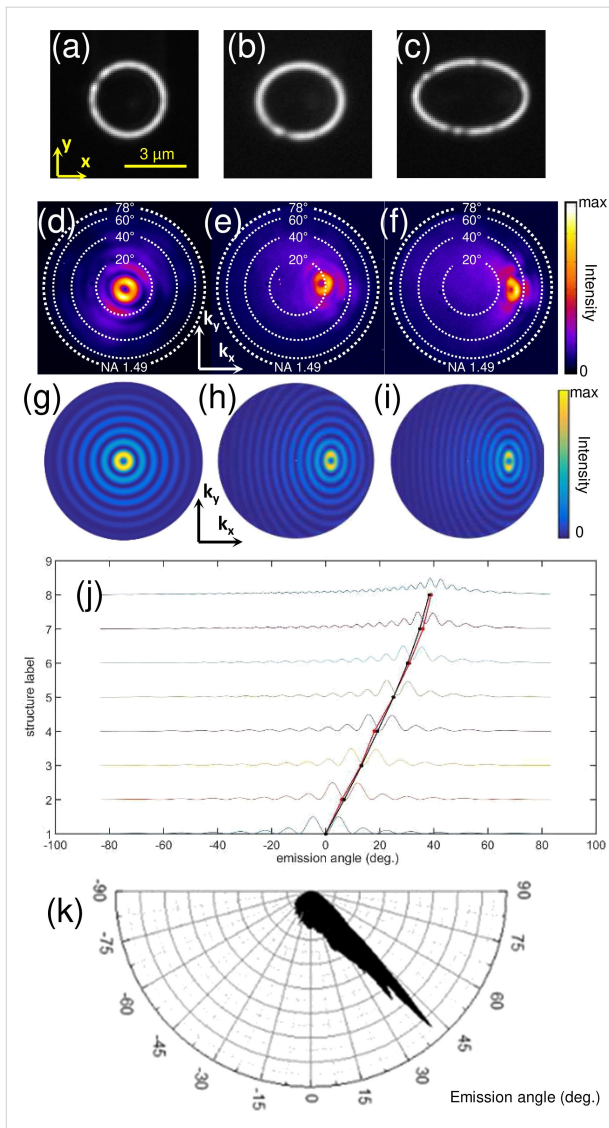
Figure 4: Control of the emission direction: effect of the eccentricity. (a–c) Transmission optical images under white light illumination, (d–f) experimental and (g–i) theoretical Fourier-space images of the light emitted upon electrical excitation of structures 1, 4 and 6, respectively (see Table 1). The STM tip is located in the center of structure 1, and at the focus $F(-c,0)$ of structures 4 and 6. (j) Intensity profiles taken from theoretical Fourier-space images along k_x, as well as the measured experimental emission angle (in red) and the calculated theoretical emission angle (in black) are shown. The calculated emission angle is determined from Equation 2. The intensity profiles are normalized and vertically offset for clarity. (k) Polar plot of the angular emission pattern retrieved from an experimental Fourier-space image of the light emitted upon electrical excitation of structure 8 (see Table 1) at the focus $F(-c,0)$. Further experimental and theoretical Fourier-space images are provided in the Supporting Information File 1.

by the eccentricity of the ellipse. Three different slits are used, i.e., structures 1, 4 and 6 in Table 1 (see also Figure 4a–c). They have eccentricities of 0 (circular slit), 0.51 and 0.77 (elliptical slits), respectively. The Fourier-space images recorded upon excitation with the tunnel electrons from the STM tip at one of the focii are shown in Figure 4d–f. Good agreement is found be-

tween the experimental data and the simulated images shown in Figure 4g–i. These simulated images are obtained using a model based on an ensemble of in-plane oscillating electric dipoles located along the slit and oriented orthogonally to the ellipse in the plane of the sample [45,46]. The same model was used to calculate the emission pattern from circular slits in [40]. Figure 4j shows the intensity profiles from the simulated Fourier-space images and the average emission angles retrieved from the experimental data for the eight elliptical slits the eccentricities of which are given in Table 1. The chosen eccentricity values are those corresponding to the intersection of a cylinder with a plane at angles of 0°, 10°…70°. On the same graph the theoretical value of the emission angle as obtained from Equation 2 is plotted, which reads

$$\theta = \arcsin\left(\frac{k_{\text{SPP}}}{n_2 k_0} e\right),$$

where $(k_{\text{SPP}}/k_0) = 1.037$ at $\lambda_0 = 700$ nm and $n_2 = 1.518$. In addition, Figure 4k shows a polar plot of the angular emission pattern retrieved from an experimental Fourier-space image of the light emitted upon electrical excitation of structure 8 (see Table 1) at the focus $F(-c,0)$.

Table 1: Parameters of the elliptical slit antennas. The major axis $2a$ and the eccentricity e are given (the minor axis is always $2b = 3$ μm).

structure	1	2	3	4	5	6	7	8
$2a$ (μm)	3	3.05	3.20	3.46	3.92	4.67	6	8.77
e (μm)	0	0.18	0.35	0.51	0.64	0.77	0.87	0.94
arcsin e	0°	10°	20°	30°	40°	50°	60°	70°

Figure 5 shows the effect of the SPP source location on the far-field emission pattern. The emission of light from an elliptical slit (structure 8 in Table 1) is obtained using the STM nanosource at different positions along the major axis of the ellipse, namely: on the focii $F(-c,0)$ and $F'(c,0)$, in the center $O(0,0)$, and at intermediate positions, $(-c/2,0)$ and $(c/2,0)$. The corresponding experimental and theoretical Fourier-space images are shown in Figure 5. Intricated interference patterns, covering broad polar and azimuthal angular ranges, are produced when the SPP source is not located at one of the ellipse focii. Only when the excitation is located at a focus does the elliptical slit antenna yield angularly narrow light beams. As expected, the emission patterns upon excitation at F and F' are perfect mirror symmetries of each other with respect to the (**yz**)-plane.

From the experimental Fourier-space images we retrieve the angular spread of the emitted light beams in the k_x and k_y recip-
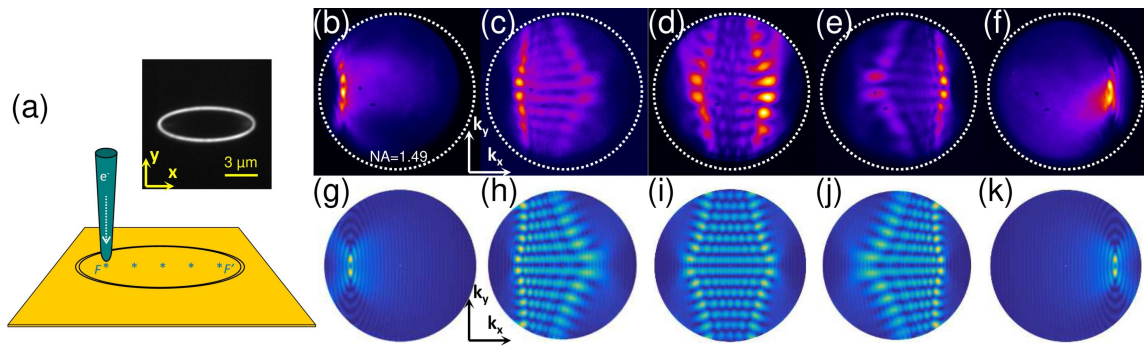
Figure 5: Angular emission pattern: effect of the excitation site. (a) Schematic of the experiment (inset: a transmission optical image under white light illumination). (b–f) Experimental and (g–k) theoretical Fourier-space images of the light emitted upon electrical excitation of structure 8 (see Table 1) at (from b to f) $F'(c,0)$, $(c/2,0)$, $(0,0)$, $(−c/2,0)$ and $F(−c,0)$, respectively.

rocal-space directions. Here we define the angular spread Δk as the half width at half maximum (HWHM) of the light spot in the Fourier space. The results obtained for structures 1–8 (see Table 1) are plotted in Figure 6a as a function of the ellipse eccentricity. We see that the lateral size of the antenna deter-
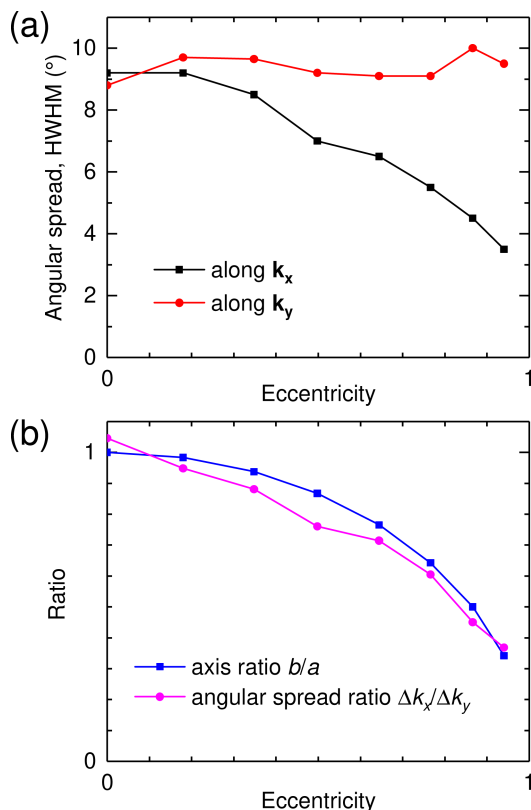

Figure 6: Angular spread: effect of the eccentricity. (a) Half width at half maximum (HWHM) of the angular distribution of the light emitted in glass. This data is obtained from experimental Fourier-space images along the k_x and k_y axes for structures 1–8. Here the HWHM is plotted as a function of the eccentricity of the ellipse. (b) Ratio of the minor and major semi-axes (b/a) and of the angular spread along k_x and k_y as a function of the ellipse eccentricity.

mines the angular spread. The angular spread along k_x decreases as the eccentricity increases since the major axis $2a$ is increased while keeping the minor axis $2b = 3$ µm constant. For instance, angular spreads of 9° and of 4.5° along k_x are measured for structure 1 ($2a = 3$ µm) and 7 ($2a = 6$ µm), respectively. No significant change occurs along k_y where the angular spread remains within a range of 9–10°.

Figure 6b compares the angular spread ratio $(\Delta k_x)/(\Delta k_y)$ to the minor-to-major axis ratio b/a of the ellipse. Close agreement is found between the two ratios. Due to the properties of Fourier transforms, the aspect ratio of the slit antenna in real space (a/b) and its emission pattern in Fourier space $(\Delta k_x)/(\Delta k_y)$ are inversely proportional to each other. When elliptical slit antennas are fed at their focus, the angular spread of the emitted light beam is determined by the ellipse semiradii and the emission wavelength. It is worthy of note that despite higher SPP propagation losses is some directions, increasing a does not result in a broadening of the half width at half maximum along k_x.

To further describe the emission from an elliptical slit antenna, we now examine the "shape" of the emission lobes as calculated at the vacuum wavelength of $\lambda_0 = 700$ nm using the method described in [47,48]. In Figure 7a–h, the flux of the Poynting vector per unit solid angle is represented in real space for structures 1–8 (see Table 1). Electrical excitation at $F(−c,0)$ is modeled as a monochromatic ($\lambda_0 = 700$ nm) **z**-oriented oscillating dipole. Both the emission in the air (upward direction) and in the glass (downward direction) is shown. The air–glass interface is at $z = 0$ and the ellipse is centered at $(x,y) = (0,0)$. In general, Figure 7 confirms that light beams are emitted both downward in the substrate and upward in the superstrate. The light is emitted at larger angles in the medium of lower refractive index (i.e., in air). Moreover, we see that a stronger beaming effect occurs in glass as compared to air. The light beam in glass has a lower angular spread and less intense side
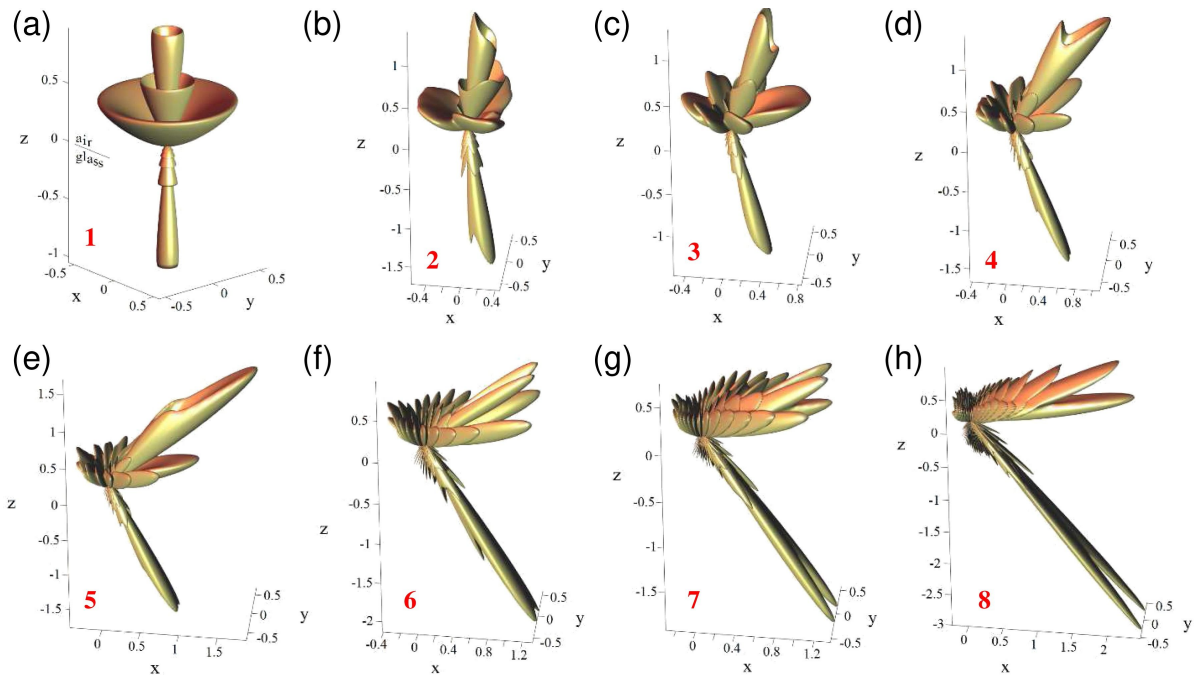
Figure 7: Lobe shapes. (a–h) Theoretical emission patterns from the elliptical slit antennas upon excitation by a **z**-oriented oscillating electric dipole located at the focus $F(-c,0)$ of the ellipse. These patterns are calculated at a vacuum wavelength of $\lambda_0 = 700$ nm for structures 1–8 (see Table 1).

lobes. Even though higher directivity is obtained in glass with comparatively more light in the beaming direction than for the case in air, more intensity on average is emitted upward than downward. Figure 8 shows that the flux of the Poynting vector integrated over the lower half space represents only 10–25% of the total radiation (i.e., integrated over 4π sr).
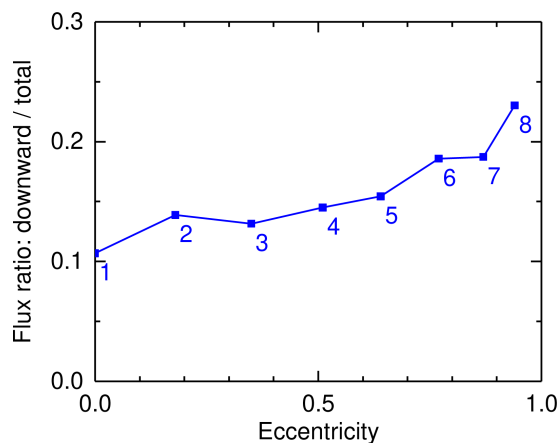

Figure 8: Where does the light go? Theoretical calculation of the Poynting vector: ratio of the light flux emitted downward (in the glass) to the total emitted flux (in air and glass) as calculated for structures 1–8 (see Table 1) from the diagrams shown in Figure 7. The data is plotted as a function of the ellipse eccentricity. Structure numbers are indicated next to the data points.

Field distribution in the slit

Finally, we calculate the theoretical spatial distribution of the square modulus of the total electric field and its **x**- and **y**-components in the slit, i.e., in the (**xy**) plane, using the method described in [47,48]. Figure 9 shows the results for structures 1 (circular slit) and 7 (elliptical slit with $a/b = 2$, see Table 1). When SPPs are isotropically excited in the center of a circular slit antenna, the intensity of the scattered field inside the slit is spatially homogeneous (see Figure 9a) since the source-to-slit distance is the same for all points along the slit. The fact that the SPP propagation is orthogonal to the slit for all positions on the slit has two consequences: The SPP-to-light scattering efficiency is the same all along the slit, and the polarization of the scattered light is purely radial (see Figure 9b,c). This is in contrast to the elliptical slit antenna where the distance between the SPP source (located at one focus) and the slit depends on the direction. Therefore, the SPP amplitude decay due to propagation losses is direction-dependent as well, and the SPP amplitude at the slit depends on the location. Another effect that makes the SPP flux at the slit inhomogeneous (see Figure 9d) is the angle at which the SPP wavefront meets the slit. For the case of an ellipse and excitation at a focus, this angle will vary as a function of position on the slit. As a result, except along the major axis, the SPP wave does not meet the slit orthogonally. Consequently, the SPP-to-light scattering efficiency is likely to vary as a function of position along the slit.
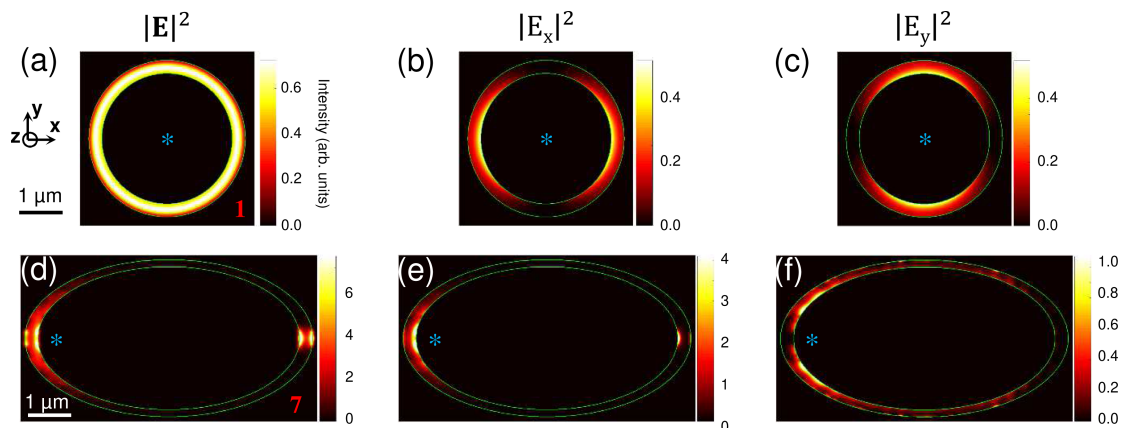
Figure 9: Theoretical **E**-field maps in the slit. (a–f) Spatial distribution of the square modulus of the total electric field $|\mathbf{E}|^2 = |E_x|^2 + |E_y|^2 + |E_z|^2$ and of its components $|E_x|^2$ and $|E_y|^2$ along the **x**- and **y**-axes, as calculated inside the slit of structures 1 (circular) and 7 (elliptical, see Table 1). The excitation is modeled as a monochromatic ($\lambda_0 = 700$ nm) **z**-oriented oscillating electric dipole located at the center $F(0,0)$ of the circular slit and at the "left focus" $F(-c,0)$ of the elliptical slit (here, $c = 2.60$ μm). Both structures are centered at $O(0,0)$. The dipole position is indicated with an asterisk.

In addition, the fact that the SPP propagation is not orthogonal to the slit has an effect on the polarization of the scattered light. SPP-to-light scattering at the slit essentially relies on the excitation of surface plasmons that oscillate in the plane of the sample in the direction perpendicular to the slit [45]. If this direction coincides with the radial direction for all positions along the slit (i.e., from the center of the structure to the slit), then the polarization of the scattered light is purely radial. This is true in the case of a circular slit; it is not true for an ellipse (see Figure 9e,f), where the radius and the direction of propagation only coincide along the major axis. Radial polarization yields a zero of intensity at the center of the light spot in Fourier space due to a polarization singularity along the propagation axis of the resulting light beam [49]. This zero of intensity is indeed observed in the experimental and theoretical data shown in Figure 4d and Figure 4g for the circular antenna. The Fourier-space images measured and calculated for the elliptical structures also exhibit a doughnut-shaped spot with a marked intensity dip, which, however, does not fall completely to zero. This confirms that the polarization is not purely radial and a combination of linear and radial polarization must occur with an increasing linear contribution as the ellipse eccentricity increases. Nevertheless, the radial component must dominate over the linear component even at an eccentricity as high as 0.94, otherwise no intensity dip would be seen. For symmetry reasons, the linear contribution to the polarization of the light beam must be oriented along the major axis of the ellipse (the off-center location of the SPP nanosource along the **x**-axis breaks the mirror symmetry of the system with respect to the **yz**-plane).

Conclusion

We have introduced the working principle of an electrically driven elliptical slit antenna, which is a highly directive, low-energy, electrical microsource of light beams emitting in controlled directions. The emission direction is tailored by design by controlling the eccentricity of the ellipse. The model of a cylinder intersecting a plane may be used to describe the dependence of the beam direction and geometry on the structure eccentricity and the refractive index of the surrounding medium in a simple way. We have shown that the angular spread of the emitted beam depends on the length of the ellipse axes and not on its eccentricity. In addition, light beaming is robust to amplitude inhomogeneities of the scattered field from the slit (which becomes more inhomogeneous as the eccentricity increases) but is highly sensitive to its phase distribution (which changes when moving the SPP source from the ellipse focus). This is expected since light beaming from a slit is essentially a far-field interference effect. From calculations of the field in the slit, we infer that the polarization of the emitted beam is predominantly radial with a minor linear contribution (along the major axis) that increases with eccentricity. Future improvements of these optical antennas include the integration of the electrical SPP nanosource in the design of the microstructure (e.g., as an integrated metal-oxide–metal tunnel junction) and the engineering of the refractive indices of substrate and superstrate for greater control of the emission pattern, of the upward/downward power distribution and of the propagation losses. The principles of electrically driven elliptical slit antennas may be extended to similar chiral slit structures, e.g., elliptical spirals, in order to control the optical orbital angular moment of the emitted light beams [50,51].

Experimental

Figure 10 shows a schematic representation of the experimental setup. It consists of a commercial STM head (JPK Instruments, NanoWizard 3) mounted on top of an inverted optical micro-

scope (Nikon Instruments, Eclipse Ti-U) equipped with a nanopositioning stage and an oil-immersion, high numerical aperture (NA = 1.49), 100× objective lens (Nikon CFI Apochromat TIRF objective). The STM is operated in air under ambient conditions [52]. STM tips are electrochemically etched tungsten wires.
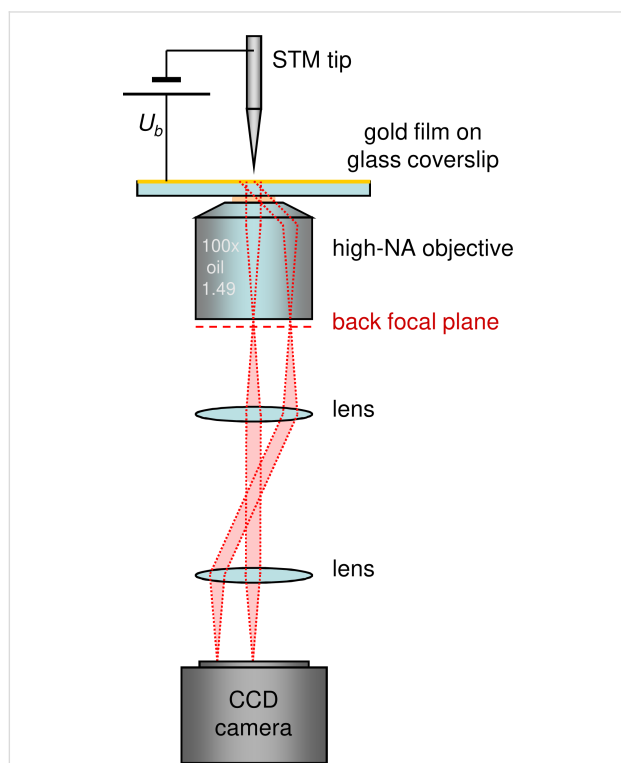

Figure 10: Schematic of the experimental setup. An STM head is mounted on top of an inverted optical microscope. The light emitted in the substrate upon electrical excitation of the sample with tunnel electrons from the tip is collected by the objective. The principle of Fourier-space imaging is illustrated with red dotted lines: parallel light rays emitted from the sample converge at the same point in the back focal plane of the objective. Thus, the angular distribution of the emitted light is retrieved from the image of the back focal plane on a CCD camera.

A set of achromatic doublet lenses (Thorlabs, AC254-200-B) arranged in a *4f* geometry is used to project an image of the back focal plane of the objective on a cooled CCD camera (Andor, IKON-M), to record the Fourier-space images (angular distribution of the collected light). The Fourier-space images shown in this paper are recorded under the following conditions: acquisition time 300 s, sample bias 2.8 V, setpoint current 1 nA.

The sample consists of a 200 nm thick gold film thermally evaporated on a standard, 170 μm thick, microscope glass coverslip coated with a transparent, 100 nm thick, conducting indium tin oxide (ITO) layer (purchased from SOLEMS, Palaiseau, France). ITO is used to electrically connect the inner

gold area delineated by the elliptical slit to the rest of the gold film as is required for applying the tip–sample bias voltage for the STM measurements. The elliptical slits are milled in the gold film using a focused ion beam (FIB) at the NanoFab facility (Institut Néel, Grenoble, France). A scanning electron microscopy image of an elliptical slit is shown in Supporting Information File 1.

Supporting Information

Additional experimental data, a scanning electron microscopy image of an elliptical slit and a description of the method to retrieve the angular spread from Fourier-space images are all provided.

Supporting Information File 1
Additional experimental data.
[https://www.beilstein-journals.org/bjnano/content/supplementary/2190-4286-9-221-S1.pdf]

Acknowledgements

ORCID® iDs

Shuiyan Cao - https://orcid.org/0000-0001-6448-2940
Quanbo Jiang - https://orcid.org/0000-0001-5835-8177

References

1. Hryciw, A.; Jun, Y. C.; Brongersma, M. L. *Nat. Mater.* **2010,** *9,* 3–4. doi:10.1038/nmat2598
2. Neutens, P.; Lagae, L.; Borghs, G.; Van Dorpe, P. *Nano Lett.* **2010,** *10,* 1429–1432. doi:10.1021/nl1003416
3. Walters, R. J.; van Loon, R. V. A.; Brunets, I.; Schmitz, J.; Polman, A. *Nat. Mater.* **2010,** *9,* 21–25. doi:10.1038/nmat2595
4. Sorger, V. J.; Oulton, R. F.; Ma, R.-M.; Zhang, X. *MRS Bull.* **2012,** *37,* 728–738. doi:10.1557/mrs.2012.170
5. Fan, P.; Colombo, C.; Huang, K. C. Y.; Krogstrup, P.; Nygård, J.; Fontcuberta i Morral, A.; Brongersma, M. L. *Nano Lett.* **2012,** *12,* 4943–4947. doi:10.1021/nl302521v
6. Huang, K. C. Y.; Seo, M.-K.; Sarmiento, T.; Huo, Y.; Harris, J. S.; Brongersma, M. L. *Nat. Photonics* **2014,** *8,* 244–249. doi:10.1038/nphoton.2014.2
7. Wang, T.; Nijhuis, C. A. *Appl. Mater. Today* **2016,** *3,* 73–86. doi:10.1016/j.apmt.2016.03.001
8. Du, W.; Wang, T.; Chu, H.-S.; Wu, L.; Liu, R.; Sun, S.; Phua, W. K.; Wang, L.; Tomczak, N.; Nijhuis, C. A. *Nat. Photonics* **2016,** *10,* 274–280. doi:10.1038/nphoton.2016.43

9. Wu, X.; Jiang, P.; Razinskas, G.; Huo, Y.; Zhang, H.; Kamp, M.; Rastelli, A.; Schmidt, O. G.; Hecht, B.; Lindfors, K.; Lippitz, M. *Nano Lett.* **2017,** *17,* 4291–4296. doi:10.1021/acs.nanolett.7b01284

10. Pohl, D. W.; Rodrigo, S. G.; Novotny, L. *Appl. Phys. Lett.* **2011,** *98,* 023111. doi:10.1063/1.3541544

11. Huang, K. C.; Seo, M.-K.; Huo, Y.; Sarmiento, T.; Harris, J. S.; Brongersma, M. L. *Nat. Commun.* **2012,** *3,* 1005. doi:10.1038/ncomms1985

12. Rai, P.; Hartmann, N.; Berthelot, J.; Arocas, J.; Colas des Francs, G.; Hartschuh, A.; Bouhelier, A. *Phys. Rev. Lett.* **2013,** *111,* 026804. doi:10.1103/physrevlett.111.026804

13. Li, J.; Wei, H.; Shen, H.; Wang, Z.; Zhao, Z.; Duan, X.; Xu, H. *Nanoscale* **2013,** *5,* 8494–8499. doi:10.1039/c3nr02749j

14. Kern, J.; Kullock, R.; Prangsma, J.; Emmerling, M.; Kamp, M.; Hecht, B. *Nat. Photonics* **2015,** *9,* 582–586. doi:10.1038/nphoton.2015.141

15. Parzefall, M.; Bharadwaj, P.; Jain, A.; Taniguchi, T.; Watanabe, K.; Novotny, L. *Nat. Nanotechnol.* **2015,** *10,* 1058–1063. doi:10.1038/nnano.2015.203

16. Vardi, Y.; Cohen-Hoshen, E.; Shalem, G.; Bar-Joseph, I. *Nano Lett.* **2016,** *16,* 748–752. doi:10.1021/acs.nanolett.5b04622

17. Bigourdan, F.; Hugonin, J.-P.; Marquier, F.; Sauvan, C.; Greffet, J.-J. *Phys. Rev. Lett.* **2016,** *116,* 106803. doi:10.1103/physrevlett.116.106803

18. Uskov, A. V.; Khurgin, J. B.; Protsenko, I. E.; Smetanin, I. V.; Bouhelier, A. *Nanoscale* **2016,** *8,* 14573–14579. doi:10.1039/c6nr01931e

19. Du, W.; Wang, T.; Chu, H.-S.; Nijhuis, C. A. *Nat. Photonics* **2017,** *11,* 623–627. doi:10.1038/s41566-017-0003-5

20. Lambe, J.; McCarthy, S. L. *Phys. Rev. Lett.* **1976,** *37,* 923–925. doi:10.1103/physrevlett.37.923

21. Hone, D.; Mühlschlegel, B.; Scalapino, D. J. *Appl. Phys. Lett.* **1978,** *33,* 203–204. doi:10.1063/1.90275

22. Johansson, P. *Phys. Rev. B* **1998,** *58,* 10823–10834. doi:10.1103/physrevb.58.10823

23. Wang, T.; Boer-Duchemin, E.; Zhang, Y.; Comtet, G.; Dujardin, G. *Nanotechnology* **2011,** *22,* 175201. doi:10.1088/0957-4484/22/17/175201

24. Zhang, Y.; Boer-Duchemin, E.; Wang, T.; Rogez, B.; Comtet, G.; Le Moal, E.; Dujardin, G.; Hohenau, A.; Gruber, C.; Krenn, J. R. *Opt. Express* **2013,** *21,* 13938. doi:10.1364/oe.21.013938

25. Le Moal, E.; Marguet, S.; Rogez, B.; Mukherjee, S.; Dos Santos, P.; Boer-Duchemin, E.; Comtet, G.; Dujardin, G. *Nano Lett.* **2013,** *13,* 4198–4205. doi:10.1021/nl401874m

26. Coenen, T.; Bernal Arango, F.; Femius Koenderink, A.; Polman, A. *Nat. Commun.* **2014,** *5,* 3250. doi:10.1038/ncomms4250

27. Le Moal, E.; Marguet, S.; Canneson, D.; Rogez, B.; Boer-Duchemin, E.; Dujardin, G.; Teperik, T. V.; Marinica, D.-C.; Borisov, A. G. *Phys. Rev. B* **2016,** *93,* 035418. doi:10.1103/physrevb.93.035418

28. Hofmann, H. F.; Kosako, T.; Kadoya, Y. *New J. Phys.* **2007,** *9,* 217. doi:10.1088/1367-2630/9/7/217

29. Coenen, T.; Vesseur, E. J. R.; Polman, A.; Koenderink, A. F. *Nano Lett.* **2011,** *11,* 3779–3784. doi:10.1021/nl201839g

30. Curto, A. G.; Volpe, G.; Taminiau, T. H.; Kreuzer, M. P.; Quidant, R.; van Hulst, N. F. *Science* **2010,** *329,* 930–933. doi:10.1126/science.1191922

31. Kosako, T.; Kadoya, Y.; Hofmann, H. F. *Nat. Photonics* **2010,** *4,* 312–315. doi:10.1038/nphoton.2010.34

32. Livneh, N.; Strauss, A.; Schwarz, I.; Rosenberg, I.; Zimran, A.; Yochelis, S.; Chen, G.; Banin, U.; Paltiel, Y.; Rapaport, R. *Nano Lett.* **2011,** *11,* 1630–1635. doi:10.1021/nl200052j

33. Livneh, N.; Harats, M. G.; Yochelis, S.; Paltiel, Y.; Rapaport, R. *ACS Photonics* **2015,** *2,* 1669–1674. doi:10.1021/acsphotonics.5b00433

34. Lezec, H. J.; Degiron, A.; Devaux, E.; Linke, R. A.; Martin-Moreno, L.; Garcia-Vidal, F. J.; Ebbesen, T. W. *Science* **2002,** *297,* 820–822. doi:10.1126/science.1071895

35. Jun, Y. C.; Huang, K. C.; Brongersma, M. L. *Nat. Commun.* **2011,** *2,* 283. doi:10.1038/ncomms1286

36. Osorio, C. I.; Coenen, T.; Brenny, B. J. M.; Polman, A.; Koenderink, A. F. *ACS Photonics* **2016,** *3,* 147–154. doi:10.1021/acsphotonics.5b00596

37. Esteban, R.; Teperik, T. V.; Greffet, J. J. *Phys. Rev. Lett.* **2010,** *104,* 026802. doi:10.1103/physrevlett.104.026802

38. Mohtashami, A.; Coenen, T.; Antoncecchi, A.; Polman, A.; Koenderink, A. F. *ACS Photonics* **2014,** *1,* 1134–1143. doi:10.1021/ph500225j

39. Clarke, B. P.; MacDonald, K. F.; Zheludev, N. I. *Appl. Phys. Lett.* **2018,** *112,* 021109. doi:10.1063/1.5008985

40. Cao, S.; Le Moal, E.; Boer-Duchemin, E.; Dujardin, G.; Drezet, A.; Huant, S. *Appl. Phys. Lett.* **2014,** *105,* 111103. doi:10.1063/1.4895769

41. Cao, S.; Le Moal, E.; Bigourdan, F.; Hugonin, J.-P.; Greffet, J.-J.; Drezet, A.; Huant, S.; Dujardin, G.; Boer-Duchemin, E. *Phys. Rev. B* **2017,** *96,* 115419. doi:10.1103/physrevb.96.115419

42. Schoen, D. T.; Coenen, T.; García de Abajo, F. J.; Brongersma, M. L.; Polman, A. *Nano Lett.* **2013,** *13,* 188–193. doi:10.1021/nl303850v

43. Teperik, T. V.; Archambault, A.; Marquier, F.; Greffet, J. J. *Opt. Express* **2009,** *17,* 17483–17490. doi:10.1364/oe.17.017483

44. Berini, P. *Adv. Opt. Photonics* **2009,** *1,* 484–588. doi:10.1364/aop.1.000484

45. Mollet, O.; Bachelier, G.; Genet, C.; Huant, S.; Drezet, A. *J. Appl. Phys.* **2014,** *115,* 093105. doi:10.1063/1.4867395

46. Berthel, M.; Jiang, Q.; Chartrand, C.; Bellessa, J.; Huant, S.; Genet, C.; Drezet, A. *Phys. Rev. E* **2015,** *92,* 033202. doi:10.1103/physreve.92.033202

47. Hugonin, J. P.; Lalanne, P. *J. Opt. Soc. Am. A* **2005,** *22,* 1844–1849. doi:10.1364/josaa.22.001844

48. Yang, J.; Hugonin, J.-P.; Lalanne, P. *ACS Photonics* **2016,** *3,* 395–402. doi:10.1021/acsphotonics.5b00559

49. Zhan, Q. *Adv. Opt. Photonics* **2009,** *1,* 1–57. doi:10.1364/aop.1.000001

50. Gorodetski, Y.; Drezet, A.; Genet, C.; Ebbesen, T. W. *Phys. Rev. Lett.* **2013,** *110,* 203906. doi:10.1103/physrevlett.110.203906

51. Pham, A.; Berthel, M.; Jiang, Q.; Bellessa, J.; Huant, S.; Genet, C.; Drezet, A. *Phys. Rev. A* **2016,** *94,* 053850. doi:10.1103/physreva.94.053850

52. Rogez, B.; Cao, S.; Dujardin, G.; Comtet, G.; Le Moal, E.; Mayne, A.; Boer-Duchemin, E. *Nanotechnology* **2016,** *27,* 465201. doi:10.1088/0957-4484/27/46/465201

Nanoantenna structures for the detection of phonons in nanocrystals

Alexander G. Milekhin[*1,2], Sergei A. Kuznetsov[2,3], Ilya A. Milekhin[1,2],
Larisa L. Sveshnikova[2], Tatyana A. Duda[2], Ekaterina E. Rodyakina[1,2],
Alexander V. Latyshev[1,2], Volodymyr M. Dzhagan[4] and Dietrich R. T. Zahn[5]

Abstract

We report a study of the infrared response by localized surface plasmon resonance (LSPR) modes in gold micro- and nanoantenna arrays with various morphologies and surface-enhanced infrared absorption (SEIRA) by optical phonons of semiconductor nanocrystals (NCs) deposited on the arrays. The arrays of nano- and microantennas fabricated with nano- and photolithography reveal infrared-active LSPR modes of energy ranging from the mid to far-infrared that allow the IR response from very low concentrations of organic and inorganic materials deposited onto the arrays to be analyzed. The Langmuir–Blodgett technology was used for homogeneous deposition of CdSe, CdS, and PbS NC monolayers on the antenna arrays. The structural parameters of the arrays were confirmed by scanning electron microscopy. 3D full-wave electromagnetic simulations of the electromagnetic field distribution around the micro- and nanoantennas were employed to realize the maximal SEIRA enhancement for structural parameters of the arrays whereby the LSPR and the NC optical phonon energies coincide. The SEIRA experiments quantitatively confirmed the computational results. The maximum SEIRA enhancement was observed for linear nanoantennas with optimized structural parameters determined from the electromagnetic simulations. The frequency position of the feature's absorption seen in the SEIRA response evidences that the NC surface and transverse optical phonons are activated in the infrared spectra.

Introduction

Surface-enhanced infrared absorption (SEIRA) by organic species placed on metal surfaces proposed in [1] has been the subject of intensive research over the past years [2-4]. Several groups showed that the IR response by organic molecules can be significantly enhanced in a variety of organic systems by depositing the molecules on nanostructured surfaces of noble metals (Ag, Au, Cu, etc.) [5-7]. The origin of the IR signal enhancement is the localized electromagnetic field of plasmons excited near metallic surfaces. In the case of flat metal films, the IR response from an organic molecule in the plasmon field can be increased by a factor of 10^3 [8]. For island metal films, the enhancement was found to depend on the island aspect ratio and the size of the gap between nanoclusters [9,10]. It is worth noting that SEIRA is maximized for elongated metal nanoclusters (nanorods or nanoantennas) with a high aspect ratio (length-to-width ratio) and a small gap between nanoclusters [11]. However, stochastical distribution of metal nanoclusters in terms of size, shape, and orientation reduces the IR enhancement and impedes the study of SEIRA regularities. Further progress was achieved with the development of nanolithography techniques which made possible the fabrication of arrays of metal nanoantennas with structural parameters that were well-controlled at the nanometer scale [12,13]. The most common, linear-shaped nanoantennas exhibit two LSPR modes polarized parallel and perpendicular to the nanoantenna axis (herein, referred to as the longitudinal and transverse modes, respectively). The longitudinal mode has a LSPR energy in the IR spectral range and is utilized for SEIRA experiments. This energy can be gradually tuned from near- to far-infrared (or terahertz) via increasing the nanoantenna length [14,15]. The transverse mode has a much shorter wavelength – appearing in the visible spectral range and of interest for optical spectroscopy [16].

It was shown that regular linear nanoantennas fabricated by nanolithography demonstrate enhancement of the SEIRA signal from vibrational modes in organic molecules such as octadecanethiol (ODT) [17] and 4,4'-bis(*N*-carbazolyl)-1,1'-biphenyl (CBP) by a factor of 10^5 [18]. The highest SEIRA response was obtained by adjusting the LSPR energy of the nanoantennas to the energy of the vibrational modes [17]. The high sensitivity of SEIRA to vibrational modes allowed the detection of organic and biological substances of extremely low concentrations. For example, Adato et al. demonstrated the detection of a concentration as low as 145 protein molecules per nanoantenna [19]. SEIRA has been extended to the far-IR spectral range for which special nanoscale slot-antenna arrays were designed to determine glucose and fructose concentrations in solutions, including market beverages [20] with concentrations as low as 10 mg/dL.

Despite the significant progress in SEIRA of organic molecules at ultra-low concentrations, the plasmonic enhancement of IR absorption by inorganic nanomaterials like nanocrystals (NCs) has not been extensively examined to date. Recently, A. Toma et al. [21] published the first report on SEIRA for detection of an optical phonon mode (so-called Froehlich mode) from a monolayer of CdSe NCs deposited on Au nanoantenna arrays. The SEIRA enhancement induced by the nanoantennas was estimated to be as high as 1×10^6. In our earlier papers we demonstrated SEIRA in the mid- and far-infrared for both organic molecules and inorganic NCs deposited on Au linear nanoantenna arrays fabricated on Si substrates by nanolithography [22,23]. The influence of a thin SiO_2 layer (0–100 nm) beneath the nanoantenna arrays on the LSPR energy, as well as the LSP penetration depth into SiO_2 were established [12]. We also showed that diffraction modes in linear Au nanoantenna arrays propagating along the Si surface and perpendicular to the nanoantennas [24] can be effectively employed for further enhancement of SEIRA by optical phonons in semiconductor NCs [23]. The electromagnetic field distribution around the linear antennas was calculated using three-dimensional electrodynamics simulations, where the maximal SEIRA enhancement was realized for an array period of about 15 μm when the energy of a diffraction mode coincides with that of the LSPR mode [23].

Besides linear nanoantennas, plasmonic structures with more sophisticated geometries have been probed in SEIRA experiments. These structures include fan-shaped nanoantennas [25], H- and U-shaped nanoantennas [26], Jerusalem-cross-shaped nanoapertures [27], nanorings [28], and nanoslits [29]. A detailed description of various nanoantenna geometries can be found in the comprehensive review [30].

In this paper, we report on a systematic study of the effect of SEIRA by the phonon response from monolayers of CdSe, CdS, and PbS NCs deposited on periodic arrays of Au nano- and microantennas of linear and H-like shapes having the LSPR energy close to the surface optical phonon energy of in the corresponding NCs. It should be mentioned that although the same conceptual framework and methodological toolkit were used in this paper as in [23] (including sample design, and analytical and computational analysis approaches), we probe and compare the plasmonic properties of nanoantennas with various sample geometry as well as their SEIRA performance. We show that even though SEIRA is evidenced for all plasmonic micro- and nanostructures under investigation, the maximal local enhancement of the NC phonon response is obtained for NCs deposited on the linear nanoantennas with structural parameters optimized via 3D full-wave electromagnetic simulations.

Experimental

The uniform, periodic, linear, Au nanoantenna arrays with the overall dimensions of 3×3 mm^2, differing in nanoantenna length and lateral periodicity, were fabricated on bare Si(001) substrates and substrates covered with SiO$_2$ layers of different (5–100 nm) thicknesses by direct electron beam writing (Raith-150, Germany) as described earlier [23,31]. For H-shaped nanoantennas, additional Au symmetric cross-arms were introduced on the nanoantenna edges of the linear nanoantennas.

The microantenna arrays with the overall dimensions of 8×8 mm^2 were patterned on Si(001) substrates using a conventional photolithography technique. The width (height) of microantennas was chosen to be 4 µm (50 nm), while the antenna length varied in the range of 7–31 µm. The optimal values of the latter were determined numerically using 3D full-wave simulations in the ANSYS Electromagnetics Suite R18 software [32] to adjust the plasmon resonance to a specific wavelength in the far-infrared (terahertz) spectral region.

The monolayers (MLs) of CdS and PbS NCs fabricated and MLs of commercially available colloidal CdSe NCs were homogeneously deposited on the prepared plasmonic substrates using the Langmuir–Blodgett (LB) technique as described earlier [23,33-35].

The size, shape, and areal density of NCs, as well as the structural parameters of nanoantennas (length, width, and lateral periodicity) were measured by scanning electron microscopy (SEM) using the same Raith-150 system at 10 kV acceleration

voltage, 30 µm aperture, and 6 mm working distance. The structural parameters of the microantennas were controlled by optical microscopy. The diameter of the CdS and PbS NCs determined from SEM measurements was found to be 4.5 ± 1.5 nm and 7 ± 3 nm, respectively [23], while the diameter of the colloidal CdSe NCs purchased from Lumidot was 5.0 ± 0.3 nm.

FTIR transmission measurements of Au nano- and microantenna arrays were carried out in the spectral range of 30–5000 cm^{-1} using a Bruker Vertex 80v Fourier transform spectrometer. The IR spectra were recorded for different angles of incidence (from 0 to 55°) and polarizations (TE and TM). For further evaluation, the ratio of the IR transmission spectra corresponding to the light polarization along the nanoantenna axis and perpendicular to it was calculated and analyzed.

Results and Discussion
LSPR modes in nanoantennas with different morphology

The typical SEM and optical images of nano- and microantenna arrays used as substrates for the deposition of NCs are shown in Figure 1. The length and transverse period of the nanoantennas in different arrays were changed, while the nanoantenna width and the inter-antenna gap were fixed to be about 100 nm.

In Figure 2a and 2b, the IR transmission spectra of the linear nanoantenna arrays fabricated with different nanoantenna lengths are presented. The spectra demonstrate distinct deep
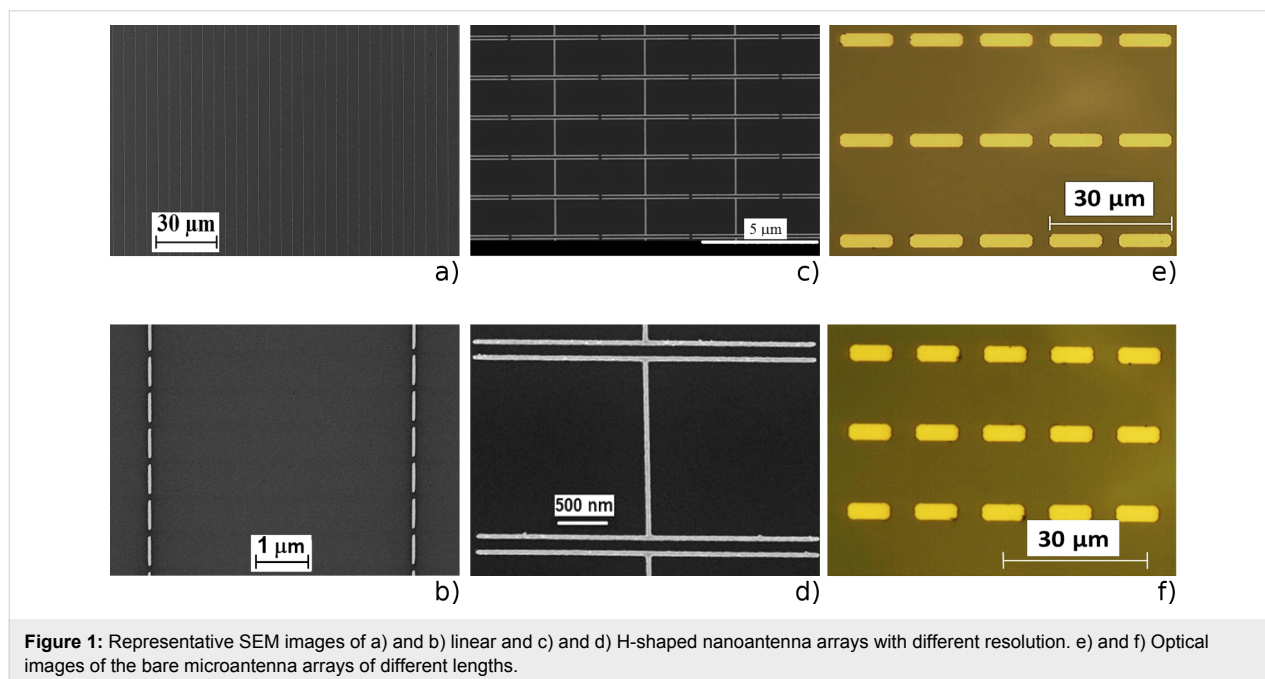

Figure 1: Representative SEM images of a) and b) linear and c) and d) H-shaped nanoantenna arrays with different resolution. e) and f) Optical images of the bare microantenna arrays of different lengths.
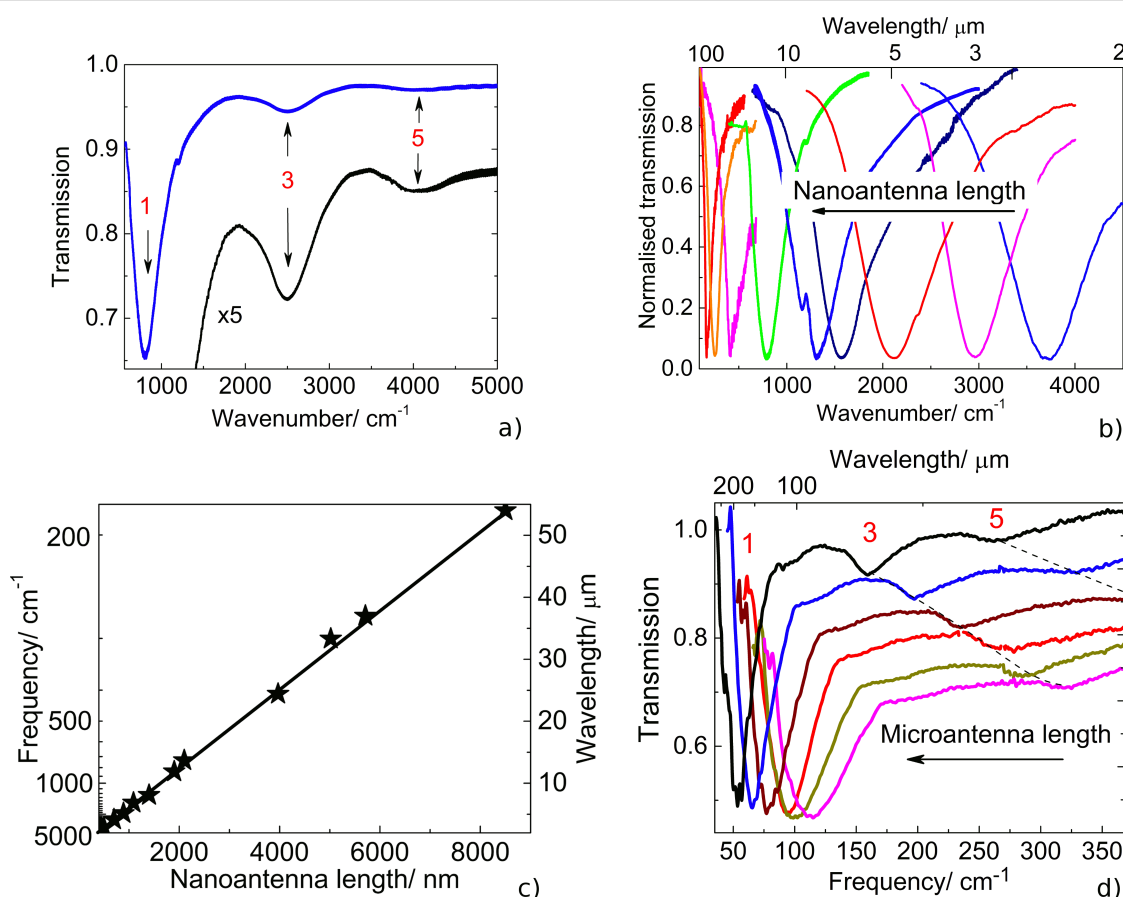
Figure 2: a) Typical IR transmission spectrum for the array of nanoantennas with a length of 1800 nm. The lower curve (black, labeled as ×5) shows the magnified IR spectrum (blue) to emphasize the higher-order plasmon modes. b) Normalized IR transmission spectra of linear antennas with different lengths (adopted from [12]). c) LSPR energy in nanoantenna arrays fabricated on bare Si surfaces as a function of the nanoantenna length (adopted from [12]). d) Normalized IR transmission spectra of the fabricated microantennas with different lengths (14.7; 16.4; 17.8; 20.2; 24.3; 30.6 μm). The numbers in the figures indicate the order of the LSPR modes.

minima, the position of which corresponds to the LSPR energy. The weaker minima, corresponding to higher-order LSPR modes, are also observed at odd multiples (3rd and 5th) of the fundamental LSPR wavenumber (Figure 2a), whereas the even order LSPR modes remain inactive in the IR spectra recorded under normal incidence.

As it can be clearly seen from Figure 2b, the experimentally determined LSPR wavelength reveals a linear dependence on the antenna length in the investigated spectral range. The linear nanoantennas effectively couple to the incident electromagnetic waves once their wavelength coincides with the doubled antenna length [36]. This coupling also depends on the dielectric function of the surrounding medium that causes an increase in the LSPR energy when a thin SiO_2 layer (with a thickness of 0.5–100 nm) is introduced beneath the nanoantennas [12].

Similar to nanoantenna arrays, the LSPR wavelength of the Au microantennas also undergoes a red shift with increasing the

antenna length. However, this shift exhibits a nonlinear behavior owing to the fact that for short microantennas their length becomes comparable to the antenna width. Due to the nonlinear scaling, prior to fabricating the microantennas with the desired LSPR energy, additional 3D full-wave simulations were carried out.

The H-shaped nanoantennas possess two LSPR modes polarized parallel and perpendicular to the nanoantenna axis with frequencies located in the IR spectral region. It is worth noting that for the LSPR mode polarized parallel to the H-shaped nanoantennas, the enhancement of the electromagnetic field averaged over the total surface of the nanoantenna arrays can exceed that for linear nanoantenna arrays.

In this work, we propose the idea of using H-shaped nanoantennas instead of the linear-shaped ones to further enhance the averaged E-field intensity $<E^2>$ in the vicinity of nanoantennas. The H-shape is obtained by introducing symmetric cross-arms

on the antenna edges as shown in Figure 3, thereby enabling control of the LSPR frequency through two length parameters: L and L_H. Note that the cross-arms increase the intra-antenna capacitive coupling as compared to the linear nanoantennas. This results in smaller values of the length L versus the cross-arm-free case when fixing the LSPR frequency at a prescribed value. Despite the fact that, with all other parameters being equal, the linear antennas yield the highest peak magnitude of the local field among all geometries (see Figure 4 below), the smaller longitudinal unit cell size and quasi-uniform field distribution between the cross-arms of adjacent H-shaped antennas results in an increase of the $<E^2>$ value volumetrically averaged over the antenna height within the array unit cell. When increasing L_H, such augmentation is to be manifested up to some limit below which the electric field becomes too small and incapable of compensating the unit cell size decrease. This effect is illustrated in Figure 3 where the optimized nanoantenna length L and the averaged electric field intensity $<E^2>$ are plotted as a function of the cross-arm length L_H for the example of H-shaped nanoantennas with the LSPR energy fixed at 190 cm^{-1}. Optimization was carried out in the ANSYS EM Suite software; details of the electric field averaging procedure are described in [23]. When choosing the transverse spacing between nanoantennas G_y we exploited the condition of superposing the LSPR wavelength λ_{LSPR} and the 1st diffraction harmonics excited in a Si wafer to maximize the E-field enhancement [23]: $\lambda_{LSPR}/n_{Si} = G_y = 15380$ nm, where $n_{Si} = 3.421$ is the refractive index of silicon. The results presented in Figure 3 prove: a) the existence of the optimal cross-arm length L_H (1880 nm) and b) higher $<E^2>$ values attainable for the

H-shaped nanoantennas as compared to the linear ones. In the current example, the H-shaped antennas exhibit a maximal gain of 175% relative to that of the linear antennas.

Figure 4 illustrates the computed surface E-field distribution for three different types of antenna arrays optimized for the LSPR frequency of 190 cm^{-1} and fabricated in this work to compare their efficiency in terms of the field enhancement: linear nanoantennas (a, a'), H-shaped nanoantennas (b, b'), and linear microantennas (c). In all three cases the transverse period $G_y = 15380$ nm was chosen to coincide with the 1st diffraction lobe onset point as explained above. The relative E-field peak enhancement reaches 1500 for the linear nanoantennas, while decreasing down to 600 and 60 for the H-shaped nanoantennas and the linear microantennas, respectively.

Higher-order LSPR modes

It should be noted that the even higher-order LSPR modes are not observed in the IR spectra of linear antennas under normal illumination due to the vector symmetry of the surface currents induced by the incident wave. Such an effect is known for microwave frequency selective surfaces [14] for which the LSPR mode can be interpreted as a standing wave excited on the structure's unit cell. For even modes, different parts of the standing wave tend to oscillate in antiphase such that the locally induced dipole moment of the cell is minimized and thereby prevents manifesting the LSPR features in the far field. Though the even LSPR modes are considered to be "dipole forbidden", they can be activated by breaking the current's symmetry. The simplest way to the symmetry breakdown is to deform the
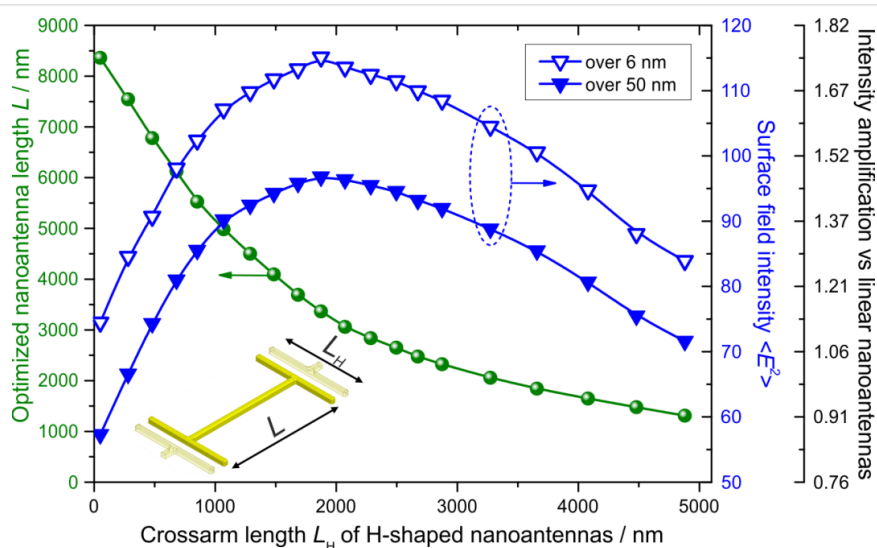
Figure 3: Optimized nanoantenna length L vs the transverse crossarm length L_H for H-shaped nanoantennas with the LSPR energy fixed at 190 cm^{-1} (circles) and the dependence of the averaged electric field intensity $<E^2>$ on L_H (triangles). The transverse spacing between antennas is chosen to coincide with the wavelength of the first 1st diffraction harmonics: $G_y = 15380$ nm. The rightmost vertical scale represents $<E^2>$ normalized to that of linear nanoantennas optimized for 190 cm^{-1}.

Figure 4: Distribution of the normalized LSPR electric field magnitude on top of the Si surface underlying the antenna arrays optimized for the LSPR energy of 190 cm^{-1}: (a), (a') linear nanoantennas, L = 8360 nm; (b), (b') H-shaped nanoantennas, L = 3290 nm, L_H = 1880 nm; (c) linear microantennas, L = 7.7 μm. The transverse period G_y = 15380 nm coinciding with the 1st diffraction lobe onset point is chosen for all the cases. The E-field is normalized to that when the antenna array is removed from Si surface, thereby displaying relative antenna-induced field amplification. The framed numbers indicate the peak values. Normal excitation, $\mathbf{E_0}$ ∥ $\mathbf{X}$.

nanoantenna shape. Such a defect-induced activation of the 2nd-order LSPR mode was observed for non-ideal nanoantennas at normal incidence [37]. The second way to the symmetry breakdown condition is off-normal illumination [38]. In our work this effect was experimentally studied both for nano- and microantennas as shown in Figure 5a and 5b, respectively. These graphs demonstrate the angle-induced excitation of the 2nd-order LSPR modes, the intensity of which increases when the angle of incidence augments. In this case, the even LSPR modes appear due to a "retardation effect", which implies that the incident wavefront reaches different points of the antenna at different times, thus inducing out-of-phase ohmic currents in the antenna metal and yielding the non-compensated dipole moment.

To quantitatively illustrate the "retardation effect" in terms of the induced dipole moment under oblique illumination, in Figure 6a we present the results of simulating the magnitude of the second time derivative $\partial^2\mathbf{d}/\partial t^2$ of the dipole moment $\mathbf{d}$ as a function of frequency by the example of linear nanoantennas with a length of 1800 nm. The results are obtained for three different angles of incidence θ = 0, 25, and 50°. Since the longitudinal LSPR mode can be excited either by TE- ($\mathbf{E_0}$ ∥ $\mathbf{X}$) or TM-polarized ($\mathbf{H_0}$ ∥ $\mathbf{Y}$) waves, both geometries are considered

in the simulations. Note that switching to the second derivative of $\mathbf{d}$ instead of the dipole moment itself is explained by the fact that the far field radiation that is scattered (re-emitted) by the nanoantenna array is summed from the dipole radiation of individual antennas, where a specific intensity per unit solid angle is governed by the classical formula [39]:

$$\partial I/\partial \Omega = \left(4\pi c^3\right)^{-1} \cdot \left[\!\left[\partial^2\mathbf{d}/\partial t^2 \times \mathbf{n}\right]\!\right]^2,$$

where c is the speed of light and $\mathbf{n}$ is the unit radius vector directed from the nanoantenna to the observation point. The simulations were accomplished with the help of ANSYS EM Suite R18 software, wherein the regime of Floquet ports and periodic boundary conditions was employed to model the nanoantenna array as a uniform periodic structure, while a Drude model with linear plasma and damping frequencies of 72,500 cm^{-1} and 216 cm^{-1}, respectively, was applied to correctly describe the frequency response of gold [12]. To avoid undesirable computational effects arising from wave interference in the Si wafer of finite thickness, the Si medium supporting the nanoantenna array was assumed to fill semi-infinite space. This was implemented in ANSYS EM Suite by allowing the Si medium to touch one of the Floquet ports. In simulations,
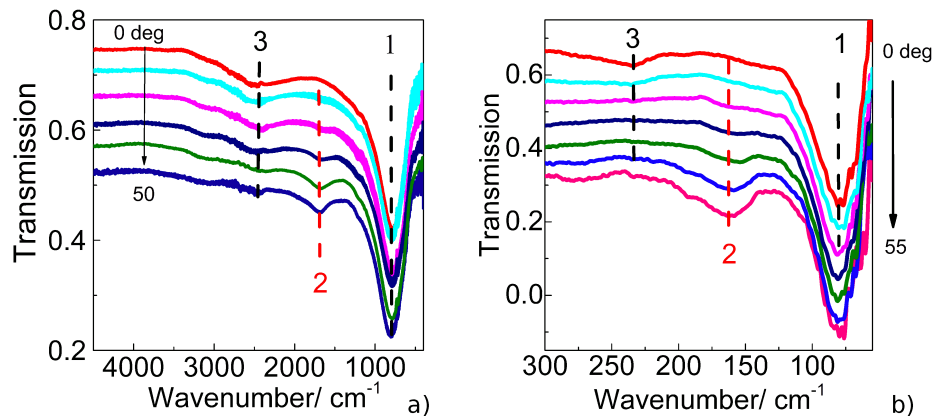
Figure 5: IR transmission spectra of the array of a) nanoantennas and b) microantennas measured at different angles of incidence, TM polarization. The vertical dashed lines with numbers indicate the positions of the LSPR modes of the corresponding order.
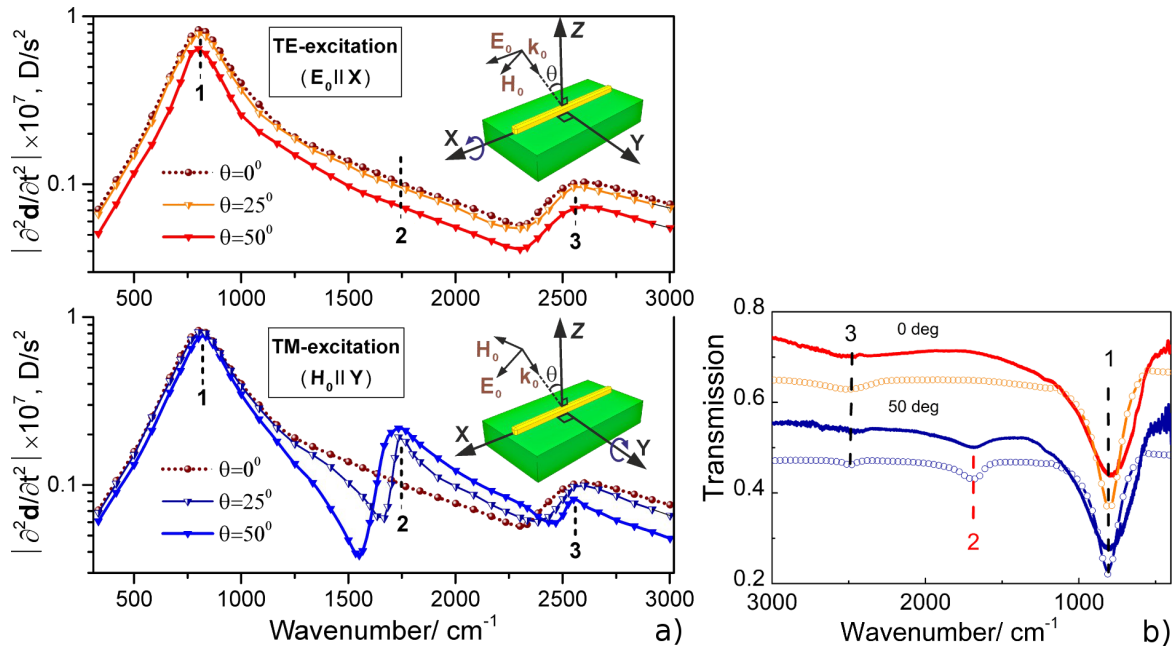

Figure 6: a) Evaluating the spectral behavior of the dipole radiation from a unit cell of the Si-backed array of linear nanoantennas at different angles of incidence θ and different polarizations: antenna length – 1800 nm, Y-period – 5000 nm. The graphs correspond to the wave power of $P_0 \cdot \cos\theta$ with P_0 = 1 W impinging upon the unit cell. b) Experimental (solid lines) and simulated (circles) SEIRA spectra of the linear nanoantennas for angles of incidence θ = 0 and 50° and TM polarization. The vertical dashed lines with numbers indicate the positions of the LSPR modes of the corresponding order.

the procedure of adaptive meshing was accomplished at the highest frequency in the region of interest (3000 cm^{-1}) that required taking into account 98 non-evanescent Floquet modes for the Si-touching Floquet port and 14 ones for the vacuum-touching port. When numerically computing the quantity of $\left| \partial^2 \mathbf{d} / \partial t^2 \times \mathbf{n} \right|$, its value was determined with the ANSYS built-in field calculator via integrating the complex vector magnitude of the ohmic current density $\mathbf{j(t)}$ over the nanoantenna volume according to the formula:

$$\partial^2 \mathbf{d} / \partial t^2 = \partial\left(\int \mathbf{j(r)} dV\right) / \partial t = i\omega \cdot \int \mathbf{j(r)} dV$$
$$= i\omega \cdot \left(\int \mathbf{j}_x(\mathbf{r}) dV, \int \mathbf{j}_y(\mathbf{r}) dV, \int \mathbf{j}_z(\mathbf{r}) dV\right),$$

where ω is the radiation angular frequency, *i* is the imaginary unit.

The results presented in Figure 6 clearly show that LSPR modes are present in the dipole moment spectra as peaks of decaying

amplitudes. For TE polarization, the electric field of which is parallel to the nanoantenna axis ($\mathbf{E_0}$ II $\mathbf{X}$) at any θ, there is no retardation effect and the even the LSPR mode remains dipole inactive. For TM polarization, the situation is fundamentally different: due to the appearance of the nonzero *z*-component of the electric field under oblique illumination, different parts of the antenna are excited at different times, thus inducing a non-compensated dipole moment for the even order LSPR mode and making it dipole active.

SEIRA by semiconductor NCs on Au nanoantenna arrays

As it was shown in [21], the SEIRA spectra of 1 ML of CdSe NCs deposited on Au nanoantenna arrays reveal the fundamental surface optical (SO) mode of CdSe NCs at 190 cm^{-1}. Hence, the optimal structural parameters of nano- and microantennas were determined from the calculations to ensure LSPR energies corresponding to SO phonons in CdSe (190 cm^{-1}) [40-42], CdS (270 cm^{-1}) [43], and PbS (190 cm^{-1}) [43,44] NCs, and thereafter antenna arrays with the corresponding structural parameters, and consequently with required LSPR energies, were fabricated. Variants of the antenna arrays, including linear-shaped nano- and microantennas and H-shaped nanoantennas, were used for further SEIRA investigations. These arrays with appropriate structural parameters were also used for depositing CdSe, CdS, and PbS NCs in the Langmuir–Blodgett experiments. As it is seen from representative SEM images in Figure 7, a homogeneous monolayer of CdSe NCs is formed near the gaps of linear and H-shaped nanoantennas where the maximal field enhancement for the light polarization along the nanoantennas is expected.

The IR transmission spectra of the samples with linear nanoantenna arrays before and after deposition of CdSe and CdS NCs with different ML quantities were recorded and are presented in Figure 8a and Figure 8b, respectively. The IR spectra of the as-prepared nanoantennas reveal sharp minima near 190 or 265 cm^{-1} in accordance with the LSPR energies predicted by the simulations.

The deposition of 1 ML of CdSe and CdS NCs on linear nanoantennas (Figure 8a and 8b) as well as of PbS and CdSe NCs on the H-shaped nanoantennas (Figure 8c and 8d) induces clearly resolved features in the SEIRA spectra near 190 and 250 cm^{-1}, respectively, which are superimposed onto the LSPR minima attributed to the SO modes of the NCs. With increasing number of deposited NC monolayers, their intensity increase entails a high frequency shift of the LSPR minima, which is more pronounced for H-shaped nanoantennas (Figure 8c and 8d). This shift occurs due to the change in dielectric function of the medium surrounding the nanoantennas. At a relatively thick CdSe NC coating on H-shaped nanoantenna arrays, the SEIRA response by NCs consists of at least two obvious components of the SO mode: one at 191 cm^{-1} and a weaker feature at 171 cm^{-1}. Their frequencies were determined from the best fit using two Lorentzian curves. The appearance of the latter feature is attributed to the absorption by TO phonon modes in CdSe NCs normally active in IR spectra. As it was shown in our earlier paper [23], the intensity of the SEIRA response of NCs on a linear nanoantenna array can be maximized by a proper choice of the array period when the energy of a diffraction mode coincides with that of the LSPR mode. Note, however, that the overall intensities of the phonon modes of NCs deposited on the linear and H-shaped nanoantenna arrays are comparable. Thus, the local SEIRA enhancement of linear nanoantennas appears to be significantly larger than that of H-shaped nanoantennas due to the lower values of the electromagnetic field localized between the cross-arms of H-shaped elements. The comparable intensities of the phonon modes of NCs deposited on the linear and H-shaped nanoantenna seen in Figure 8a and 8d, respectively, are not consistent with the calculations predicting the higher gain (175%) for the H-shaped

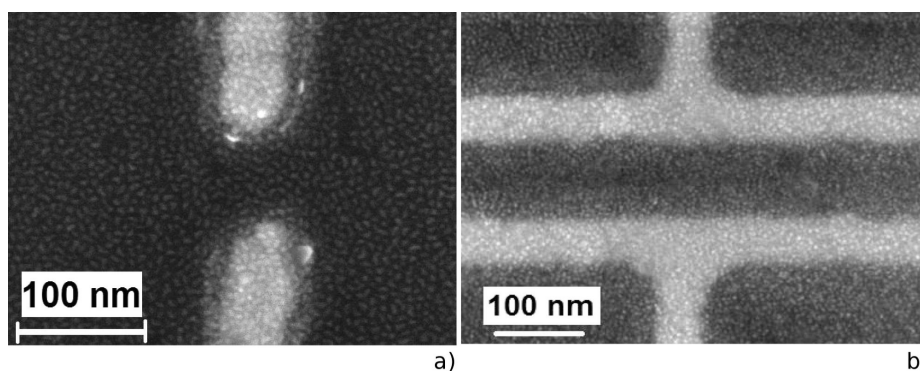a)   b)

Figure 7: SEM images of the nanoantenna edges for a) linear and b) H-shaped nanoantennas taken after deposition of 1 ML of CdSe NCs. Figure 7a is reprinted with permission from [23], copyright 2017 American Chemical Society.
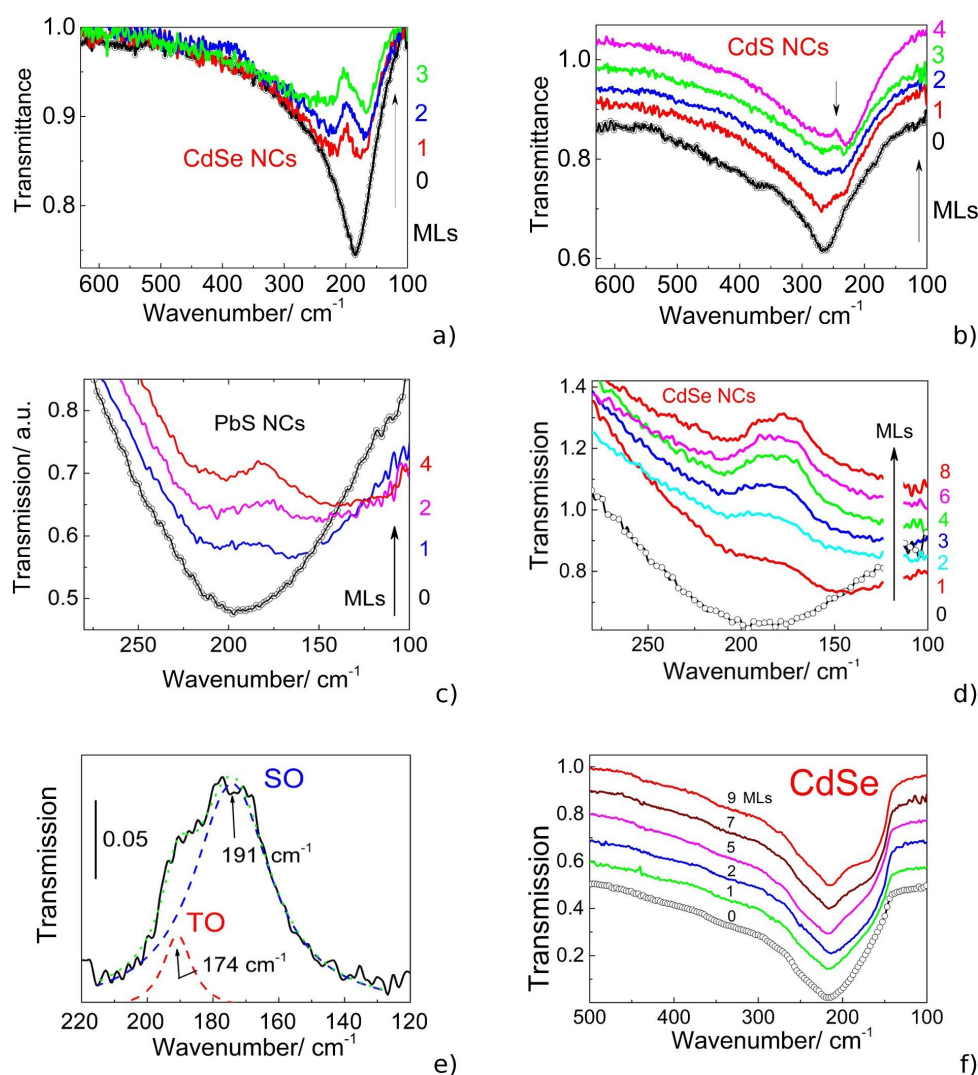
Figure 8: IR transmission spectra of the linear nanoantenna arrays before nanocrystal (NC) deposition (black circles) and after covering with different ML quantities for (a) CdSe and (b) CdS NCs. IR transmission spectra of H-shaped nanoantenna arrays before NC deposition (black circles) and after covering with different ML quantities for (c) PbS and (d) CdSe NCs. e) Fragment of the IR spectrum of 9 MLs of CdSe NCs deposited on the H-shaped nanoantenna arrays (Figure 8d, curve 8) after background subtraction. f) IR transmission spectra of microantenna arrays before NC deposition (black circles) and after covering with different ML quantities for CdSe NCs. Figure 8a and 8b are reprinted with permission from [23], copyright 2017 American Chemical Society.

nanoantennas relative to that of the linear ones. The reason for such a discrepancy between the theoretical expectations and experimental data is most likely explained by lower areal density of the NC located in the gap between the cross-arms of the H-shaped antennas that originates from the LB deposition process.

Conclusion

We report on systematic experimental and theoretical investigations of mid- and far-infrared LSPRs in arrays of linear and H-shaped Au nanoantennas and linear Au microantennas. We demonstrate comparative SEIRA experiments with semiconductor NCs deposited on the antenna arrays with the optimal struc-

tural parameters. This ensures that the LSPR frequencies are adjusted to the range of optical phonons in semiconductor NCs. We show that although the overall IR response by NCs deposited on Au antenna arrays with different morphologies is comparable, the maximal SEIRA enhancement is achieved for the linear geometry due to a highly localized electromagnetic field between the nanoantenna edges.

Acknowledgements

ORCID® iDs

Ekaterina E. Rodyakina - https://orcid.org/0000-0003-4940-7074
Volodymyr M. Dzhagan - https://orcid.org/0000-0002-7839-9862
Dietrich R. T. Zahn - https://orcid.org/0000-0002-8455-4582

References

1. Little, L. H. *Infrared Spectra of Adsorbed Species;* Academic Press, Inc.: London, United Kingdom, 1966.
2. Hoffmann, F. M. *Surf. Sci. Rep.* **1983,** *3,* 109–192. doi:10.1016/0167-5729(83)90001-8
3. Aroca, R. F.; Ross, D. J.; Domingo, C. *Appl. Spectrosc.* **2004,** *58,* 324A–338A. doi:10.1366/0003702042475420
4. Röseler, A.; Korte, E. H. *Fresenius' J. Anal. Chem.* **1998,** *362,* 51–57. doi:10.1007/s002160051034
5. Osawa, M. In *Handbook of Vibrational Spectroscopy;* Chalmers, J. M.; Griffiths, P. R., Eds.; John Wiley and Sons: New York, NY, U.S.A., 2002; p 785. doi:10.1002/0470027320.s0603
6. Aroca, R. *Surface-Enhanced Vibrational Spectroscopy;* John Wiley & Sons, Ltd: Chichester, United Kingdom, 2006. doi:10.1002/9780470035641
7. Priebe, A.; Sinther, M.; Fahsold, G.; Pucci, A. *J. Chem. Phys.* **2003,** *119,* 4887–4890. doi:10.1063/1.1597232
8. Hartstein, A.; Kirtley, J. R.; Tsang, J. C. *Phys. Rev. Lett.* **1980,** *45,* 201–204. doi:10.1103/physrevlett.45.201
9. Osawa, M. Surface-Enhanced Infrared Absorption. In *Near-Field Optics and Surface Plasmon Polaritons;* Kawata, S., Ed.; Topics in Applied Physics, Vol. 81; Springer: Berlin, Germany, 2001; pp 163–187. doi:10.1007/3-540-44552-8_9
10. Orendorff, C. J.; Gole, A.; Sau, T. K.; Murphy, C. J. *Anal. Chem.* **2005,** *77,* 3261–3266. doi:10.1021/ac048176x
11. de la Chapelle, M.; Pucci, A., Eds. *Nanoantenna;* Pan Stanford Publishing Pte Ltd.: Singapore, 2013; 10.1201/b14594. doi:10.1201/b14594
12. Milekhin, I. A.; Kuznetsov, S. A.; Rodyakina, E. E.; Milekhin, A. G.; Latyshev, A. V.; Zahn, D. R. T. *Beilstein J. Nanotechnol.* **2016,** *7,* 1519–1526. doi:10.3762/bjnano.7.145
13. Biagioni, P.; Huang, J.-S.; Hecht, B. *Rep. Prog. Phys.* **2012,** *75,* 024402. doi:10.1088/0034-4885/75/2/024402
14. Bryant, G. W.; García de Abajo, F. J.; Aizpurua, J. *Nano Lett.* **2008,** *8,* 631–636. doi:10.1021/nl073042v
15. Razzari, L.; Toma, A.; Clerici, M.; Shalaby, M.; Das, G.; Liberale, C.; Chirumamilla, M.; Zaccaria, R. P.; De Angelis, F.; Peccianti, M.; Morandotti, R.; Di Fabrizio, E. *Plasmonics* **2013,** *8,* 133–138. doi:10.1007/s11468-012-9439-0
16. D'Andrea, C.; Bochterle, J.; Toma, A.; Huck, C.; Neubrech, F.; Messina, E.; Fazio, B.; Maragò, O. M.; Di Fabrizio, E.; Lamy de La Chapelle, M.; Gucciardi, P. G.; Pucci, A. *ACS Nano* **2013,** *7,* 3522–3531. doi:10.1021/nn4004764
17. Neubrech, F.; Pucci, A.; Cornelius, T. W.; Karim, S.; García-Etxarri, A.; Aizpurua, J. *Phys. Rev. Lett.* **2008,** *101,* 157403. doi:10.1103/physrevlett.101.157403
18. Huck, C.; Neubrech, F.; Vogt, J.; Toma, A.; Gerbert, D.; Katzmann, J.; Härtling, T.; Pucci, A. *ACS Nano* **2014,** *8,* 4908–4914. doi:10.1021/nn500903v
19. Adato, R.; Yanik, A. A.; Amsden, J. J.; Kaplan, D. L.; Omenetto, F. G.; Hong, M. K.; Erramilli, S.; Altug, H. *Proc. Natl. Acad. Sci. U. S. A.* **2009,** *106,* 19227–19232. doi:10.1073/pnas.0907459106
20. Lee, D.-K.; Kang, J.-H.; Lee, J.-S.; Kim, H.-S.; Kim, C.; Hun Kim, J.; Lee, T.; Son, J.-H.; Park, Q.-H.; Seo, M. *Sci. Rep.* **2015,** *5,* 15459. doi:10.1038/srep15459
21. Toma, A.; Tuccio, S.; Prato, M.; De Donato, F.; Perucchi, A.; Di Pietro, P.; Marras, S.; Liberale, C.; Proietti Zaccaria, R.; De Angelis, F.; Manna, L.; Lupi, S.; Di Fabrizio, E.; Razzari, L. *Nano Lett.* **2015,** *15,* 386–391. doi:10.1021/nl503705w
22. Milekhin, A. G.; Cherkasova, O.; Kuznetsov, S. A.; Milekhin, I. A.; Rodyakina, E. E.; Latyshev, A. V.; Banerjee, S.; Salvan, G.; Zahn, D. R. T. *Beilstein J. Nanotechnol.* **2017,** *8,* 975–981. doi:10.3762/bjnano.8.99
23. Milekhin, A. G.; Kuznetsov, S. A.; Sveshnikova, L. L.; Duda, T. A.; Milekhin, I. A.; Rodyakina, E. E.; Latyshev, A. V.; Dzhagan, V. M.; Zahn, D. R. T. *J. Phys. Chem. C* **2017,** *121,* 5779–5786. doi:10.1021/acs.jpcc.6b11431
24. Weber, D.; Albella, P.; Alonso-González, P.; Neubrech, F.; Gui, H.; Nagao, T.; Hillenbrand, R.; Aizpurua, J.; Pucci, A. *Opt. Express* **2011,** *19,* 15047–15061. doi:10.1364/oe.19.015047
25. Brown, L. V.; Yang, X.; Zhao, K.; Zheng, B. Y.; Nordlander, P.; Halas, N. J. *Nano Lett.* **2015,** *15,* 1272–1280. doi:10.1021/nl504455s
26. Zarrabi, F. B. *Optik (Munich, Ger.)* **2016,** *127,* 4490–4494. doi:10.1016/j.ijleo.2016.01.189
27. Cetin, A. E.; Kaya, S.; Mertiri, A.; Aslan, E.; Erramilli, S.; Altug, H.; Turkmen, M. *Photonics Nanostruct. - Fundam. Appl.* **2015,** *15,* 73–80. doi:10.1016/j.photonics.2015.04.001
28. Cetin, A. E.; Etezadi, D.; Altug, H. *Adv. Opt. Mater.* **2014,** *2,* 866–872. doi:10.1002/adom.201400171
29. Huck, C.; Vogt, J.; Sendner, M.; Hengstler, D.; Neubrech, F.; Pucci, A. *ACS Photonics* **2015,** *2,* 1489–1497. doi:10.1021/acsphotonics.5b00390
30. Neubrech, F.; Huck, C.; Weber, K.; Pucci, A.; Giessen, H. *Chem. Rev.* **2017,** *117,* 5110–5145. doi:10.1021/acs.chemrev.6b00743
31. Milekhin, A. G.; Yeryukov, N. A.; Sveshnikova, L. L.; Duda, T. A.; Rodyakina, E. E.; Sheremet, E. S.; Ludemann, M.; Gordan, O. D.; Latyshev, A. V.; Zahn, D. R. T. *Thin Solid Films* **2013,** *543,* 35–40. doi:10.1016/j.tsf.2013.03.070
32. ANSYS, Inc.. https://www.ansys.com/products/electronics.
33. Milekhin, A.; Sveshnikova, L.; Duda, T.; Surovtsev, N.; Adichtchev, S.; Ding, L.; Zahn, D. R. T. *J. Vac. Sci. Technol., B: Nanotechnol. Microelectron.: Mater., Process., Meas., Phenom.* **2010,** *28,* C5E22–C5E24. doi:10.1116/1.3442799
34. Milekhin, A. G.; Sveshnikova, L. L.; Duda, T. A.; Yeryukov, N. A.; Rodyakina, E. E.; Gutakovskii, A. K.; Batsanov, S. A.; Latyshev, A. V.; Zahn, D. R. T. *Phys. E (Amsterdam, Neth.)* **2016,** *75,* 210–222. doi:10.1016/j.physe.2015.09.013
35. Milekhin, A. G.; Sveshnikova, L. L.; Duda, T. A.; Rodyakina, E. E.; Dzhagan, V. M.; Sheremet, E.; Gordan, O. D.; Himcinschi, C.; Latyshev, A. V.; Zahn, D. R. T. *Appl. Surf. Sci.* **2016,** *370,* 410–417. doi:10.1016/j.apsusc.2016.02.185
36. Novotny, L. *Phys. Rev. Lett.* **2007,** *98,* 266802. doi:10.1103/physrevlett.98.266802
37. Munk, B. A. *Frequency Selective Surfaces;* John Wiley & Sons, Inc.: Hoboken, NJ, U.S.A., 2000. doi:10.1002/0471723770
38. Neubrech, F.; Garcia-Etxarri, A.; Weber, D.; Bochterle, J.; Shen, H.; Lamy de la Chapelle, M.; Bryant, G. W.; Aizpurua, J.; Pucci, A. *Appl. Phys. Lett.* **2010,** *96,* 213111. doi:10.1063/1.3437093

39. Landau, L. D.; Lifshitz, E. M. *The Classical Theory of Fields,* 3rd ed.; Course of Theoretical Physics Series, Vol. 2; Butterworth-Heinemann, 1980. doi:10.1016/b978-0-08-023039-9.50021-4

40. Dzhagan, V. M.; Valakh, M. Y.; Milekhin, A. G.; Yeryukov, N. A.; Zahn, D. R. T.; Cassette, E.; Pons, T.; Dubertret, B. *J. Phys. Chem. C* **2013,** *117,* 18225–18233. doi:10.1021/jp4046808

41. Vasilevskiy, M. I.; Rolo, A. G.; Artemyev, M. V.; Filonovich, S. A.; Gomes, M. J. M.; Rakovich, Y. P. *Phys. Status Solidi B* **2001,** *224,* 599–604. doi:10.1002/1521-3951(200103)224:2<599::aid-pssb599>3.0.co;2-k

42. Dzhagan, V. M.; Lokteva, I.; Valakh, M. Y.; Raevska, O. E.; Kolny-Olesiak, J.; Zahn, D. R. T. *J. Appl. Phys.* **2009,** *106,* 084318. doi:10.1063/1.3248357

43. Milekhin, A. G.; Sveshnikova, L. L.; Repinsky, S. M.; Gutakovsky, A. K.; Friedrich, M.; Zahn, D. R. T. *Thin Solid Films* **2002,** *422,* 200–204. doi:10.1016/s0040-6090(02)00991-4

44. Krauss, T. D.; Wise, F. W.; Tanner, D. B. *Phys. Rev. Lett.* **1996,** *76,* 1376–1379. doi:10.1103/physrevlett.76.1376

License and Terms

Polarization-dependent strong coupling between silver nanorods and photochromic molecules

Gwénaëlle Lamri[1], Alessandro Veltri[2], Jean Aubard[3], Pierre-Michel Adam[1], Nordin Felidj[3] and Anne-Laure Baudrion[*1]

Abstract

Active plasmonics is a key focus for the development of advanced plasmonic applications. By selectively exciting the localized surface plasmon resonance sustained by the short or the long axis of silver nanorods, we demonstrate a polarization-dependent strong coupling between the plasmonic resonance and the excited state of photochromic molecules. By varying the width and the length of the nanorods independently, a clear Rabi splitting appears in the dispersion curves of both resonators.

Introduction

For decades, plasmonic systems have been extensively studied for their potential applications in many research fields. Due to their localized surface plasmon resonance (LSPR), metallic nanoparticles have been used to enhance the sensitivity of bio- or chemo-sensors [1], enhance and direct the light emitted by quantum dots or molecules [2,3], and to kill cancer cells [4]. This resonance is directly linked to the intrinsic properties of the metallic nanoparticles (depending on the geometry or the nature of the metal), which makes it difficult to easily control its

spectral position. Many approaches have been explored to actively control these plasmonic properties without changing the topographic features of the nanoparticles themselves. Liquid crystals [5], thermosensitive polymers [6], transition metal dichalcogenides [7] and graphene [8] monolayers have been used for this purpose. The change in the refractive index or the doping ability of these materials allows the plasmonic system's environment to be actively changed and the plasmonic properties to be controlled. Another way to control LSPR is to use

photochromic molecules. These molecules can switch their conformation from a transparent state to a colored state by absorbing UV light and can return to their original state by a heating process [9] or by absorbing visible light [10]. Indeed, the photochromic transition is reversible and can undergo several cycles [11]. Current applications of these molecules are mainly found in macroscopic optical components, such as lenses [12] or sunglasses [13]. From the plasmonic perspective, the photochromic molecules can allow for the active control of the plasmonic resonance. The coupling between molecular exciton and plasmonic resonance can lead to weak [14] or strong coupling [15]. The latter is always observed when the plasmon or the molecular exciton presents a large oscillator strength and leads to the splitting of the main resonance. We previously demonstrated a reversible, strong coupling between silver cylindrical nanoparticles and photochromic molecules, both considered as largely damped oscillators [16]. It is of note that the main dipolar plasmonic resonance sustained by a cylindrical nanoparticle is not dependent on the in-plane incident polarization due to the symmetry center of the nanoparticle. However, a polarization-dependent control of the optical properties of a nanosource would be useful in nano-optics applications. As an example, Zhou et al. were able to fabricate a two-color

hybrid nanosource by trapping different emitters in the close vicinity of a cylindrical nanoparticle [17]. The color emitted by this nanosource then depends on the incident in-plane polarization. In this context, a polarization-dependent external control of the plasmonic properties could be of prime interest for active plasmonic devices. In this work, we make use of the same protocol as in [16] and apply it to nanorods to demonstrate a polarization-dependent strong coupling between plasmonic resonances and the excited state of photochromic molecules, as well as the existence of a strong coupling regime when the plasmonic resonance matches the wavelength of the molecular transition. Theoretical calculations confirm our experimental findings.

Experimental

We used standard electron-beam lithography to fabricate large arrays of silver nanorods on a glass substrate. The pitch of the arrays has been varied to keep the filling factor approximately equal to 10% and to avoid any lattice mode contribution in the optical spectra. For three different nanorod widths (70, 90 and 110 nm), the nanorod length was varied from the width value to the double width value. The height of the nanorods was fixed at 50 nm. Figure 1a shows a scanning electron microscope (SEM)
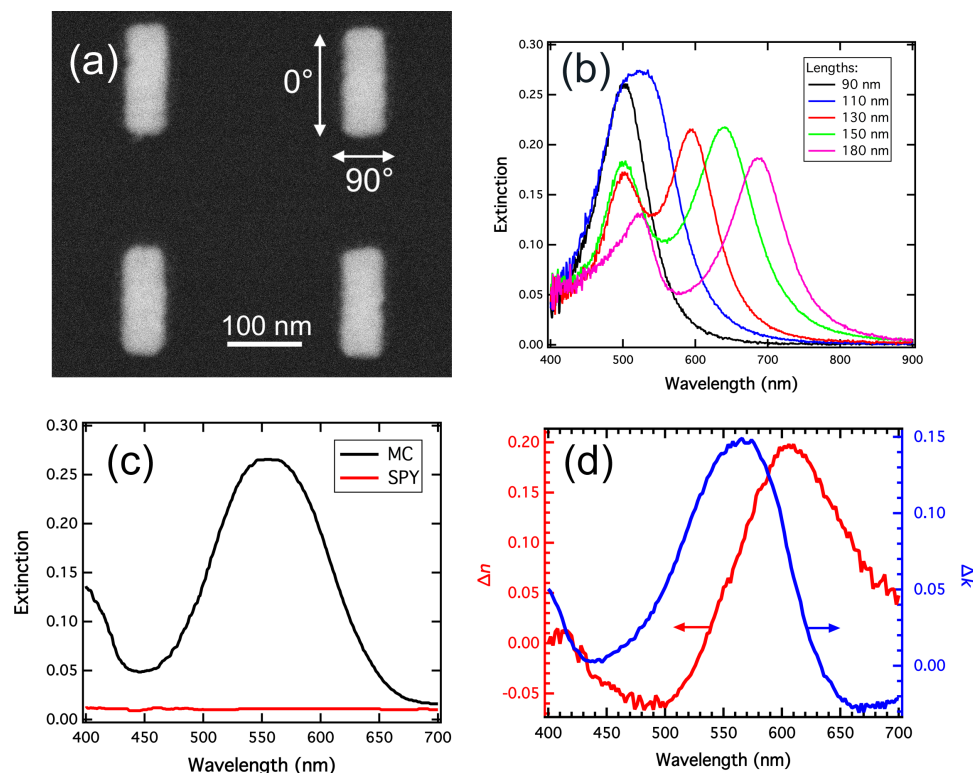
Figure 1: (a) SEM image of silver nanorods. The 0° and 90° polarization orientations correspond to the nanorod long and short axes, respectively. (b) Extinction spectra of silver nanorods in air. The width is 90 nm and the lengths vary from 90 to 180 nm. (c) Absorbance spectrum of a 60 nm thick active layer before (SPY) and after (MC) the photochromic transition. (d) Variations of the refractive index real and imaginary parts of the organic layer due to the photochromic transition, measured by ellipsometry.

image of a nanorod array recorded after the fabrication process. We used standard extinction spectroscopy to record the LSPR on each array. A halogen lamp is used to illuminate the sample from the glass side and the transmitted light is recorded through a 20× bright-field objective. The signal is then sent to a spectrometer to record extinction spectra. The Figure 1b shows typical extinction spectra recorded on five different nanorod arrays, presenting the same width (90 nm) and different lengths. In that case, the halogen lamp is not polarized and one can observe two different peaks on each spectrum, corresponding to the well-known dipolar LSPR excited on the short and the long axes of the nanorods. The photochromic molecules we used are 1′,3′-dihydro-8-methoxy-1′,3′,3′-trimethyl-6-nitrospiro[2*H*-1-benzopyran-2,2′-(2*H*)-indole] molecules (from Sigma-Aldrich). They are able to switch from their transparent spiropyran isomer (SPY) to their colored merocyanine isomer (MC) by absorbing ultraviolet light. To achieve a polymer coating, we diluted the sample in a poly(methyl methacrylate) (PMMA) solution in toluene and spin-coated them onto the sample. The phototransition is realized by illuminating the sample with a Xe lamp filtered with a 400 nm low-pass filter. The excitation lasts two minutes and the polymer film becomes violet. Indeed, the MC isomer presents an absorption maximum at 570 nm (Figure 1c). We characterized this film (without any metallic nanoparticles) by ellipsometry measurements and verified that the photochromic transition is accompanied by a high refractive index change. Figure 1d shows the variations of the refractive index real part (n) and imaginary part (k) due to the photochromic transition. One can observe that Δk is maximum at 570 nm, corresponding to the absorption of the colored MC isomer. Moreover, the photochromic transition leads to a negative variation of Δn for incident wavelengths below 520 nm and a positive variation for incident wavelengths above 520 nm. It is important to note that the reverse photochromic transition (from MC to SPY) can be realized either by absorbing green light (in the MC absorption band) or by heating the sample [18]. In our case, the spectroscopic measurements performed on the sample after the photochromic transition were sufficiently fast to avoid this reverse photochromic transition, which was confirmed by measuring the absorption of the MC layer before and after the measurements.

The surface plasmon resonance of the coated Ag nanorods was characterized by extinction spectroscopy before and after the photochromic transition. The incident light was polarized either along the long axis (0°) or along the short axis (90°) of the nanorods, as represented on the Figure 1a. For each polarization, all the spectra obtained on the arrays were normalized by the spectra measured nearby the nanorod arrays in order to eliminate the contribution of the molecular absorption band of the MC isomer.

Results and Discussion

Figure 2 shows the extinction spectra for nanorod widths of 70 nm (a–c) and 90 nm (d–f). In each graph, the blue curves are related to the short axis plasmonic resonances and the black curves are related to the long axis plasmonic resonances. Moreover, a vertical dashed line represents the MC absorption band at 570 nm. The influence of the photochromic transition on the spectra can be studied by comparing on one side the dark blue and the light blue curves, for the short axis resonance, and on the other side the black and the grey curves, for the long axis resonance. Firstly, one can observe in Figure 2a that before the photochromic transition (in the SPY isomer), the 70 × 70 nm nanorods display two different plasmonic resonances in the short axis (dark blue curve) and in the long axis (black curve). Indeed, the nanorod width is slightly shorter than the nanorod length and the dipolar resonance for a 0° polarization is red-shifted compared to the one for the 90° polarization. It is important to note that both resonances are located at wavelengths shorter than the MC absorption band maximum. After the photochromic transition in the MC isomer, both main resonances are blue-shifted. Moreover, a small shoulder appears near 600 nm in both the light-blue and grey curves. The 8 nm blue-shift measured for the main peak for both polarizations can be related to the negative value of the real part of the refractive index which takes place for wavelengths below 520 nm. The small shoulder comes directly from the coupling between the plasmonic resonance and the excited state of the MC molecule. In order to explore this coupling in more detail, we present the extinction spectra recorded on the nanorods in Figure 2b, presenting a width of 70 nm and a length of 90 nm. In that case, in the SPY form, the plasmonic resonance at 0° (black curve), i.e., in the nanorod long axis, coincides with the MC absorption band, whereas the plasmonic resonance at 90° (dark blue curve), i.e., in the nanorod short axis, remains as before blue-shifted compared to the MC absorption band. The photochromic transition (from the black to the grey curve) leads to a decrease of the main peak amplitude and to a clear enlargement of its spectral width. Our previous study with nanocylinders [16] allowed us to identify this behavior as a strong coupling regime, where the coincidence of the MC absorption band with the plasmonic regime leads to the formation of two distinct peaks and a so-called Rabi splitting [19]. The strong coupling regime is usually observed on high quality resonators as atoms or cavities [15]. As plasmonic resonances are low quality resonators, the strong coupling regime has been mainly studied with molecular J-aggregates, exhibiting very sharp excitonic peaks [20,21]. Even if some studies have also used rhodamine 6G and metallic nanoparticles, which are both bad resonators, they used lattice resonances and benefited from the sharp Fano-type resonance to observe the strong coupling anti-crossing behavior [22]. In our case, each resonator (the LSPR and the molecular exciton)
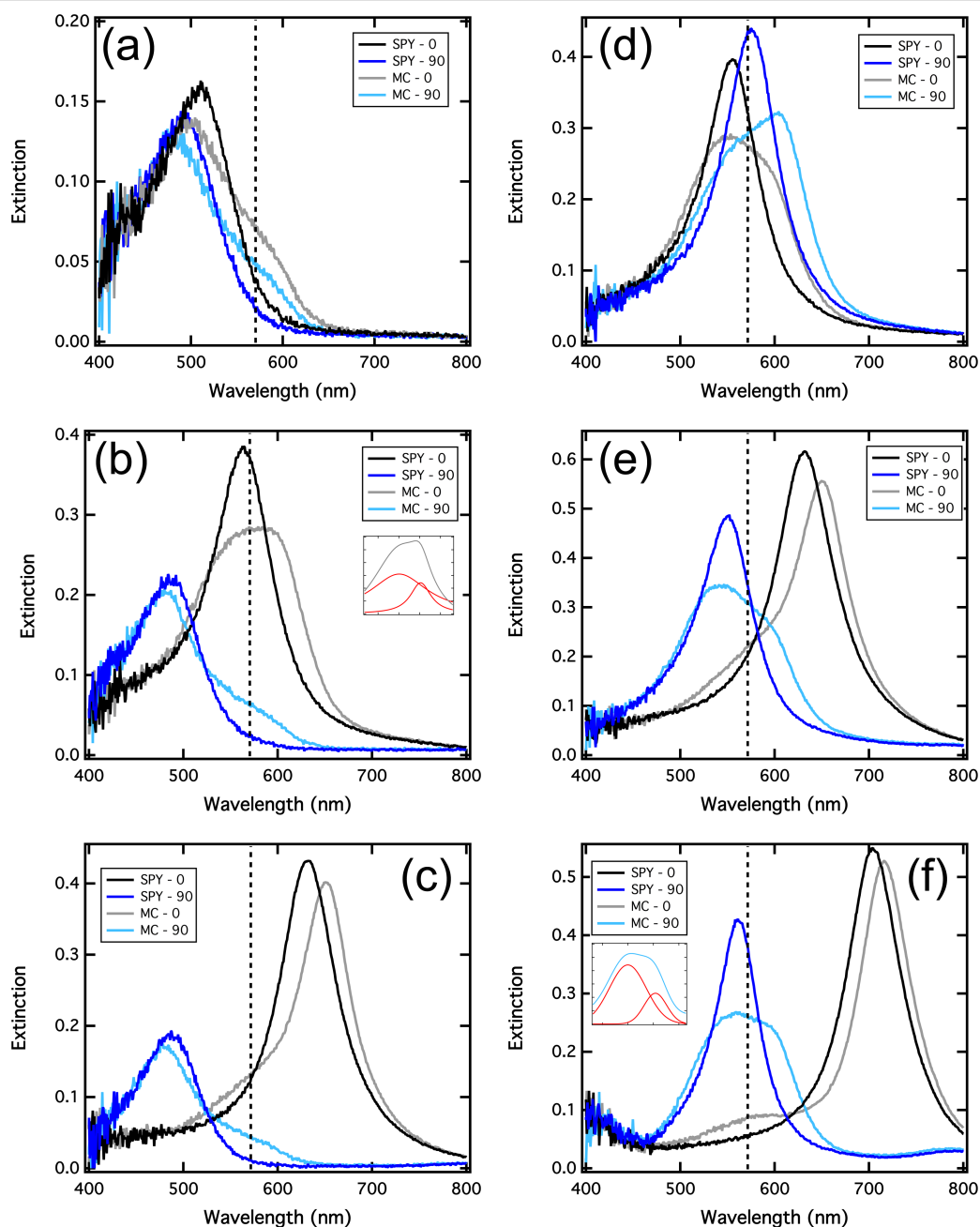
Figure 2: Extinction spectra of the silver nanorod arrays covered with photochromic molecules before (in SPY) and after (in MC) the photochromic transition. The 0° and 90° polarization orientations, corresponding to the excitation of the long and the short axis, are in black/grey and in dark/light blue, respectively. (a), (b) and (c) are measurements on nanorods presenting a width of 70 nm and lengths of 70, 90 and 110 nm, respectively. (d), (e) and (f) are measurements on nanorods presenting a width of 90 nm and lengths of 90, 110 and 130 nm, respectively.

presents a large full width at half maximum (FWHM). Indeed, the black curve of the Figure 2b gives a FWHM of 75 nm, corresponding to 300 meV. Moreover, the FWHM of the MC absorption (Figure 1c) is measured at about 130 nm, corresponding to 500 meV. The Rabi splitting, originating in the cross between the dispersion curves of the two resonant modes, is usually observable if its energy is larger than the sum of their line widths [19]. This condition implies that the Rabi oscilla-

tion period is shorter than the damping time of the plasmon and of the organic exciton. In our case, the fitted decomposition of the curves into two Lorentzian curves (inset of the Figure 2b) leads to an energy splitting of 190 meV, far lower than the 400 meV (150 + 250 meV) necessary to its observation. Although it can be attributed to a line narrowing due to the coupling [23], we think that this peak analysis is not relevant in our case as we measure the plasmonic resonance and the molecular

excitons over a large number of metallic nanoparticles and molecules respectively. Indeed, the nanofabrication process does not allow us to obtain identical geometries over this large number of particles, especially for this nanorod geometry where a rounding of the corners occurs. The extinction measurements do not reflect the quality of the strong coupling between one single nanorod and the molecular exciton. Indeed, even if one single nanorod couples strongly and coherently to an ensemble of molecules, it does not mean that this coupled system can coherently couple to the neighbor coupled systems. This incoherent sum of the contributions and the averaging of the extinction signal over a large number of particles increases the resonance's FWHM. It is worth noting that our previous results on arrays of nanocylinders allowed us to observe two distinct peaks, probably because of the geometry deviations that are minimized for nanocylinders.

Finally, Figure 2c shows the extinction spectra recorded on 70 nm wide and 110 nm long nanorods. The short axis resonance before and after the photochromic transition (blue curves) are identical to Figure 2a and 2b, but in this case, the long axis resonance in the SPY form (black curve) is located at a longer wavelength compared to the MC absorption band. The photo-

chromic transition leads here to a red-shift of the main resonance of about 20 nm, corresponding to a positive Δn of 0.16. Figure 2d–f corresponds to the extinction spectra recorded on 90 nm wide nanorods with varying lengths of 90, 110 and 130 nm, respectively. On each graph, the dark blue plasmonic resonance coincides with the MC absorption band, and the strong coupling regime can thus be observed on the transverse axis of the nanorods in the MC isomer (light blue curves). In the longitudinal plasmonic resonance in the SPY form, varying from 550 nm (Figure 2d) to 700 nm (Figure 2f), the photochromic transition leads to a strong coupling regime for the 90 nm long nanorods and to a weak coupling regime for 130 nm long nanorods.

This spectral analysis was performed for various nanorod geometries and we plotted the position of the plasmonic peaks as a function of the rod width and the rod length for a 110 nm fixed length and a 70 nm fixed width, respectively (Figure 3a and 3c). For each graph, the surface plasmon resonance in the SPY isomer is given by the black line whereas the blue curves show the evolution of the peaks after UV irradiation. The dashed horizontal red lines represent the position of the MC absorption band. Either for the transverse, or for the longitu-
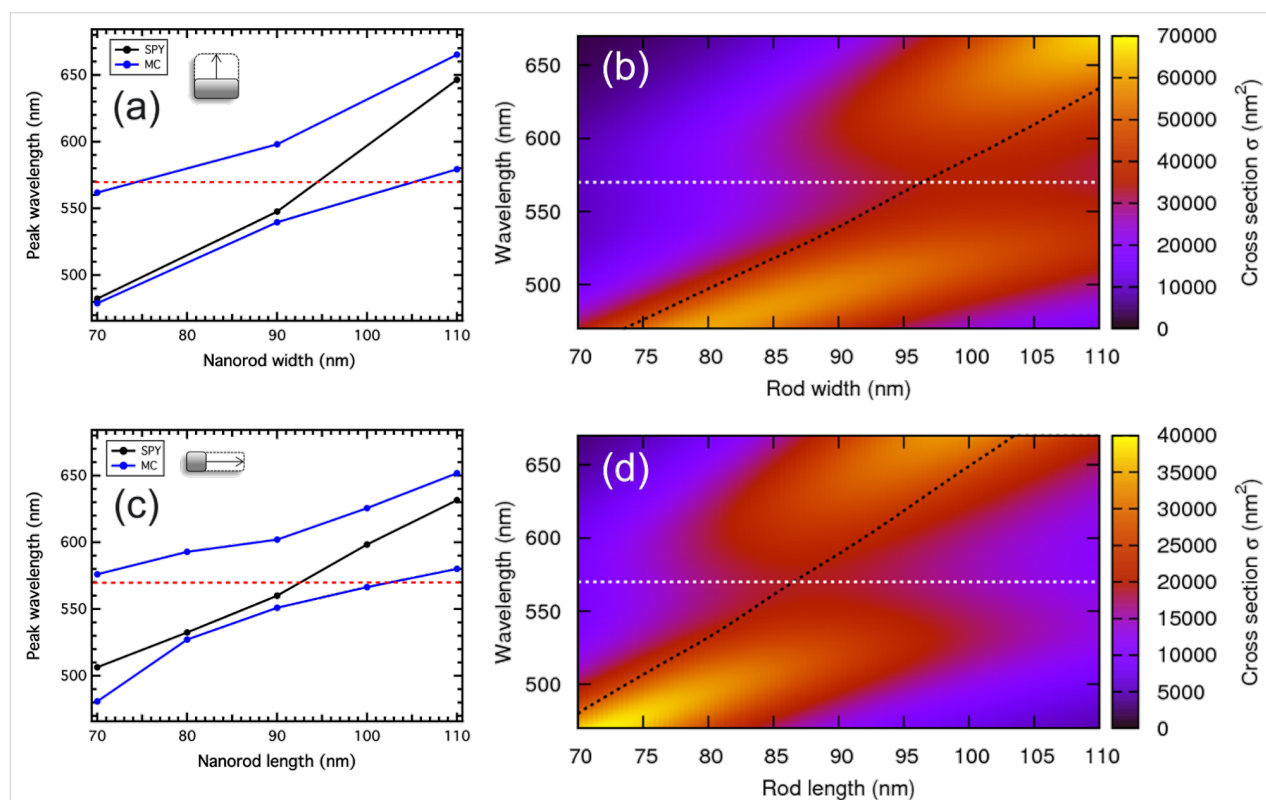
Figure 3: (a) Experimental spectral evolution of the transverse (90°) plasmonic peak as a function of the rod width for a fixed length of 110 nm. (b) Calculated extinction cross-section map for the corresponding ellipsoids as a function of the wavelength and the ellipsoid width. (c) Experimental spectral evolution of the longitudinal (0°) plasmonic peak as a function of the rod length for a fixed width of 70 nm. (d) Calculated extinction cross-section map for the corresponding ellipsoids as a function of the wavelength and the ellipsoid length.

dinal plasmonic resonances, one can observe a clear splitting of the plasmonic mode, centered at the intersection of the MC absorption band and the plasmonic resonance in the SPY isomer. This anti-crossing behavior is a signature of a strong coupling regime. To support these experimental results, analytical calculations were made. The polarizability of the silver nanorod is calculated using a prolate spheroid in the dipole approximation:

$$\alpha_{\parallel,\perp} = 3\varepsilon_2 V_p \frac{\varepsilon_1 + \varepsilon_2}{3\varepsilon_2 + 3L_{\parallel,\perp}(\varepsilon_1 + \varepsilon_2)}, \quad (1)$$

where $\parallel$ and $\perp$ refer to the polarization of the incoming light, V_p is the volume of the particle, ε_1 is silver permittivity, ε_2 is the permittivity of the host medium, deduced by the ellipsometric measurements; while $L_{\parallel}$ and $L_{\perp}$ are geometrical factors given by:

$$L_{\parallel} = \frac{1-e^2}{e^2}\left(-1 + \frac{1}{2e}\ln\frac{1+e}{1-e}\right);$$
$$L_{\perp} = \frac{1-L_{\parallel}}{2}. \quad (2)$$

Here e is the eccentricity calculated as $e = \sqrt{1-\rho^2}$, with ρ the aspect ratio of the spheroid.

In order to account for the energy-shifting part of the retardation effect and the radiative loss, which are missing in the model, the equation was modified in a similar way as in [24] which led to Equation 3.

Here $\theta = 2\pi\omega/c$, while $\Xi = 1.4$ is a phenomenological weighting factor we introduced to obtain an optimal fit of the experimental results.

The results are presented in Figure 3b and 3d for ellipsoids presenting a fixed 110 nm length and varying widths and for ellipsoids presenting a fixed 70 nm width and varying lengths, respectively. On each map, the dashed black curve represents the spectral position of the maximum of the extinction cross-section of the ellipsoids in the SPY medium (the corresponding maps are not shown here) and the horizontal dashed white line corresponds to the MC absorption band. On both maps, a clear anti-crossing is then observed when the black dashed curves cross the white dashed lines. Indeed, in Figure 3b, the anti-crossing appears for a rod width of 95 nm and in Figure 3d, it appears for a rod length of about 85 nm. These values are in agreement with the experimental values, specially knowing that the given geometrical parameters of the nanorods, mainly width and length, correspond to the designed values. Indeed, only few images have been recorded by electronic microscopy after the nanofabrication process and small variations between the designed and the real sizes can occur.

To confirm the observation of a strong coupling regime, we compared the linewidths of the hybrid modes obtained experimentally and theoretically for 70 nm wide and 90 nm long nanorods in the MC isomer (Figure 4). The incident polariza-

$$\alpha = 3\varepsilon_2 V_p \frac{1 - 0.1(\varepsilon_1 + \varepsilon_2)\theta^2/4}{3\varepsilon_2 + \dfrac{3L_{\parallel,\perp}(\varepsilon_1 + \varepsilon_2)}{\varepsilon_1} + \varepsilon_2 - (0.1\varepsilon_1 + \varepsilon_2)\theta^2/4 - \Xi\varepsilon_2^2\theta^4 - i(2/3)\varepsilon_3^{3/2}\theta^3} \quad (3)$$
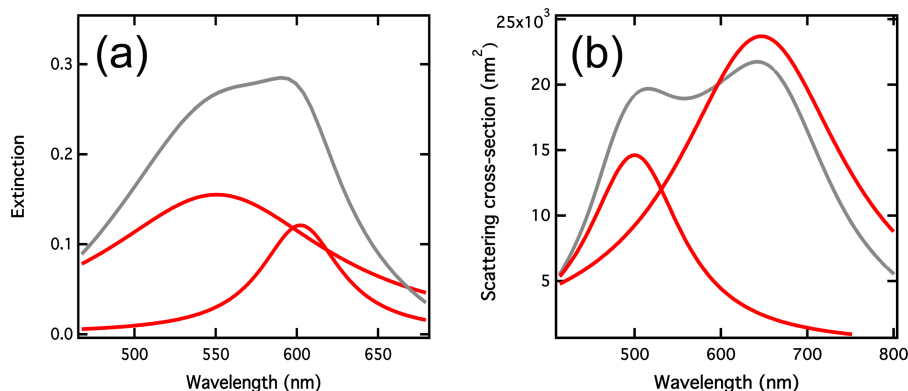

Figure 4: (a) Extinction spectrum (grey curve) recorded with a 70 nm wide and 90 nm long nanorod array covered with the MC isomer. The red curves correspond to the Lorentzian fitted peaks. (b) Extinction cross-section and the fitted peak decomposition, calculated for an ellipsoid of the same dimensions.

tion has been chosen to be aligned to the nanorod long axis (0°). Figure 4a shows the extinction spectrum (grey curve) recorded experimentally and the corresponding Lorentzian fitted peaks (red curves). The peaks are located at 551 and 602 nm and their spectral width are equal to 129 and 50 nm, leading to linewidths of 527 and 171 meV. Figure 4b shows the scattering cross-section spectrum obtained with our analytical model for a single ellipsoid in the MC isomer. The fitted peaks are located at 500 and 647 nm, indicating a Rabi splitting of 560 meV. This large value allowed us to conclude the observation of a strong coupling regime at the single nanorod level. Moreover, the spectral widths of the theoretical peaks are equal to 132 and 235 nm, leading to linewidths of 655 and 697 meV. This difference in the hybrid mode linewidths has already been observed for a gold nanogroove arrays coated with a J-aggregate dye film [25]. In this work, they observed different damping rates for the hybrid modes attributed to the interplay between the coherent dipole coupling between exciton and plasmon and the incoherent exchange of photon energy between both systems. This can happen when the damping of both separate oscillators is different, which is our case with the plasmonic resonance and the MC molecular exciton. The large linewidth difference we experimentally obtain for both hybrid modes is also probably due to the geometry dispersion in the nanorod array.

Conclusion

In conclusion, we observed a polarization-dependent strong coupling between silver nanorods and the excited state of photochromic molecules. By properly designing the nanorods, the strong coupling can happen either with the longitudinal plasmonic mode, or with the transverse plasmonic mode, or even both. We also proved the existence of a strong coupling regime when the plasmonic resonance coincides with the molecular transition. Moreover, the calculations were in good agreement with our observations. Thus, we proved that the incident polarization allows for control of the plasmonic hybridization and the spectral position of the nanorod plasmon modes. This plasmonic hybridization is known to be reversible and can be enhanced by application of better resonators. As a perspective future application, this polarization-dependent strong coupling could be a prime interest for nanorods coupled to different emitters such as those in [17]. Indeed, in the anti-crossing region, the strong local field produced by the plasmonic resonance could be optically switched on and off, resulting in the controlled enhancement of the photoluminescence produced by the emitter.

ORCID® iDs

Alessandro Veltri - https://orcid.org/0000-0002-2256-9439
Anne-Laure Baudrion - https://orcid.org/0000-0001-9751-9957

References

1. Li, M.; Cushing, S. K.; Wu, N. *Analyst* **2015,** *140,* 386–406. doi:10.1039/c4an01079e
2. Curto, A. G.; Volpe, G.; Taminiau, T. H.; Kreuzer, M. P.; Quidant, R.; van Hulst, N. F. *Science* **2010,** *329,* 930–933. doi:10.1126/science.1191922
3. Viste, P.; Plain, J.; Jaffiol, R.; Vial, A.; Adam, P. M.; Royer, P. *ACS Nano* **2010,** *4,* 759–764. doi:10.1021/nn901294d
4. Abadeer, N. S.; Murphy, C. J. *J. Phys. Chem. C* **2016,** *120,* 4691–4716. doi:10.1021/acs.jpcc.5b11232
5. Berthelot, J.; Bouhelier, A.; Huang, C.; Margueritat, J.; Colas-des-Francs, G.; Finot, E.; Weeber, J.-C.; Dereux, A.; Kostcheev, S.; Ibn El Ahrach, H.; Baudrion, A.-L.; Plain, J.; Bachelot, R.; Royer, P.; Wiederrecht, G. P. *Nano Lett.* **2009,** *9,* 3914–3921. doi:10.1021/nl902126z
6. Nguyen, M.; Sun, X.; Lacaze, E.; Winkler, P. M.; Hohenau, A.; Krenn, J. R.; Bourdillon, C.; Lamouri, A.; Grand, J.; Lévi, G.; Boubekeur-Lecaque, L.; Mangeney, C.; Félidj, N. *ACS Photonics* **2015,** *2,* 1199–1208. doi:10.1021/acsphotonics.5b00280
7. Liu, W.; Lee, B.; Naylor, C. H.; Ee, H.-S.; Park, J.; Johnson, A. T. C.; Agarwal, R. *Nano Lett.* **2016,** *16,* 1262–1269. doi:10.1021/acs.nanolett.5b04588
8. Fang, Z.; Thongrattanasiri, S.; Schlather, A.; Liu, Z.; Ma, L.; Wang, Y.; Ajayan, P. M.; Nordlander, P.; Halas, N. J.; García de Abajo, F. J. *ACS Nano* **2013,** *7,* 2388–2395. doi:10.1021/nn3055835
9. Nakagaki, R.; Kobayashi, T.; Nakamura, J.; Nagakura, S. *Bull. Chem. Soc. Jpn.* **1977,** *50,* 1909–1912. doi:10.1246/bcsj.50.1909
10. Waldeck, D. H. *J. Mol. Liq.* **1993,** *57,* 127–148. doi:10.1016/0167-7322(93)80051-v
11. Nakamura, S.; Irie, M. *J. Org. Chem.* **1988,** *53,* 6136–6138. doi:10.1021/jo00261a035
12. Smith, G. P. *J. Mater. Sci.* **1967,** *2,* 139–152. doi:10.1007/bf00549573
13. Higgins, S. *Chim. Oggi* **2003,** *21,* 63–67.
14. Spangenberg, A.; Métivier, R.; Yasukuni, R.; Shibata, K.; Brosseau, A.; Grand, J.; Aubard, J.; Yu, P.; Asahi, T.; Nakatani, K. *Phys. Chem. Chem. Phys.* **2013,** *15,* 9670–9678. doi:10.1039/c3cp50770j
15. Schwartz, T.; Hutchison, J. A.; Genet, C.; Ebbesen, T. W. *Phys. Rev. Lett.* **2011,** *106,* 196405. doi:10.1103/physrevlett.106.196405
16. Baudrion, A.-L.; Perron, A.; Veltri, A.; Bouhelier, A.; Adam, P.-M.; Bachelot, R. *Nano Lett.* **2013,** *13,* 282–286. doi:10.1021/nl3040948
17. Zhou, X.; Wenger, J.; Viscomi, F. N.; Le Cunff, L.; Béal, J.; Kochtcheev, S.; Yang, X.; Wiederrecht, G. P.; Colas des Francs, G.; Bisht, A. S.; Jradi, S.; Caputo, R.; Demir, H. V.; Schaller, R. D.; Plain, J.; Vial, A.; Sun, X. W.; Bachelot, R. *Nano Lett.* **2015,** *15,* 7458–7466. doi:10.1021/acs.nanolett.5b02962
18. Sasaki, K.; Nagamura, T. *Appl. Phys. Lett.* **1997,** *71,* 434–436. doi:10.1063/1.119571
19. Bellessa, J.; Bonnand, C.; Plenet, J. C.; Mugnier, J. *Phys. Rev. Lett.* **2004,** *93,* 036404. doi:10.1103/physrevlett.93.036404
20. Wurtz, G. A.; Evans, P. R.; Hendren, W.; Atkinson, R.; Dickson, W.; Pollard, R. J.; Zayats, A. V.; Harrison, W.; Bower, C. *Nano Lett.* **2007,** *7,* 1297–1303. doi:10.1021/nl070284m
21. Zengin, G.; Johansson, G.; Johansson, P.; Antosiewicz, T. J.; Käll, M.; Shegai, T. *Sci. Rep.* **2013,** *3,* 3074. doi:10.1038/srep03074
22. Väkeväinen, A. I.; Moerland, R. J.; Rekola, H. T.; Eskelinen, A.-P.; Martikainen, J.-P.; Kim, D.-H.; Törmä, P. *Nano Lett.* **2014,** *14,* 1721–1727. doi:10.1021/nl4035219

23. Hakala, T. K.; Toppari, J. J.; Kuzyk, A.; Pettersson, M.; Tikkanen, H.; Kunttu, H.; Törmä, P. *Phys. Rev. Lett.* **2009,** *103,* 053602. doi:10.1103/physrevlett.103.053602

24. Kuwata, H.; Tamaru, H.; Esumi, K.; Miyano, K. *Appl. Phys. Lett.* **2003,** *83,* 4625–4627. doi:10.1063/1.1630351

25. Wang, W.; Vasa, P.; Pomraenke, R.; Vogelgesang, R.; De Sio, A.; Sommer, E.; Maiuri, M.; Manzoni, C.; Cerullo, G.; Lienau, C. *ACS Nano* **2014,** *8,* 1056–1064. doi:10.1021/nn405981k

Silencing the second harmonic generation from plasmonic nanodimers: A comprehensive discussion

Jérémy Butet[*], Gabriel D. Bernasconi and Olivier J. F. Martin

Abstract

The silencing of the second harmonic generation process from plasmonic nanostructures corresponds to the limited far-field second harmonic radiation despite the huge fundamental electric field enhancement in the interstice between two plasmonic nanoparticles forming a nanodimer. In this article, we report a comprehensive investigation of this effect using a surface integral equation method. Various geometries are considered, including nanoantennas with cylindrical and rectangular arms as well as nanodimers with surface defects. The existence of the silencing of the second harmonic generation from plasmonic nanogaps is first confirmed, and the problem of the origin of the second harmonic light from these plasmonic nanostructures is addressed in detail. Our results show that the distribution of the second harmonic sources, especially on the arm sides, plays a non-negligible role in the overall second harmonic emission. This contribution is induced by retardation effects at the pump wavelength and results in a dipolar second harmonic emission.

Introduction

Due to their high density of free electrons, plasmonic nanostructures offer the possibility to concentrate light into subwavelength regions [1,2]. The collective oscillations of these electrons in a given plasmonic nanostructure are called localized surface plasmon resonances (LSPRs) [3-5]. The high electric field enhancement associated with the optical excitation of such a resonance has been proven to be an important, practical way to control light–matter interaction down to the nanoscale [3-5]. To even further enhance this interaction, it was proposed to couple two plasmonic nanostructures by bringing them close to each other, resulting in a nanoantenna made of two arms separated by a gap of a few nanometers [6]. Several methods have

been developed for the fabrication of these nanoantennas, including both top-down and bottom-up approaches [7]. The challenge of loading the interstice between the two arms with different materials, including single molecules [8], quantum dots [9], and nonlinear nanocrystals [10-12], has been taken up, enabling a strong control of light–matter interaction in these hybrid nanostructures.

At the same time, it was proposed to use nanoantennas for the observation of nonlinear optical processes at the nanoscale [13]. The basic idea in nonlinear plasmonics is to take advantage of the huge field enhancement associated with the excitation of LSPR in nanoantennas to obtain a high nonlinear conversation rate, despite very small interaction volumes (much smaller than μm^3) [13]. This strategy has been proven to be very successful for various nonlinear optical processes, such as multiphoton photoluminescence [6], third harmonic generation [14,15], and four-wave mixing [16,17]. However, the enhancement of the nonlinear conversion rate for second harmonic generation (SHG) was found to be surprisingly low [18,19]. This is in contrast with the observations made for third order nonlinear optical processes. In that context, Berthelot et al. reported for the first time what they called the "silencing" of SHG from nanogaps, which could explain the low SHG observed experimentally [18]. These authors measured the SHG from the interstice between two gold nanowires with various gap sizes. They observed that the SHG does not increase as the gap between the two nanowires decreases, despite an increase of the fundamental field enhancement. Their experimental observations were supported by numerical results demonstrating that the SHG from nanogaps is not efficiently radiated out. Indeed, due to the specific selection rules of SHG [20], the second harmonic sources standing on each side of the nanogap are out of phase, i.e., point in opposite directions at a given time, and tend to cancel out in the far-field. The problem of the "silencing" of the SHG has also been addressed in the case of connected gold nanodimers by comparing the evolution of the SHG with that of the two-photon photoluminescence [21]. It was shown that, although these two nonlinear optical processes involved two fundamental photons, they did not have the same incident polarization dependence, revealing distinct behaviors as the fundamental near-field distribution changes. The role of the antenna modes at the second harmonic wavelength in the enhancement of the SHG has also been addressed for symmetric and asymmetric antennas, showing that the SHG is strongly modified by a gap displacement with respect to the antenna center [22]. In any case, the "silencing" of SHG from gold nanoantennas has not been addressed in detail so far. For example, the spatial origin of the second harmonic signal collected from plasmonic nanoantennas has not been clearly identified.

In this article, we report a comprehensive discussion of the SHG from gold dimers focusing on the implications of the silencing effect. The linear and second harmonic responses of the dimers have been computed using a surface integral equations method. The first dimers considered in this article are made of cylindrical nanorods with hemispherical extremities and various gap distances. In order to unveil the role of the silencing effect, computations of the SHG considering only the surface second harmonic sources on specific parts of the dimers are also presented. The meshes describing the dimers are then slightly deformed to mimic the presence of defects on the nanorod surfaces. Finally, gold dimers made of rectangular arms are considered.

Numerical Methods

The linear optical response was calculated using a surface integral formulation [23,24]. All the nanostructures are embedded in a homogeneous medium with refractive index $n = 1.33$, corresponding to water. The dielectric constants of gold are taken from experimental data at both the fundamental and second harmonic wavelengths [25]. For the SHG computations, the linear surface currents are used for the evaluation of the fundamental electric fields just below the gold surfaces and then used for the calculation of the surface SH polarization [26,27]. Only the $\chi_{surf,nnn}$ component of the surface tensor (where *n* denotes the component normal to the surface) is considered. Recent experimental results show that this term dominates the surface response of metallic nanoparticles [28,29]. Note that other contributions to the SH signal, namely the $\chi_{surf,ttn}$ component of the surface tensor (where *t* denotes the component tangential to the surface) and bulk contribution, are theoretically allowed but these terms contribute only weakly to the total SH wave [28,29]. The SH surface currents are obtained by solving the surface integral equation formulation taking into account the nonlinear polarization and enforcing the boundary conditions at the nanostructure surfaces [30]. As the linear surface currents, the SH surface currents are expanded on Rao–Wilton–Glisson (RWG) basis functions. The expansion coefficients are found by applying the method of moments with Galerkin's testing [23,24]. A Poggio–Miller–Chang–Harrington–Wu–Tsai formulation is used to ensure accurate solutions even at resonant conditions [23,24]. The SH electric field is then deduced from the SH surface currents [26,27].

Results and Discussion
Gold dimers made of cylindrical nanorods

We first consider the case of dimers made of gold nanorods, see Figure 1a. The diameter of the nanorods is 40 nm and their length is 85 nm. The smallest considered gap between the nanorods is 5 nm. Such small gaps can easily be achieved using capillary assembly with optimized templates, for example [7].

The linear optical properties of gold dimers with gaps of 5 nm, 20 nm, and 60 nm are considered first. The scattered intensity is shown as a function of the incident wavelength in Figure 1b. For comparison, the scattering from a single nanorod is also shown as a dashed line. In all the scattering spectra, one can observe a peak corresponding to the excitation of a LSPR. This LSPR corresponds to the bonding dipolar mode, resulting from the in-phase coupling of the longitudinal dipolar modes supported by each nanorod. As expected, this mode redshifts as the gap between the nanorods decreases, i.e., as the coupling increases [2]. As a consequence of this coupling, the bonding dipolar mode for a dimer always arises at a longer wavelength than the longitudinal electric dipole mode of the corresponding single nanorod. On the other hand, the scattering efficiency from the single nanorod is lower than that of the considered dimers, as shown in Figure 1b.

We now turn our attention to the SHG from the same gold dimers and a single nanorod. Figure 2c shows the far-field second harmonic intensity as a function of the fundamental wavelength for gold dimers with gaps of 5 nm, 20 nm, and 60 nm and a single nanorod. For each nanostructure, a maximum of the second harmonic scattering is observed when the fundamental wavelength is close to the resonant wavelength of the bonding dipolar mode. This effect is well-known and has been reported in various publications – it has been established, as a cornerstone of nonlinear plasmonics, that the nonlinear optical responses of plasmonic nanostructures is boosted by LSPRs [31,32]. Indeed, a strong near-field enhancement is associated with the collective oscillations of the conduction electrons, resulting in an increased nonlinear polarization and then in an increase of the nonlinear optical conversion for example. It is however apparent in Figure 1c that the maximum of SHG is not directly related to the gap size as one would expect. To understand and explain this phenomenon, the near-field intensity enhancement is now discussed.

The fundamental intensity enhancements for the gold dimers have been evaluated at the dimer extremities, respectively in the nanogap, and are shown in Figure 2 as a function of the fundamental wavelength, respectively in panels (a) and (b). In order to track the SH sources at the surface of the different nanostructures, the intensity enhancement is always evaluated 2.5 nm away from the nearest surface, i.e., not at the center of the gaps for $g = 20$ nm and 60 nm. In this context, it is worth noting that the fundamental electric field used to compute the SH sources is directly evaluated from the linear surface currents. Furthermore, the boundary conditions of the electromagnetic field are linear and a stronger fundamental electric field in the gap leads to stronger SH sources in this area. At both the nanodimer extremities and the nanogap, the field enhancement increases as the
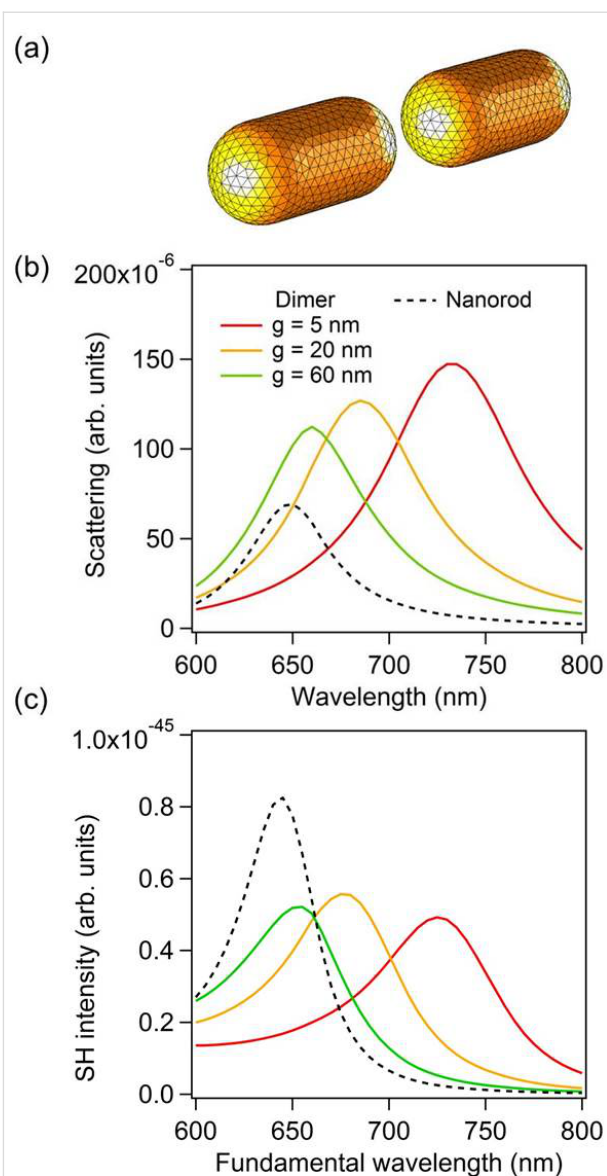
Figure 1: (a) Example of one mesh used for the simulations. The nanorod overall length and diameter are 85 nm and 40 nm, respectively. In the present case, the gap *g* is 20 nm. (b) Scattering intensity as a function of the wavelength for nanodimers with gaps *g* = 5 nm, 20 nm, and 60 nm as well as for a single nanorod. (c) Second harmonic intensity as a function of the wavelength for nanodimers with gaps *g* = 5 nm, 20 nm, and 60 nm as well as for a single nanorod.

gap between the nanorods decreases, although the evolution of the intensity enhancement is more dramatic in the gap (note the different scales in Figure 2a,b). Indeed, the intensity enhancement in the gap increases from ≈300 for a gap of 60 nm to ≈8000 for a gap $g = 5$ nm. From this last observation, one can naively think that the SHG would be much higher for the smallest gap, due to the strong near-field intensity. However, this is not the behavior observed in Figure 1b. Indeed, the far-field SH intensity tends to increase with the gap between the nanorods. This effect is known as the "silencing" of the SHG,

Figure 2: (a) Enhancement of the fundamental intensity evaluated at the nanorod extremities (2.5 nm away from the surface) as a function of the wavelength for nanodimers with gaps *g* = 5 nm, 20 nm, and 60 nm as well as for a single nanorod. (b) Enhancement of the fundamental intensity evaluated at the gap center as a function of the wavelength for nanodimers with gaps *g* = 5 nm, 20 nm, and 60 nm as well as for a single nanorod. The field enhancement is evaluated at 2.5 nm away from the nearest surface.

meaning that the far-field SH intensity decreases despite an increase of the fundamental near-field intensity.

This particular behavior is explained by the specific symmetry properties of SHG. The second harmonic sources standing at each side of the nanogaps are out of phase, i.e., pointing towards each other, resulting in a vanishing SHG in the electric dipole approximation. As a consequence, the far-field SH radiation decreases when the distance between the SH sources shrinks. While this is the standard interpretation of the silencing effect, there are several points that need to be clarified. The first one is the role of the resonant wavelength of the bonding dipolar mode. The SHG from centrosymmetric nanostructures is induced by retardation effects, i.e., the field variation across the structure both at the excitation and emission stage, which in-

creases as the fundamental and SH wavelengths decrease [33,34]. For this reason, the redshift of the bonding dipolar mode observed for small gaps between the nanorods is not beneficial for a high SHG. Please note that for the range of SH wavelengths considered in this study, the imaginary part of the dielectric constant of gold is constant and does not modify the losses at the SH wavelength. Figure 3 shows the maximal SHG induced by the resonant excitation of the bonding dipolar mode at the fundamental wavelength for gaps ranging from 5 nm to 400 nm. For the largest gaps, the bonding dipolar mode is spectrally close to the longitudinal mode of the single nanorod and does not shift with gap size variations. Thus, in the large gap case, the variation of the SHG is due to interference of the fields radiated by each nanorod, which simply changes with the distance between the arms since the LSPR does not shift. Quite surprisingly, the highest SHG is obtained for the largest gaps, despite a weak enhancement of the fundamental intensity in the gap between the nanorods. The far-field second harmonic intensity is identical to that of the single nanorod for a gap of 130 nm and is more than twice that of the single nanorod for gaps larger than 220 nm, see Figure 3. Note that, if the local field enhancement is negligible (equal to unity), then the highest possible SHG from a dimer is 4 times that of the single nanorod, since SHG is a coherent optical process. The slight modulation of the second harmonic intensity observed for gaps larger than 220 nm is attributed to the radiative coupling between the nanorods, which slightly modifies the fundamental near-field enhancement as the distance between the nanorods varies. Having discussed the role of the resonant wavelength with respect to the silencing of the SHG, we now turn our attention to the second important point: the position of the second harmonic sources and their contribution to the overall far-field SH signal.
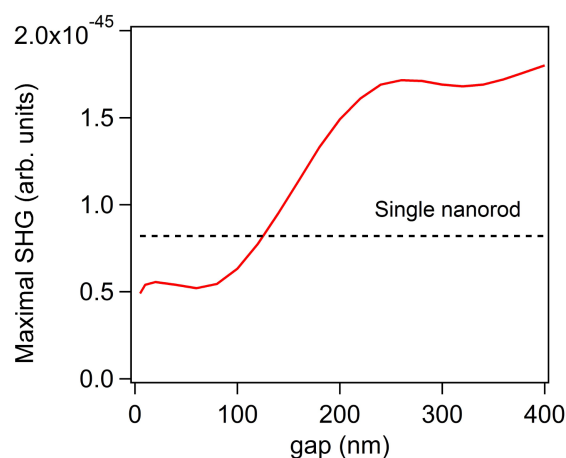

Figure 3: Maximal second harmonic generation (SHG) as a function of the gap between the nanorods. The maximal SHG has been extracted from the second harmonic spectra, see Figure 1c for example. The SH intensity from a single nanorod is shown as a dotted black line.

Decomposition of the second harmonic sources

In this section, the important question of the relationship between the location of the second harmonic sources and their contributions to the overall far-field SH intensity is addressed. Indeed, the second harmonic sources are distributed over the entire gold nanodimer surface. It is clear that the second harmonic sources, i.e., the second harmonic surface polarization, are the strongest in the nanogaps, due to the huge fundamental field-enhancement in those locations. However, as discussed previously, these sources do not radiate efficiently into the far-field due to the silencing of the SHG and the link between the SH source locations and their contribution to the collected SH signal is still an open question. To address this point, we perform computations of the SHG from the gold dimers, limiting the surface covered with second harmonic sources. Note that the entire nanostructure is considered for the computations, meaning that the modal distribution is conserved at the SH wavelength, and only portions of the nonlinear surface polarization are suppressed, see Figure 4. Thus, the partial nonlinear sources still induce nonlinear currents over the entire structure, which can then scatter the SH field. Furthermore, to preserve the symmetry of the problem, the nonlinear surface polarization is identically suppressed for both arms. The percentages in Figure 4 indicate the length over which the nonlinear surface polarization is maintained. Note that the central region

of the nanodimer always has a non-vanishing surface SH polarization. The far-field SH intensity has been evaluated for various partial surface nonlinear polarizations (25%, 50%, 75%, and 100%) for a gap of 5 nm, Figure 5a, and a gap of 20 nm, Figure 5b. Removing the nonlinear polarization at the extremities of the nanorods increases slightly (g = 5 nm) or does not change (g = 20 nm) the SH emission, meaning that these SH sources do not really contribute to the far-field emission and can even interfere destructively with other sources. Considering the SH sources in the nanogap only (coverage of 25%), the far-field SH intensity drops by a factor 7 for a gap g = 5 nm and by a factor 10 for a gap g = 20 nm in comparison with the entire nonlinear polarization, emphasizing again the weak emission from this area, especially for small gaps. On the basis of these observations, one can conclude that the second harmonic sources on the side of the nanorods give an important contribution to the second harmonic radiation. At this point, it is worth reminding that the SHG from centrosymmetric nanostructures is induced by retardation effects. The phase variation of the incident wave induces one channel for the second harmonic emission, which corresponds to a second harmonic dipole along the propagation direction of the pump wave.

Influence of surface defects on the SHG

SHG from centrosymmetric nanostructures is forbidden in the electric dipole approximation and one can expect that SHG
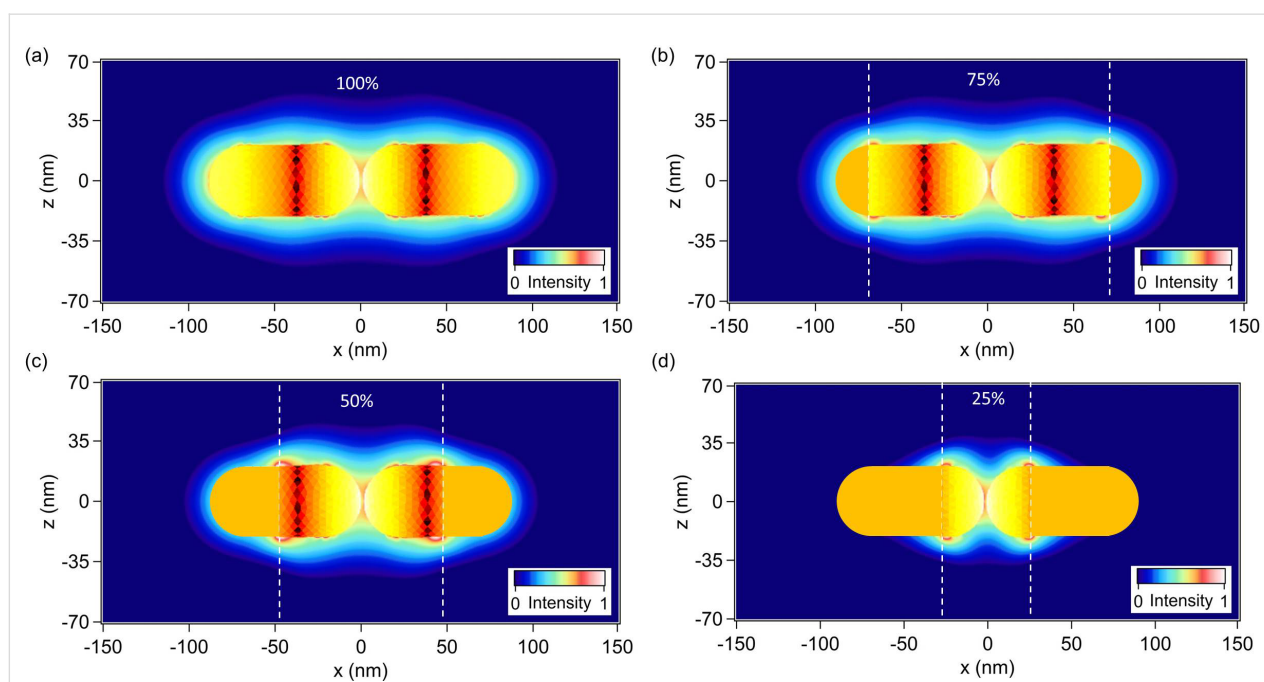
Figure 4: Normalized near-field distributions of the second harmonic electric field intensity close to the gold nanodimer with a gap g = 5 nm evaluated (a) for the entire surface nonlinear polarization and for (b–d) partial surface nonlinear polarizations. The percentages indicate the ratio between the length over which the surface nonlinear polarization is maintained and the total length of the nanorod. For example, 50% indicates that only half of the surface nonlinear polarization is considered as shown in panel (c). The same color scale is used for all the panels.

Figure 5: Far-field second harmonic intensity for the entire surface nonlinear polarization (100%) and for partial surface nonlinear polarizations. The percentages indicate the ratio between the length over which the surface nonlinear polarization does not vanish and the length of the nanorod, see Figure 4. The gap between the nanorods is 5 nm for the panel (a) and 20 nm for panel (b).

have been modified as follows. A few points over the mesh are first randomly selected. Each of these points and their nearest neighbors are then smoothly moved towards the interior of the structure, while the deformation is maximal at the selected point and vanishes a few nanometers away. As expected, the far-field second harmonic intensity increases due to the defects on the nanorod surfaces, see Figure 6. However, the second harmonic intensity increase is relatively modest, only 10%, meaning that the SHG is mainly due to the retardation effects for this range of nanorod sizes and deformations. This observation stands for the overall second harmonic emission, integrated over a sphere. Nonetheless, the centrosymmetry breaking induced by the defects modifies the selection rules. As a consequence, the second harmonic intensity does not vanish anymore in the forward and backward directions. This is an important observation from a practical point of view, since the second harmonic

Figure 6: (a) Mesh used for the dimers with defects. In this example, the gap is 20 nm. Far-field second harmonic intensity for a dimer made of perfect nanorods (solid lines) and with defects (dashed lines). The gap between the nanorods is 5 nm for panel (b) and 20 nm for panel (c).

would be sensitive to any centrosymmetry breaking [35,36]. As discussed in the previous sections, the centrosymmetry can be indeed broken by the retardation of the incident field, resulting in the excitation of a second harmonic dipole along the propagation direction of the incident planewave for example [33,34]. The second possibility is a centrosymmetry breaking induced by the nanoparticle shape [35,36]. Indeed, although important progress has been made in nanofabrication, it still impossible to fabricate nanostructures of perfect shape and, for real experiments, one must consider the influence of shape variations of the nanostructures on SHG. This issue has been thoroughly considered in the case of SHG from chemically synthetized plasmonic nanospheres in solution, revealing an interesting competition between the centrosymmetry breaking induced by the field variation and the nanoparticle shape [35,37-39]. To investigate this issue [40], the meshes describing the nanodimers

light is often collected in these two directions. Note that the case of a single defect located in the gap has been considered in a previous publication, showing the same behavior [36].

Gold dimers made of rectangular arms

In this last section, the case of gold dimers made of rectangular arms is considered, Figure 7a. The purpose is to show that the
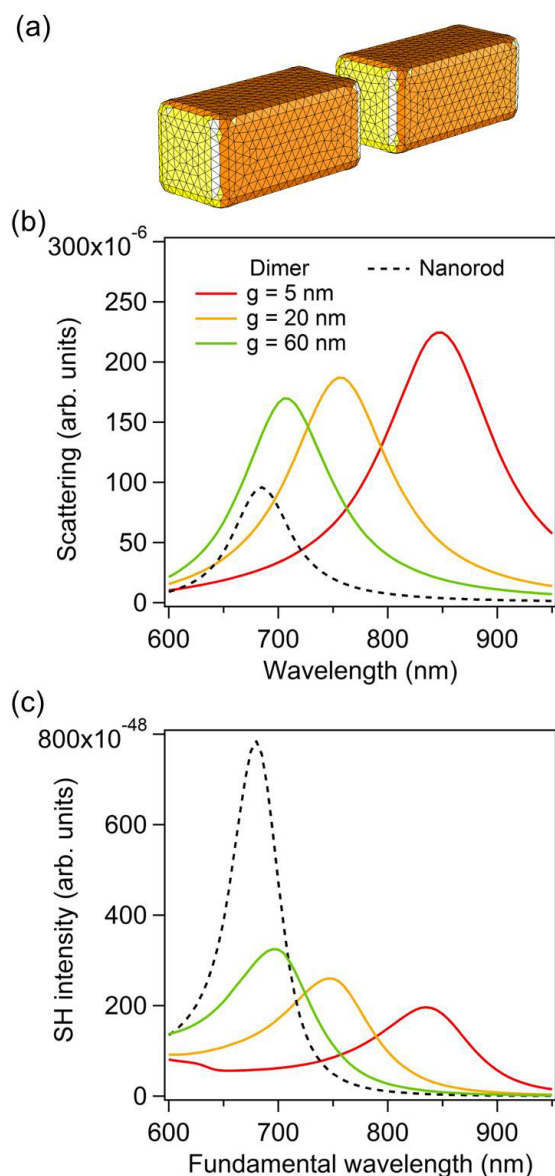

Figure 7: (a) Example of one mesh used for the simulations for the dimers with rectangular arms. The nanoparticle length is 85 nm and the height and width are 40 nm. In the present case, the gap *g* is 20 nm. (b) Scattering as a function of the wavelength for nanodimers with gaps *g* = 5 nm, 20 nm, and 60 nm as well as for a single nanoparticle. (c) Second harmonic intensity as a function of the wavelength for nanodimers with gaps *g* = 5 nm, 20 nm, and 60 nm as well as for a single nanorod.

observations made for cylindrical nanorods still stand for other geometries. Both geometries can be obtained with specific nanofabrication techniques. While cylindrical nanorods would be the building blocks of plasmonic nanoantennas made by capillary assembly, rectangular arms will be obtained with top-down fabrication techniques, such as nanolithography for example. The arm dimensions are similar to those of the cylindrical nanorods discussed previously; the arm length is 85 nm and its width and height are 40 nm. The scattering spectra for such gold dimers with gaps of 5 nm, 20 nm, and 60 nm are shown in Figure 7b, revealing a redshift of the LSPR as the gap between the arms decreases as expected. This redshift of the LSPR decreases the retardation effects, and then the maximal SHG, as the gap between both arms decreases, Figure 7c. Contrary to the cylindrical nanorods, the SHG continuously decreases while the gap increases from 5 nm to 60 nm. This difference is probably due to the gap geometry. Indeed, with rectangular arms, the near-field coupling is much stronger since flat surfaces result in higher charge interaction in the nanogap, and then in a larger LSPR shift. For the same gap variation, i.e., from 5 nm to 60 nm, the shift of the LSPR for the rectangular arms is twice that observed for cylindrical nanorods. Apart from the plasmon shift amplitudes, the near-field behavior is similar for the rectangular arms, i.e., a strong near-field enhancement is observed in the gap for the smallest gaps (Figure 8), meaning that the SHG from this kind of nanoantennas is also ruled by the "silencing effect". Finally, the original approach proposed in this article is applied to the nanoantennas with rectangular arms. Figure 9 shows the far-field second harmonic intensity considering all or some parts of the nonlinear surface polarization for gaps of 5 nm and 20 nm. As for the cylindrical nanorods, the results indicate that the second harmonic sources on the sides of the arms play a non-negligible role in the total second harmonic radiation. To summarize the results of this section, one can note that the geometry of the arms does not play a significant role, beyond the resonant wavelength, in the "silencing" of the SHG, which is intrinsic to the geometry of nanogaps. Of course, the "silencing" of the SHG can be reduced by designing non-centrosymmetric gaps, as the one observed in T-shaped nano-structures [41], V-shaped nanoantennas coupled to nanorods [42], and nanorod–nanodisk systems [43].

Conclusion

In conclusion, this article reports a comprehensive study of the "silencing" effect in the SHG from gold nanoantennas using a surface integral equation method. To investigate this phenomenon in detail, various geometries have been considered, including nanoantennas with cylindrical and rectangular arms, as well as surface defects. To quantify the "silencing" effect, a new numerical approach, in which only specific parts of the nonlinear surface polarization are considered, has been developed. The
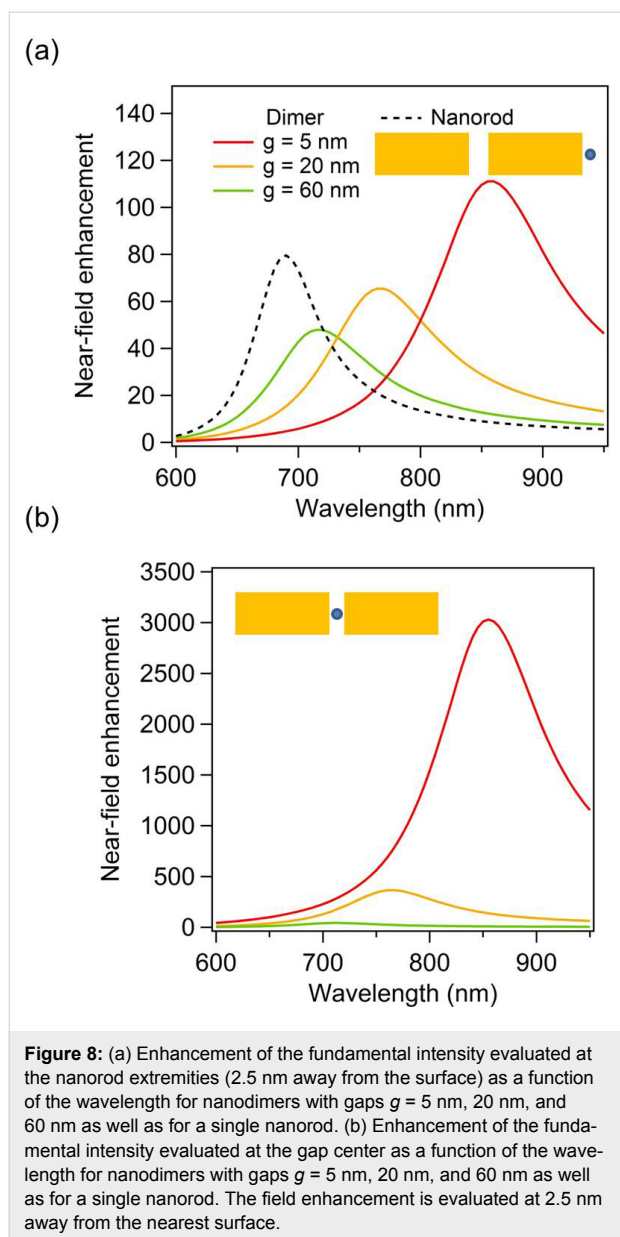
Figure 8: (a) Enhancement of the fundamental intensity evaluated at the nanorod extremities (2.5 nm away from the surface) as a function of the wavelength for nanodimers with gaps *g* = 5 nm, 20 nm, and 60 nm as well as for a single nanorod. (b) Enhancement of the fundamental intensity evaluated at the gap center as a function of the wavelength for nanodimers with gaps *g* = 5 nm, 20 nm, and 60 nm as well as for a single nanorod. The field enhancement is evaluated at 2.5 nm away from the nearest surface.

Figure 9: Far-field second harmonic intensity for the entire surface nonlinear polarization (100%) and for partial surface nonlinear polarizations as indicated in the legends. The percentages indicate the ratio between the length over which the surface nonlinear polarization is maintained and the length of the nanorod, as in Figure 4 for the nanodimers with cylindrical sections. The gap between the nanorods is 5 nm for the panel (a) and 20 nm for panel (b).

results show that only a small part of the overall SH emission indeed comes from the nanogaps, as a consequence of the "silencing" effect. The numerical results reported in this article clearly demonstrate that the SH sources located away from the gap, especially those on the arm sides, play a significant role in the overall SH emission. This point had not yet been discussed in the literature, probably because the "silencing" effect had first been reported for nanogaps between long arms [18], the properties of which are different from those of typical nanoantennas, resulting in different SH source distributions. The present discussion provides new directions for the design of efficient nanosources of SH light and meta-atoms for the fabrication of nonlinear metasurfaces [44-46], especially regarding the role of the SH source distribution over nanostructure sur-

faces. On the other hand, SHG was used to monitor the gap distance between gold nanoparticles and gold films [47]. The present study underlines the fact that the relationship between SHG and field enhancement in nanogaps is not straightforward and nonlinear plasmonic nanorulers need to be carefully calibrated [48]. Finally, it would be interesting to extend the present study to aluminum nanoantennas, since a significant bulk quadrupolar SHG is expected in this case [49].

Acknowledgements

References

1. Lal, S.; Link, S.; Halas, N. J. *Nat. Photonics* **2007,** *1,* 641–648. doi:10.1038/nphoton.2007.223

2. Halas, N. J.; Lal, S.; Chang, W.-S.; Link, S.; Nordlander, P. *Chem. Rev.* **2011,** *111,* 3913–3961. doi:10.1021/cr200061k

3. Kottmann, J. P.; Martin, O. J. F.; Smith, D. R.; Schultz, S. *New J. Phys.* **2000,** *2,* 27. doi:10.1088/1367-2630/2/1/327

4. Gramotnev, D. K.; Bozhevolnyi, S. I. *Nat. Photonics* **2010,** *4,* 83–91. doi:10.1038/nphoton.2009.282

5. Schuller, J. A.; Barnard, E. S.; Cai, W.; Jun, Y. C.; White, J. S.; Brongersma, M. L. *Nat. Mater.* **2010,** *9,* 193–204. doi:10.1038/nmat2630

6. Mühlschlegel, P.; Eisler, H.-J.; Martin, O. J. F.; Hecht, B.; Pohl, D. W. *Science* **2005,** *308,* 1607–1608. doi:10.1126/science.1111886

7. Flauraud, V.; Mastrangeli, M.; Bernasconi, G. D.; Butet, J.; Alexander, D. T.; Shahrabi, E.; Martin, O. J. F.; Brugger, J. *Nat. Nanotechnol.* **2017,** *12,* 73–80. doi:10.1038/nnano.2016.179

8. Aćimović, S. S.; Kreuzer, M. P.; González, M. U.; Quidant, R. *ACS Nano* **2009,** *3,* 1231–1237. doi:10.1021/nn900102j

9. Curto, A. G.; Volpe, G.; Taminiau, T. H.; Kreuzer, M. P.; Quidant, R.; van Hulst, N. F. *Science* **2010,** *329,* 930–933. doi:10.1126/science.1191922

10. Aouani, H.; Rahmani, M.; Navarro-Cía, M.; Maier, S. A. *Nat. Nanotechnol.* **2014,** *9,* 290–294. doi:10.1038/nnano.2014.27

11. Metzger, B.; Hentschel, M.; Schumacher, T.; Lippitz, M.; Ye, X.; Murray, C. B.; Knabe, B.; Buse, K.; Giessen, H. *Nano Lett.* **2014,** *14,* 2867–2872. doi:10.1021/nl500913t

12. Linnenbank, H.; Grynko, Y.; Förstner, J.; Linden, S. *Light: Sci. Appl.* **2016,** *5,* e16013. doi:10.1038/lsa.2016.13

13. Kauranen, M.; Zayats, A. V. *Nat. Photonics* **2012,** *6,* 737–748. doi:10.1038/nphoton.2012.244

14. Hentschel, M.; Utikal, T.; Giessen, H.; Lippitz, M. *Nano Lett.* **2012,** *12,* 3778–3782. doi:10.1021/nl301686x

15. Hanke, T.; Cesar, J.; Knittel, V.; Trügler, A.; Hohenester, U.; Leitenstorfer, A.; Bratschitsch, R. *Nano Lett.* **2012,** *12,* 992–996. doi:10.1021/nl2041047

16. Danckwerts, M.; Novotny, L. *Phys. Rev. Lett.* **2007,** *98,* 026104. doi:10.1103/PhysRevLett.98.026104

17. Harutyunyan, H.; Volpe, G.; Quídant, R.; Novotny, L. *Phys. Rev. Lett.* **2012,** *108,* 217403. doi:10.1103/PhysRevLett.108.217403

18. Berthelot, J.; Bachelier, G.; Song, M.; Rai, P.; Colas des Francs, G.; Dereux, A.; Bouhelier, A. *Opt. Express* **2012,** *20,* 10498–10508. doi:10.1364/OE.20.010498

19. Slablab, A.; Le Xuan, L.; Zielinski, M.; de Wilde, Y.; Jacques, V.; Chauvat, D.; Roch, J.-F. *Opt. Express* **2012,** *20,* 220–227. doi:10.1364/OE.20.000220

20. Butet, J.; Brevet, P.-F.; Martin, O. J. F. *ACS Nano* **2015,** *9,* 10545–10562. doi:10.1021/acsnano.5b04373

21. Wang, J.; Butet, J.; Baudrion, A.-L.; Horrer, A.; Leveque, G.; Martin, O. J. F.; Meixner, A. J.; Fleischer, M.; Adam, P. M.; Horneber, A.; Zhang, D. *J. Phys. Chem. C* **2016,** *120,* 17699–17710. doi:10.1021/acs.jpcc.6b04850

22. de Ceglia, D.; Vincenti, M. A.; de Angelis, C.; Locatelli, A.; Haus, J. W.; Scalora, M. *Opt. Express* **2015,** *23,* 1715–1729. doi:10.1364/OE.23.001715

23. Kern, A. M.; Martin, O. J. F. *Nano Lett.* **2011,** *11,* 482–487. doi:10.1021/nl1032588

24. Kern, A. M.; Martin, O. J. F. *J. Opt. Soc. Am. A* **2009,** *26,* 732–740. doi:10.1364/JOSAA.26.000732

25. Johnson, P. B.; Christy, R. W. *Phys. Rev. B* **1972,** *6,* 4370–4379. doi:10.1103/PhysRevB.6.4370

26. Mäkitalo, J.; Suuriniemi, S.; Kauranen, M. *Opt. Express* **2011,** *19,* 23386–23399. doi:10.1364/OE.19.023386

27. Butet, J.; Gallinet, B.; Thyagarajan, K.; Martin, O. J. F. *J. Opt. Soc. Am. B* **2013,** *30,* 2970–2979. doi:10.1364/JOSAB.30.002970

28. Wang, F. X.; Rodríguez, F. J.; Albers, W. M.; Ahorinta, R.; Sipe, J. E.; Kauranen, M. *Phys. Rev. B* **2009,** *80,* 233402. doi:10.1103/PhysRevB.80.233402

29. Bachelier, G.; Butet, J.; Russier-Antoine, I.; Jonin, C.; Benichou, E.; Brevet, P.-F. *Phys. Rev. B* **2010,** *82,* 235403. doi:10.1103/PhysRevB.82.235403

30. Heinz, T. F. Second-Order Nonlinear Optical Effects at Surfaces and Interfaces. In *Nonlinear Surface Electromagnetic Phenomena;* Ponath, H.-E.; Stegeman, G. I., Eds.; Elsevier: Amsterdam, Netherlands, 1991; Vol. 29, pp 353–416. doi:10.1016/B978-0-444-88359-9.50011-9

31. Hubert, C.; Billot, L.; Adam, P.-M.; Bachelot, R.; Royer, P.; Grand, J.; Gindre, D.; Dorhenoo, K. D.; Fort, A. *Appl. Phys. Lett.* **2007,** *90,* 181105. doi:10.1063/1.2734503

32. Kim, M.-K.; Sim, H.; Yoon, S. J.; Gong, S.-H.; Ahn, C. W.; Cho, Y.-H.; Lee, Y.-H. *Nano Lett.* **2015,** *15,* 4102–4107. doi:10.1021/acs.nanolett.5b01204

33. Dadap, J. I.; Shan, J.; Eisenthal, K. B.; Heinz, T. F. *Phys. Rev. Lett.* **1999,** *83,* 4045–4048. doi:10.1103/PhysRevLett.83.4045

34. Dadap, J. I.; Shan, J.; Heinz, T. F. *J. Opt. Soc. Am. B* **2004,** *21,* 1328–1347. doi:10.1364/JOSAB.21.001328

35. Nappa, J.; Revillod, G.; Russier-Antoine, I.; Benichou, E.; Jonin, C.; Brevet, P. F. *Phys. Rev. B* **2005,** *71,* 165407. doi:10.1103/PhysRevB.71.165407

36. Butet, J.; Thyagarajan, K.; Martin, O. J. F. *Nano Lett.* **2013,** *13,* 1787–1792. doi:10.1021/nl400393e

37. Russier-Antoine, I.; Jonin, C.; Nappa, J.; Benichou, E.; Brevet, P.-F. *J. Chem. Phys.* **2004,** *120,* 10748. doi:10.1063/1.1737733

38. Nappa, J.; Russier-Antoine, I.; Benichou, E.; Jonin, C.; Brevet, P.-F. *Chem. Phys. Lett.* **2005,** *415,* 246–250. doi:10.1016/j.cplett.2005.08.143

39. Nappa, J.; Russier-Antoine, I.; Benichou, E.; Jonin, C.; Brevet, P.-F. *J. Chem. Phys.* **2006,** *125,* 184712. doi:10.1063/1.2375095

40. Trügler, A.; Tinguely, J.-C.; Krenn, J. R.; Hohenau, A.; Hohenester, U. *Phys. Rev. B* **2011,** *83,* 081412. doi:10.1103/PhysRevB.83.081412

41. Canfield, B. K.; Husu, H.; Laukkanen, J.; Bai, B. F.; Kuittinen, M.; Turunen, J.; Kauranen, M. *Nano Lett.* **2007,** *7,* 1251–1255. doi:10.1021/nl0701253

42. Celebrano, M.; Wu, X.; Baselli, M.; Großmann, S.; Biagioni, P.; Locatelli, A.; De Angelis, C.; Cerullo, G.; Osellame, R.; Hecht, B.; Duò, L.; Ciccacci, F.; Finazzi, M. *Nat. Nanotechnol.* **2015,** *10,* 412–417. doi:10.1038/nnano.2015.69

43. Gennaro, S. D.; Rahmani, M.; Giannini, V.; Aouani, H.; Sidiropoulos, T. P. H.; Navarro-Cía, M.; Maier, S. A.; Oulton, R. F. *Nano Lett.* **2016,** *16,* 5278–5285. doi:10.1021/acs.nanolett.6b02485

44. Czaplicki, R.; Husu, H.; Siikanen, R.; Mäkitalo, J.; Kauranen, M. *Phys. Rev. Lett.* **2013,** *110,* 093902. doi:10.1103/PhysRevLett.110.093902

45. Keren-Zur, S.; Avayu, O.; Michaeli, L.; Ellenbogen, T. *ACS Photonics* **2016,** *3,* 117–123. doi:10.1021/acsphotonics.5b00528

46. Yang, K.-Y.; Verre, R.; Butet, J.; Yan, C.; Antosiewicz, T. J.; Käll, M.; Martin, O. J. F. *Nano Lett.* **2017,** *17,* 5258–5263. doi:10.1021/acs.nanolett.7b01412

47. Shen, S.; Meng, L.; Zhang, Y.; Han, J.; Ma, Z.; Hu, S.; He, Y.; Li, J.; Ren, B.; Shih, T.-M.; Wang, Z.; Yang, Z.; Tian, Z. *Nano Lett.* **2015,** *15,* 6716–6721. doi:10.1021/acs.nanolett.5b02569
48. Butet, J.; Martin, O. J. F. *ACS Nano* **2014,** *8,* 4931–4939. doi:10.1021/nn500943t
49. Ethis de Corny, M.; Chauvet, N.; Laurent, G.; Jeannin, M.; Olgeirsson, L.; Drezet, A.; Huant, S.; Dantelle, G.; Nogues, G.; Bachelier, G. *ACS Photonics* **2016,** *3,* 1840–1846. doi:10.1021/acsphotonics.6b00351

BEILSTEIN JOURNAL OF NANOTECHNOLOGY

Low cost tips for tip-enhanced Raman spectroscopy fabricated by two-step electrochemical etching of 125 µm diameter gold wires

Antonino Foti[*1,§], Francesco Barreca[2], Enza Fazio[2], Cristiano D'Andrea[3], Paolo Matteini[3], Onofrio Maria Maragò[1] and Pietro Giuseppe Gucciardi[*1]

Full Research Paper

Address:
[1]CNR-IPCF, Istituto per i Processi Chimico-Fisici, Viale F. Stagno D'Alcontres 37, 98168 Messina, Italy, [2]Dipartimento di Scienze Matematiche e Informatiche, Scienze Fisiche e Scienze della Terra, Università degli Studi di Messina, Viale F. Stagno d'Alcontres 31, 98166 Messina, Italy and [3]IFAC-CNR, Institute of Applied Physics "Nello Carrara", National Research Council, Via Madonna del Piano 10, 50019 Sesto Fiorentino, Italy

Email:
Antonino Foti[*] - antonino.foti@polytechnique.edu;
Pietro Giuseppe Gucciardi[*] - gucciardi@ipcf.cnr.it

* Corresponding author
§ Now at LPICM, Ecole Polytechnique, CNRS, 91128 Palaiseau, France

Keywords:
amyloid; enhanced spectroscopy; gold tips; plasmonics; TERS

Abstract

Tip-enhanced Raman spectroscopy (TERS) has become a well-applied technique for nanospectroscopy, allowing for single molecule sensitivity with sub-nanometer spatial resolution. The demand for efficient, reproducible and cost-effective probes for TERS is increasing. Here we report on a new electrochemical etching protocol to fabricate TERS tips starting from 125 µm diameter gold wires in a reproducible way. The process is reliable (50% of the tips have radius of curvature <35 nm, 66% <80 nm), fast (less than 2 min) and 2.5 times cheaper than the etching of standard 250 µm diameter wires. The TERS performance of the tips is tested on dyes, pigments and biomolecules and enhancement factors higher than 10^5 are observed. TERS mapping with a spatial resolution of 5 nm is demonstrated.

Introduction

Tip-enhanced Raman spectroscopy (TERS) combines the chemical and structural information of Raman spectroscopy with the large signal gain provided by plasmonic resonances in metal tips and the high spatial resolution mapping offered by scanning probe microscopy [1-5]. In TERS, sharp metallic (or metallized) tips act as optical nanoantennas [6,7]. The tips effi-

ciently enhance and confine the electromagnetic field at the nanoscale [8,9] or even at sub-nanometer levels [10]. TERS has a sensitivity that can reach the single molecule level [11,12]. TERS setups based on atomic force microscopy (AFM) [1,13], scanning tunneling microscopy (STM) [14] and shear-force microscopy (ShFM) [15] allow for chemical imaging of nano-structured materials, surfaces and (bio)molecular layers with a spatial resolution of 4–10 nm in ambient conditions [15,16], and can even reach atomic-level sensitivity in ultrahigh vacuum (UHV) [17-19]. Excellent reviews on the applications of TERS can be found in [20-25]. TERS features unique advantages as compared with scanning electron microscopy (SEM), scanning near-field Raman microscopy (Raman-SNOM) [26] and far-field nanoscopy [27,28]: (i) it is a label-free technique, i.e., it does not require sample pretreatment, (ii) it can be operated in ambient conditions, liquid environments, as well as in UHV and at low temperatures, (iii) it combines the surface morphology information with the chemical information, (iv) optical excita-tion powers are virtually unlimited, and (v) it can attain atomic-level resolution. The presence of commercial setups on the market has further increased the application of TERS outside of the traditional chemistry and physics laborato-ries, suggesting TERS could be used as a future routine charac-terization tool like AFM, UV–vis, Raman or FTIR spectrosco-pies.

The tip is the key element in TERS. Its field enhancement and confinement capabilities determine the signal amplification, the spatial resolution and the reproducibility of the results. The ma-terial, morphology, aspect ratio and size of the tip apex are ex-pected to determine the optical properties of the tip [29,30]. TERS tips are nowadays produced by the chemical/electro-chemical etching of metal wires [31-35], metal coatings of AFM tips [36-38], electroless deposition, [39] galvanic dis-placement [40] or by advanced nanostructuration techniques such as electron beam induced deposition (EBID) and focused ion beam (FIB) milling [41-43] (see [30,44] for reviews). Fabri-cation methods capable of guaranteeing high reproducibility, cost-effectiveness and scalability to industrial production are, however, still not available at present. Metal vapor deposition on AFM tips is intrinsically scalable and tips of any kind of ma-terial can be used, but the reproducibility is low and the field enhancement is not excellent. Nanofabrication methods guar-antee optimal control of the dimensions and reproducibility, but they are serial techniques, i.e., slow, and fabrication costs are high. In addition, all the above-cited methods require very expensive lab equipment and skilled operators. Electrochemical etching, although suffering from surface roughness issues (mainly for silver), reproducibility issues and lack of tip dimen-sion control, is a technique that is easy to implement, acces-sible to every laboratory, and requires low-cost equipment and
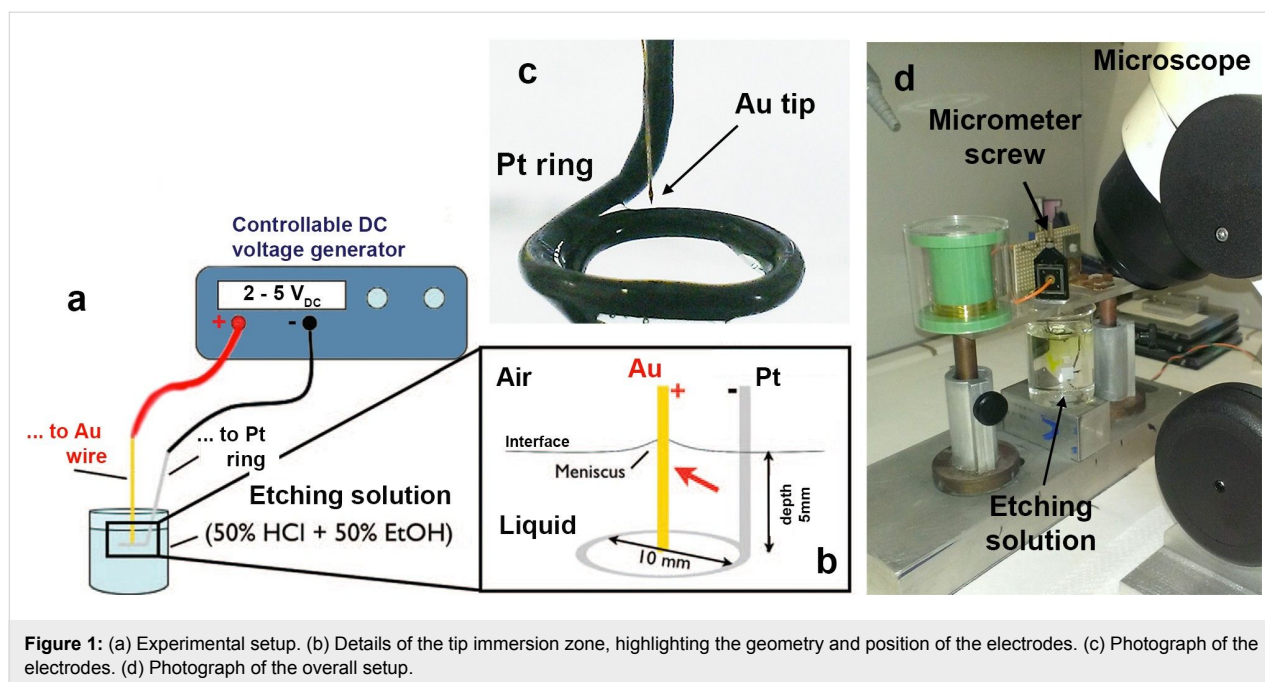
minimum training of the personnel. When applied to gold, elec-trochemical etching yields tips with good surface quality and a small radius of curvature in minutes, at reasonable costs, that can be safely stored for months [31,45,46]. Smooth tips with a radius of curvature smaller than 50 nm are reliably obtained with >80% success rate by etching 250 μm gold wires at low voltages (≈2.4 VDC, in order to avoid bubbling in the etching solution) by controlling the current [31], or monitoring the etching time [46].

Decreasing the diameter of the gold wire is a way to reduce the costs. The price of a tip can be calculated as the sum of the price of the gold wire plus that of the chemicals needed for the etching. We do not consider the cost of the labor here, since it can be highly variable depending on whether the operator is a diploma student or a technician/researcher. At the current market prices, a stock (5 m) of gold wire with 250 μm diameter costs 820–910 €, compared to 350–410 € for the same length of 125 μm diameter wire (Advent/Goodfellow). The average cost per tip (typically 1.0–1.5 cm long) ranges between 1.7–2.4 €/tip using 250 μm wires, and 0.7–1.1 €/tip using 125 μm wires. The cost of the chemicals is also different. In our experience, with 30 mL of HCl/ethanol solution, we can prepare up to five tips by etching 250 μm wires, whereas 10 mL are enough for 125 μm wires, corresponding to 0.45 €/tip and 0.15 €/tip, re-spectively. The final average cost per tip is thus 2.50 €/tip for 250 μm wires, against 1.05 €/tip for 125 μm wires.

In this article we report on a new protocol to produce TERS tips by electrochemical etching of 125 μm gold wires. The protocol tailors a two-step procedure [46] in which the first step is carried out at high voltage to quickly shrink the wire diameter and the second one is carried out at low voltage, in smooth, bubble-free conditions. Smooth TERS-effective tips are ob-tained in 80% of the cases. Tips with a radius of curvature of 35 nm are obtained with a 50% success rate, with etching times of approximately 2 min. The tips can be easily manipulated and safely mounted, by gluing or clamping them into STM- or ShF-based TERS setups. The good performance of the tips is high-lighted by TERS spectra of dyes, pigments and biomolecules. The enhancement factor in the range of 10^4–10^5 was found. Finally, a spatial resolution of ≈5 nm is shown on TERS maps of rhodamine 6G (R6G) sub-monolayers absorbed onto gold monocrystals.
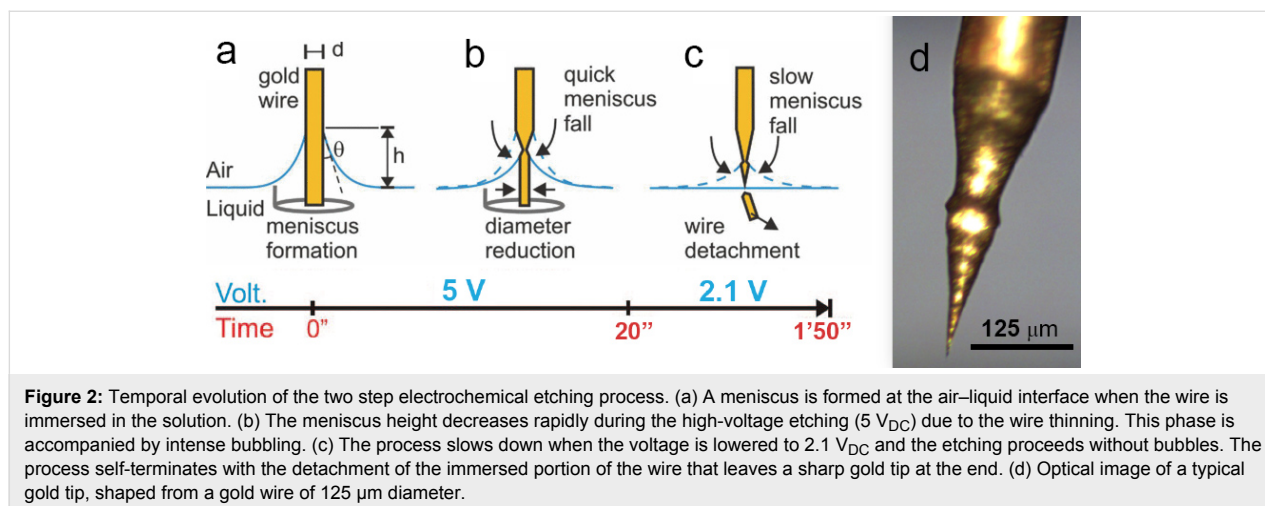
Experimental

Gold wires (125 μm diameter, Advent AU517311, high purity 99.99%, temper hard) are etched in a 10 mL solution 1:1 v/v of fuming hydrochloric acid (>37 wt %) and absolute ethanol (>99.5 wt %). All the reagents used are of analytical grade. The experimental setup is shown in Figure 1.

Figure 1: (a) Experimental setup. (b) Details of the tip immersion zone, highlighting the geometry and position of the electrodes. (c) Photograph of the electrodes. (d) Photograph of the overall setup.

The setup includes (Figure 1a) an adjustable DC voltage generator connected to (Figure 1b) the gold wire to be etched (the anode) and to a platinum wire (500 µm diameter, Advent PT5408, temper hard) shaped to form a ring of 10 mm diameter, acting as the cathode. A micrometric translator is used to manipulate the gold wire during the immersion and extraction from the solution. The gold wire is placed at the center of the ring-shaped cathode (Figure 1c) and oriented orthogonal to the liquid surface. Both electrodes are dipped 5 mm below the air–liquid interface (Figure 1b). The etching process is inspected with a stereo microscope (Figure 1d) mounted with a CCD camera (Thorlabs). The etching is carried out in two steps as depicted in Figure 1a–c and shown in Supporting Information File 2. When we immerse the gold wire in the ethanol–HCl

solution we observe the formation of a meniscus at the metal–air–liquid interface, due to capillary forces (Figure 2a) [47].

A pre-etching step of the gold wire is performed at a voltage $V_1 = 5$ V$_{DC}$ for a time $t_1 = 15$–20 s (Figure 2b) and permits quick reduction of the wire diameter and, consequently, almost halves the overall tip production time. During this step the wire diameter at the meniscus is thinned at a rate $\delta d/\delta t \approx 3.5$–4 µm/s and intense bubbling is observed. As a rule of thumb, the pre-etching should be limited to 20 s in order to prevent a reduction of the diameter below 40–50 µm, which would make it too fragile and subject to bending or early detachment. Bubbling, in fact, intensely shakes the wire portion protruding into the solu-

Figure 2: Temporal evolution of the two step electrochemical etching process. (a) A meniscus is formed at the air–liquid interface when the wire is immersed in the solution. (b) The meniscus height decreases rapidly during the high-voltage etching (5 V$_{DC}$) due to the wire thinning. This phase is accompanied by intense bubbling. (c) The process slows down when the voltage is lowered to 2.1 V$_{DC}$ and the etching proceeds without bubbles. The process self-terminates with the detachment of the immersed portion of the wire that leaves a sharp gold tip at the end. (d) Optical image of a typical gold tip, shaped from a gold wire of 125 µm diameter.

tion (red arrow in Figure 1b). Any bending or early detachment of this wire part would yield a crooked or blunt tip. The second etching step is carried out by lowering the DC voltage in the 2.1–2.3 V range (Figure 2c). No bubbling occurs under these conditions. The tip slowly forms at the air–liquid interface, with an etching rate $\delta d/\delta t \approx$ 0.5–1.5 μm/s depending on the exact voltage applied (the higher the voltage, the higher the etching rate). The process self-terminates when the portion of the wire immersed in the solution detaches (Figure 2c), which typically occurs after t_{tot} = 60–150 s. A wire with a double taper and a sharp tip at the end is thus obtained (Figure 2d). The voltage is turned off immediately after the precipitation of the immersed wire portion in order to avoid over-etching, which would blunt the tip. Stop-voltage circuits have been developed [48,49] to automatize this task. The tips are finally washed by shaking in the etching solution and, subsequently, by pouring a few drops of HCl and rinsing in ethanol and water. This eliminates residual impurities from the surface.
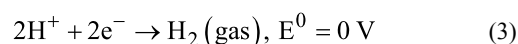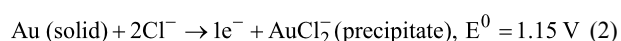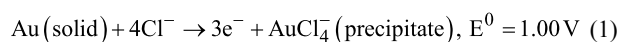
Scanning electron microscopy (SEM) inspection of the produced tips is carried out to characterize the tip apex using a Zeiss Merlin field emission electron microscope, equipped with a Gemini II column.

The analysis of the tips' TERS performance is carried out in gap-mode [14], using a commercial setup that couples a micro-Raman spectrometer (XploRA Plus, Horiba) with an AFM/STM (Smart SPM-1000, AIST-NT). The setup, shown in Supporting Information File 1, works in a side-illumination configuration with a 638 nm laser beam, *p*-polarized, focused onto the tip axis through a 100× long working distance objective (Mitutoyo, WD 6.0 mm, NA 0.7), oriented at 60° with respect to the vertical axis. The backscattered TERS signal is collected by the same objective. The signal is dispersed by a grating featuring 1200 gr/mm and sent to a Peltier cooled CCD camera (Syncerity, Horiba Jobin Yvon). The laser spot is positioned on the tip apex with the aid of a piezoelectric *x*–*y*–*z* table that scans the objective position. The *x*–*y* scan plane is orthogonal to the optical axis (*z*) of the objective.

Results and Discussion
Gold etching and tip formation mechanism
The gold electrochemical corrosion is driven by a well-known redox process in acidic environment [31], whose main reactions are:

$$\mathrm{Au\,(solid)} + 4\mathrm{Cl}^- \rightarrow 3\mathrm{e}^- + \mathrm{AuCl}_4^-\,(\text{precipitate}),\ \mathrm{E}^0 = 1.00\,\mathrm{V} \quad (1)$$

$$\mathrm{Au\,(solid)} + 2\mathrm{Cl}^- \rightarrow 1\mathrm{e}^- + \mathrm{AuCl}_2^-\,(\text{precipitate}),\ \mathrm{E}^0 = 1.15\,\mathrm{V} \quad (2)$$

$$2\mathrm{H}^+ + 2\mathrm{e}^- \rightarrow \mathrm{H}_2\,(\text{gas}),\ \mathrm{E}^0 = 0\,\mathrm{V} \quad (3)$$

Here the superficial gold atoms are oxidized, transforming into either Au(I) or Au(III). The chlorine ions combine with Au(I) or Au(III) (reactions 1 and 2), yielding a yellow precipitate. At the same time, H$^+$ ions are reduced at the platinum wire surface, leading to H$_2$ gas formation (reaction 3). The H$_2$, together with O$_2$ and Cl$_2$ present in the solution, can cause intense bubbling when the reaction is fast enough, as for example at 5 V$_{DC}$ (first step of the process). At lower voltages (2.1–2.2 V$_{DC}$), as in the second step of the process, the reaction proceeds much more slowly. The ethanol acts effectively as a quencher, hindering any production of bubbles. The tip formation is ruled by the meniscus lowering consequent to the wire thinning under electrochemical attack [46,50]. The etching process is not homogeneous along the wire profile immersed in solution. The etching at the meniscus is ≈1.5 times faster than in the bulk. As can be seen in Supporting Information File 2, at the beginning of the low voltage step the wire diameter at the meniscus is thinner than the portion immersed in the liquid. This difference is likely due to the anisotropic distribution of the reaction products (AuCl^{4-} and AuCl^{2-}) along the wire surface that hinders the renewal of fresh etchant. The reaction products generated at the meniscus fall due to gravity, covering the surface of the wire still immersed in the bulk solution, affecting the concentration distribution of the chlorine ions along the wire. A higher local concentration of Cl$^-$ ions at the meniscus with respect to the bulk can justify the observed anisotropic etching rate.

Morphological analysis
The tip morphology was characterized using SEM. Figure 3a (details shown in (b, c)) show a typical pilum-shaped tip obtained after the two-step etching process, ending with a radius of curvature of $r_{tip} \approx$ 12 nm (d).

A double taper, ≈350 μm long (Figure 4a) tip is observed, resulting from the two etching steps. The overall tip length is a factor of two shorter with respect to that observed on 250 μm diameter Au wires. The lower taper (≈180 μm) features an apical angle of ≈24° and ends with a sharp tip. The lower taper is also characterized by a wavy profile, which smooths towards the apex region (Figure 3c). This is a consequence of the burst-like behavior observed during the etching process. The tip length and its aspect ratio are determined by the meniscus height h (Equation 4), where h depends on the wire diameter, d, and contact angle, θ_c according to [46]

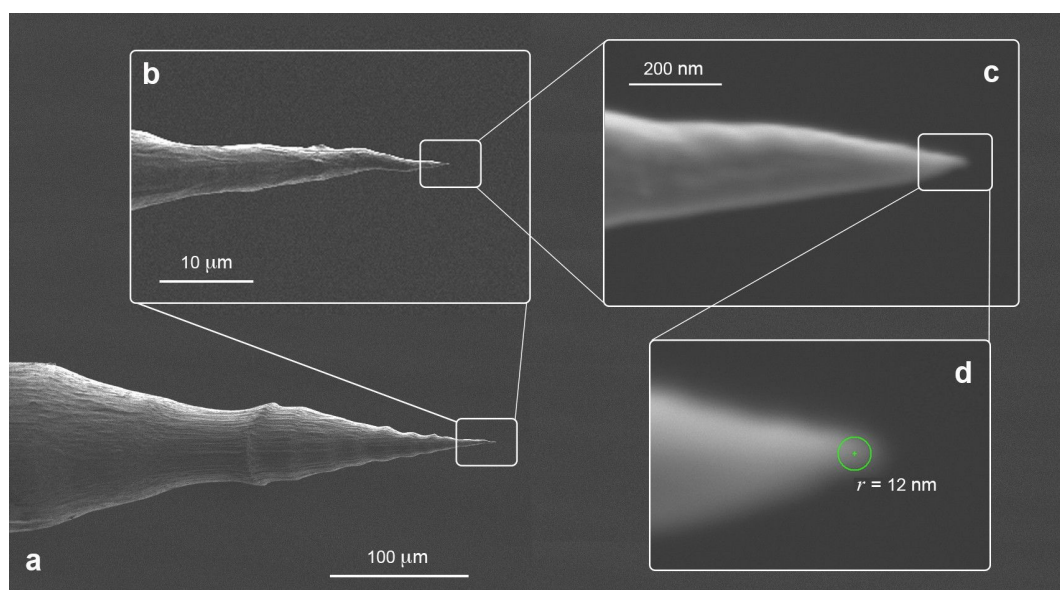$$h = (d/2)\cos\theta \left\{ \log\left[\frac{4a}{(d/2)(1+\sin\theta)} \right] - \gamma_E \right\} \quad (4)$$

Figure 3: (a) SEM images of a pilum-shaped tip with details shown in (b), (c) and (d) on the apical part, showing a radius of curvature $r_{tip} \approx 12$ nm and an apical angle of $\approx 24°$ ($t_1 = 20$ s, $V_1 = 5$ V$_{DC}$, $t_2 = 90$ s, $V_2 = 2.1$ V$_{DC}$).
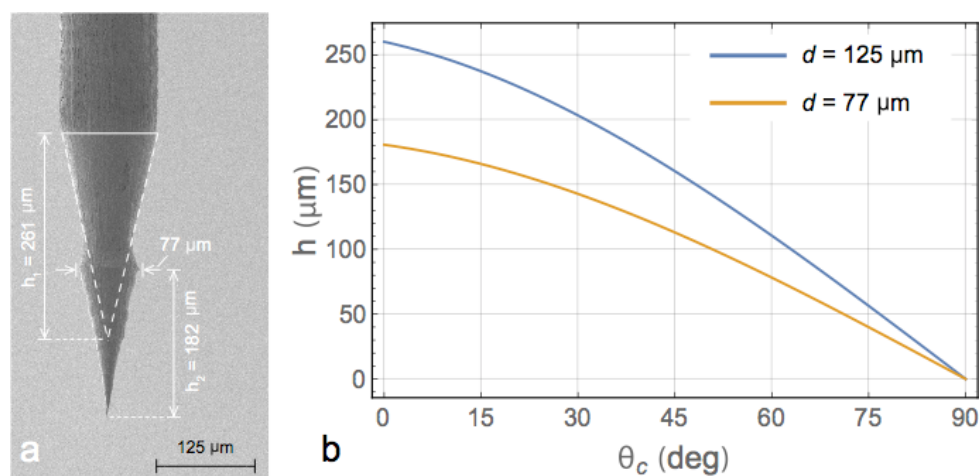

Figure 4: (a) SEM image of a tip highlighting the dimensions of the tapered zones. The dashed lines are a contour of the upper taper that would have been obtained in a single step etching. (b) Plot of the expected meniscus height as a function of the contact angle assuming a wire diameter of 125 µm (blue line, upper taper) and of 77 µm (orange line, lower taper).

where $\gamma_E \approx 0.577$ is Euler's constant, $g = 981$ cm/s^2 is the gravitational constant and $a = \sqrt{\gamma / \rho g}$ is the capillary constant, where $\gamma \approx 30$ dyn/cm and $\rho = 0.98$ g/cm^3 are the surface tension and the density of the HCl/ethanol solution, respectively. In Figure 4b we plot the predicted values of the meniscus extension h as a function of the contact angle for a starting diameter of 125 µm (blue line) and 77 µm (orange line), corresponding to the initial wire size and to the wire diameter at the beginning of the second etching step. The meniscus height h_2 predicted for the second etching step assuming very small contact angles

($\theta_c \approx 0$, Figure 4b, orange line) matches very well with the taper length ($h_2 = 182$ µm, Figure 4a). The overall tip length found in the experiments (≈ 360 µm) is, however, longer than meniscus height $h_1 = 260$ µm predicted for a wire diameter of 125 µm, even for $\theta_c \approx 0$ (Figure 4b, blue line). The value of h_1, however, matches remarkably well the length of the tip expected if we had completed the etching at high voltage (261 µm, Figure 4a, dotted line). This observation suggests that the length discrepancy can be attributed to the bubbling phenomenon. As visible in Supporting Information File 2, bubbles originating from

the wire immersed in the solution reach the surface and explode. The effect is particularly intense in proximity of the liquid–air–metal interface. As a consequence, the motion of the bubbles results in a force that raises the meniscus contact point with the metal wire with respect to the equilibrium conditions described by Equation 4. We believe that this phenomenon is at the origin of the ≈100 µm meniscus upshift and overall tip length increase.

The intrinsic morphology of the metal wires plays a key role in determining the final tip characteristics [30]. We find that when randomly etching different sections of the gold wire supplied by the producer, we end up with very rough tips (Figure 5), even in the presence of "fresh" solutions. Rough surfaces have been explained [46] with the presence of dislocations and grains in the 100–500 nm scale (consequence of the wire production process), in which the etching occurs through the detachment of large pieces of gold, instead of in a smooth atom-by-atom fashion. Sharp protrusions are occasionally observed at the apex of rough tips. At present it is not possible to predict and control such phenomenon. A statistical analysis on ten tips shows that 80% of the tips are TERS-active, while 50% of the tips have a radius of curvature smaller than 35 nm.

Light emission from the tip apex

Tightly coupled plasmonic metals, such as nanorods dimers [51], nanocubes on surfaces [52], or TERS tips in contact with surfaces [53,54], emit light over a broad continuum, even if excited at energies below the sp/d interband transition. Enhanced inelastic electron tunneling through the gap seems to be the origin of photon emission [52,55], leading to electronic

Raman scattering (ERS) of the laser photons [53] which is at the origin of the background observed in TERS and SERS [54-56]. The spectral features of such a light continuum bring information on the plasmonic modes of the nanoantenna system. For processes concerning single tips, i.e., withdrawn from the substrates, the origin of the light emission has not yet been unambiguously ascertained. Calculations on nanocube monomers [53] predict a 100-fold smaller light emission with respect to the nanocube-on-surface configuration, and the origin of the signal is attributed to photoluminescence rather than to ERS. Sanders et al. [57], working on Au-coated spherical AFM tips, have shown a remarkable correlation between the dark-field scattering peak, attributed to plasmon excitations, and the position of the maximum integrated SERS background of the tip, confirming that the background is enhanced by the localized plasmon resonance in the apical region. On sharp Au tips, the same authors report an almost flat scattering (from the visible to the NIR), associated with a less intense background in the 600–700 nm region. In any case, it is a matter of evidence that a stronger background is typically associated to a more intense SERS/TERS emission [54,57], suggesting the presence of a more effective substrate/tip near-field coupling.

For our purposes, mapping the light emission from the tip is important for two reasons. Firstly, we have empirically verified that optimal tips for TERS are those that show some degree of light emission from their apex. Secondly, the process allows us to precisely focus the laser spot on the tip apex, maximizing the overall TERS signal. Measurements were carried out by scanning the laser spot with a piezoelectric stage attached to the objective (Figure 6a).

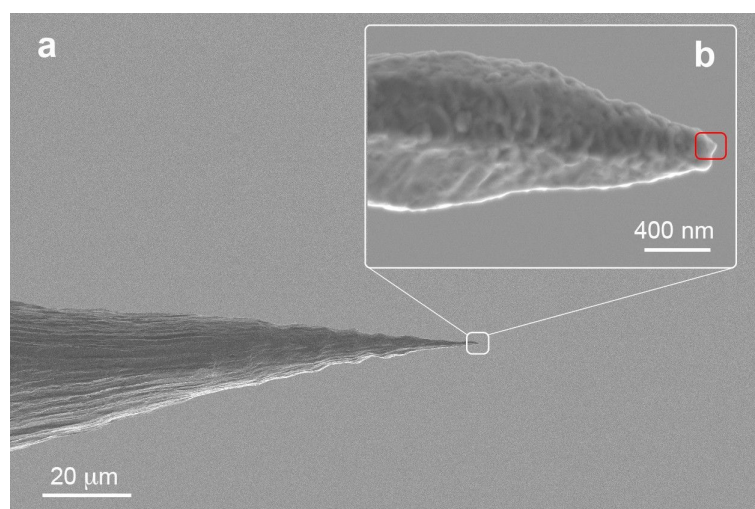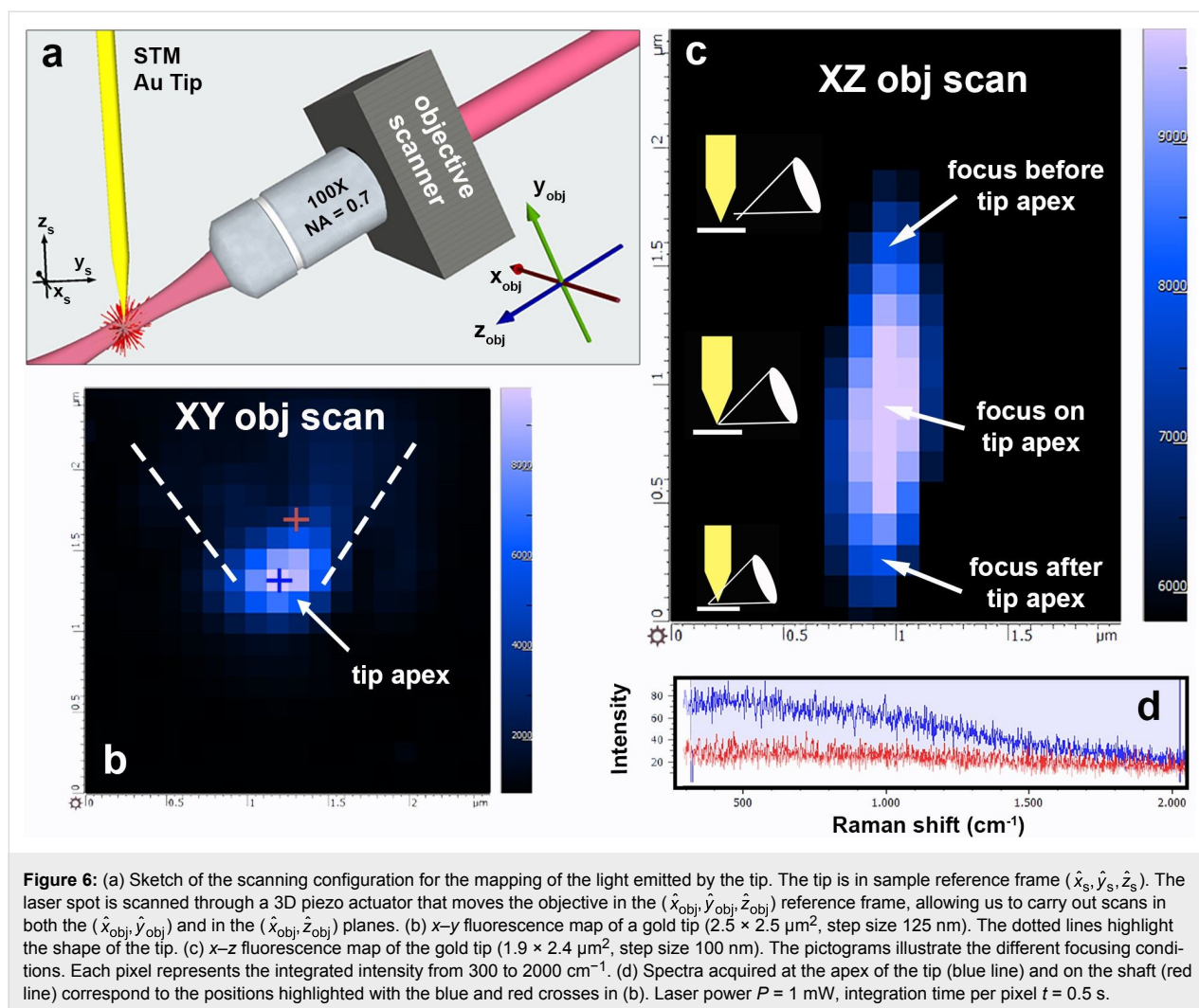**Figure 5:** (a) SEM image of an etched tip (t_1 = 20 s, V_1 = 5 V_{DC}, t_2 = 75 s, V_2 = 2.1 V_{DC}) and details on its apex (b), showing the roughness of the gold surface. Sharp protrusions ($r ≈ 15$ nm) can occur at the apex of such blunt tips (red square).

Figure 6: (a) Sketch of the scanning configuration for the mapping of the light emitted by the tip. The tip is in sample reference frame ($\hat{x}_s, \hat{y}_s, \hat{z}_s$). The laser spot is scanned through a 3D piezo actuator that moves the objective in the ($\hat{x}_{obj}, \hat{y}_{obj}, \hat{z}_{obj}$) reference frame, allowing us to carry out scans in both the ($\hat{x}_{obj}, \hat{y}_{obj}$) and in the ($\hat{x}_{obj}, \hat{z}_{obj}$) planes. (b) x–y fluorescence map of a gold tip (2.5 × 2.5 μm^2, step size 125 nm). The dotted lines highlight the shape of the tip. (c) x–z fluorescence map of the gold tip (1.9 × 2.4 μm^2, step size 100 nm). The pictograms illustrate the different focusing conditions. Each pixel represents the integrated intensity from 300 to 2000 cm^{-1}. (d) Spectra acquired at the apex of the tip (blue line) and on the shaft (red line) correspond to the positions highlighted with the blue and red crosses in (b). Laser power P = 1 mW, integration time per pixel t = 0.5 s.

Two maps are acquired: one to localize the tip apex position (Figure 6b) in which we scan the laser spot in the ($\hat{x}_{obj}, \hat{y}_{obj}$) plane that, given the large incidence angle, is almost coincident with the tip plane ($\hat{x}_s, \hat{z}_s$); the second one is to optimize the laser focus on the tip apex (Figure 6c), and is carried out by scanning the laser beam in the ($\hat{x}_{obj}, \hat{z}_{obj}$) plane, i.e., moving the beam orthogonally to the tip axis while changing the focusing conditions. In each map we report the intensity of the background signal (Figure 6d) integrated in the 300–2000 cm^{-1} range. Spectra acquired inside (blue cross) and outside (red cross) the apical region show the presence of a continuum background (Figure 6d, blue line) at the apex, compared to a flat signal on the shaft (red line). Typical laser powers are 1.0–2.5 mW and integration times are 0.5–1.0 s per pixel.

TERS spectra of dyes, pigments and biomolecules

The tips have been applied to evaluate the spectra of analyze standard dye molecules such as rhodamine 6G (R6G), crystal violet (CV), methylene blue (MB), pigments of cultural heritage interest (alizarin-s, AZ-s) [58] and highly toxic protein oligomers [59]. Tests are carried out in gap-mode, absorbing the probe molecules on gold films with side-illumination at an excitation wavelength of 638 nm. Molecular solutions at different concentrations are prepared in deionized water. Target molecules are absorbed on Au(111) flat films that have undergone standard flame annealing in order to obtain crystalline terraces of about 100 nm in size. The gold film substrates are immersed for 2 h and 30 min and subsequently rinsed in deionized water in order to remove the molecules excess. Finally, they are dried under a nitrogen flux. Figure 7 shows the TERS spectra acquired on R6G at 10^{-4} M (a), CV at 10^{-5} M (b), MB at 10^{-5} M (c) and AZ-s at 10^{-3} M (d).

The TERS spectra highlight a high contrast with respect to the signal acquired when the tip is removed from the near-field region of the sample, just excluding the feedback loop of the STM system. Vibrational bands of all molecules agree with the
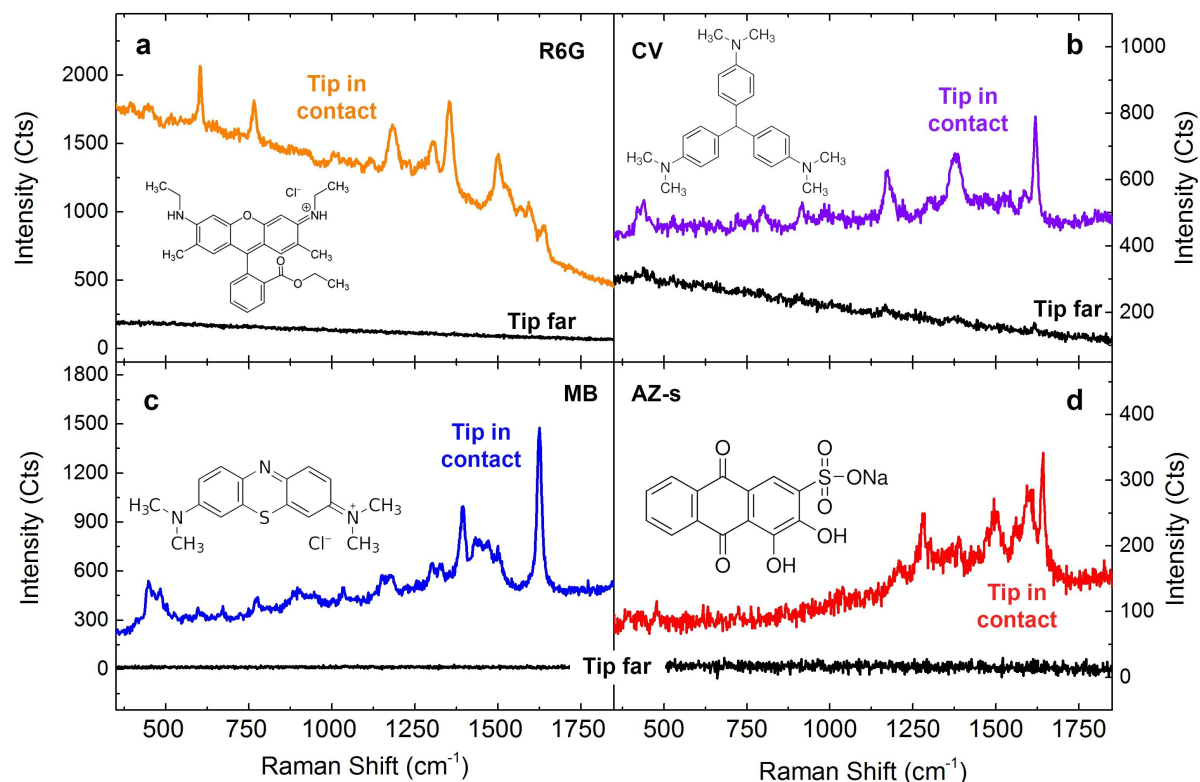
Figure 7: TERS spectra (colored lines) of different molecules acquired with the tip in contact with the surface: (a) R6G (*P* = 1 mW, *t* = 5 s), (b) CV (*P* = 1 mW, *t* = 3 s), (c) MB (*P* = 0.1 mW, *t* = 1 s), (d) AZ-s (*P* = 1 mW, *t* = 5 s). Black lines represent signal intensity acquired in the same conditions when the tip is far from the sample.

literature [60-63]. We finally apply our tips to obtain TERS spectra from the N-terminal domain of the *Escherichia coli* protein HypF (HypF-N). This a small stably folded α/β protein with 91-residues (10 kDa) [64] that is capable of forming amyloid species like those associated with neurological diseases such as Alzheimer's and Parkinson's [65], and have recently been the subject of TERS investigations [66-68]. In particular, we focus on the detection of toxic HypF-N oligomers that precede the formation of mature amyloid fibrils [69,70]. HypF-N oligomers (48 μM) are obtained by controlled aggregation (4 h, 25 °C, pH 5.5) of the HypF-N monomer in 50 mM acetate buffer, 12% (v/v) trifluoroethanol and 2 mM dithiothreitol [66]. The gold films are then immersed overnight in the oligomer solution, followed by rinsing in water to remove the excess of protein and then drying in air. TERS spectra are acquired with a tip featuring a tip radius r_{tip} = 15 nm. Figure 8 (red line) shows evidence of a strong TERS effect on oligomers, with the appearance of some of typical vibrational bands of protein samples such as the phenylalanine (Phe) ring breathing mode at 1004 cm^{-1} or the amide II band at 1550 cm^{-1} due to the C–N stretching mode and N–H bending mode of the atoms forming the peptide chain.
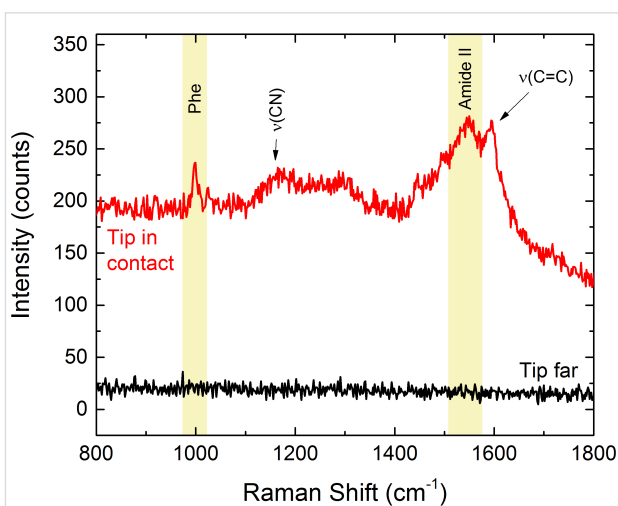

Figure 8: TERS signal of oligomers when the STM feedback loop is on (red line) and when it is off (black line). Experimental conditions: λ_{exc} = 638 nm, *P* = 0.11 mW, *t* = 10 s.

No signal is detected when the tip is not in contact with the surface Figure 8 (black line). After each TERS measurement, the tip is retracted from the sample and its emission is mapped in

order to be sure the TERS signal does not come from molecules adsorbed on the tip apex.

Evaluation of the enhancement factor

An estimation of the enhancement factor (EF) can be given by comparing the TERS signal increase with respect to the Raman signal measured when the tip is out of contact (far-field excitation conditions), normalizing to the different areas probed in each case [71]:

$$EF = \frac{I_{NF} - I_{FF}}{I_{FF}} \frac{S_{Raman}}{S_{TERS}}, \tag{5}$$

where I_{NF} is the near-field TERS signal, I_{FF} is the far-field Raman signal, S_{TERS} is the area probed when the tip is in contact and S_{Raman} is the area probed in far-field excitation conditions. S_{TERS} is calculated as the surface of the circle $S_{TERS} = \pi r^2_{tip}$ underneath the tip radius r_{tip}. For the Raman signal, the probed area is calculated as the area of the elliptical intersection between the point spread function (PSF) of the objective

(inclined by $\theta_{inc} = 60°$ with respect to the vertical) and the horizontal plane. Considering $a = b = \lambda/2 \cdot NA$ and $c = 2\lambda/NA^2$ the semi-axes of the PSF, we find $S_{Raman} = \pi \cdot a \cdot c'$, where $a' = a \approx$ 450 nm and $c' = ac / \sqrt{c^2 \cos^2 \theta_{inc} + a^2 \sin^2 \theta_{inc}} \approx 870$ nm. Equation 5 provides meaningful results if $I_{FF} \neq 0$. When no signal is detected in far-field conditions, we can still use the signal noise level (RMS) as a reference to estimate a lower bound of the EF. Measurements on HypF-N oligomers carried out with a tip whose radius of curvature has been observed by SEM to be r_{tip} = 15 nm show that indeed the EF is larger than 10^5. Assuming the same tip radius for the other molecules we find $EF \geq 8 \times 10^4$ for R6G, $EF = 1.6 \times 10^4$ for CV, $EF \geq 2.4 \times 10^4$ for AZs, and $EF \geq 1.2 \times 10^5$ for MB. These values compare well with the best results found in the literature [25,44].

Assessment of the spatial resolution in TERS imaging

Nanoscale resolution is shown in simultaneous morphological (STM) and chemical (TERS) mapping of R6G molecules (10^{-4} M) absorbed on Au(111). Experiments are carried out in
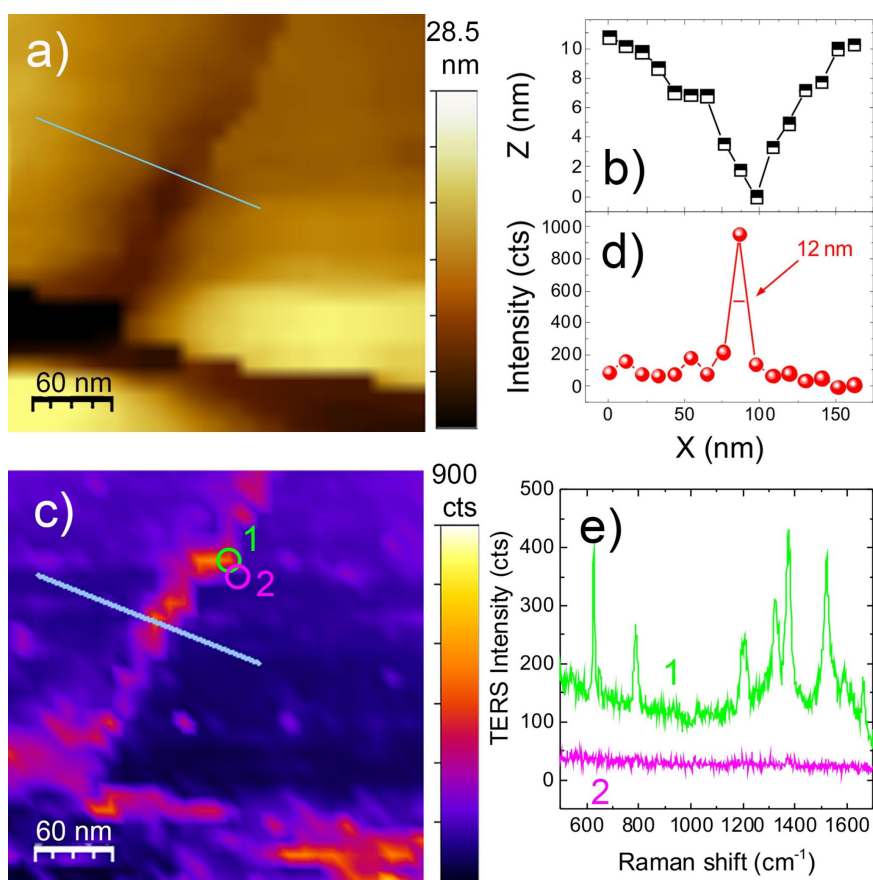
Figure 9: (a) STM image of Au(111) terraces on which R6G 10^{-4} M is adsorbed ($\Delta V = 0.05$ V – tip positive, current set point is 80 pA). The gray line indicates the zone where the line profile plotted in (b) is drawn. (c) Simultaneous TERS image at 1524 cm^{-1} ($P = 1.0$ mW, $t = 0.5$ s). The gray line indicates the zone where the line profile plotted in (d) is drawn. (e) TERS spectra acquired in correspondence with the circled areas in (c) taken at a distance of only one scanning step away from one another (10 nm).

gap-mode, with excitation at 638 nm. Figure 9a shows the STM topography acquired on a 300×300 nm^2 area with step size of 10 nm. It displays adjacent gold terraces separated by trenches.

The top diagonal trench has a depth of ≈10 nm and width of ≈50 nm at its largest point (line profile in Figure 9b). The bottom trench is approximately two times deeper. The TERS map in Figure 9c displays a strongly enhanced signal from the two trenches. This could in principle be due to a higher concentration of molecules in the channels, in combination with the presence of enhanced electric fields [72], caused by molecular diffusion into SERS-active sites [62]. Whatever the origin of the signal, we are able to map this effect with a spatial resolution equivalent to the scan step (10 nm). This is evident from the line profile of Figure 9d (drawn along the gray line in c), showing a full width at half maximum of 12 nm. The two spectra in Figure 9e, acquired at just one pixel distance from each other, corresponding to the circled areas in Figure 9c, highlight the possibility to probe the presence of R6G (green) or its absence (magenta) with 10 nm resolution. Furthermore, such a strong signal variability between two adjacent pixels, just 10 nm apart, suggests potential sub-pixel spatial resolution [72]. This conclusion is supported by TERS mapping of a 150×150 nm^2 area (30×30 points) with step size of 5 nm (Figure 10a) in a different zone of the sample in which R6G absorbs in a patchy-like fashion. Spectra acquired on adjacent points (Figure 10b) show the capability to map the confinement of R6G molecules in a region smaller or equal to 5 nm consisting indeed of just a few molecules.

Conclusion

In summary, we demonstrate a fast and inexpensive protocol to produce TERS tips by electrochemical etching of 125 µm diameter gold wires. The tips are robust and easy to manipulate. Their cost (1.05 €/tip) is 2.5 times cheaper than using standard 250 µm diameter wires, whereas the etching time (less than 2 min) is more than halved. 80% of the tips are TERS active. 50% of the tips have radius of curvature smaller than 35 nm. The tips have been tested on dyes, pigments and biomolecules showing enhancement factors ≈10^5 (lower bound) in gap-mode. TERS maps of sub-monolayer films of R6G on Au(111) are shown with optical resolution better than 5 nm. The procedure can in principle be applied to thinner wires to further reduce costs and production times, although issues related to the fragility of the tip and difficulties in the manipulation and mounting have to be solved when working with very thin wires (e.g., 50 µm). Our protocol can be extended to other materials and requires minimal lab equipment and technical skills.

Supporting Information

Supporting Information File 1
Picture of the TERS experimental setup.
[https://www.beilstein-journals.org/bjnano/content/supplementary/2190-4286-9-254-S1.png]

Supporting Information File 2
A movie illustrating the electrochemical etching process.
[https://www.beilstein-journals.org/bjnano/content/supplementary/2190-4286-9-254-S2.mp4]
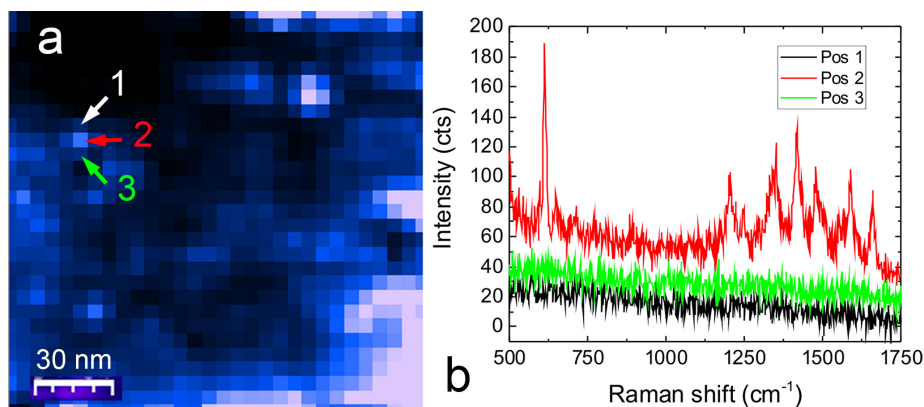
Acknowledgements

Figure 10: (a) TERS map and point spectra (b) acquired at the locations indicated with the labels 1, 2, 3, at a distance 5 nm from each other. Laser power 1 mW, integration time 0.5 s. The TERS signal in (a) is the integrated emission in the 1100–1500 cm^{-1} range.

ORCID® iDs

Antonino Foti - https://orcid.org/0000-0002-9824-3099
Cristiano D'Andrea - https://orcid.org/0000-0001-5807-3067
Paolo Matteini - https://orcid.org/0000-0002-8488-5867
Onofrio Maria Maragò - https://orcid.org/0000-0002-7220-8527
Pietro Giuseppe Gucciardi - https://orcid.org/0000-0003-1826-9174

References

1. Stöckle, R. M.; Suh, Y. D.; Deckert, V.; Zenobi, R. *Chem. Phys. Lett.* **2000,** *318,* 131–136. doi:10.1016/s0009-2614(99)01451-7
2. Anderson, M. S. *Appl. Phys. Lett.* **2000,** *76,* 3130–3132. doi:10.1063/1.126546
3. Hayazawa, N.; Inouye, Y.; Sekkat, Z.; Kawata, S. *Opt. Commun.* **2000,** *183,* 333–336. doi:10.1016/s0030-4018(00)00894-4
4. Pettinger, B.; Picardi, G.; Schuster, R.; Ertl, G. *Electrochemistry* **2000,** *68,* 942–949.
5. Novotny, L.; Hecht, B. *Principles of Nano-optics;* Cambridge University Press: Cambridge, United Kingdom, 2012. doi:10.1017/cbo9780511794193
6. Novotny, L.; van Hulst, N. *Nat. Photonics* **2011,** *5,* 83–90. doi:10.1038/nphoton.2010.237
7. Shi, X.; Coca-López, N.; Janik, J.; Hartschuh, A. *Chem. Rev.* **2017,** *117,* 4945–4960. doi:10.1021/acs.chemrev.6b00640
8. Yang, Z.; Aizpurua, J.; Xu, H. *J. Raman Spectrosc.* **2009,** *40,* 1343–1348. doi:10.1002/jrs.2429
9. Kottmann, J. P.; Martin, O. J. F.; Smith, D. R.; Schultz, S. J. *J. Microsc. (Oxford, U. K.)* **2001,** *202,* 60–65. doi:10.1046/j.1365-2818.2001.00866.x
10. Barbry, M.; Koval, P.; Marchesin, F.; Esteban, R.; Borisov, A. G.; Aizpurua, J.; Sánchez-Portal, D. *Nano Lett.* **2015,** *15,* 3410–3419. doi:10.1021/acs.nanolett.5b00759
11. Zhang, W.; Yeo, B. S.; Schmid, T.; Zenobi, R. *J. Phys. Chem. C* **2007,** *111,* 1733–1738. doi:10.1021/jp064740r
12. Sonntag, M. D.; Klingsporn, J. M.; Garibay, L. K.; Roberts, J. M.; Dieringer, J. A.; Seideman, T.; Scheidt, K. A.; Jensen, L.; Schatz, G. C.; Van Duyne, R. P. *J. Phys. Chem. C* **2012,** *116,* 478–483. doi:10.1021/jp209982h
13. Kharintsev, S. S.; Hoffmann, G. G.; Dorozhkin, P. S.; With, G. d.; Loos, J. *Nanotechnology* **2007,** *18,* 315502. doi:10.1088/0957-4484/18/31/315502
14. Pettinger, B.; Ren, B.; Picardi, G.; Schuster, R.; Ertl, G. *Phys. Rev. Lett.* **2004,** *92,* 096101. doi:10.1103/physrevlett.92.096101
15. Hartschuh, A.; Sánchez, E. J.; Xie, X. S.; Novotny, L. *Phys. Rev. Lett.* **2003,** *90,* 095503. doi:10.1103/physrevlett.90.095503
16. Yano, T.-a.; Verma, P.; Saito, Y.; Ichimura, T.; Kawata, S. *Nat. Photonics* **2009,** *3,* 473–477. doi:10.1038/nphoton.2009.74
17. Steidtner, J.; Pettinger, B. *Phys. Rev. Lett.* **2008,** *100,* 236101. doi:10.1103/physrevlett.100.236101
18. Zhang, R.; Zhang, Y.; Dong, Z. C.; Jiang, S.; Zhang, C.; Chen, L. G.; Zhang, L.; Liao, Y.; Aizpurua, J.; Luo, Y.; Yang, J. L.; Hou, J. G. *Nature* **2013,** *498,* 82–86. doi:10.1038/nature12151
19. Jiang, S.; Zhang, Y.; Zhang, R.; Hu, C.; Liao, M.; Luo, Y.; Yang, J.; Dong, Z.; Hou, J. G. *Nat. Nanotechnol.* **2015,** *10,* 865–869. doi:10.1038/nnano.2015.170
20. Mauser, N.; Hartschuh, A. *Chem. Soc. Rev.* **2014,** *43,* 1248–1268. doi:10.1039/c3cs60258c
21. Wang, X.; Huang, S.-C.; Huang, T.-X.; Su, H.-S.; Zhong, J.-H.; Zeng, Z.-C.; Li, M.-H.; Ren, B. *Chem. Soc. Rev.* **2017,** *46,* 4020–4041. doi:10.1039/c7cs00206h
22. Sharma, G.; Deckert-Gaudig, T.; Deckert, V. *Adv. Drug Delivery Rev.* **2015,** *89,* 42–56. doi:10.1016/j.addr.2015.06.007
23. Zhang, Z.; Sheng, S.; Wang, R.; Sun, M. *Anal. Chem.* **2016,** *88,* 9328–9346. doi:10.1021/acs.analchem.6b02093
24. Zrimsek, A. B.; Chiang, N.; Mattei, M.; Zaleski, S.; McAnally, M. O.; Chapman, C. T.; Henry, A.-I.; Schatz, G. C.; Van Duyne, R. P. *Chem. Rev.* **2017,** *117,* 7583–7613. doi:10.1021/acs.chemrev.6b00552
25. Bonhommeau, S.; Lecomte, S. *ChemPhysChem* **2018,** *19,* 8–18. doi:10.1002/cphc.201701067
26. Gucciardi, P. G.; Trusso, S.; Vasi, C.; Patanè, S.; Allegrini, M. *Appl. Opt.* **2003,** *42,* 2724–2729. doi:10.1364/ao.42.002724
27. Hell, S. W. *Science* **2007,** *316,* 1153–1158. doi:10.1126/science.1137395
28. Montgomery, P. C.; Leong-Hoi, A.; Anstotz, F.; Mitev, D.; Pramatarova, L.; Haeberlé, O. *J. Phys.: Conf. Ser.* **2016,** *682,* 012010. doi:10.1088/1742-6596/682/1/012010
29. Maouli, I.; Taguchi, A.; Saito, Y.; Kawata, S.; Verma, P. *Appl. Phys. Express* **2015,** *8,* 032401. doi:10.7567/apex.8.032401
30. Huang, T.-X.; Huang, S.-C.; Li, M.-H.; Zeng, Z.-C.; Wang, X.; Ren, B. *Anal. Bioanal. Chem.* **2015,** *407,* 8177–8195. doi:10.1007/s00216-015-8968-8
31. Ren, B.; Picardi, G.; Pettinger, B. *Rev. Sci. Instrum.* **2004,** *75,* 837–841. doi:10.1063/1.1688442
32. Sasaki, S. S.; Perdue, S. M.; Perez, A. R.; Tallarida, N.; Majors, J. H.; Apkarian, V. A.; Lee, J. *Rev. Sci. Instrum.* **2013,** *84,* 096109. doi:10.1063/1.4822115
33. Bonaccorso, F.; Calogero, G.; Di Marco, G.; Maragò, O. M.; Gucciardi, P. G.; Giorgianni, U.; Channon, K.; Sabatino, G. *Rev. Sci. Instrum.* **2007,** *78,* 103702. doi:10.1063/1.2782682
34. Taguchi, A.; Hayazawa, N.; Furusawa, K.; Ishitobi, H.; Kawata, S. *J. Raman Spectrosc.* **2009,** *40,* 1324–1330. doi:10.1002/jrs.2287
35. Kalbacova, J.; Rodriguez, R. D.; Desale, V.; Schneider, M.; Amin, I.; Jordan, R.; Zahn, D. R. T. *Nanospectroscopy* **2015,** *1,* 12–18. doi:10.2478/nansp-2014-0002
36. Yeo, B.-S.; Zhang, W.; Vannier, C.; Zenobi, R. *Appl. Spectrosc.* **2006,** *60,* 1142–1147. doi:10.1366/000370206778664662
37. Asghari-Khiavi, M.; Wood, B. R.; Hojati-Talemi, P.; Downes, A.; McNaughton, D.; Mechler, A. *J. Raman Spectrosc.* **2012,** *43,* 173–180. doi:10.1002/jrs.3021
38. Rodriguez, R. D.; Sheremet, E.; Müller, S.; Gordan, O. D.; Villabona, A.; Schulze, S.; Hietschold, M.; Zahn, D. R. T. *Rev. Sci. Instrum.* **2012,** *83,* 123708. doi:10.1063/1.4770140
39. Saito, Y.; Murakami, T.; Inouye, Y.; Kawata, S. *Chem. Lett.* **2005,** *34,* 920–921. doi:10.1246/cl.2005.920

40. Brejna, P. R.; Griffiths, P. R. *Appl. Spectrosc.* **2010,** *64,* 493–499.
doi:10.1366/000370210791211682
41. De Angelis, F.; Das, G.; Candeloro, P.; Patrini, M.; Galli, M.; Bek, A.;
Lazzarino, M.; Maksymov, I.; Liberale, C.; Andreani, L. C.;
Di Fabrizio, E. *Nat. Nanotechnol.* **2010,** *5,* 67–72.
doi:10.1038/nnano.2009.348
42. Farahani, J. N.; Pohl, D. W.; Eisler, H.-J.; Hecht, B. *Phys. Rev. Lett.*
2005, *95,* 017402. doi:10.1103/physrevlett.95.017402
43. Fleischer, M.; Weber-Bargioni, A.; Altoe, M. V. P.; Schwartzberg, A. M.;
Schuck, P. J.; Cabrini, S.; Kern, D. P. *ACS Nano* **2011,** *5,* 2570–2579.
doi:10.1021/nn102199u
44. Fujita, Y.; Walke, P.; De Feyter, S.; Uji-i, H. *Jpn. J. Appl. Phys.* **2016,**
55, 08NA02. doi:10.7567/jjap.55.08na02
45. Eisele, M.; Krüger, M.; Schenk, M.; Ziegler, A.; Hommelhoff, P.
Rev. Sci. Instrum. **2011,** *82,* 026101. doi:10.1063/1.3534078
46. Lopes, M.; Toury, T.; de La Chapelle, M. L.; Bonaccorso, F.;
Giuseppe Gucciardi, P. *Rev. Sci. Instrum.* **2013,** *84,* 073702.
doi:10.1063/1.4812365
47. James, D. F. *J. Fluid Mech.* **1974,** *63,* 657–664.
doi:10.1017/s0022112074002126
48. Baykul, M. C. *Mater. Sci. Eng., B* **2000,** *74,* 229–233.
doi:10.1016/s0921-5107(99)00566-8
49. Wang, X.; Liu, Z.; Zhuang, M.-D.; Zhang, H.-M.; Wang, X.; Xie, Z.-X.;
Wu, D.-Y.; Ren, B.; Tian, Z.-Q. *Appl. Phys. Lett.* **2007,** *91,* 101105.
doi:10.1063/1.2776860
50. Foti, A.; D'Andrea, C.; Bonaccorso, F.; Lanza, M.; Calogero, G.;
Messina, E.; Maragò, O. M.; Fazio, B.; Gucciardi, P. G. *Plasmonics*
2013, *8,* 13–23. doi:10.1007/s11468-012-9371-3
51. Qian, H.; Hsu, S.-W.; Gurunatha, K.; Riley, C. T.; Zhao, J.; Lu, D.;
Tao, A. R.; Liu, Z. *Nat. Photonics* **2018,** *12,* 485–488.
doi:10.1038/s41566-018-0216-2
52. Mertens, J.; Kleemann, M.-E.; Chikkaraddy, R.; Narang, P.;
Baumberg, J. J. *Nano Lett.* **2017,** *17,* 2568–2574.
doi:10.1021/acs.nanolett.7b00332
53. Pettinger, B.; Domke, K. F.; Zhang, D.; Schuster, R.; Ertl, G.
Phys. Rev. B **2007,** *76,* 113409. doi:10.1103/physrevb.76.113409
54. Wang, X.; Braun, K.; Zhang, D.; Peisert, H.; Adler, H.; Chassé, T.;
Meixner, A. J. *ACS Nano* **2015,** *9,* 8176–8183.
doi:10.1021/acsnano.5b02361
55. Carles, R.; Bayle, M.; Benzo, P.; Benassayag, G.; Bonafos, C.;
Cacciato, G.; Privitera, V. *Phys. Rev. B* **2015,** *92,* 174302.
doi:10.1103/physrevb.92.174302
56. Hugall, J. T.; Baumberg, J. J. *Nano Lett.* **2015,** *15,* 2600–2604.
doi:10.1021/acs.nanolett.5b00146
57. Sanders, A.; Bowman, R. W.; Zhang, L.; Turek, V.; Sigle, D. O.;
Lombardi, A.; Weller, L.; Baumberg, J. J. *Appl. Phys. Lett.* **2016,** *109,*
153110. doi:10.1063/1.4964601
58. Schweppe, H.; Winter, J. Madder and Alizarin. In *Artists' Pigments;*
West Fitzhugh, E., Ed.; Oxford University Press: Oxford, United
Kingdom, 1997; pp 109–134.
59. Chiti, F.; Dobson, C. M. *Annu. Rev. Biochem.* **2006,** *75,* 333–366.
doi:10.1146/annurev.biochem.75.101304.123901
60. Cañamares, M. V.; Chenal, C.; Birke, R. L.; Lombardi, J. R.
J. Phys. Chem. C **2008,** *112,* 20295–20300. doi:10.1021/jp807807j
61. Kudelski, A. *Chem. Phys. Lett.* **2005,** *414,* 271–275.
doi:10.1016/j.cplett.2005.08.075
62. Holmgren, A.; Wu, L.; Forsling, W. *Spectrochim. Acta, Part A* **1999,** *55,*
1721–1730. doi:10.1016/s1386-1425(98)00342-4
63. D'Andrea, C.; Fazio, B.; Gucciardi, P. G.; Giordano, M. C.; Martella, C.;
Chiappe, D.; Toma, A.; Buatier de Mongeot, F.; Tantussi, F.;
Vasanthakumar, P.; Fuso, F.; Allegrini, M. *J. Phys. Chem. C* **2014,** *118,*
8571–8580. doi:10.1021/jp5007236
64. Tatini, F.; Pugliese, A. M.; Traini, C.; Niccoli, S.; Maraula, G.;
Ed Dami, T.; Mannini, B.; Scartabelli, T.; Pedata, F.; Casamenti, F.;
Chiti, F. *Neurobiol. Aging* **2013,** *34,* 2100–2109.
doi:10.1016/j.neurobiolaging.2013.03.020
65. Campioni, S.; Mannini, B.; Zampagni, M.; Pensalfini, A.; Parrini, C.;
Evangelisti, E.; Relini, A.; Stefani, M.; Dobson, C. M.; Cecchi, C.;
Chiti, F. *Nat. Chem. Biol.* **2010,** *6,* 140–147. doi:10.1038/nchembio.283
66. van den Akker, C. C.; Deckert-Gaudig, T.; Schleeger, M.;
Velikov, K. P.; Deckert, V.; Bonn, M.; Koenderink, G. H. *Small* **2015,**
11, 4131–4139. doi:10.1002/smll.201500562
67. Deckert-Gaudig, T.; Kurouski, D.; Hedegaard, M. A. B.; Singh, P.;
Lednev, I. K.; Deckert, V. *Sci. Rep.* **2016,** *6,* 33575.
doi:10.1038/srep33575
68. Kurouski, D.; Deckert-Gaudig, T.; Deckert, V.; Lednev, I. K. *Biophys. J.*
2014, *106,* 263–271. doi:10.1016/j.bpj.2013.10.040
69. Cleary, J. P.; Walsh, D. M.; Hofmeister, J. J.; Shankar, G. M.;
Kuskowski, M. A.; Selkoe, D. J.; Ashe, K. H. *Nat. Neurosci.* **2005,** *8,*
79–84. doi:10.1038/nn1372
70. D'Andrea, C.; Foti, A.; Cottat, M.; Banchelli, M.; Capitini, C.;
Barreca, F.; Canale, C.; de Angelis, M.; Relini, A.; Maragò, O. M.;
Pini, R.; Chiti, F.; Gucciardi, P. G.; Matteini, P. *Small* **2018,** *14,*
1800890. doi:10.1002/smll.201800890
71. Patane, S.; Gucciardi, P. G.; Labardi, M.; Allegrini, M.
Riv. Nuovo Cimento Soc. Ital. Fis. **2004,** *27,* 1–46.
72. Bhattarai, A.; Joly, A. G.; Hess, W. P.; El-Khoury, P. Z. *Nano Lett.*
2017, *17,* 7131–7137. doi:10.1021/acs.nanolett.7b04027

License and Terms

Fabrication of silver nanoisland films by pulsed laser deposition for surface-enhanced Raman spectroscopy

Bogusław Budner, Mariusz Kuźma, Barbara Nasiłowska, Bartosz Bartosewicz, Malwina Liszewska and Bartłomiej J. Jankiewicz[*]

Abstract

The results of studies on the fabrication and characterization of silver nanoisland films (SNIFs) using pulsed laser deposition (PLD) and the evaluation of these films as potential surface-enhanced Raman scattering (SERS) substrates are reported. The SNIFs with thicknesses in a range of 4.7 ± 0.2 nm to 143.2 ± 0.2 nm were deposited under different conditions on silicon substrates. Size and morphology of the fabricated silver nanoislands mainly depend on the substrate temperature, and number and energy of the laser pulses. SERS properties of the fabricated films were evaluated by measuring SERS spectra of *para*-mercaptoaniline (pMA) molecules adsorbed on them. SERS enhancement factors are shown to depend on the SNIF morphology, which is modified by changes of the deposition conditions. The highest enhancement factor in the range of 10^5 was achieved for SNIFs that have oval and circular silver nanoislands with small distances between them.

Introduction

In recent years, SERS has been intensively investigated as a sensing tool in many applications [1-3]. Of particular interest is the use of SERS as a method for highly sensitive detection of hazardous materials such as chemical and biological agents or explosive materials [4,5]. However, despite many studies SERS remains mainly a laboratory technique. To bring it closer to real-life applications there is a need to develop cheap, reliable, reproducible and efficient SERS substrates. The SERS effect is generally assumed to mainly originate in the electromagnetic field enhancement caused by a localized surface plasmon excitation in nanostructures through the incident laser light. With respect to the substrate. It depends on the size, shape, and arrangements of nanostructures, the material they are made of and the surrounding medium [6]. One of the easiest nanostructures to produce are metallic nanoparticles (NPs). Alone or in composites with other materials, they find numerous applications in plasmonic photocatalysis [7-9], photovoltaics [10] or optical sensing through localized surface plasmon resonance

(LSPR) [11]. It is therefore not surprising that quite a number of studies have been initiated and performed in order to design and fabricate highly active SERS substrates based on metallic nanoparticles and nanoparticle films [12-14]. Metallic NPs of different sizes and shapes are prepared in solution mainly by chemical synthesis using various reducing agents and conditions [13]. However, physical methods such as laser ablation are also often used [15]. Other examples of nanoparticle fabrication using physical methods include fabrication of nanostructured silver films by electron-beam evaporation [16], gas aggregation [17] and radio-frequency sputtering [18]. The advantages of certain physical methods over chemical methods include that there is no reagent contamination and that the monodispersity of fabricated NPs can be controlled very well [13].

One of the less commonly used physical methods for the fabrication of SERS active gold and silver nanoisland films is pulsed laser deposition (PLD) [19-25]. In PLD, the materials are deposited on a substrate through laser ablation from a target located opposite to the substrate. Deposition is typically performed in vacuum [20] or argon atmosphere [19] and by the change of parameters such as laser wavelength, pulse duration or laser fluence it is possible to modify the structure of the fabricated nanoislands. Until now, gold and silver nanoisland films have been fabricated by PLD using different lasers with different wavelengths and parameters [19-25]. The most commonly used lasers are KrF excimer lasers with a wavelength of 248 nm [20-24], however other wavelengths from UV (193 nm, 266 nm, 308 nm, 355 nm), through vis (527 nm, 532 nm [19]) to IR (1064 nm) have also been used. Even though several studies were reported on the PLD fabrication of plasmonic metal films, there are only a few recent studies discussing an influence of a wider range of deposition process parameters on the morphology and optical properties of the films [19]. There are no studies that correlate a high number of PLD process parameters to the SERS properties of fabricated plasmonic metal nanoislands films.

Herein, we report the results of studies on the influence of several parameters of the fabrication of silver nanoisland films (SNIFs) using PLD on their morphology, optical and SERS enhancement properties. We first describe the PLD fabrication process and the influence of the deposition process parameters on the morphology of the fabricated films determined by SEM and AFM measurements. Then, we present the results of measurements of the chemical composition of the fabricated SNIFs by using X-ray photoelectron spectroscopy (XPS) and their optical properties by using UV–vis spectroscopy. Finally, we describe the SERS performance of SNIFs in the measurements of *para*-mercaptoaniline (pMA) molecules.

Results and Discussion
Preparation of silver nanoisland films

We investigated ten samples with silver nanoisland films deposited under different conditions, designated "A" to "I". The deposition processes were carried out using an ArF excimer laser (wavelength 193 nm) at the same pressure and laser repetition rate but at different temperatures of the resistively heated furnace on which the substrates were mounted (room temperature (RT), 190 ± 3 °C, 340 ± 3 °C), different numbers of laser pulses (1000, 2000, 4000, 8000, 16000) and with two laser fluence values (5.56 ± 0.37 J/cm^2 or 2.52 ± 0.17 J/cm^2) (Table 1).

Temperature is the most important factor influencing the formation of SNIFs on the silicon substrates. An increase in the temperature of the substrate increases the kinetic energy of the silver atoms and results in a higher ordering of the structure, while the applied amount of laser pulses allows for the control of the dimensions of the obtained silver nanoislands.

In all experiments, the same laser repetition of 5 Hz was used. Increase or decrease of the repetition rate of the laser has a similar effect on the morphology as changing the laser pulse energy. The low laser repetition rate adopted in the experiment allowed

Table 1: The parameters used during the deposition of the SNIFs by PLD (repetition rate 5 Hz; pressure 4.6×10^{-5} mbar).

sample	laser fluence [J/cm^2]	number of laser pulses	temperature [°C]	calculated thickness of the layer [nm]
A	5.56 ± 0.37	1000	190 ± 3	9.0 ± 0.2
B	5.56 ± 0.37	2000	190 ± 3	17.9 ± 0.2
C	5.56 ± 0.37	4000	190 ± 3	35.8 ± 0.2
D	5.56 ± 0.37	8000	190 ± 3	71.6 ± 0.2
E	5.56 ± 0.37	16000	190 ± 3	143.2 ± 0.2
F	2.52 ± 0.17	1000	190 ± 3	4.7 ± 0.2
G	2.52 ± 0.17	2000	190 ± 3	9.3 ± 0.2
H	2.52 ± 0.17	1000	340 ± 3	4.7 ± 0.2
I	2.52 ± 0.17	2000	340 ± 3	9.3 ± 0.2

us to examine the influence of other deposition conditions on the structure of SNIFs produced. The applied laser fluence and the number of laser pulses affect the structural parameters of the obtained SNIFs, such as the size and spacing of the silver nanoislands.

Calculations of the growth rate of silver nanoisland films per laser pulse

The thickness of the silver nanoisland films as a function of the number of applied laser pulses is shown in Figure 1. The plot
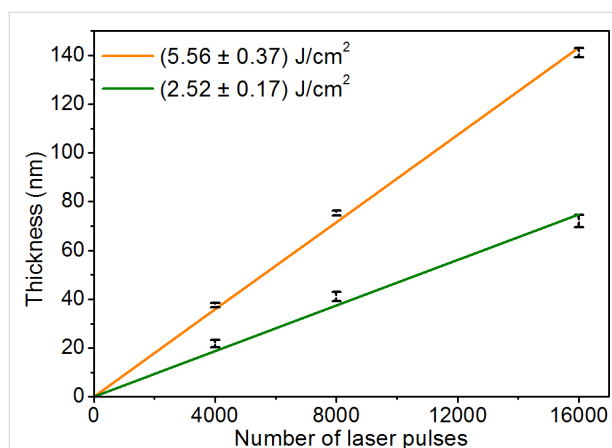

Figure 1: Thickness of the silver nanoisland films as a function of the number of applied laser pulses. Results obtained based on the AFM measurements of the reference samples prepared for laser fluences of 5.56 ± 0.37 J/cm^2 and 2.52 ± 0.17 J/cm^2.

was made based on AFM measurements of reference Si samples with silver films deposited at room temperature for both fluences of laser radiation used (three samples for each fluence). The reference silver films had different thicknesses depending on the number of laser pulses used (4000, 8000, 16000 pulses). The dependence of layer thickness from the number of laser pulses was approximated by a linear function.

The growth rate of the silver films was calculated as the directional coefficient of the approximation function. In the case when the fluence of the laser radiation was 5.56 ± 0.37 J/cm^2, the calculated layer growth rate was 9.0 ± 0.2 nm per 1000 laser pulses. When the laser fluence was about half as low, 2.52 ± 0.17 J/cm^2, the calculated growth rate was 4.7 ± 0.2 nm per 1000 laser pulses. The growth rates achieved permit calculation of the approximate thickness of the silver nanoisland films obtained (Table 1). Depending on the number of laser pulses used, the estimated thickness of the deposited layers ranges approximately from 4.7 ± 0.2 nm to 142 ± 0.2 nm (Table 1).

Morphology and dimensions of silver nanoisland films

SEM images of the deposited silver nanoisland films are shown in Figure 2. In the case of silver deposition without heating the substrate (Figure S1 in Supporting Information File 1), the obtained silver film is continuous. In other cases, when the substrates are heated to 190 ± 3 °C and 340 ± 3 °C, silver
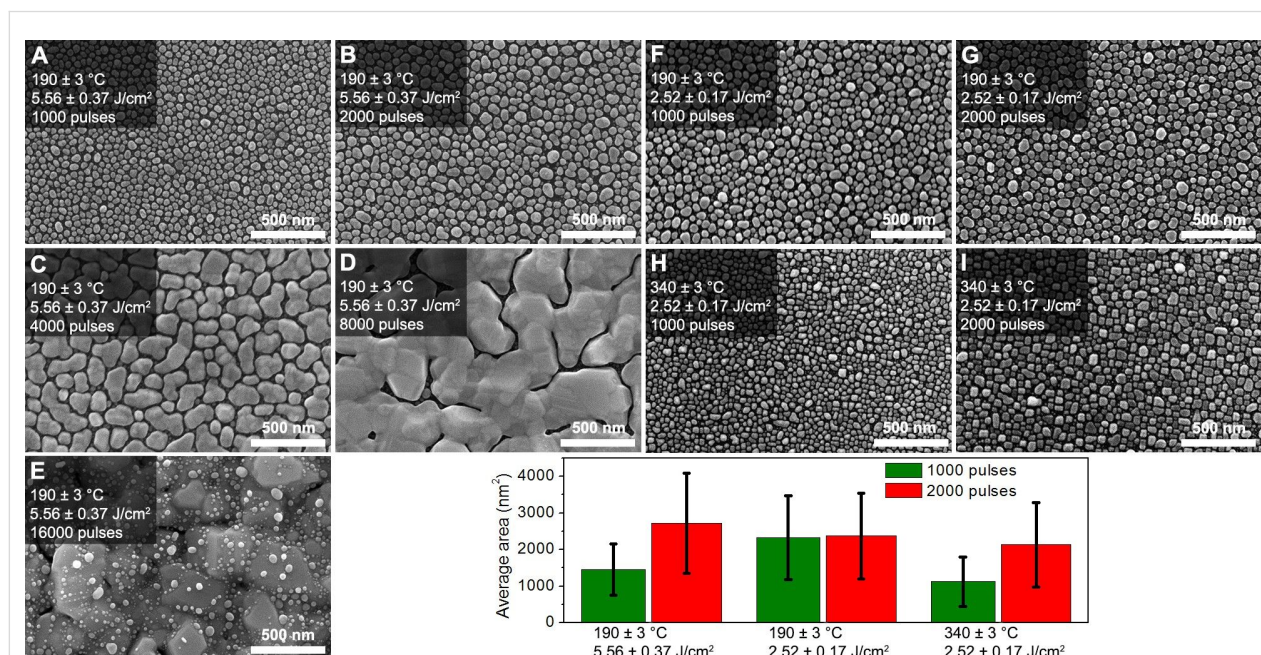

Figure 2: SEM images of the nanostructured silver films deposited on Si substrates by the PLD method using different process parameters. A bar graph showing the average surface of the silver nanoislands as a function of the deposition parameters for 1000 and 2000 laser pulses.

nanoisland films are formed. This effect is related to the Volmer–Weber island growth model [26]. The thermal energy supplied to the silver atoms increases their kinetic energy and thus enables their diffusion and ordering on the surface of the substrate. The ordering of nanoislands, their shape and the homogeneity, strongly depends on the temperature. In the case when the temperature of the furnace is 190 ± 3 °C and the number of pulses does not exceed 2000 the shape of the silver nanoislands resembles the oval shape. At a temperature of 340 ± 3 °C, the islands that are formed have a clearly cubic shape (comparing Figure 2F to 2H and 2G to 2I) which is related to different dynamics of the layer growth process and translates into their higher crystallization.

The dimensions of the silver nanoislands are determined by the number of laser pulses used during deposition. Island dimensions increase from about 40 nm for sample A (Figure 2A) to 300 nm for sample C (Figure 2C). In the case of 4000 laser pulses for sample C, the coalescence of neighboring islands into larger structures with elongated shape (Figure 2C) is also visible. After 8000 laser pulses, the embedded silver islands are already that large that almost all of them are connected and a semicontinuous layer with an irregular structure is formed (Figure 2D). After 16000 laser pulses the nucleation and growth of silver nanoislands occurs on the semicontinuous silver layer formed earlier (Figure 2E). The change of laser fluence from 5.56 ± 0.37 J/cm^2 to 2.52 ± 0.17 J/cm^2 does not cause noticeable changes in the shape of the silver islands (comparing Figure 2A to Figure 2F and Figure 2B to Figure 2G), but it affects the size of the islands. The smaller fluence leads to smaller increase in layer thickness. Hence, the islands obtained have a slightly smaller size (comparing Figure 2B to Figure 2G).

The distributions of the surface areas of the fabricated silver nanoislands were determined based on the SEM images. For silver layers deposited with 1000 and 2000 laser pulses, the average surfaces area values of silver nanoislands were calculated. The analysis was not carried out for samples D and E because they can be characterized as continuous or semicontinuous films. The results are shown on Figure 2 together with error bars of one standard deviation from the average value of the silver nanoislands surface. The calculated average area of the silver nanoislands is 1448 ± 701 nm^2, 2324 ± 1141 nm^2 and 1126 ± 674 nm^2 for samples A, F and H, respectively, prepared using 1000 laser pulses (green bars) and 2717 ± 1268 m^2, 2375 ± 1169 nm^2 and 2132 ± 1155 nm^2 for the samples B, G and I, respectively, prepared using 2000 laser pulses (red bars). As can be seen from the presented data, both fluence and temperature of the resistively heated furnace have a large impact on the average surface area of the obtained silver nanoislands.

After the reduction of the laser fluence by almost one half, which results in a proportional reduction of the growth rate of the layers, the average area of the silver islands is greater than one would expect. The lower fluence of laser radiation while maintaining the same temperature of the substrate (190 ± 3 °C) favors the growth of silver nanoislands with a larger area. In addition, the average area of silver islands for 1000 and 2000 laser pulses are also very similar. The process of silver nanoisland growth is even different when the furnace temperature rises to 340 ± 3 °C. Under these conditions, the average area of silver islands obtained for 2000 laser pulses is almost twice as high as for 1000 laser pulses. In addition, the average surface area of the obtained silver islands with the same number of laser pulses is smaller compared to the case of layer growth at a lower temperature.

A detailed analysis of surface distribution of silver nanoislands for samples A, B, F, G, H and I are shown in Figure 3 in the form of histograms. The calculated areas of silver nanoislands were grouped in compartments with a width of 100 nm^2. The distribution of the surface of the silver islands varies from 0 to 6050 nm^2. The dominant area of the silver nanoislands taken as the maximum of the histogram is about 1050, 2150, 1850, 1950, 850 and 1450 nm^2 respectively for samples A, B, F, G, H and I. The narrowest distributions of the surface area of the silver nanoislands were obtained for samples A and H with SNIFs deposited using the smallest number of laser pulses. Comparing the histogram obtained for sample H with samples F or A, it is
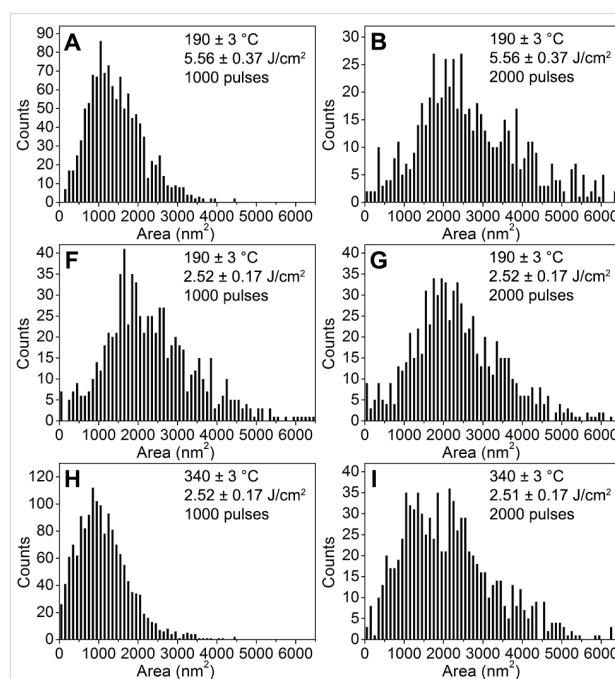
Figure 3: Histograms of the silver nanoisland surface areas made on the basis of SEM images.

also apparent that the deposition of silver layers on substrates with a higher temperature leads to the formation of more homogeneous and smaller silver nanoislands.

We also assume that the deposition conditions of the SNIFs determine the distances between the Ag nanoislands and the formation of so called hot spots. These areas are created in places where the distances between neighboring particles are equal to 2–5 nm. The results of the SERS measurement discussed in further sections of this article suggest that the distances between the silver nanoislands are increasing as the temperature of the substrate increases. This conclusion is consistent with the observed reduction of the enhancement factor (EF) achieved for the Raman signal when the substrate temperature rises.

Chemical composition of the silver nanoisland films

The chemical composition of the PLD-deposited silver nanoisland films was investigated by using XPS spectroscopy. The results of XPS measurements are shown in Figure 4. The XPS spectrum registered over a wide range of binding energy indicates that in addition to silver there are small amounts of carbon and oxygen impurities. These impurities may be located on the silicon substrates used. The position, shape and half-width of peaks registered for the Ag 3d band are typical for silver in metallic form: Ag $3d_{3/2}$ − 374.16 eV, FWHM 0.97 eV; Ag $3d_{5/2}$ − 368.16 eV, FWHM 0.96 eV. This is also confirmed by the spectra of the Auger band, which is typical for metallic silver [27]. The metallic form of silver has also been confirmed by comparing the recorded spectra of the sample with the spectra recorded for Ag foil with 99.95% purity. XPS studies there-

fore confirm that silver deposited by the PLD method does not oxidize during deposition under vacuum conditions.

Optical properties of fabricated Ag nanoisland films

The UV–vis spectra of fabricated silver nanoisland films are shown in Figure 5. In the case of a continuous layer of silver (4000 pulses, RT), the monotonically increase of the reflectance is visible as the wavelength increases. Samples D and E, with the thickest layers of Ag, show similar shapes of the UV–vis spectra. These samples, however, have a lower reflectance in the range of 350 to 850 nm and local minima at around 540 nm and 370 nm, respectively.
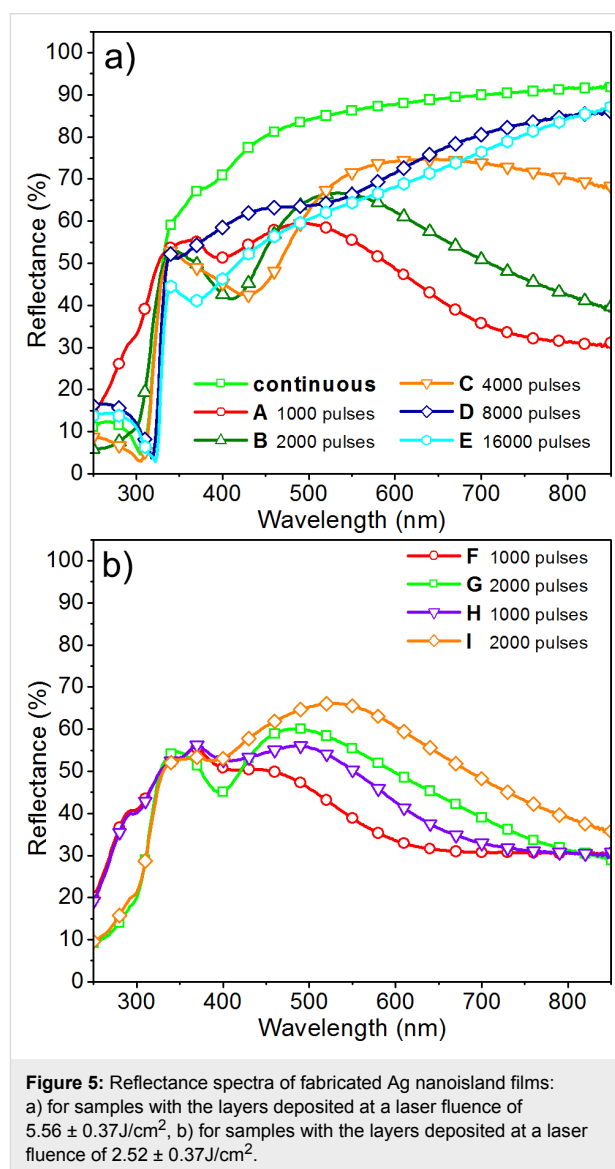
Figure 5: Reflectance spectra of fabricated Ag nanoisland films: a) for samples with the layers deposited at a laser fluence of 5.56 ± 0.37J/cm^2, b) for samples with the layers deposited at a laser fluence of 2.52 ± 0.37J/cm^2.

The samples with the smallest dimensions of silver nanoislands (samples A, B, F, G, H, and I) have completely different shapes
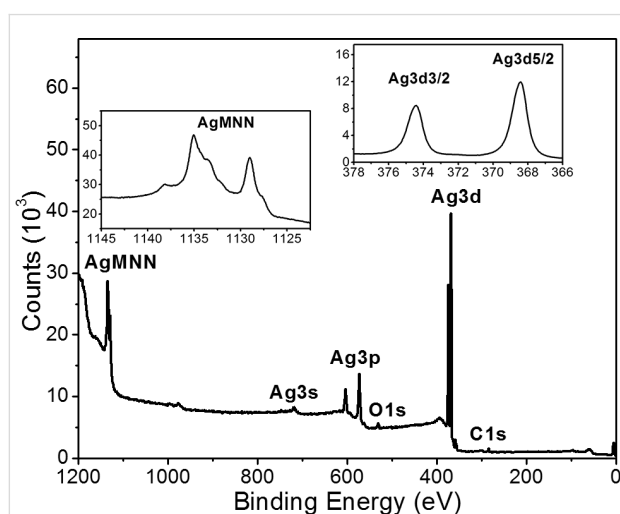

Figure 4: XPS spectra of silver nanoisland films deposited on the Si substrate by laser ablation (PLD) registered in a wide range of binding energy, and Ag 3d and Ag-MNN Auger band registered in a narrow range of energy (insert).

of spectra. These samples have a much lower reflectance in the range of 350 to 850 nm with one characteristic minimum between 400 and 430 nm, which corresponds to plasmon resonance of Ag NPs. The small shift of the plasmon resonance peak may be related to rather small variations of the size of particles between samples obtained using various deposition process parameters. Then reflectance increases and reaches a maximum in the range of 450 to 520 nm and decreases again towards the infrared region. The reflectance above 500 nm depends on the number of laser pulses and the temperature of the substrate and increases with the increase in the number of pulses and the temperature of the substrates. This is because of the growing size of the silver nanoislands and the strong coupling between them. The strange behavior of samples B, G and I at lower wavelengths (270–280 nm) may be associated with the optical properties of the silicon substrate. Because silicon has the maximum of reflectance in this area, its effect is visible in the spectra of the thinnest silver films.

SERS activity of fabricated silver nanoisland films

All fabricated Ag films were tested to determine their suitability for SERS measurements using pMA as a test analyte. An example of averaged SERS spectra for sample B is presented in Figure 6. The black line represents the average spectrum and the red shade represents the standard deviation around the average spectrum. This spectrum was obtained as a result of averaging the SERS spectra from 351 measurement points.

For registered maps composed of 351 measurement points a statistical analysis was made determining the average intensity of the peak at 1080 cm^{-1} and the standard deviation of the peak intensity. Then based on the standard deviation of the 1080 cm^{-1} peak intensity, for each measurement, the relative intensity deviation was calculated. The evaluation of the aver-
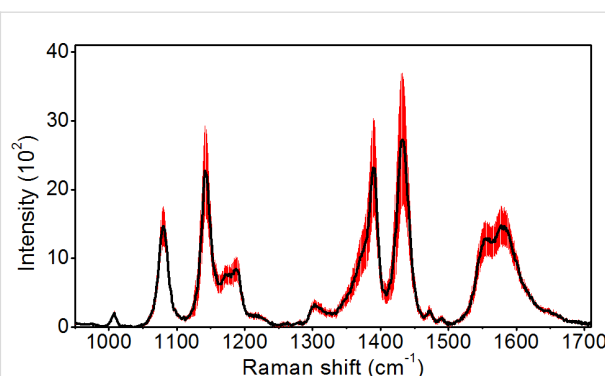
Figure 6: SERS spectrum recorded for sample B (black line – the average SERS spectrum; red area – the standard deviation of the signal.

age intensity of the 1080 cm^{-1} peak and its relative intensity deviation allows us to determine which samples have the highest EF of the Raman signal and the highest EF repeatability. Results of the statistical analysis of the SERS spectra obtained are presented in Table 2.

As we can see from Table 2, the average peak intensity and relative intensity deviation depend on the size of the silver nanoislands obtained. In the case of samples deposited with a laser fluence of 5.56 ± 0.37 J/cm^2 and a substrate temperature of 190 ± 3 °C, with an excitation wavelength of 532 nm the average intensity of the peak increases from 996 for sample A to 2086 for sample D and then slightly decreases to 1446 for sample E. When we compare this data with the SEM images (Figure 2), an increase in the average peak intensity is correlated with the increase in the size of the silver nanostructures, until the connection of silver nanoislands into one structure occurs. With the increase in the size of the silver nanoislands, the relative intensity deviation of the peak increases also. As a result, sample A has the smallest relative intensity deviation

Table 2: Parameters of nanostructured silver layers determined based on SERS measurements.

sample	excitation wavelength 532 nm (measurement parameters: 75 µW, 1 s)			Excitation wavelength 633 nm (measurement parameters: 27 µW, 5 s)		
	average intensity of peak 1080 cm^{-1}	relative intensity dev. (%)	EF (×10^3)	average intensity of peak 1080 cm^{-1}	relative intensity dev. (%)	EF (×10^3)
A	996	11	276.3	2141	21	25.3
B	1455	19	403.7	3098	17	36.6
C	1886	18	523.4	2637	52	31.1
D	2086	68	578.8	1375	67	16.2
E	1446	29	401.4	1840	51	21.7
F	843	12	233.8	1427	20	16.9
G	2440	17	677.2	4673	20	55.2
H	474	6	131.5	611	6	7.2
I	757	7	210.1	1000	6	11.8

value of 11%, whereas for sample D this parameter reaches the highest value of 68%. In the case of sample E having a smaller average intensity of the peak at 1080 cm^{-1}, the relative intensity deviation also decreases to 29%. This means that the layers with the smallest size of the silver nanoislands have the highest EF reproducibility, but at the same time they have a smaller EF of the Raman signal. A similar trend in changes in the intensity of the peak at 1080 cm^{-1} is visible for 633 nm excitation. In this case, however, sample B has the highest intensity of the peak at 1080 cm^{-1} and then it decreases when the dimensions of the silver nanoislands increase. Also, the relative intensity deviation values obtained for 633 nm excitation are very similar to the values obtained for 532 nm excitation.

In the case of a lower fluence of the laser radiation 2.52 ± 0.17 J/cm^2 and the two temperatures of the substrate 190 ± 3 °C and 340 ± 3 °C, the situation is more complicated. For both excitation wavelengths, the highest 1080 cm^{-1} peak intensity was obtained for sample G (2440 and 4673 for excitation wavelengths of 533 and 633 nm, respectively). These values are also the largest in the group of all examined samples. It is important to note that reducing the rate of deposition of silver layers also leads to a reduction of the relative intensity deviation. The relative intensity deviation ranges, for both excitation wavelengths, from 12% to 20%, which means that the layers obtained are characterized by a greater uniformity of the enhancement factor of the Raman signal. In turn, the use of a substrate temperature of 340 ± 3 °C, resulting in a high crystallization of silver nanoislands, leads to a very large decrease in the intensity of the recorded peak for both excitation wavelengths. In this case, however, the obtained relative intensity deviation is the lowest of all samples and ranges from 6 to 7%.

The usefulness of the prepared SNIFs as SERS substrates depends on the enhancement factor achieved for the Raman signal. Several ways to calculate the EF have been reported in the literature [23,28,29]. In the simplest case, the EF is determined as the intensity ratio of the selected peak for the tested compound in the form of a monolayer on the SERS substrates and in the bulk form [23]. This method, however, is very inaccurate because of the different number of measured molecules of the tested substance contained in a monolayer and in the volume of the material. To obtain better results, the EF was calculated based on the Raman spectrum registered for a pMA monolayer adsorbed on the surface of a platinum foil with 99.998% purity. According to literature reports, a pMA monolayer can be made on the surface of platinum, as well as on the surface of silver and gold, a pMA monolayer can be made [30,31]. EF values were calculated according to the procedure described in Supporting Information File 1. In our EF calculations we have assumed that the intensity of the Raman pMA

signal on Pt increased due to the chemical factor of 10^2 and corrected the obtained EF values by this number [32,33].

The values of the EF of the Raman signal for SNIFs were determined based on the intensity of the peak located at 1080 cm^{-1}, which in the pMA molecule corresponds to vibrations of the C–S bond [34]. The calculated average values of EF of the Raman signal are presented in Table 2.

As mentioned above, the average EF of the Raman signal depends on the wavelength of the excitation radiation. In the case of 633 nm excitation, the calculated average EF changes from 7.2 × 10^3 to 55.2 × 10^3 and sample G exhibits the highest EF of 55.2 × 10^3. The average EF obtained for 532 nm excitation is 11-times to 36-times higher than that of the 633 nm excitation and takes values from 131.5 × 10^3 to 677.2 × 10^3. For this excitation wavelength, sample G also shows the largest average EF.

Samples C and D with the largest Ag nanoislands or semicontinuous Ag layers also show high EF values in the range of 532.4 × 10^3 to 578.8 × 10^3. Considering also the relative intensity deviation it can be concluded that deposited SNIFs differ from each other in the number of active SERS sites and their EF. The average SERS activity of a sample with a large number of SERS active sites but with low EF can be lower than the one of a sample with few active sites but with high EF. This may be the reason for the increase of EF and its relative intensity deviation in the case of samples A to F. With the increase in the number of laser pulses silver nanoislands get larger and their mutual distance decreases, which leads to the formation of gaps where the EF can reach higher values. If the deposition goes on, Ag islands start to coalesce and the number of gaps decreases. However, the smaller dimensions of the gaps can lead to higher EF values. At the same time, the SERS active sites are characterized by an increasing spread of EF. Thus the highest EF and relative intensity deviation of sample D can be due to the formation of highly SERS active sites (in the gaps) but with a non-homogenous spatial distribution. The SERS activity of samples F, G and H, I behaves similar to that of samples A–E as the number of laser pulses increases. However, the use of a lower laser fluence during the deposition changes the kinetics of Ag nanoisland growth, which gives a higher average EF value while maintaining the relative intensity deviation at 17%. In contrast, an increase in the temperature of the furnace to the 340 ± 3 °C (samples H and I) leads to a reduction of EF to less than half the value of the layers deposited at the same number of laser pulses but at a lower substrate temperature. A similar dependence of the EF change on the silver layer deposition conditions was observed for the 633 nm excitation. In this case, however, the EF of samples C and D is lower than the values

expected from the results obtained with excitation at 532 nm. In summary, it should be noted that the EF calculation confirms the possibility of using silver nanoisland films deposited by the PLD method on silicon wafers as a SERS substrate.

The SERS spectra of materials adsorbed on the surface of SERS substrates are usually different from Raman spectra of the bulk materials. In our research the SERS spectra of pMA adsorbed on the surface of the SNIFs have a different shape, number of peaks, peak position and intensity than Raman spectra of bulk pMA. A detailed analysis of this phenomenon was made based on Raman and SERS spectra recorded for sample C using three excitation wavelengths of 532, 633 and 785 nm (Figure 7 and Figure 8).
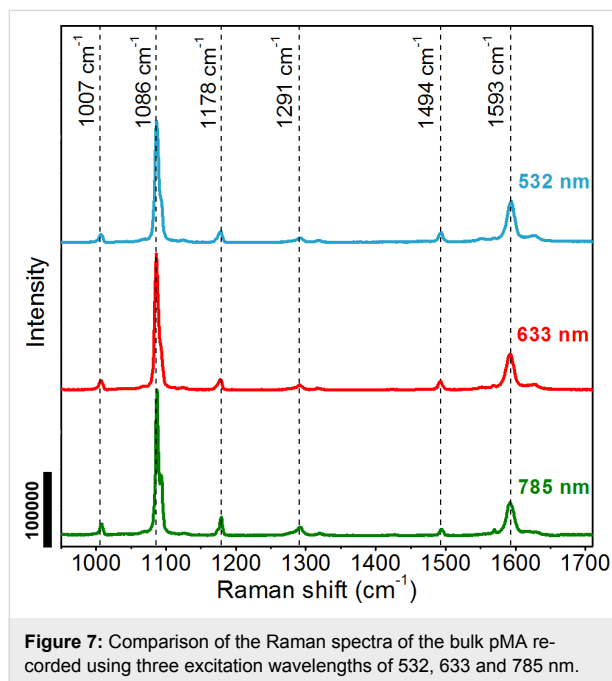

Figure 8: Comparison of the SERS spectra of the pMA monolayer formed on the silver nanoislands film (sample C) recorded using three excitation wavelengths of 532, 633 and 785 nm.

Figure 7: Comparison of the Raman spectra of the bulk pMA recorded using three excitation wavelengths of 532, 633 and 785 nm.

In the Raman spectrum of bulk pMA, recorded in a range of 950 to 1700 cm^{-1}, there are two main peaks with the highest intensities at 1086 and 1593 cm^{-1} and four peaks with low intensities (at 1007, 1178, 1291 and 1494 cm^{-1}) (Figure 7). The recorded Raman spectra are very similar regardless of the excitation wavelength. As shown in Table 3, the peak intensity ratios vary in a small range when the excitation wavelength is changed. For example, the intensity ratio for peaks 1086 and 1007 cm^{-1} is 9.66, 9.79 and 7.17 for 532, 633 and 785 nm excitation respectively. The spread of the intensity ratio of the peak at 1086 cm^{-1} relative to the other peaks is also very similar for all excitation wavelengths.

In the case of monolayers of pMA in sample C, large changes in the shape of the recorded SERS spectra were observed
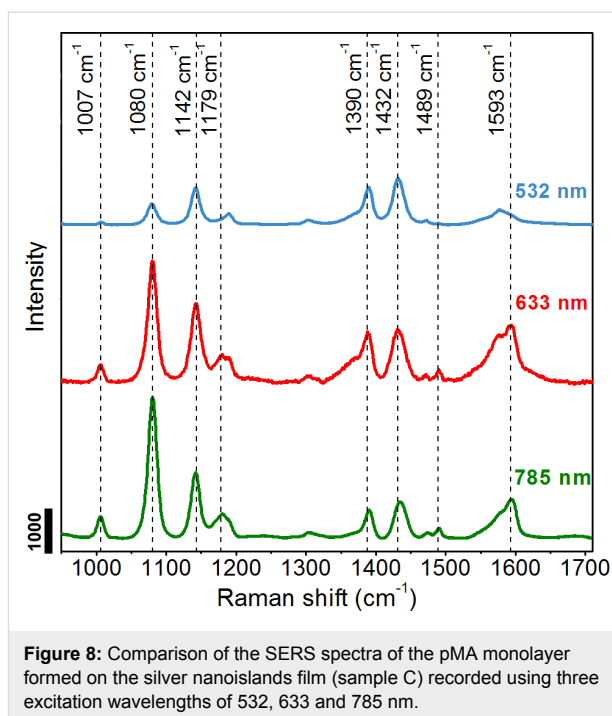
(Figure 8). First, in a range of 950 to 1700 cm^{-1}, the number of peaks increased. In Figure 8 three additional high-intensity peaks appear at 1142, 1390 and 1432 cm^{-1}. All observed peaks also slightly change their position relative to bulk pMA. Most striking, however, is the strong increase in the half-width of the registered peaks and their change of intensity relative to the 1080 cm^{-1} peak. The intensity of the peaks and the ratio of their intensities depend more on the wavelength of the excitation radiation (Table 3). The biggest changes are visible in the case of 532 nm excitation in which the main peak located at 1080 cm^{-1} has a lower intensity than the remaining peaks in the spectrum. This relationship is inverse compared to the other excitation wavelengths. The spectra obtained at 633 nm and 785 nm excitation, however, are very similar to each other [35]. A similar effect was reported by Jian Ye and co-authors for 4-ATP (4-aminothiophenol) and 4-MOTP (4-methoxy-thiophenol) [36]. The authors suggested that because of the change in the wavelength of the excitation laser and the use of the shorter wavelengths an extra non-electromagnetic enhancement effect occurs. This effect is visible during excitation with 633 nm, but the enhancement becomes even more pronounced when the excitation wavelength shifts to 532 nm. As it is known, the total enhancement of the Raman scattering signal in the SERS phenomenon depends on the EM (electromagnetic) and CT (charge transfer) effect. In the CT mechanism the charge transfer between the molecules of the analyte and metallic nanostructures is excited, which leads to a resonant increase in the total EF. When the laser energy matches the energy gap between the HOMO and LUMO of molecules, a direct resonant Raman scat-

Table 3: Comparison of the intensity ratio of selected peaks in the Raman spectrum of bulk pMA and SERS spectrum of pMA monolayer on the surface of sample C.

	pMA monolayer on the surface of sample C		
intensity ratio	excitation wavelength 532 nm	excitation wavelength 633 nm	excitation wavelength 785 nm
I_{1080}/I_{1007}	8.1	6.6	6.4
I_{1080}/I_{1142}	0.6	1.6	2.1
I_{1080}/I_{1179}	1.9	4.3	5.8
I_{1080}/I_{1432}	0.4	2.3	5.1
I_{1080}/I_{1489}	15.9	9.1	15.0
I_{1080}/I_{1593}	1.4	2.1	3.6
	bulk pMA		
intensity ratio	excitation wavelength 532 nm	excitation wavelength 633 nm	excitation wavelength 785 nm
I_{1086}/I_{1007}	9.7	9.8	7.2
I_{1086}/I_{1178}	7.9	8.9	5.2
I_{1086}/I_{1494}	8.4	10.2	9.9
I_{1086}/I_{1593}	2.8	3.4	3.4

tering can be excited in the general CT mechanism. On the other hand a "resonance Raman-like" process can appear as result of an indirect coupling by CT through the metal [37,38]. The authors of the publication [36] attributed the effect of changing the shape of the band in the SERS spectra for the CT effect, the contribution of which to the total enhancement can be different for different Raman bands and depends also on the excitation wavelength as well as the structure of the molecule. However, other publications also suggest the formation of new intense peaks and a shape change of the bands is a result of photo-induced chemical transformation or plasmon-assisted (or "hot electrons") catalytic reaction of molecules [39,40].

Conclusion

In this work, we have shown that pulsed laser deposition (PLD) with simultaneous heating of the substrate permits the controlled fabrication of silver nanoisland films with good SERS properties. Dimensions and shapes of silver nanoislands can be controlled by varying the temperature of the substrate and the fluence of the laser radiation, while the thickness of the deposited layers is determined by the number of laser pulses. This method allows for the production of silver nanoislands with good homogeneity in shape and size in different areas of the films, with very sharp edges on the borders of nanoislands and small distances between them. The results of the XPS measurements confirm that the silver PLD-deposited occurs only in metallic form. Acquisition of Raman spectra of pMA molecules adsorbed on the fabricated silver nanoisland films showed that these nanostructures strongly amplify the Raman signal from adsorbed molecules. The best SERS performance (the highest enhancement factor) was observed for SNIFs deposited

at a temperature of 190 ± 3 °C, laser fluence 2.52 ± 0.17 J/cm^2 and 2000 laser pulses. The average EF of the Raman signal for the substrate prepared under these conditions was 677.2×10^3 for 532 nm excitation and 55.2×10^3 for 633 nm excitation. The highest homogeneity of SNIFs was obtained by using lower laser fluences, smaller numbers of laser pulses and a substrate temperature of 340 ± 3 °C.

Experimental
Deposition of nanostructured layers of silver

Silver nanoisland films were fabricated on an n-type doped silicon substrate with orientation <100> and dimension $10.0 \times 10.0 \times 0.5$ mm. The SNIFs were prepared by using pulse laser deposition (PLD) with an ArF excimer laser (LPX 305i, Lambda Physik Company). The laser used in the experiment is characterized by the following parameters: $\lambda = 193$ nm, $E = 700$ mJ, $\tau \approx 15$–20 ns.

Deposition was performed in a vacuum chamber at a pressure of around $4.6 \pm 0.65 \times 10^{-5}$ mbar and with different temperatures of the resistively heated furnace in which the substrates were mounted (room temperature (RT), 190 ± 3 °C, 340 ± 3 °C) (Table 1).

A rotating silver target with a purity of 99.95% was used. The laser beam was focused on the target at an incident angle of 45° and the distance between the target and the substrate was constant and equal to 65.0 ± 0.5 mm. The measured area of the laser spot on the surface of the target was 6.12 ± 0.17 mm^2. Laser fluence on the target surface, calculated based on the area of the laser focus and energy of the laser pulse, was

5.56 ± 0.37 J/cm^2 or 2.52 ± 0.17 J/cm^2 (Table 1). Change in fluence of the laser pulse leads to a change in the mass of silver deposited per laser pulse. This, in turn, affects the rate of growth of the layer and the size and shape of the formed silver nanoislands.

Characterization of nanostructured silver layers

The morphology of the deposited silver layers was visualized using a scanning electron microscope (SEM, Quanta 3D FEG, FEI Company). SEM images were also used for the surface analysis of the obtained silver islands. The analysis was carried out in the Gwyddion software dedicated to the processing and visualization of scanning probe microscopy images.

The thickness of the deposited reference silver layers was measured with an atomic force microscope (AFM, NT-MDT Company) in non-contact mode. To perform AFM measurements, the silver layers were removed in random places on the sample by scratching its surface with a sharp needle. A very sharp edge for height (layer thickness) measurements was obtained in this way due to the low adhesion of the silver films to the Si substrate. AFM measurements were carried out in three different areas on the surface of each sample. Then for each sample ten AFM cross sections from different scanning areas were made and averaged. As a result, the average layer thickness and the standard deviation of thickness were determined for each sample. The determined thicknesses of reference silver films were then used to prepare the graph shown in Figure 1.

To determine the chemical composition of the deposited silver layers X-ray photoelectron spectroscopy (XPS) was used (XPS spectrometer, Prevac Company). The measurements were made using an X-ray source equipped with an Al anode emitting X-ray radiation with photon energy of 1486.6 eV. The analysis of registered XPS spectra was performed in the CasaXPS software.

UV–vis reflectance spectra were measured at room temperature using a Lambda 650 UV–vis spectrophotometer (Perkin Elmer), equipped with a 150 mm integrating sphere, in the 250–900 nm spectral range with increment of 2 nm. Due to the lack of transmission through the applied substrates, measurements were carried out on the samples placed behind the integrating sphere. In this configuration the reflectance spectrum was recorded for each sample.

Raman and SERS measurements

Both Raman and SERS measurements were carried out using Renishaw InVia Raman microscope equipped with an EMCCD (1600 × 200 pixels) detector. The Raman signal was acquired using laser radiation with a wavelength of 532, 633 and/or 785 nm. The laser excitation power on the sample depended on the type of measurement and the laser wavelength used. The laser beam was directed to the sample through a 100× (NA = 0.85) objective lens. For the lens used, the diameter of the measuring point from which the Raman signal is recorded was approximately 1 μm. The wavelength of the instrument was calibrated using an internal silicon wafer, and the spectrum was centered at 520.5 cm^{-1}.

Raman spectra of bulk pMA were measured first to compare them with the SERS spectra obtained on SNIFs substrates. For pMA bulk, measurements were made on excitation lengths of 532, 633 and 785 nm. The laser beam power measured on the surface of the pMA bulk was 151 ± 5 μW, 269 ± 11 μW and 464 ± 32 μW for the excitation with 532, 633 and 785 nm, respectively. The acquisition time and the number of acquisitions for all excitation wavelengths were set to 10 s and 5 s, respectively.

For SERS measurements, the pMA monolayers were deposited on the fabricated silver nanoislands. For this purpose, samples with deposited SNIFs were placed in Petri dishes and 2 mL of 0.01 M pMA solution in ethanol was added to the dish. The samples were left in solution for about 60 min. After removing the samples from the solution, they were rinsed twice with pure ethanol and then allowed to dry.

SERS spectra of all samples A–I were recorded using two lasers with wavelengths of 532 and 633 nm. Additionally, for sample C SERS spectra were also recorded at 785 nm excitation. The laser beam power measured on the surface of the samples was 75 ± 3 μW for 532 nm, 27 ± 1 μW for 633 nm excitation, and 464 ± 32 μW for 785 nm excitation (sample C). The acquisition times for a single point were 1 s, 5 s and 0.5 s for 532 nm, 633 nm, and 785 nm excitation wavelengths, respectively. The measurement parameters were adjusted to different nominal output power values of the lasers to obtain a good signal-to-noise ratio for a single measuring point. SERS measurements were made for maps consisting of 351 points per sample. Based on them the average spectrum was obtained and the standard deviation of the signal was determined, which is an indicator of the homogeneity of the deposited layers and Raman signal amplification obtained. Statistical analysis of the intensity of the recorded spectra and their standard deviation were made for the 1080 cm^{-1} peak. The average intensity of the peak calculated based on 351 measurement points and the standard deviation of the intensity allow us to determine which samples have the highest Raman signal amplification and highest homogeneity of the silver nanoisland films. To facilitate the evaluation of the reproducibility of Raman amplification, a calculation of the

relative intensity deviation was also made. These parameters were counted as a ratio of standard deviation intensity and average intensity of the 1080 cm^{-1} peak.

To determine the EF of the Raman signal, the Raman measurements of the pMA adsorbed on the surface of the platinum film were also done. Compared to SERS substrates, obtaining a spectrum with the appropriate signal-to-noise ratio required increasing the laser power and extended measurement time. For the 532 nm excitation, a laser power of 755 ± 26 µW was used and the measurement time for one point was 100 s. In contrast, for the 633 nm excitation, a laser power of ca. 54 ± 2 µW was used and the measurement time for one point was 100 s. In both cases, measurements were taken at several points and the average spectrum was taken as a result. The EF values for the SERS substrate were calculated taking into account coefficients of proportionality arising from different laser power and different measurement times. All spectra were background-corrected before EF calculation.

Supporting Information

Supporting Information File 1

SEM image of continuous Ag film, description of procedure of the determination of the enhancement factor (EF) and Raman spectrum of pMA on platinum foil. [https://www.beilstein-journals.org/bjnano/content/supplementary/2190-4286-10-89-S1.pdf]

Acknowledgements

ORCID® iDs

Bogusław Budner - https://orcid.org/0000-0002-9395-6073
Mariusz Kuźma - https://orcid.org/0000-0001-9865-670X
Barbara Nasiłowska - https://orcid.org/0000-0003-0960-5260
Bartosz Bartosewicz - https://orcid.org/0000-0002-8053-6563
Malwina Liszewska - https://orcid.org/0000-0001-5102-641X
Bartłomiej J. Jankiewicz - https://orcid.org/0000-0002-1172-8764

References

1. Cialla-May, D.; Zheng, X.-S.; Weber, K.; Popp, J. *Chem. Soc. Rev.* **2017,** *46,* 3945–3961. doi:10.1039/c7cs00172j
2. Yu, B.; Ge, M.; Li, P.; Xie, Q.; Yang, L. *Talanta* **2019,** *191,* 1–10. doi:10.1016/j.talanta.2018.08.032
3. Laing, S.; Jamieson, L. E.; Faulds, K.; Graham, D. *Nat. Rev. Chem.* **2017,** *1,* 0060. doi:10.1038/s41570-017-0060
4. Bartosewicz, B.; Andersson, P. O.; Dzięcielewski, I.; Jankiewicz, B.; Weyher, J. L. *Mater. Sci. Semicond. Process.* **2019,** *91,* 97–101. doi:10.1016/j.mssp.2018.11.012
5. Liszewska, M.; Bartosewicz, B.; Budner, B.; Nasiłowska, B.; Szala, M.; Weyher, J. L.; Dzięcielewski, I.; Mierczyk, Z.; Jankiewicz, B. J. *Vib. Spectrosc.* **2019,** *100,* 79–85. doi:10.1016/j.vibspec.2018.11.002
6. Cialla, D.; März, A.; Böhme, R.; Theil, F.; Weber, K.; Schmitt, M.; Popp, J. *Anal. Bioanal. Chem.* **2012,** *403,* 27–54. doi:10.1007/s00216-011-5631-x
7. Wang, P.; Huang, B.; Dai, Y.; Whangbo, M. H. *Phys. Chem. Chem. Phys.* **2012,** *14,* 9813–9825. doi:10.1039/c2cp40823f
8. Valenti, M.; Jonsson, M. P.; Biskos, G.; Schmidt-Ott, A.; Smith, W. A. *J. Mater. Chem. A* **2016,** *4,* 17891–17912. doi:10.1039/c6ta06405a
9. Bricchi, B. R.; Ghidelli, M.; Mascaretti, L.; Zapelli, A.; Russo, V.; Casari, C. S.; Terraneo, G.; Alessandri, I.; Ducati, C.; Li Bassi, A. *Mater. Des.* **2018,** *156,* 311–319. doi:10.1016/j.matdes.2018.06.051
10. Clavero, C. *Nat. Photonics* **2014,** *8,* 95–103. doi:10.1038/nphoton.2013.238
11. Rodrigues, M. S.; Costa, D.; Domingues, R. P.; Apreutesei, M.; Pedrosa, P.; Martin, N.; Correlo, V. M.; Reis, R. L.; Alves, E.; Barradas, N. P.; Sampaio, P.; Borges, J.; Vaz, F. *Appl. Surf. Sci.* **2018,** *438,* 74–83. doi:10.1016/j.apsusc.2017.09.162
12. Ko, H.; Singamaneni, S.; Tsukruk, V. V. *Small* **2008,** *4,* 1576–1599. doi:10.1002/smll.200800337
13. Dhand, C.; Dwivedi, N.; Loh, X. J.; Jie Ying, A. N.; Verma, N. K.; Beuerman, R. W.; Lakshminarayanan, R.; Ramakrishna, S. *RSC Adv.* **2015,** *5,* 105003–105037. doi:10.1039/c5ra19388e
14. Cañamares, M. V.; Garcia-Ramos, J. V.; Sanchez-Cortes, S.; Castillejo, M.; Oujja, M. *J. Colloid Interface Sci.* **2008,** *326,* 103–109. doi:10.1016/j.jcis.2008.06.052
15. Besner, S.; Kabashin, A. V.; Winnik, F. M.; Meunier, M. *Appl. Phys. A: Mater. Sci. Process.* **2008,** *93,* 955–959. doi:10.1007/s00339-008-4773-y
16. Drachev, V. P.; Thoreson, M. D.; Nashine, V.; Khaliullin, E. N.; Ben-Amotz, D.; Davisson, V. J.; Shalaev, V. M. *J. Raman Spectrosc.* **2005,** *36,* 648–656. doi:10.1002/jrs.1356
17. Gracia-Pinilla, M. Á.; Pérez-Tijerina, E.; Antúnez-García, J.; Fernández-Navarro, C.; Tlahuice-Flores, A.; Mejía-Rosales, S.; Montejano-Carrizales, J. M.; José-Yacamán, M. *J. Phys. Chem. C* **2008,** *112,* 13492–13498. doi:10.1021/jp804085q
18. Mandal, S. K.; Roy, R. K.; Pal, A. K. *J. Phys. D: Appl. Phys.* **2002,** *35,* 2198–2205. doi:10.1088/0022-3727/35/17/317
19. Ghidelli, M.; Mascaretti, L.; Bricchi, B. R.; Zapelli, A.; Russo, V.; Casari, C. S.; Li Bassi, A. *Appl. Surf. Sci.* **2018,** *434,* 1064–1073. doi:10.1016/j.apsusc.2017.11.025
20. Kamakshi, K.; Silva, J. P. B.; Sekhar, K. C.; Marslin, G.; Moreira, J. A.; Conde, O.; Almeida, A.; Pereira, M.; Gomes, M. J. M. *Appl. Phys. B: Lasers Opt.* **2016,** *122,* 1–8. doi:10.1007/s00340-016-6385-0
21. D'Andrea, C.; Neri, F.; Ossi, P. M.; Santo, N.; Trusso, S. *Laser Phys.* **2011,** *21,* 818–822. doi:10.1134/s1054660x11070048
22. Verma, S.; Rao, B. T.; Bhartiya, S.; Sathe, V.; Kukreja, L. M. *Appl. Surf. Sci.* **2015,** *346,* 379–387. doi:10.1016/j.apsusc.2015.04.008
23. Fazio, E.; Neri, F.; D'Andrea, C.; Ossi, P. M.; Santo, N.; Trusso, S. *J. Raman Spectrosc.* **2011,** *42,* 1298–1304. doi:10.1002/jrs.2861

24. Agarwal, N. R.; Neri, F.; Trusso, S.; Lucotti, A.; Ossi, P. M.
Appl. Surf. Sci. **2012,** *258,* 9148–9152.
doi:10.1016/j.apsusc.2011.12.030

25. Smyth, C. A.; Mirza, I.; Lunney, J. G.; McCabe, E. M. *Appl. Surf. Sci.*
2013, *264,* 31–35. doi:10.1016/j.apsusc.2012.09.078

26. Koch, R.; Hu, D.; Das, A. K. *Phys. Rev. Lett.* **2005,** *94,* 146101.
doi:10.1103/physrevlett.94.146101

27. http://www.xpsfitting.com/search/label/Silver.

28. Maitani, M. M.; Ohlberg, D. A. A.; Li, Z.; Allara, D. L.; Stewart, D. R.;
Williams, R. S. *J. Am. Chem. Soc.* **2009,** *131,* 6310–6311.
doi:10.1021/ja809347y

29. Taylor, C. E.; Pemberton, J. E.; Goodman, G. G.; Schoenfisch, M. H.
Appl. Spectrosc. **1999,** *53,* 1212–1221.
doi:10.1366/0003702991945687

30. Kudelski, A. *Vib. Spectrosc.* **2005,** *39,* 200–213.
doi:10.1016/j.vibspec.2005.03.005

31. Wu, D.-Y.; Liu, X.-M.; Duan, S.; Xu, X.; Ren, B.; Lin, S.-H.; Tian, Z.-Q.
J. Phys. Chem. C **2008,** *112,* 4195–4204. doi:10.1021/jp0760962

32. Campion, A.; Ivanecky, J. E.; Child, C. M.; Foster, M.
J. Am. Chem. Soc. **1995,** *117,* 11807–11808. doi:10.1021/ja00152a024

33. Weyher, J. L.; Bartosewicz, B.; Dzięcielewski, I.; Krajczewski, J.;
Jankiewicz, B.; Nowak, G.; Kudelski, A. *Appl. Surf. Sci.* **2019,** *466,*
554–561. doi:10.1016/j.apsusc.2018.10.076

34. Zheng, J.; Zhou, Y.; Li, X.; Ji, Y.; Lu, T.; Gu, R. *Langmuir* **2003,** *19,*
632–636. doi:10.1021/la011706p

35. Álvarez-Puebla, R. A. *J. Phys. Chem. Lett.* **2012,** *3,* 857–866.
doi:10.1021/jz201625j

36. Ye, J.; Hutchison, J. A.; Uji-i, H.; Hofkens, J.; Lagae, L.; Maes, G.;
Borghs, G.; Van Dorpe, P. *Nanoscale* **2012,** *4,* 1606–1611.
doi:10.1039/c2nr11805j

37. Osawa, M.; Matsuda, N.; Yoshii, K.; Uchida, I. *J. Phys. Chem.* **1994,**
98, 12702–12707. doi:10.1021/j100099a038

38. Adrian, F. J. *J. Chem. Phys.* **1982,** *77,* 5302–5314.
doi:10.1063/1.443800

39. Huang, Y.-F.; Zhu, H.-P.; Liu, G.-K.; Wu, D.-Y.; Ren, B.; Tian, Z.-Q.
J. Am. Chem. Soc. **2010,** *132,* 9244–9246. doi:10.1021/ja101107z

40. Dong, B.; Fang, Y.; Xia, L.; Xu, H.; Sun, M. *J. Raman Spectrosc.* **2011,**
42, 1205–1206. doi:10.1002/jrs.2937

Correlation of surface-enhanced Raman scattering (SERS) with the surface density of gold nanoparticles: evaluation of the critical number of SERS tags for a detectable signal

Vincenzo Amendola

Full Research Paper

Address:
Department of Chemical Sciences, University of Padova, Padova,
Italy

Email:
Vincenzo Amendola - vincenzo.amendola@unipd.it

Abstract

The use of plasmonic nanotags based on the surface-enhanced Raman scattering (SERS) effect is highly promising for several applications in analytical chemistry, biotechnological assays and nanomedicine. To this end, a crucial parameter is the minimum number of SERS tags that allows for the collection of intense Raman signals under real operating conditions. Here, SERS Au nanotags (AuNTs) based on clustered gold nanoparticles are deposited on a substrate and analyzed in the same region using Raman spectroscopy and transmission electron microscopy. In this way, the Raman spectra and the surface density of the SERS tags are correlated directly, showing that 1 tag/μm^2 is enough to generate an intense signal above the noise level at 633 nm with an excitation power of only 0.65 mW and an acquisition time of just 1 s with a 50× objective. The AuNT density can be even lower than 1 tag/μm^2 when the acquisition time is extended to 10 s, but must be increased to 3 tags/μm^2 when a 20× objective is employed under the same excitation conditions. In addition, in order to observe a linear response, it was found that 10 SERS AuNTs inside the probed area are required. These findings indicate that a better signal-to-noise ratio requires high-magnification optics, while linearity versus tag number can be improved by using low-magnification optics or a high tag density. In general the suitability of plasmonic SERS labels for ultrasensitive analytical and biomedical applications is evident.

Introduction

In surface-enhanced Raman scattering (SERS), the Raman scattering cross-section of molecules adsorbed on the surface of plasmonic nanostructures is enormously increased compared to the same isolated molecules [1-5]. In particular, the SERS enhancement factor can reach values as high as 10^{12}, which can be attributed to two phenomena, the local electric field enhancement due to the surface plasmon resonance of the metal nanostructure (electromagnetic enhancement) and the charge transfer

between the molecule and the metal substrate (chemical enhancement) [6-8]. In addition, given the generally low Raman scattering cross-section of molecules, Raman signals are exceptionally intense when the SERS effect occurs simultaneously with the electronic resonance of the molecule at the excitation wavelength used for Raman spectroscopy, a condition called surface-enhanced resonant Raman scattering [9-12]. Resonant SERS allows the generation of Raman scattering signals as intense as that of fluorescent compounds and, in fact, can be exploited for Raman labelling [13-17]. A SERS tag is typically composed of a plasmonic nanostructure capable of large electromagnetic field enhancement, coated with organic molecules (Raman reporters) resonant at the probe wavelength, where the entire structure is embedded in a stabilizing matrix [13,16-19]. When selectivity is required, the surface of the Raman tag should expose a targeting function for binding the analyte [13,16,17]. When the analytes can be concentrated on a surface or in a well-defined volume, SERS tags allow for the collection of an intense Raman signal revealing the presence of the targeted molecule. Analyte accumulation on a surface may happen, for instance, through a sandwich configuration as in the well-established enzyme-linked immunosorbent assay (ELISA) tests, but the analyte may also be naturally immobilized on a surface, such as an antigen overexpressed in cancerous cell membrane [20-22]. SERS labels are also useful to probe the uptake of nanomaterial inside living cells [23-26].

There are many advantages connected to the use of Raman tags, mostly related to the intensity and narrow bandwidth of their Raman peaks. SERS labels can be even brighter than semiconductor quantum dots; for example, the high intensity allows for detection using only a single nanotag with an ordinary Raman spectrometer [27,28]. The narrowness of the Raman bands allows multiplexing analysis by associating Raman reporters with different, non-overlapping peaks, which serve as a spectroscopic fingerprint that can be associated with different analytes [18,29,30]. Additional favorable features of SERS tags are their photostability, namely the absence of blinking or bleaching, and the possibility to excite in the red or near infrared spectral range, where most matrixes and substrates have low fluorescence background [13,17].

Therefore, due to the increasing demand for ultrasensitive identification and quantification of specific analytes or substrates such as cancerous tissues, SERS tags are the subject of intense investigation and continuous performance improvement in analytical chemistry, nano-biotechnology and nanomedicine [13,15,21,31]. For all of these applications, the crucial parameter is the minimum number of SERS tags required for the detection of an intense signal in real operating conditions [13,18,32,33], which often employ an ordinary micro-Raman

spectroscopy set up [34] or portable Raman spectrometer [35-37]. In recent years, this has fostered a number of studies aimed at quantifying SERS performance from plasmonic nanoparticles dispersed on a substrate [38], inside microcavities [39], or even while monitoring electrochemical reactions [40].

This work reports on the study of SERS tags obtained by laser ablation synthesis in liquid solution (LASiS) of gold (Au) nanoparticles, their coating with three different Raman reporters that are resonant at 633 nm, and their stabilization with a biocompatible and hydrophilic coating. Their performance was tested by correlating the Raman signal to the density of Au nanotags (AuNTs) per unit area, as obtained by transmission electron microscopy (TEM) analysis of the same area probed by Raman spectroscopy. In this way, the minimum number of AuNTs required to generate a detectable signal under ordinary experimental conditions can be identified. In addition, a threshold or minimum number of AuNTs within the probed area that can produce a linear response is identified, which can be obtained more easily with low-magnification optics when the surface density of the SERS tags is as low as a few units per micrometer square. These results contribute to the optimization of the experimental conditions for the use of SERS tags in analytical and biomedical analysis with high sensitivity.

Experimental
Synthesis of Au nanotags
AuNPs with an average diameter of 10 ± 5 nm and log-normal size distribution (see Figure S1 in Supporting Information File 1) were obtained by LASiS using an Nd:YAG laser (1064 nm, 9 ns, 50 Hz) focused to 8 J/cm^2 with a 10 cm focus lens on a 99.9% pure gold plate placed at the bottom of a cell containing a 10^{-4} M NaCl solution in double distilled water [18,19,41]. Dye solutions of either hexacyanin 3 (HITC, perchlorate, Exciton), malachite green (MG, oxalate salt, Sigma-Aldrich) or malachite green isothiocyanate (MGITC, Invitrogen) were added to a 2 nM AuNP solution at a 1:100 volume ratio. After 30 min under mild stirring, an aqueous solution of thiolated polyethylene glycol (PEG, MW 5000, Sigma-Aldrich) was added to the AuNPs with a final concentration of 30 μM. After stirring for 14 h at room temperature, the mixtures were washed with deionized water four times by centrifugation at 3000 rcf for 10 min and finally filtered with hydrophilic 0.45 μm cellulose filters. The reproducibility of the procedure was successfully verified on two distinct batches of MG-labelled AuNTs dispersed in water (Figure S2 in Supporting Information File 1).

The samples for TEM analysis were obtained by mixing the AuNT solution (0.2 mg/mL in Au) 1:5 with a 10 mg/mL aqueous solution of polyvinyl alcohol (PVA, 200,000 M_w, on

average, from Fluka) and depositing one drop on a copper grid coated with a holey carbon film, according to a well-established procedure which serves to prevent particle agglomeration after drying the drop [42].
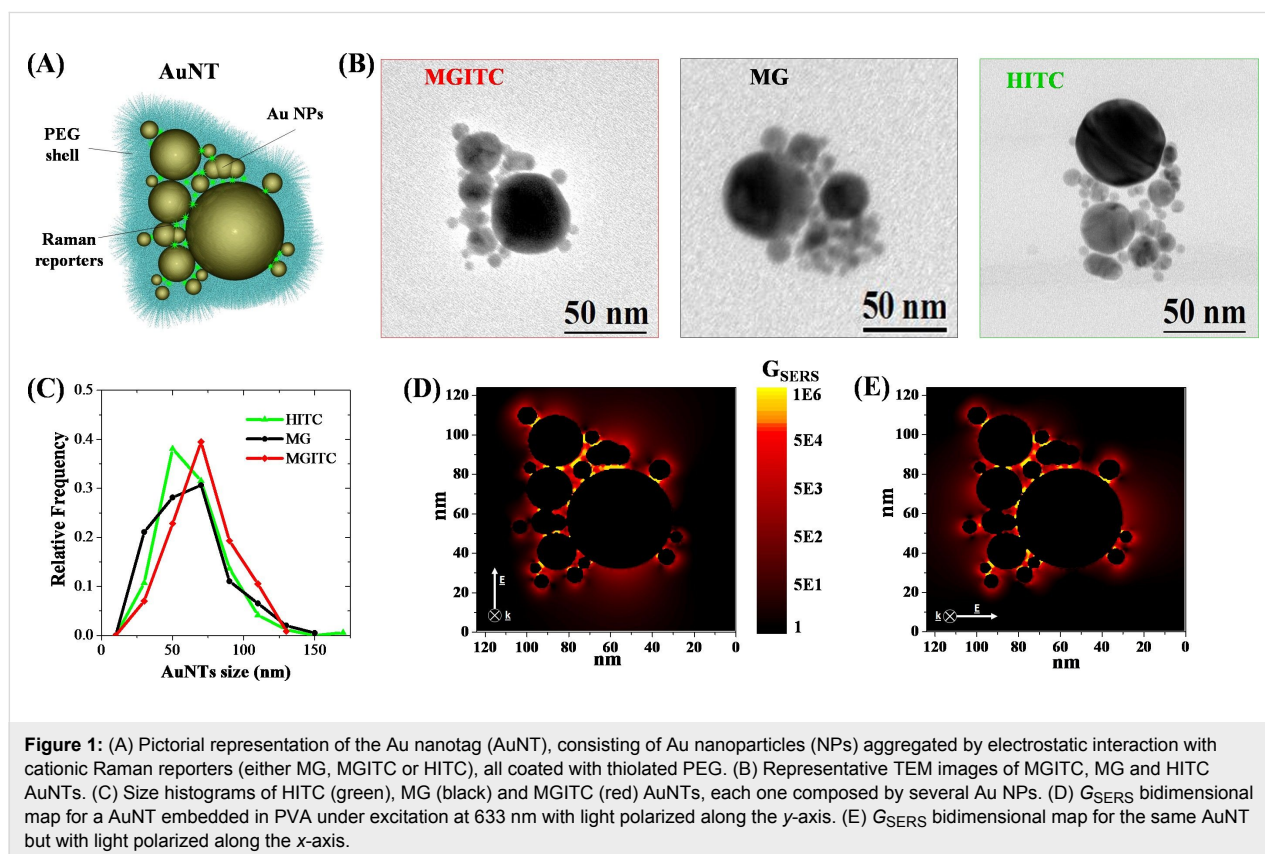
Characterization

UV–visible spectroscopy was performed with a Varian Cary 5 spectrometer in 2 mm optical path length quartz cells. The AuNP concentration was estimated from UV–visible spectra and the application of Mie theory, as previously reported [43]. Transmission electron microscopy (TEM) was performed on an FEI Tecnai G2 12 instrument operating at 100 kV and equipped with a TVIPS CCD camera. The micro-Raman measurements were recorded with a 20× (NA 0.40, 64% coverage) or a 50× (NA 0.75, 100% coverage) Olympus objective on the micro-Raman instrument (CCD detector with 100 mm slits) on the TEM grids containing the AuNTs and using the 633 nm line of a He–Ne laser. The laser power at the entrance pupil of the microscope objective was 0.85 mW, corresponding to 0.65 mW at the output of the microscope objective (measured with a Scientec Vector calorimeter). The Raman signal was collected on an internal silicon chip which could account for small (less than 5%) intensity fluctuations of the Raman spectrometer and allowed for quantification of the noise intensity in the two measurement conditions. The acquisition time was fixed at 100 s.

Numerical calculations

The local field, E_{loc}, was calculated with the discrete dipole approximation (DDA) method using the software DDSCAT 7.1 and the related DDFIELD code [44-46]. A nanoaggregate of Au nanoparticles was created with same structure taken from a representative TEM picture of a real AuNT, and two different polarization directions were considered, namely parallel and perpendicular to the main axis of the nanoaggregate. For metal particles in the 2–200 nm size range, an error smaller than 10% is achieved using a number of dipoles at least of the order of 10^4 and using an interdipole spacing much smaller than the wavelength of interest [44,45,47]. Therefore, in the present case, 4×10^5 dipoles were used for the target, corresponding to an interdipole spacing of less than 0.5 nm.

Results and Discussion

In this study, AuNTs consist of a cluster of Au nanoparticles aggregated in the presence of Raman active molecules, all coated with thiolated PEG (Figure 1A). The AuNTs assemble spontaneously because laser-generated Au nanoparticles are negatively charged and the selected Raman reporters are cationic molecules [19,48]. AuNTs containing MG, MGITC and HITC, examples of which are shown in Figure 1B, have a hierarchical structure with one or more large Au nanoparticles surrounded by smaller particles, all grouped in a nanoaggregate

Figure 1: (A) Pictorial representation of the Au nanotag (AuNT), consisting of Au nanoparticles (NPs) aggregated by electrostatic interaction with cationic Raman reporters (either MG, MGITC or HITC), all coated with thiolated PEG. (B) Representative TEM images of MGITC, MG and HITC AuNTs. (C) Size histograms of HITC (green), MG (black) and MGITC (red) AuNTs, each one composed by several Au NPs. (D) G_{SERS} bidimensional map for a AuNT embedded in PVA under excitation at 633 nm with light polarized along the *y*-axis. (E) G_{SERS} bidimensional map for the same AuNT but with light polarized along the *x*-axis.

with size of the order of tens of nanometers. In particular, the size distribution of the nanoaggregates is similar among the three samples, as shown in Figure 1C, resulting in a comparable mean size of 63 ± 21 nm for HITC, 62 ± 25 nm for MG and 70 ± 22 nm for MGITC.
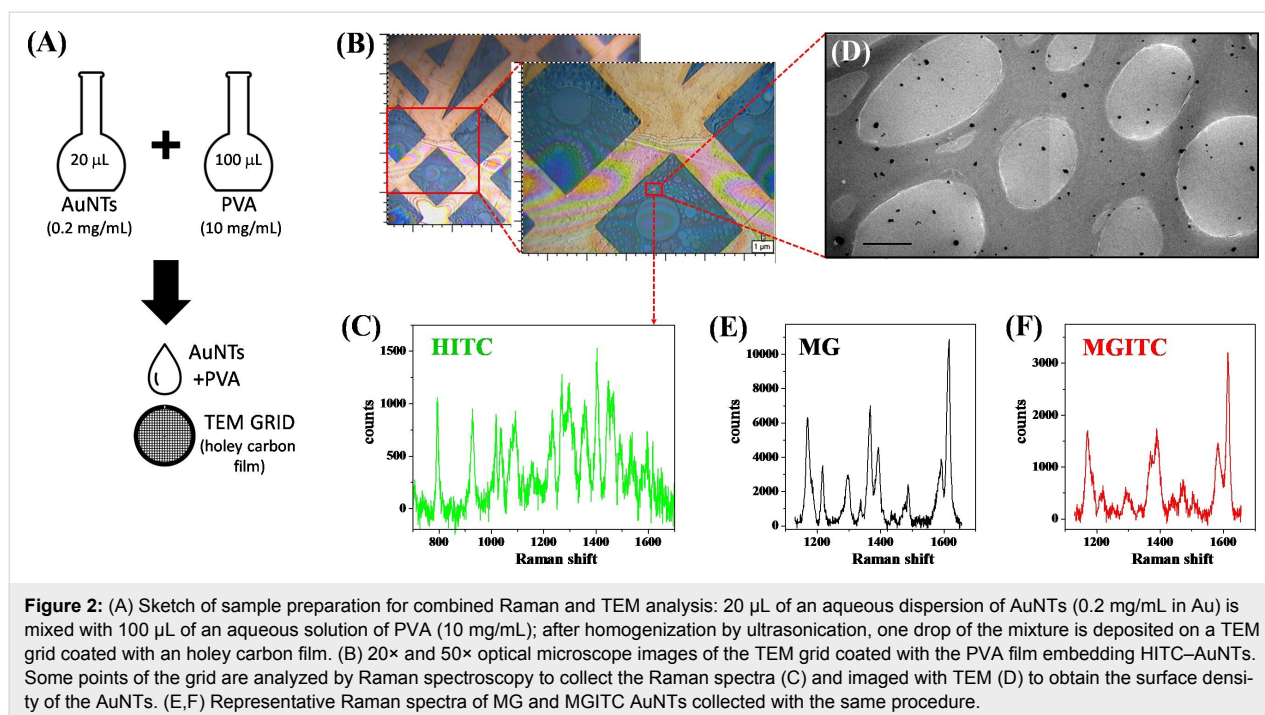
Importantly, the AuNTs show several junctions between plasmonic nanoparticles, which are well known sites of electromagnetic enhancement, as required for SERS [49-54]. This corresponds to a constellation of electromagnetic hot spots inside each nanoaggregate, where the local field enhancement is achieved in order to amplify the Raman signal of the adsorbed molecules by several orders of magnitude. This is further substantiated by numerical calculations of local field enhancement in a AuNT with structure reproducing the aggregate in Figure 1B. In particular, the SERS enhancement factor (G_{SERS}) was obtained from the 4th power of the ratio between the local electric field, E_{loc}, in the proximity to the surface of the metal nanostructure and the incident electric field, E_0, from linearly polarized 633 nm electromagnetic radiation propagating in a medium with refractive index of PVA (n = 1.526) [6,55]. As shown in Figure 1D, G_{SERS} can reach values as high as 10^6 and consistently between 10^5–10^6, depending on the hot spot considered.
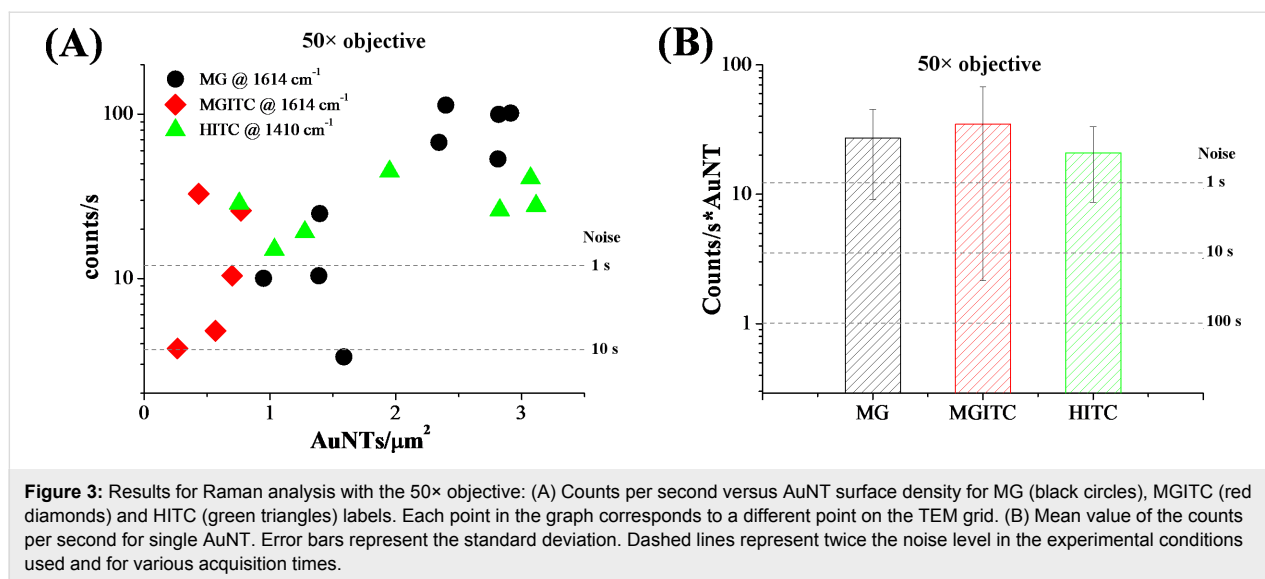
Importantly, by changing the direction of polarization of incident light, the AuNTs always have several active hot spots, which reduces the number of "dark" tags in real operating conditions using polarized laser light sources, such as in

ordinary Raman spectrometers [56]. This is demonstrated in Figure 1E, were the bidimensional map of G_{SERS} in the AuNT was calculated for a different polarization direction: G_{SERS} values span the same range as in Figure 1D, but the hot spots are mostly located at different points within the nanoaggregate.

To quantify the Raman scattering intensity versus concentration of nanoparticles, the three aqueous dispersions of AuNTs were mixed with a PVA solution and deposited on a TEM grid (Figure 2A). In this way, after evaporation of the liquid, the AuNTs remained dispersed in a PVA film with nanometric thickness (Figure 2B), according to a well-established procedure [42]. After sampling several points of each grid by Raman spectroscopy (see for instance Figure 2B,C), TEM images were collected in the same area (Figure 2D) in order to relate the surface density of AuNTs to their signal intensity.

The Raman spectra collected on the grids showed sharp signals clearly ascribable to the fingerprints of the three Raman reporters. The spectrum of HITC shows a rich progression of vibrational bands over the whole range from 700 to 1700 cm^{-1}, with the most intense band located at 1410 cm^{-1} (Figure 2C). For MG, distinctive vibrational peaks are present at about 1200, 1400 and 1600 cm^{-1}, the most intense of which is peaked at 1614 cm^{-1} (Figure 2E). MGITC, being the isothiocyanate derivative of MG, has a very similar vibrational fingerprint with the most prominent band also centered at 1614 cm^{-1} (Figure 2F).

Figure 2: (A) Sketch of sample preparation for combined Raman and TEM analysis: 20 µL of an aqueous dispersion of AuNTs (0.2 mg/mL in Au) is mixed with 100 µL of an aqueous solution of PVA (10 mg/mL); after homogenization by ultrasonication, one drop of the mixture is deposited on a TEM grid coated with an holey carbon film. (B) 20× and 50× optical microscope images of the TEM grid coated with the PVA film embedding HITC–AuNTs. Some points of the grid are analyzed by Raman spectroscopy to collect the Raman spectra (C) and imaged with TEM (D) to obtain the surface density of the AuNTs. (E,F) Representative Raman spectra of MG and MGITC AuNTs collected with the same procedure.

Figure 3: Results for Raman analysis with the 50× objective: (A) Counts per second versus AuNT surface density for MG (black circles), MGITC (red diamonds) and HITC (green triangles) labels. Each point in the graph corresponds to a different point on the TEM grid. (B) Mean value of the counts per second for single AuNT. Error bars represent the standard deviation. Dashed lines represent twice the noise level in the experimental conditions used and for various acquisition times.
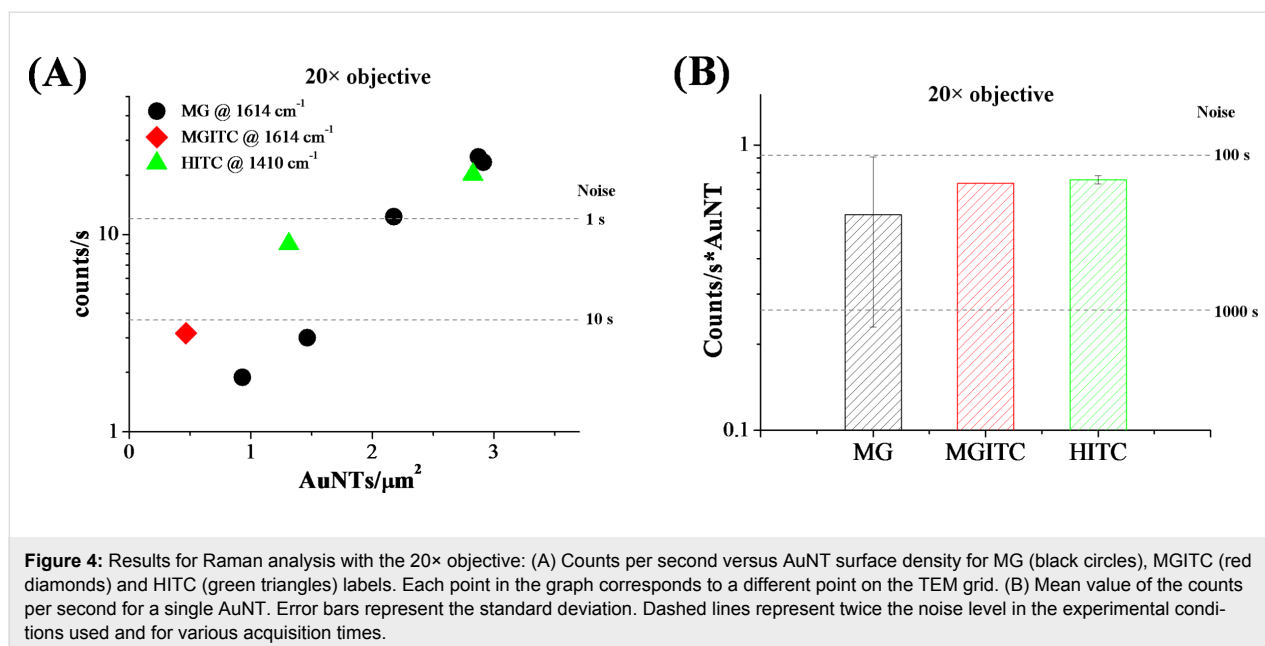
In Figure 3A the results of Raman measurements performed with the 50× objective are reported. A clear signal is detectable above the noise level corresponding to only 1 s of acquisition time, even for a density of 2–3 AuNTs/μm^2 in the MG and HITC labels and of less than 1 AuNT/μm^2 in the MGITC case. For less than 1 AuNT/μm^2, the signal intensity becomes generally comparable to the noise level at 1 s acquisition, but in most cases it is still higher than the noise level for 10 s of acquisition (the noise level scales as the square of the acquisition time) [57]. Considering the spot size of the laser beam on the sample, it is possible to evaluate the mean value and relative standard deviation of the counts per second from a single AuNT in the experimental conditions used (reported in Figure 3B), which is indicative of the average Raman scattering cross-section for a single label.

The signal from all of the three label types exceeds the noise level for 1 s of acquisition, meaning that, on average, one AuNT is enough to generate a well detectable signal even for such a short measurement time. From Figure 3B, it is also evident that the three labels exhibit comparable Raman intensity within the tolerance indicated by the error bars.

On the other hand, linearity is not observed in the plot of Figure 3A. Considering the random distribution of AuNTs on the TEM grids, this is attributable to the low surface density of nanolabels in combination with the small area probed with the 50× objective, which makes it highly probable that the effective number of labels probed with the laser spot changes by some units from one measurement to the other. Therefore, a higher AuNT density and/or larger spot size for Raman analysis is required to observe a linear correlation between counts per second and label density.

This hypothesis can be verified from the results of the Raman measurements performed with a 20× objective and the same excitation power, wavelength and exposure time as with the 50× objective, as reported in Figure 4A. In particular, in the case of the MG dataset, which includes a sufficiently large number of points, an appreciable correlation between AuNT density and counts per second is found. The MGITC and HITC points are not far from the MG ones, in agreement with the generally comparable brightness exhibited by the three types of AuNTs. The trend of the MGITC and HITC AuNTs also contributes to evidencing the expected growth of Raman signal with label density. This is noticeable since the AuNT preparation method, though simple and economic, does not allow high reproducibility of SERS response among all the single tags, as shown in Figure 3A.

The focused laser spot with the 20× objective is one order of magnitude larger than with the 50×, which corresponds to a lower laser intensity at a given input power, but also to a proportionally larger number of AuNTs inside the sampled area at a given of surface density. However, the numerical aperture and, thus, the solid angle of collection with the 20× objective is smaller than with the 50× objective, resulting in a signal decrease of more than one order of magnitude in our experimental conditions. Despite this, a density of 2–3 AuNTs/μm^2 is still enough to obtain a well detectable signal with an acquisition time of only 1 s. However, the lower laser intensity and collection efficiency of the 20× objective is transformed into a lower mean value of counts per second from the single AuNT, that is now within the noise range for acquisition times of 100 and 1000 s (Figure 4B). This clearly indicates that objectives with a large numerical aperture provide a better response when the number of AuNTs per unit area is as low as 1 tag per μm^2. It is

Figure 4: Results for Raman analysis with the 20× objective: (A) Counts per second versus AuNT surface density for MG (black circles), MGITC (red diamonds) and HITC (green triangles) labels. Each point in the graph corresponds to a different point on the TEM grid. (B) Mean value of the counts per second for a single AuNT. Error bars represent the standard deviation. Dashed lines represent twice the noise level in the experimental conditions used and for various acquisition times.

worth stressing that acquisition times of hundreds of seconds are compatible with the AuNTs, which showed good photo and thermal stability also after laser exposure up to 1000 s with a 50× objective and 0.65 mW (see Figure S3 in Supporting Information File 1). However, it should be noted that a density of few SERS tags per micrometer square is much lower than that typically pursued in practical cases for both analytical and biomedical purposes [13,16-22].

The good performance of AuNTs is confirmed by the fact that no Raman signal was detected from the pure dyes without AuNTs under the same experimental conditions. Moreover, it is well known from literature that the utilization of Au NPs of the same size is associated with higher SERS enhancement factors [18], therefore suggesting that the performance of the AuNTs can be further improved by employing size-selected nanospheres.

Conclusion

In this study, the performance of SERS labels based on Au NPs and organic dyes resonant at 633 nm was investigated by a combination of Raman and TEM analysis. The AuNTs were designed in order to support multiple electromagnetic hot spots for any polarization direction of the excitation beam.

The results highlight the appreciable intensity of the AuNTs, which allows a clear detection of the Raman signal above the noise threshold with a surface density of only 1 tag/μm^2 when using an excitation power of only 0.65 mW at 633 nm with a 50× objective and acquisition times as short as 1 s. The tag density can be lowered even below 1 tag/μm^2 if the acquisition

time can be extended to 10 s, but it should be increased to 3 tags/μm^2 with a 20× objective under the same excitation conditions. In case of an ultra-low AuNT density, a threshold of the total number of SERS tags inside the probed area is required to obtain a linear response, that is, on the order of 10 tags. Overall, these results suggest that a better signal-to-noise ratio requires optics with a high numerical aperture, while linearity versus tags number is improved by using low-magnification optics. However, it should be noted that the power density and tag density in this study are much lower than that typically achieved in real applications, further emphasizing the appreciable intensity of these AuNTs. Therefore, these results are useful for and contribute to the exploitation of AuNTs as ultrabright Raman tags in analytical chemistry, biotechnological assays and nanomedicine.

Supporting Information

Supporting Information File 1
Size distribution of Au nanoparticles, UV–visible spectra of Au nanotags, Mie theory fit results, MG-AuNT reproducibility, and MG-AuNT photostability.
[https://www.beilstein-journals.org/bjnano/content/supplementary/2190-4286-10-102-S1.pdf]

Acknowledgements

ORCID® iDs

Vincenzo Amendola - https://orcid.org/0000-0002-9937-7005

References

1. Bora, T. Recent Developments on Metal Nanoparticles for SERS Applications. *Noble and Precious Metals - Properties, Nanoscale Effects and Applications;* InTech: Rijeka, Croatia, 2018. doi:10.5772/intechopen.71573

2. Foti, A.; Barreca, F.; Fazio, E.; D'Andrea, C.; Matteini, P.; Maragò, O. M.; Gucciardi, P. G. *Beilstein J. Nanotechnol.* **2018,** *9,* 2718–2729. doi:10.3762/bjnano.9.254

3. Zanchi, C.; Lucotti, A.; Tommasini, M.; Trusso, S.; de Grazia, U.; Ciusani, E.; Ossi, P. M. *Beilstein J. Nanotechnol.* **2015,** *6,* 2224–2232. doi:10.3762/bjnano.6.228

4. Grosu, A. L.; Weber, W. A.; Franz, M.; Stärk, S.; Piert, M.; Thamm, R.; Gumprecht, H.; Schwaiger, M.; Molls, M.; Nieder, C. *Int. J. Radiat. Oncol., Biol., Phys.* **2005,** *63,* 511–519. doi:10.1016/j.ijrobp.2005.01.056

5. Le Ru, E. C.; Blackie, E.; Meyer, M.; Etchegoin, P. G. *J. Phys. Chem. C* **2007,** *111,* 13794–13803. doi:10.1021/jp0687908

6. Gürdal, E.; Dickreuter, S.; Noureddine, F.; Bieschke, P.; Kern, D. P.; Fleischer, M. *Beilstein J. Nanotechnol.* **2018,** *9,* 1977–1985. doi:10.3762/bjnano.9.188

7. Wang, A.; Kong, X. *Materials* **2015,** *8,* 3024–3052. doi:10.3390/ma8063024

8. Moskovits, M. *Phys. Chem. Chem. Phys.* **2013,** *15,* 5301–5311. doi:10.1039/c2cp44030j

9. Meixner, A. J.; Leiderer, P. *Beilstein J. Nanotechnol.* **2014,** *5,* 186–187. doi:10.3762/bjnano.5.19

10. McLintock, A.; Lee, H. J.; Wark, A. W. *Phys. Chem. Chem. Phys.* **2013,** *15,* 18835–18843. doi:10.1039/c3cp52946k

11. Le Ru, E. C.; Galloway, C.; Etchegoin, P. G. *Phys. Chem. Chem. Phys.* **2006,** *8,* 3083–3087. doi:10.1039/b605292d

12. Vosgröne, T.; Meixner, A. J. *ChemPhysChem* **2005,** *6,* 154–163. doi:10.1002/cphc.200400395

13. Shan, B.; Pu, Y.; Chen, Y.; Liao, M.; Li, M. *Coord. Chem. Rev.* **2018,** *371,* 11–37. doi:10.1016/j.ccr.2018.05.007

14. Gandra, N.; Singamaneni, S. *Nanomedicine (London, U. K.)* **2013,** *8,* 317–320. doi:10.2217/nnm.13.10

15. Zavaleta, C. L.; Garai, E.; Liu, J. T. C.; Sensarn, S.; Mandella, M. J.; Van de Sompel, D.; Friedland, S.; Van Dam, J.; Contag, C. H.; Gambhir, S. S. *Proc. Natl. Acad. Sci. U. S. A.* **2013,** *110,* E2288–E2297. doi:10.1073/pnas.1211309110

16. Tripp, R. A.; Dluhy, R. A.; Zhao, Y. *Nano Today* **2008,** *3,* 31–37. doi:10.1016/s1748-0132(08)70042-2

17. Wang, Y.; Yan, B.; Chen, L. *Chem. Rev.* **2013,** *113,* 1391–1428. doi:10.1021/cr300120g

18. Amendola, V.; Meneghetti, M. *Adv. Funct. Mater.* **2012,** *22,* 353–360. doi:10.1002/adfm.201101539

19. Amendola, V.; Meneghetti, M.; Fiameni, S.; Polizzi, S.; Fracasso, G.; Boscaini, A.; Colombatti, M. *Anal. Methods* **2011,** *3,* 849–856. doi:10.1039/c0ay00660b

20. Stanca, S. E.; Matthäus, C.; Neugebauer, U.; Nietzsche, S.; Fritzsche, W.; Dellith, J.; Heintzmann, R.; Weber, K.; Deckert, V.; Krafft, C.; Popp, J. *Nanomedicine (N. Y., NY, U. S.)* **2015,** *11,* 1831–1839. doi:10.1016/j.nano.2015.04.004

21. Narayanan, N.; Karunakaran, V.; Paul, W.; Venugopal, K.; Sujathan, K.; Kumar Maiti, K. *Biosens. Bioelectron.* **2015,** *70,* 145–152. doi:10.1016/j.bios.2015.03.029

22. Qian, X.; Peng, X.-H.; Ansari, D. O.; Yin-Goen, Q.; Chen, G. Z.; Shin, D. M.; Yang, L.; Young, A. N.; Wang, M. D.; Nie, S. *Nat. Biotechnol.* **2008,** *26,* 83–90. doi:10.1038/nbt1377

23. Stender, A. S.; Marchuk, K.; Liu, C.; Sander, S.; Meyer, M. W.; Smith, E. A.; Neupane, B.; Wang, G.; Li, J.; Cheng, J.-X.; Huang, B.; Fang, N. *Chem. Rev.* **2013,** *113,* 2469–2527. doi:10.1021/cr300336e

24. Vanhecke, D.; Rodriguez-Lorenzo, L.; Clift, M. J. D.; Blank, F.; Petri-Fink, A.; Rothen-Rutishauser, B. *Nanomedicine (London, U. K.)* **2014,** *9,* 1885–1900. doi:10.2217/nnm.14.108

25. Vermeulen, L. M. P.; Brans, T.; De Smedt, S. C.; Remaut, K.; Braeckmans, K. *Nano Today* **2018,** *21,* 74–90. doi:10.1016/j.nantod.2018.06.007

26. Radziuk, D.; Moehwald, H. *Phys. Chem. Chem. Phys.* **2015,** *17,* 21072–21093. doi:10.1039/c4cp04946b

27. Allgeyer, E. S.; Pongan, A.; Browne, M.; Mason, M. D. *Nano Lett.* **2009,** *9,* 3816–3819. doi:10.1021/nl902008g

28. Qian, X. M.; Nie, S. M. *Chem. Soc. Rev.* **2008,** *37,* 912–920. doi:10.1039/b708839f

29. Zavaleta, C. L.; Smith, B. R.; Walton, I.; Doering, W.; Davis, G.; Shojaei, B.; Natan, M. J.; Gambhir, S. S. *Proc. Natl. Acad. Sci. U. S. A.* **2009,** *106,* 13511–13516. doi:10.1073/pnas.0813327106

30. Wang, L.; O'Donoghue, M. B.; Tan, W. *Nanomedicine (London, U. K.)* **2006,** *1,* 413–426. doi:10.2217/17435889.1.4.413

31. Amendola, V.; Scaramuzza, S.; Litti, L.; Meneghetti, M.; Zuccolotto, G.; Rosato, A.; Nicolato, E.; Marzola, P.; Fracasso, G.; Anselmi, C.; Pinto, M.; Colombatti, M. *Small* **2014,** *10,* 2476–2486. doi:10.1002/smll.201303372

32. Tian, L.; Fei, M.; Tadepalli, S.; Morrissey, J. J.; Kharasch, E. D.; Singamaneni, S. *Adv. Healthcare Mater.* **2015,** *4,* 1502–1509. doi:10.1002/adhm.201500227

33. Bora, T.; Dousse, A.; Sharma, K.; Sarma, K.; Baev, A.; Hornyak, G. L.; Dasgupta, G. *Int. J. Smart Nano Mater.* **2019,** *10,* 116–143. doi:10.1080/19475411.2018.1541935

34. Khlebtsov, B.; Pylaev, T.; Khanadeev, V.; Bratashov, D.; Khlebtsov, N. *RSC Adv.* **2017,** *7,* 40834–40841. doi:10.1039/c7ra08113h

35. Pilot, R. *J. Raman Spectrosc.* **2018,** *49,* 954–981. doi:10.1002/jrs.5400

36. Driscoll, A. J.; Harpster, M. H.; Johnson, P. A. *Phys. Chem. Chem. Phys.* **2013,** *15,* 20415–20433. doi:10.1039/c3cp52334a

37. Bohndiek, S. E.; Wagadarikar, A.; Zavaleta, C. L.; Van de Sompel, D.; Garai, E.; Jokerst, J. V.; Yazdanfar, S.; Gambhir, S. S. *Proc. Natl. Acad. Sci. U. S. A.* **2013,** *110,* 12408–12413. doi:10.1073/pnas.1301379110

38. Tran, V.; Thiel, C.; Svejda, J. T.; Jalali, M.; Walkenfort, B.; Erni, D.; Schlücker, S. *Nanoscale* **2018,** *10,* 21721–21731. doi:10.1039/c8nr06028b

39. Zámbó, D.; Szekrényes, D. P.; Pothorszky, S.; Nagy, N.; Deák, A. *J. Phys. Chem. C* **2018,** *122,* 23683–23690. doi:10.1021/acs.jpcc.8b06716

40. Zaleski, S.; Wilson, A. J.; Mattei, M.; Chen, X.; Goubert, G.; Cardinal, M. F.; Willets, K. A.; Van Duyne, R. P. *Acc. Chem. Res.* **2016,** *49,* 2023–2030. doi:10.1021/acs.accounts.6b00327

41. Scaramuzza, S.; Zerbetto, M.; Amendola, V. *J. Phys. Chem. C* **2016,** *120,* 9453–9463. doi:10.1021/acs.jpcc.6b00161

42. Amendola, V. *J. Nanosci. Nanotechnol.* **2015,** *15,* 3545–3551. doi:10.1166/jnn.2015.9836

43. Amendola, V.; Meneghetti, M. *J. Phys. Chem. C* **2009,** *113,* 4277–4285. doi:10.1021/jp8082425

44. Draine, B. T.; Flatau, P. J. *arXiv* **2010,** 1002.

45. Draine, B. T.; Flatau, P. J. *J. Opt. Soc. Am. A* **1994,** *11,* 1491–1499. doi:10.1364/josaa.11.001491

46. Amendola, V.; Scaramuzza, S.; Agnoli, S.; Polizzi, S.; Meneghetti, M. *Nanoscale* **2014,** *6,* 1423–1433. doi:10.1039/c3nr04995g

47. Goodman, J. J.; Flatau, P. J.; Draine, B. T. *Opt. Lett.* **1991,** *16,* 1198–1200. doi:10.1364/ol.16.001198

48. Scaramuzza, S.; Badocco, D.; Pastore, P.; Coral, D. F.; Fernández van Raap, M. B.; Amendola, V. *ChemPhysChem* **2017,** *18,* 1026–1034. doi:10.1002/cphc.201600651

49. Herrmann, J. F.; Höppener, C. *Beilstein J. Nanotechnol.* **2018,** *9,* 2188–2197. doi:10.3762/bjnano.9.205

50. Butet, J.; Bernasconi, G. D.; Martin, O. J. F. *Beilstein J. Nanotechnol.* **2018,** *9,* 2674–2683. doi:10.3762/bjnano.9.250

51. Milekhin, A. G.; Kuznetsov, S. A.; Milekhin, I. A.; Sveshnikova, L. L.; Duda, T. A.; Rodyakina, E. E.; Latyshev, A. V.; Dzhagan, V. M.; Zahn, D. R. T. *Beilstein J. Nanotechnol.* **2018,** *9,* 2646–2656. doi:10.3762/bjnano.9.246

52. Amendola, V.; Saija, R.; Maragò, O. M.; Iatì, M. A. *Nanoscale* **2015,** *7,* 8782–8792. doi:10.1039/c5nr00823a

53. Kim, K. H.; Chae, S. S.; Jang, S.; Choi, W. J.; Chang, H.; Lee, J.-O.; Lee, T. I. *ACS Appl. Mater. Interfaces* **2016,** *8,* 32094–32101. doi:10.1021/acsami.6b11851

54. Kiesow, K. I.; Dhuey, S.; Habteyes, T. G. *Appl. Phys. Lett.* **2014,** *105,* 053105. doi:10.1063/1.4892577

55. Lidorikis, E. *J. Quant. Spectrosc. Radiat. Transfer* **2012,** *113,* 2573–2584. doi:10.1016/j.jqsrt.2012.04.004

56. Jiao, J.; Wang, X.; Wackenhut, F.; Horneber, A.; Chen, L.; Failla, A. V.; Meixner, A. J.; Zhang, D. *ChemPhysChem* **2012,** *13,* 952–958. doi:10.1002/cphc.201100718

57. McCreery, R. L. Raman Microscopy and Imaging. *Raman Spectroscopy for Chemical Analysis;* John Wiley & Sons, Inc.: Hoboken, NJ, U.S.A., 2005; pp 293–332. doi:10.1002/0471721646.ch11

Revisiting semicontinuous silver films as surface-enhanced Raman spectroscopy substrates

Malwina Liszewska[1], Bogusław Budner[1], Małgorzata Norek[2], Bartłomiej J. Jankiewicz[1] and Piotr Nyga[*1]

Abstract

Surface-enhanced Raman spectroscopy (SERS) is a very promising analytical technique for the detection and identification of trace amounts of analytes. Among the many substrates used in SERS of great interest are nanostructures fabricated using physical methods, such as semicontinuous metal films obtained via electron beam physical vapor deposition. In these studies, we investigate the influence of morphology of semicontinuous silver films on their SERS properties. The morphologies studied ranged from isolated particles through percolated films to almost continuous films. We found that films below the percolation threshold (transition from dielectric-like to metal-like) made of isolated silver structures provided the largest SERS enhancement of 4-aminothiophenol (4-ATP) analyte signals. The substrate closest to the percolation threshold has the SERS signal about four times lower than the highest signal sample.

Introduction

Noble metal nanostructures exhibit exceptional optical properties. They can efficiently absorb and/or scatter visible and near infrared electromagnetic radiation [1]. The origin of the above phenomena lies in localized surface plasmon resonances (LSPR). LSPRs are light induced oscillations of free electrons in metallic nanostructures. The spectral position of an LSPR depends on the dielectric constant of the metal, surrounding dielectric, shape and size of the nanostructure, and its orientation with respect to the electric component of the electromagnetic field [1,2]. At resonance, the electric field near the surface of metallic nanostructures can be greatly enhanced and localized in nanoscale regions called "hot spots" [3]. These "hot spots" can be utilized in surface-enhanced Raman spectroscopy (SERS) [4], allowing for the detection of trace amounts of

chemicals and biological materials, down to the single molecule or cell level [5].

SERS was discovered in the 1970s [6-8] and a considerable amount of research has been devoted to this topic. However, there is still a need for further development of reproducible and inexpensive SERS substrates [9]. SERS substrates can be fabricated by a multitude of techniques. These techniques can be divided into chemical and physical methods. Chemical methods allow for fabrication, in solution or on surfaces, of nanostructures of various shapes including: nanospheres [5], spheres coated with a thin dielectric shell [10], dielectric core-metallic shell particles [11,12], nanostars [13], microflowers [14] and aggregates [15], just to mention a few examples. Gold and silver nanostructured surfaces on substrates can be fabricated by self-assembly of colloidal particles into monolayers [16], in the form of island films by seeding with nanoparticles followed by a reduction of metal salt [17,18], or in the form of other high surface area structures [19,20]. Chemical fabrication methods are powerful in terms of the vast variety of attainable structure types, possible enhancement factors, and low cost of fabrication. However, reproducibility of SERS substrates can be an issue and the chemical compounds used for fabrication or stabilization of nanostructures can be a source of additional SERS signals [15], which may complicate SERS analysis with their use.

Various physical methods may be used to fabricate SERS substrates. Usually in these techniques silver or gold is deposited by physical vapor deposition (PVD) techniques. Nanostructures are obtained via various structuring methods. Electron beam lithography allows fabrication of planar [21] and 3D metallic structures [22]. Nanosphere lithography can be used to obtain nanotriangles [23] and nanocones [24]. Much attention has been also given to the deposition of metal onto nano- and microstructured surfaces made of glass [25,26], GaN [27-29], Si [30], TiO_2 [31], Al_2O_3 [32], Ti [33], polymers [34], or planar surfaces coated with nano/microspheres resulting in metal film on nanospheres MFON [35,36], and Au nanocrescents on a monolayer of polystyrene nanospheres [37]. Additionally glancing-angle deposition (GLAD) has been explored for the fabrication of vertical nanorods on planar substrates [38].

A special class of nanostructured surfaces are semicontinuous silver films (SSFs) [39,40] also known as metal island films [41], which are comprised of random fractal-type structures. SSFs can be fabricated on large area planar substrates using electron beam (or thermal) PVD techniques, and thus are simple to prepare and rather inexpensive. Island type structures can be also fabricated using pulsed laser deposition [42]. The SSFs form when 5–10 nm (mass thickness corresponding to hypothet-

ical continuous film) of silver is e-beam deposited on a proper adhesion layer (for example silicon dioxide) [43,44]. The results of simulations and experimental studies show that the hot spots exist in SSFs [2,44-47], and hence they have been extensively studied as SERS substrates [40,41,48-55]. However, transmittance, reflectance and absorption are rarely reported in these studies, and it is difficult to link the optical properties of these nanostructures with their SERS performance. In our earlier initial study we investigated SSFs as SERS substrates [55], however the set of samples was limited to only four (with mass thickness from 3 nm to 10 nm) and they were characterized with a limited number of techniques.

The aim of this work is to revisit SSFs for their applications in SERS and perform a systematic study allowing for the correlation of the optical properties of silver film structures, with their SERS properties. We have investigated SERS enhancement of 4-aminothiophenol on nine SSFs with metal structures ranging from isolated particles, through percolated, to almost continuous film. We found that the largest SERS enhancement is observed for SSFs below the percolation threshold. The sample closest to the threshold has a SERS signal about four times lower than for the highest signal case.

Experimental
Materials
Silver deposition material (99.99%) and BK7 glass substrates were purchased from Umicore. For glass substrates cleaning process, we used sulfuric acid (97%; Fluka), hydrogen peroxide (30%; Chempur), ethanol (96%; Chempur) and deionized water. SERS analyte 4-aminothiophenol (97%) was purchased from Sigma-Aldrich.

Fabrication of semicontinuous silver films
SSFs were fabricated on BK7 glass substrates using the electron beam PVD technique. The substrates were first cleaned with piranha solution (H_2SO_4/H_2O_2 3:1) for 30 minutes, then rinsed with deionized water, followed by multiple rinses with ethanol. The substrates were then placed in an electron beam vacuum evaporation chamber. The base pressure of the chamber was about 2×10^{-6} mbar. Deposition was performed at room temperature. Glass substrates were first coated with 10 nm thick layer of silicon dioxide (SiO_2). Next, without breaking vacuum, silver was deposited on the substrates. Two depositions were performed and in each of them several substrates were located at a different distance from the evaporation source to fabricate films with different thicknesses. In such way in two depositions a total of nine samples were fabricated. In order to ensure uniform thickness of SiO_2, the substrates were rotated during the deposition process. The thickness of deposited films was monitored with quartz crystal microbalance.

Characterization of semicontinuous silver films

Optical properties of SSFs were characterized using UV–vis–NIR Perkin Elmer Lambda 900 spectrometer. Transmittance was measured using a standard detector, while reflectance was measured with an integrating sphere module. Absorption was calculated assuming the sum of transmittance, reflectance, and absorption is 100%. The morphology of the fabricated structures was measured using a Quanta 3D FEG Dual Beam scanning electron microscope (SEM) and an atomic force microscope (AFM). The SEM images of SSFs were converted to black and white and metal coverage was calculated. The AFM maps were collected using an NTEGRA atomic force microscope from NT-MDT company. The surface topography measurements were made in semi-contact mode. We used HA_NC ETALON (NT-MDT) probe with 140 kHz ± 10% resonant frequency, force constant of 3.5 N/m ± 20% and standard tip curvature radius less than 10 nm. The thickness of SSFs was measured on the edge (step) formed through removing of a part of the silver film from the substrate (using a blade).

SERS measurements

The 4-aminothiophenol was used as a SERS analyte. In order to form a monolayer of 4-ATP on the silver nanostructures we immersed the SSF substrates into 10 mM ethanol solution of 4-ATP for 1 hour. Longer incubation times did not result in SERS signal increase. The excess 4-ATP molecules were removed by rinsing the SSF samples with ethanol. The solvent was allowed to evaporate slowly.

The SERS measurements of 4-ATP analyte on SSFs samples were carried out using a Renishaw inVia Raman microscope. The Raman signal was acquired in the spectral range of 250–2000 cm^{-1} using laser radiation with a wavelength of 785 nm. The laser excitation power was 75 μW on the sample. The laser beam was directed to the sample through a 50× (N.A. = 0.75) objective lens. We used a 10 second integration time. On each SSF sample we measured the Raman signal in three locations and averaged. The wavelength of the instrument was calibrated using an internal silicon wafer, the spectrum was centered at 520.5 cm^{-1}.

Results and Discussion

We fabricated a series of nine (named A–I) SSF samples with different silver thickness (Figure 1 and Figure 2). The SSFs were prepared on glass substrates using electron-beam PVD (see Experimental section for details). We used transparent substrates in order to be able to measure transmittance and reflectance. We performed two depositions. Each deposition was concurrently performed on several substrates located at different distances from the evaporation source to get different silver

film thicknesses. In such way in two depositions a total of nine SSF samples with different film thicknesses were fabricated. SEM images of the A–I SSFs are presented in Figure 1. They are arranged in a way that metal coverage (presented in Table 1) increases from A to I. Changes of the metal film thicknesses resulted in different SSFs morphologies. Sample A is comprised of small isolated particles. As the thickness increases the nanoparticles grow and their total number (per surface area) decreases (samples B–D). Next, the particles connect forming irregular fractal type shapes (samples E, F). As the amount of deposited metal further increases the metal coverage increases and the film reaches the percolation threshold – the transition from dielectric-like to metal-like (sample G is already above percolation threshold), where a metallic path forms across the sample. Finally, silver covers almost the entire surface of the substrate (sample I). The percolation point can be deducted from SEM images. One has to determine silver coverage or thickness for which a Ag path across the image/sample is formed. This can be performed through for example image analysis techniques. In the set of our nine samples we do not have a sample "at percolation". The percolation would happen for a hypothetical sample between sample F and G (as for sample F we do not observe continuous silver path and for sample G several paths across the SEM image exist).

In order to determine the physical thickness of the SSFs we carried out AFM studies (data presented in Table 1). For each of the SSFs a part of the silver film was removed to form a step like structure with two distinct areas (glass with silicon dioxide and glass with silicon dioxide and silver film) of different height. A several micrometer square AFM scan (not presented) of such step-like structures provides an estimate of the SSF height but does not show the fine structure of the SSF. In order to visualize the height and morphology of silver nanostructures we performed AFM scans of relatively small areas of SSFs (Figure 2). The AFM data in Figure 2 corresponds well with the SEM images presented in Figure 1. The size of particles increases for samples from A to I. Also, the measured height range increases.

The morphologies of SSFs strongly influence their optical properties. The measured transmittance, reflectance, and absorption of fabricated SSFs are presented in Figure 3. Film A has an absorption peak centered at about 435 nm. This peak corresponds to LSPR of isolated silver nanoparticles. With increased silver coverage the absorption peak broadens and shifts to longer wavelengths (samples B–E). Sample F has almost wavelength independent absorption (as well as transmittance and reflectance). Such behavior is known for metal films close to percolation [56]. This is because almost percolated films are comprised of nanostructures with different particle sizes and
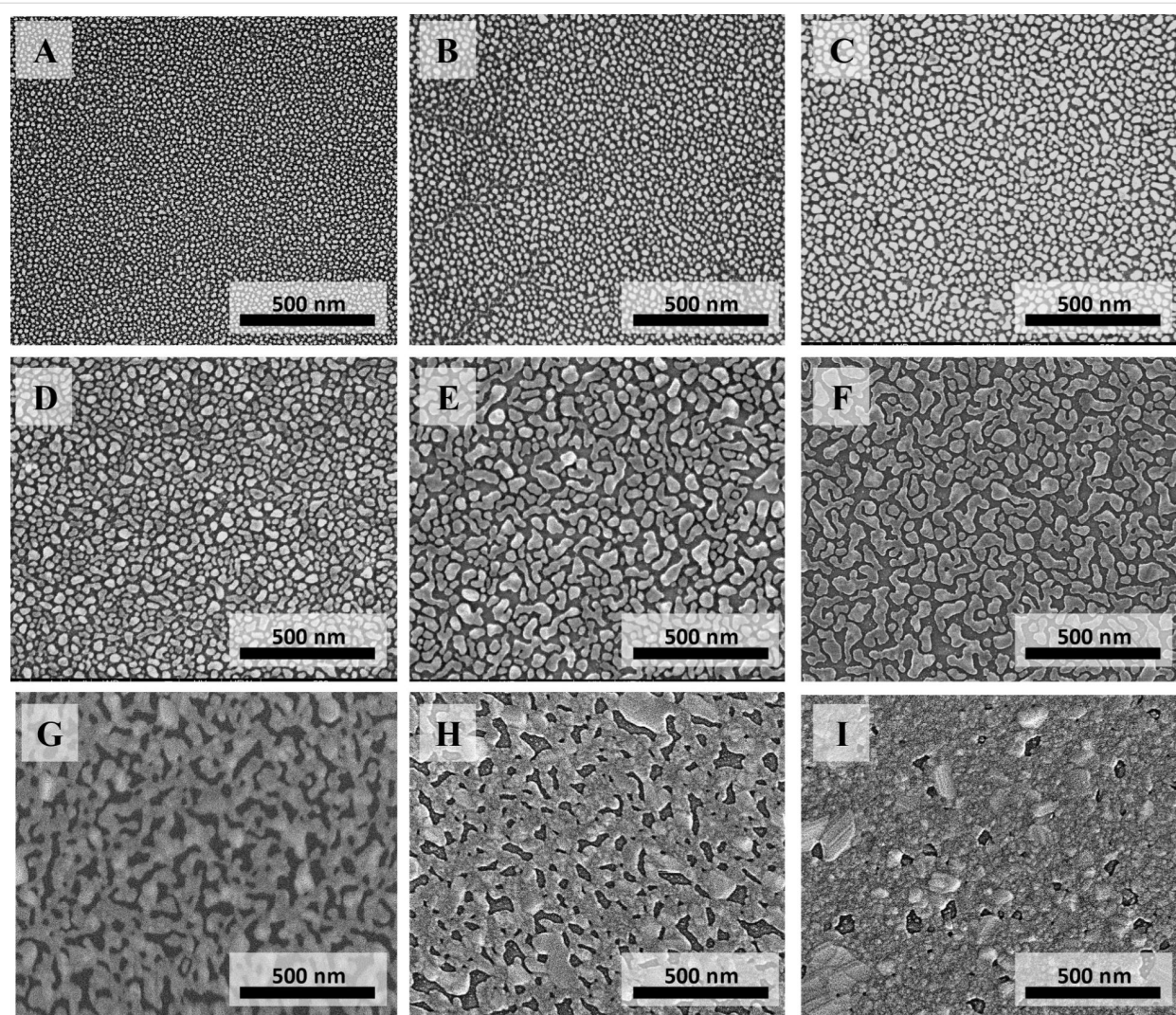
Figure 1: (A–I) SEM images of SSFs with different Ag thickness.

shapes, which results in absorption of electromagnetic energy across a broad wavelength range extending from the visible to the far infrared. For samples above percolation G-I reflectance increases (as the film is more metallic) and both absorption and transmittance decrease.

SERS properties of fabricated SSFs were examined using 4-ATP. We used 785 nm excitation wavelength. The 4-ATP SERS spectra measured on all SSFs are presented in Figure 4. In the spectra there are three prominent peaks at 389, 1080 and 1595 cm^{-1}. The first two can be assigned to the C–S stretching mode and the third to C–C stretching mode. Four relatively weak peaks at 1180, 1392, 1437 and 1490 cm^{-1} can be assigned to the same C–H bending and a combination of C–C stretching and C–H bending. The characteristic peaks observed in 4-ATP spectra are in agreement with peaks reported in the literature [57].

At the excitation wavelength of 785 nm the SSFs have different absorption (Figure 3), from 0% for sample A, increasing to about 34% for sample F and decreasing to 11% for sample I (Figure 3). Despite low absorption at the excitation wavelength, a weak SERS signal was detected on sample A. This is in an agreement with previous reports of good quality SERS spectra obtained on substrates with a LSPR far away from the excitation laser wavelength [58]. We did not observe SERS signal for the sample I with the highest metal coverage. The highest SERS signal was obtained for samples C, D and E. These samples have different absorption at excitation wavelength, but they have similar morphology. These three samples are below percolation (SEM images in Figure 1) and have similar metal coverage (0.51–0.55; Table 1). Since each of the nine SSF samples has a different metal coverage there is a different surface area available for 4-ATP binding, thus different number of molecules per unit area. In order to exclude this effect, we normal-
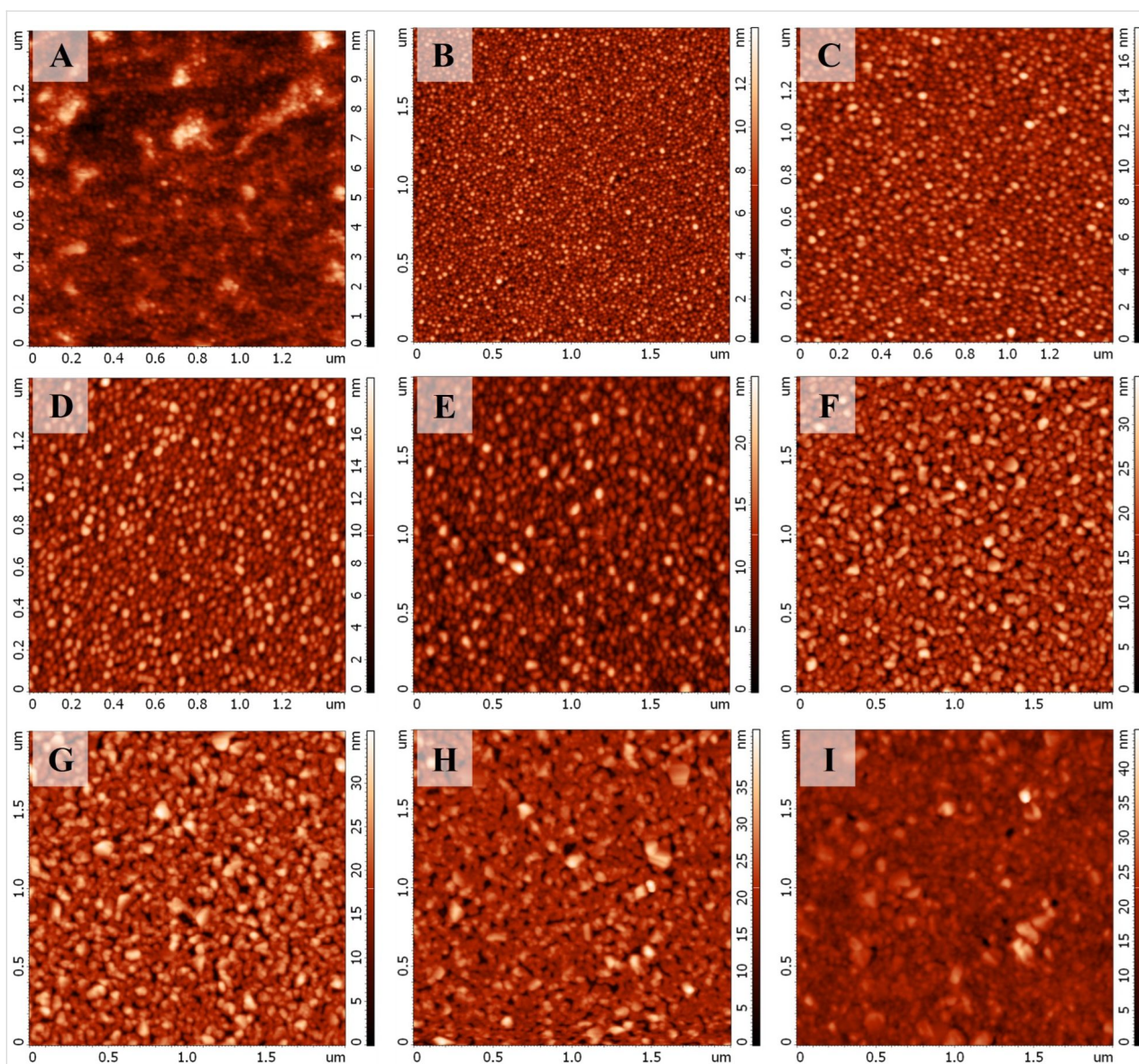
Figure 2: (A– I) AFM maps of SSFs with different Ag thickness. Samples A, C and D have a different scan area than the other samples.

Table 1: The AFM-determined thicknesses of semicontinuous Ag films and estimated values of metal filling factors.

Sample	AFM-determined Ag thickness [nm]	Ag filling factor
A	8.75	0.428 ± 0.029
B	13.24	0.430 ± 0.022
C	13.37	0.513 ± 0.012
D	12.27	0.522 ± 0.001
E	20.46	0.549 ± 0.009
F	24.51	0.572 ± 0.008
G	23.88	0.641 ± 0.024
H	25.42	0.768 ± 0.021
I	22.35	0.937 ± 0.009

ized the measured SERS signals by the metal coverage (presented in Table 1). The measured and metal coverage corrected signals of the 1080 cm^{-1} peak for A–I SSFs are presented in Figure 5. For both measured and normalized case the samples C–E show high SERS signal with the D sample having the highest signal. The 4-ATP SERS signal recorded on SSFs above percolation (samples G and H) was at least an order of magnitude lower than that for the case of the three samples with highest SERS signal. For the case of SSFs fabricated using our protocol it is possible to determine if the film is below percolation from the transmittance and/or reflectance measurements (transmittance increases, reflectance decreases for wavelengths in the range of about one micrometer) without the need for expensive and time-consuming structural characterization.
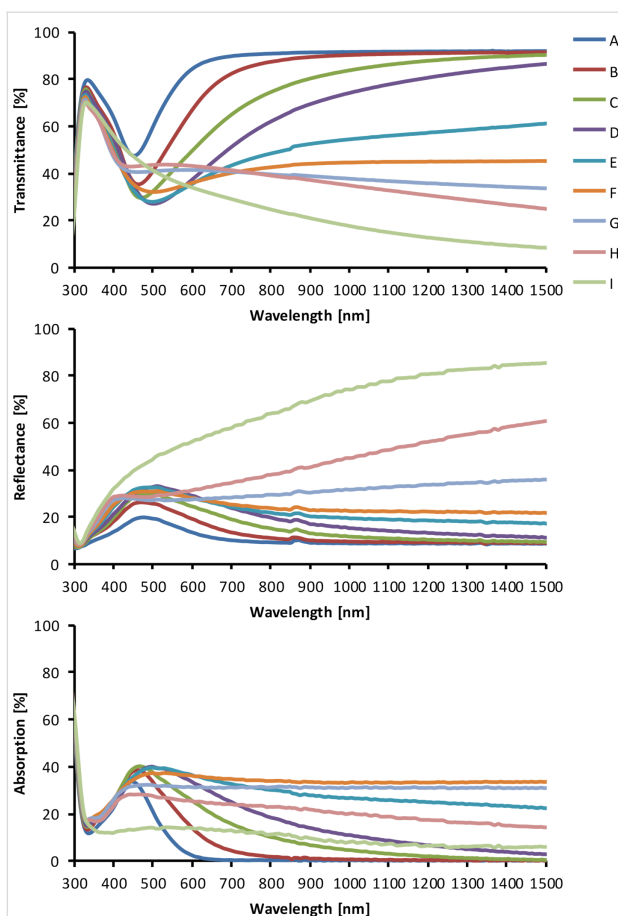
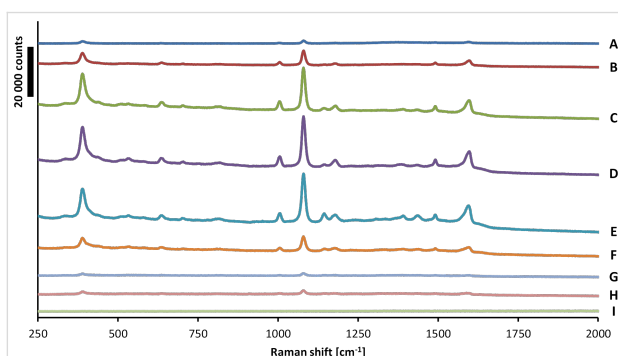**Figure 3:** Transmittance, reflectance and absorption spectra of A–I SSF films.

Figure 4: SERS spectra of 4-ATP molecules on A–I SSFs.

This could be used as a quick method for initial optimization of SSF thickness for high SERS signal.

Calculation of the SERS enhancement factor of a SERS substrate is extremely difficult since a proper reference sample is needed and there is an ongoing debate in the community regarding the appropriate procedures [59]. We decided to estimate the lower limit of the enhancement factor by adopting an
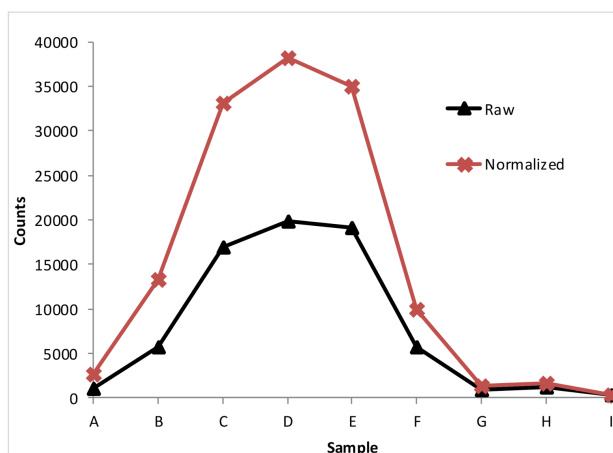

Figure 5: SERS signal of 1080 cm^{-1} band measured on SSFs A–I (Raw) and normalized by their metal coverage (Normalized).

approach similar to one used in the reference [20]. We compared the metal coverage normalized SERS signal of the D sample with the signal of the almost continuous I sample. As no SERS signal was observed on the sample I, we assumed that the upper limit of the signal is the peak-to-peak noise measurement [20]. By dividing the silver coverage corrected signal of the Raman band at 1080 cm^{-1} by the peak-to-peak noise of the measurement on the sample I we obtained a lower limit of the enhancement factor of about 630.

Conclusion

We have fabricated semicontinuous silver films with various morphologies, ranging from isolated particles, through percolated to almost continuous film, and investigated their performance as SERS substrates. The SERS activity of studied substrates was explained with relation to their morphologies and optical properties. SERS tests using 4-ATP as an analyte confirmed that the Raman signal enhancement is strongly dependent on the morphology and optical properties of the substrate, and particularly absorption of the film. We found that films below the percolation threshold, composed of isolated silver structures, provide the highest SERS signal. For the sample closest to the percolation threshold the SERS signal is about four times lower than in the highest signal case. The semicontinuous silver films above percolation threshold produced 4-ATP SERS signal at least an order of magnitude lower than the best film.

Acknowledgements

ORCID® iDs

Malwina Liszewska - https://orcid.org/0000-0001-5102-641X
Bogusław Budner - https://orcid.org/0000-0002-9395-6073
Małgorzata Norek - https://orcid.org/0000-0002-0460-486X
Bartłomiej J. Jankiewicz - https://orcid.org/0000-0002-1172-8764
Piotr Nyga - https://orcid.org/0000-0002-7591-7142

References

1. Bohren, C. F.; Huffman, D. R., Eds. *Absorption and Scattering of Light by Small Particles;* Wiley-VCH Verlag GmbH: Weinheim, Germany, 1983. doi:10.1002/9783527618156

2. Aroca, R.; Martin, F. *J. Raman Spectrosc.* **1985,** *16,* 156–162. doi:10.1002/jrs.1250160305

3. Markel, V. A.; Shalaev, V. M.; Zhang, P.; Huynh, W.; Tay, L.; Haslett, T. L.; Moskovits, M. *Phys. Rev. B* **1999,** *59,* 10903–10909. doi:10.1103/physrevb.59.10903

4. Moskovits, M. *Rev. Mod. Phys.* **1985,** *57,* 783–826. doi:10.1103/revmodphys.57.783

5. Kneipp, K.; Wang, Y.; Kneipp, H.; Perelman, L. T.; Itzkan, I.; Dasari, R. R.; Feld, M. S. *Phys. Rev. Lett.* **1997,** *78,* 1667–1670. doi:10.1103/physrevlett.78.1667

6. Fleischmann, M.; Hendra, P. J.; McQuillan, A. J. *Chem. Phys. Lett.* **1974,** *26,* 163–166. doi:10.1016/0009-2614(74)85388-1

7. Albrecht, M. G.; Creighton, J. A. *J. Am. Chem. Soc.* **1977,** *99,* 5215–5217. doi:10.1021/ja00457a071

8. Jeanmaire, D. L.; Van Duyne, R. P. *J. Electroanal. Chem. Interfacial Electrochem.* **1977,** *84,* 1–20. doi:10.1016/s0022-0728(77)80224-6

9. Liszewska, M.; Bartosewicz, B.; Budner, B.; Nasiłowska, B.; Szala, M.; Weyher, J. L.; Dzięcielewski, I.; Mierczyk, Z.; Jankiewicz, B. J. *Vib. Spectrosc.* **2019,** *100,* 79–85. doi:10.1016/j.vibspec.2018.11.002

10. Li, J. F.; Huang, Y. F.; Ding, Y.; Yang, Z. L.; Li, S. B.; Zhou, X. S.; Fan, F. R.; Zhang, W.; Zhou, Z. Y.; Wu, D. Y.; Ren, B.; Wang, Z. L.; Tian, Z. Q. *Nature* **2010,** *464,* 392–395. doi:10.1038/nature08907

11. Jackson, J. B.; Halas, N. J. *Proc. Natl. Acad. Sci. U. S. A.* **2004,** *101,* 17930–17935. doi:10.1073/pnas.0408319102

12. Talley, C. E.; Jackson, J. B.; Oubre, C.; Grady, N. K.; Hollars, C. W.; Lane, S. M.; Huser, T. R.; Nordlander, P.; Halas, N. J. *Nano Lett.* **2005,** *5,* 1569–1574. doi:10.1021/nl050928v

13. Rodríguez-Lorenzo, L.; Álvarez-Puebla, R. A.; de Abajo, F. J. G.; Liz-Marzán, L. M. *J. Phys. Chem. C* **2010,** *114,* 7336–7340. doi:10.1021/jp909253w

14. Winkler, K.; Kaminska, A.; Wojciechowski, T.; Holyst, R.; Fialkowski, M. *Plasmonics* **2011,** *6,* 697–704. doi:10.1007/s11468-011-9253-0

15. Yaffe, N. R.; Blanch, E. W. *Vib. Spectrosc.* **2008,** *48,* 196–201. doi:10.1016/j.vibspec.2007.12.002

16. Freeman, R. G.; Grabar, K. C.; Allison, K. J.; Bright, R. M.; Davis, J. A.; Guthrie, A. P.; Hommer, M. B.; Jackson, M. A.; Smith, P. C.; Walter, D. G.; Natan, M. J. *Science* **1995,** *267,* 1629–1632. doi:10.1126/science.267.5204.1629

17. Khlebtsov, B. N.; Khanadeev, V. A.; Panfilova, E. V.; Bratashov, D. N.; Khlebtsov, N. G. *ACS Appl. Mater. Interfaces* **2015,** *7,* 6518–6529. doi:10.1021/acsami.5b01652

18. Bartosewicz, B.; Gajda-Raczka, M.; Jankiewicz, B. J. *Photonics Lett. Pol.* **2013,** *5,* 48–50. doi:10.4302/plp.2013.2.05

19. Schneidewind, H.; Schüler, T.; Strelau, K. K.; Weber, K.; Cialla, D.; Diegel, M.; Mattheis, R.; Berger, A.; Möller, R.; Popp, J. *Beilstein J. Nanotechnol.* **2012,** *3,* 404–414. doi:10.3762/bjnano.3.47

20. Gürdal, E.; Dickreuter, S.; Noureddine, F.; Bieschke, P.; Kern, D. P.; Fleischer, M. *Beilstein J. Nanotechnol.* **2018,** *9,* 1977–1985. doi:10.3762/bjnano.9.188

21. Banaee, M. G.; Crozier, K. B. *Opt. Lett.* **2010,** *35,* 760–762. doi:10.1364/ol.35.000760

22. Xiao, X.; Nogan, J.; Beechem, T.; Montano, G. A.; Washburn, C. M.; Wang, J.; Brozik, S. M.; Wheeler, D. R.; Burckel, D. B.; Polsky, R. *Chem. Commun.* **2011,** *47,* 9858–9860. doi:10.1039/c1cc12072g

23. Haynes, C. L.; Van Duyne, R. P. *J. Phys. Chem. B* **2003,** *107,* 7426–7433. doi:10.1021/jp027749b

24. Horrer, A.; Schäfer, C.; Broch, K.; Gollmer, D. A.; Rogalski, J.; Fulmes, J.; Zhang, D.; Meixner, A. J.; Schreiber, F.; Kern, D. P.; Fleischer, M. *Small* **2013,** *9,* 3987–3992. doi:10.1002/smll.201300449

25. Liao, P. F.; Bergman, J. G.; Chemla, D. S.; Wokaun, A.; Melngailis, J.; Hawryluk, A. M.; Economou, N. P. *Chem. Phys. Lett.* **1981,** *82,* 355–359. doi:10.1016/0009-2614(81)85172-x

26. Oh, Y.-J.; Jeong, K.-H. *Adv. Mater. (Weinheim, Ger.)* **2012,** *24,* 2234–2237. doi:10.1002/adma.201104696

27. Kamińska, A.; Dzięcielewski, I.; Weyher, J. L.; Waluk, J.; Gawinkowski, S.; Sashuk, V.; Fiałkowski, M.; Sawicka, M.; Suski, T.; Porowski, S.; Hołyst, R. *J. Mater. Chem.* **2011,** *21,* 8662–8669. doi:10.1039/c0jm03336g

28. Weyher, J. L.; Bartosewicz, B.; Dzięcielewski, I.; Krajczewski, J.; Jankiewicz, B.; Nowak, G.; Kudelski, A. *Appl. Surf. Sci.* **2019,** *466,* 554–561. doi:10.1016/j.apsusc.2018.10.076

29. Bartosewicz, B.; Andersson, P. O.; Dzięcielewski, I.; Jankiewicz, B.; Weyher, J. L. *Mater. Sci. Semicond. Process.* **2019,** *91,* 97–101. doi:10.1016/j.mssp.2018.11.012

30. Perney, N. M. B.; Baumberg, J. J.; Zoorob, M. E.; Charlton, M. D. B.; Mahnkopf, S.; Netti, C. M. *Opt. Express* **2006,** *14,* 847–857. doi:10.1364/opex.14.000847

31. Roguska, A.; Kudelski, A.; Pisarek, M.; Lewandowska, M.; Dolata, M.; Janik-Czachor, M. *J. Raman Spectrosc.* **2009,** *40,* 1652–1656. doi:10.1002/jrs.2314

32. Malek, K.; Brzózka, A.; Rygula, A.; Sulka, G. D. *J. Raman Spectrosc.* **2014,** *45,* 281–291. doi:10.1002/jrs.4452

33. Grochowska, K.; Siuzdak, K.; Sokołowski, M.; Karczewski, J.; Szkoda, M.; Śliwiński, G. *Appl. Surf. Sci.* **2016,** *388,* 716–722. doi:10.1016/j.apsusc.2016.01.186

34. Repetto, D.; Giordano, M. C.; Foti, A.; Gucciardi, P. G.; Mennucci, C.; Buatier de Mongeot, F. *Appl. Surf. Sci.* **2018,** *446,* 83–91. doi:10.1016/j.apsusc.2018.02.163

35. Goudonnet, J. P.; Begun, G. M.; Arakawa, E. T. *Chem. Phys. Lett.* **1982,** *92,* 197–201. doi:10.1016/0009-2614(82)80105-x

36. Dick, L. A.; McFarland, A. D.; Haynes, C. L.; Van Duyne, R. P. *J. Phys. Chem. B* **2002,** *106,* 853–860. doi:10.1021/jp013638l

37. Giordano, M. C.; Foti, A.; Messina, E.; Gucciardi, P. G.; Comoretto, D.; Buatier de Mongeot, F. *ACS Appl. Mater. Interfaces* **2016,** *8,* 6629–6638. doi:10.1021/acsami.5b11843

38. Chaney, S. B.; Shanmukh, S.; Dluhy, R. A.; Zhao, Y.-P. *Appl. Phys. Lett.* **2005,** *87,* 031908. doi:10.1063/1.1988980

39. Ducourtieux, S.; Podolskiy, V. A.; Grésillon, S.; Buil, S.; Berini, B.; Gadenne, P.; Boccara, A. C.; Rivoal, J. C.; Bragg, W. D.; Banerjee, K.; Safonov, V. P.; Drachev, V. P.; Ying, Z. C.; Sarychev, A. K.; Shalaev, V. M. *Phys. Rev. B* **2001,** *64,* 165403. doi:10.1103/physrevb.64.165403

40. Drachev, V. P.; Thoreson, M.; Khaliullin, E. N.; Sarychev, A. K.; Zhang, D.; Ben-Amotz, D.; Shalaev, V. M. *Proc. SPIE* **2003,** *5221,* 76. doi:10.1117/12.510572

41. Schlegel, V. L.; Cotton, T. M. *Anal. Chem. (Washington, DC, U. S.)* **1991,** *63,* 241–247. doi:10.1021/ac00003a010

42. Budner, B.; Kuźma, M.; Nasiłowska, B.; Bartosewicz, B.; Liszewska, M.; Jankiewicz, B. J. *Beilstein J. Nanotechnol.* **2019,** *10,* 882–893. doi:10.3762/bjnano.10.89

43. Nyga, P.; Drachev, V. P.; Thoreson, M. D.; Shalaev, V. M. *Appl. Phys. B: Lasers Opt.* **2008,** *93,* 59–68. doi:10.1007/s00340-008-3145-9

44. Chettiar, U. K.; Nyga, P.; Thoreson, M. D.; Kildishev, A. V.; Drachev, V. P.; Shalaev, V. M. *Appl. Phys. B: Lasers Opt.* **2010,** *100,* 159–168. doi:10.1007/s00340-010-3985-y

45. Brouers, F.; Sarychev, A. K.; Blacher, S.; Lothaire, O. *Phys. A (Amsterdam, Neth.)* **1997,** *241,* 146–153. doi:10.1016/s0378-4371(97)00074-5

46. Grésillon, S.; Aigouy, L.; Boccara, A. C.; Rivoal, J. C.; Quelin, X.; Desmarest, C.; Gadenne, P.; Shubin, V. A.; Sarychev, A. K.; Shalaev, V. M. *Phys. Rev. Lett.* **1999,** *82,* 4520–4523. doi:10.1103/physrevlett.82.4520

47. Pavaskar, P.; Hsu, I.-K.; Theiss, J.; Hsuan Hung, W.; Cronin, S. B. *J. Appl. Phys.* **2013,** *113,* 034302. doi:10.1063/1.4775784

48. Gadenne, P.; Gagnot, D.; Masson, M. *Phys. A (Amsterdam, Neth.)* **1997,** *241,* 161–165. doi:10.1016/s0378-4371(97)00076-9

49. Oates, T. W. H.; Noda, S. *Appl. Phys. Lett.* **2009,** *94,* 053106. doi:10.1063/1.3078272

50. Oates, T. W. H.; Sugime, H.; Noda, S. *J. Phys. Chem. C* **2009,** *113,* 4820–4828. doi:10.1021/jp8097654

51. Drachev, V. P.; Thoreson, M. D.; Khaliullin, E. N.; Davisson, V. J.; Shalaev, V. M. *J. Phys. Chem. B* **2004,** *108,* 18046–18052. doi:10.1021/jp047254h

52. Drachev, V. P.; Nashine, V. C.; Thoreson, M. D.; Ben-Amotz, D.; Davisson, V. J.; Shalaev, V. M. *Langmuir* **2005,** *21,* 8368–8373. doi:10.1021/la0502490

53. Perumal, J.; Kong, K. V.; Dinish, U. S.; Bakker, R. M.; Olivo, M. *RSC Adv.* **2014,** *4,* 12995–13000. doi:10.1039/c3ra44867c

54. Šubr, M.; Kuzminova, A.; Kylián, O.; Procházka, M. *Spectrochim. Acta, Part A* **2018,** *197,* 202–207. doi:10.1016/j.saa.2018.01.055

55. Liszewska, M.; Stefaniak, M.; Firak, J.; Bartosewicz, B.; Budner, B.; Wojciechowski, T.; Jankiewicz, B. J.; Nyga, P. Influence of silver thickness on optical properties of metal island films fabricated by physical vapour deposition. 16th International Conference on Transparent Optical Networks (ICTON), Graz, Austria, July 6–10, 2014; 2014; pp 1–3. doi:10.1109/icton.2014.6876658

56. Gadenne, P.; Beghdadi, A.; Lafait, J. *Opt. Commun.* **1988,** *65,* 17–21. doi:10.1016/0030-4018(88)90433-6

57. Liu, Y.; Zhang, Y.; Ding, H.; Xu, S.; Li, M.; Kong, F.; Luo, Y.; Li, G. *J. Mater. Chem. A* **2013,** *1,* 3362–3371. doi:10.1039/c3ta00953j

58. Álvarez-Puebla, R. A. *J. Phys. Chem. Lett.* **2012,** *3,* 857–866. doi:10.1021/jz201625j

59. Le Ru, E. C.; Blackie, E.; Meyer, M.; Etchegoin, P. G. *J. Phys. Chem. C* **2007,** *111,* 13794–13803. doi:10.1021/jp0687908

Nonlinear absorption and scattering of a single plasmonic nanostructure characterized by *x*-scan technique

Tushar C. Jagadale[1,2], Dhanya S. Murali[1] and Shi-Wei Chu[*1,3]

Full Research Paper

Address:
[1]Department of Physics, National Taiwan University, No.1, Sec. 4, Roosevelt Rd., Taipei 10617, Taiwan, [2]Technical Physics Division, Bhabha Atomic Research Centre, Mumbai 400085, India and [3]Molecular Imaging Centre, National Taiwan University, No.1, Sec. 4, Roosevelt Rd., Taipei 10617, Taiwan

Email:
Shi-Wei Chu[*] - swchu@phys.ntu.edu.tw

* Corresponding author

Abstract

Nonlinear nanoplasmonics is a largely unexplored research area that paves the way for many exciting applications, such as nanolasers, nanoantennas, and nanomodulators. In the field of nonlinear nanoplasmonics, it is highly desirable to characterize the nonlinearity of the optical absorption and scattering of single nanostructures. Currently, the common method to quantify optical nonlinearity is the *z*-scan technique, which yields real and imaginary parts of the permittivity by moving a thin sample with a laser beam. However, *z*-scan typically works with thin films, and thus acquires nonlinear responses from ensembles of nanostructures, not from single ones. In this work, we present an *x*-scan technique that is based on a confocal laser scanning microscope equipped with forward and backward detectors. The two-channel detection offers the simultaneous quantification for the nonlinear behavior of scattering, absorption and total attenuation by a single nanostructure. At low excitation intensities, both scattering and absorption responses are linear, thus confirming the linearity of the detection system. At high excitation intensities, we found that the nonlinear response can be derived directly from the point spread function of the *x*-scan images. Exceptionally large nonlinearities of both scattering and absorption are unraveled simultaneously for the first time. The present study not only provides a novel method for characterizing nonlinearity of a single nanostructure, but also reports surprisingly large plasmonic nonlinearities.

Introduction

It is well known that the optical properties of plasmonic nanostructures differ significantly from those of the corresponding bulk materials, mainly because of two reasons, i.e., the enhancement in the surface-to-volume ratio and the appearance of resonance effects such as surface plasmon resonance (SPR). For example, the color, or more precisely the scattering and absorption spectra, of metallic nanostructures can be completely different from their bulk counterparts. Plasmonic nanostructures, in general, are characterized by strong scattering, great photostability, high brightness and exceptional localization precision.

In addition, SPR increases the local electric fields, and thus optical nonlinear interactions are significantly enhanced in metallic nanostructures [1-3]. Nonlinear nanoplasmonics is an emerging field that deals with the nanoscale-confined enhancement of optical fields as well as with the giant nonlinearity provided by plasmonic nanostructures [4-6].

The potential applications of nonlinear nanoplasmonics include nanolasers [7], nanoantennas [8], surface plasmon polariton (SPP)-based waveguides [9], nanostructure-based optical limiters [10], nanoscopy instruments [11,12], and nanoelectronics as integrated optical circuits or transistors for information processing and storage [13]. For the evaluation of plasmonic nonlinear nanophotonics, a technique capable of characterizing the nonlinearity of a single plasmonic nanostructure is highly desirable. Currently, various characterization techniques allow for measurements of nonlinear optical constants such as the absorption coefficient (β) or the refractive index (n_2). These techniques include the *z*-scan method (both β and n_2) [14], degenerate four-wave mixing (only n_2) [15], nearly degenerate three-wave mixing (only n_2) [16], optical Kerr gate and ellipse rotation measurements (both β and n_2) [17], self-phase modulation (only n_2) [18] and Mach–Zehnder interferometry (both β and n_2) [19]. However, please note that all these methods measure nonlinearity in the bulk phase or in thin films [20]. Among them, *z*-scan is probably the most widely adopted technique because of its experimental feasibility and the capability to determine both the nonlinear refractive index and the nonlinear absorption [21]. Below, we briefly address the principle of *z*-scan and its limitations.

The *z*-scan technique is based on measurement of transmittance as a thin sample moves along the propagation path (*z*-axis) of a focused laser beam. The thickness of the sample should be much smaller than the confocal parameter of the beam. Two measurement methods are commonly used, namely open-aperture and closed-aperture *z*-scan. In the open-aperture setup, the transmitted light is completely collected by a large-area power detector. If there is no nonlinearity, the transmittance will be constant no matter where the sample is. However, when there is nonlinear absorption, the transmittance changes as the sample is in the vicinity of the focus, where the intensity is highest along the beam path. Therefore, the open-aperture setup is sensitive to nonlinear absorption and measures the imaginary part of the nonlinear refractive index. In the closed-aperture setup, the transmittance is measured through a small aperture in front of the power detector, so the detected signal is sensitive to beam divergence/convergence, which is determined by the real part of the nonlinear refractive index in the thin sample. When there is no nonlinearity, the transmittance is again constant no matter where the thin sample is. When nonlinear refractive index

exists, the sample acts like a *z*-dependent lens that modifies the transmission beam shape. In the closed-aperture method, the power dependency in *z*-direction quantifies the real part of the nonlinear refractive index [21].

In brief, in case of linear responses, the *z*-scan output will be a horizontal line, i.e., constant versus *z*; while for nonlinear responses, the *z*-scan result deviates from a horizontal line, providing a high-sensitivity detection scheme for nonlinearity. However, *z*-scan measurements typically acquire nonlinear responses from thin samples in which multiple nanostructures are illuminated simultaneously, and collective behavior is monitored. The *z*-scan technique has extensively been applied to study the nonlinear absorption of thin plasmonic films [20], but not that of a single plasmonic nanostructure.

In this study, we propose a different method named *x-scan* to characterize the optical nonlinearity of a single nanostructure. The method is based on laser scanning microscopy, where an excitation beam spot moves in the lateral *x*-direction across a single nanostructure. Similar to the requirements of *z*-scan, but converted into the *x*-direction, the diameter of the nanostructure should be much smaller than the point spread function (PSF) of the laser focus. At low excitation intensities, when there is no nonlinear response, a Gaussian profile of the scanned image due to convolution of the laser PSF and the nanostructure is expected. However, when nonlinearity arises in the nanostructure at higher excitation intensities, the image profile is expected to deviate from the Gaussian profile, thus providing a high-sensitivity detection method for nonlinearity, similar to the *z*-scan technique.

In order to fully characterize the nonlinearity of a single nanostructure, our *x*-scan setup is equipped with two optical detection paths in forward and backward direction, where the former determines the attenuation signal and the latter measures the backscattering signal. Similar to open- and closed-aperture *z*-scan, our *x*-scan technique simultaneously quantifies absorption and scattering, relating to the imaginary and real parts of the refractive index. Applying the novel two-path *x*-scan method to a single gold nanostructure, we have unraveled unprecedented large nonlinearities of both scattering and absorption.

Results and Discussion
Microscopic measurement of a single plasmonic nanostructure

The idea for characterizing the nonlinear absorption and scattering of a single plasmonic nanostructure using a standard laser scanning microscope is schematically shown in Figure 1a. An inverted microscope is employed with the excitation laser beam

in upward direction focused on a single plasmonic nanostructure using an objective with numerical aperture (NA) equal to 1.4. The backscattered light is collected by the same high-NA objective, while the transmitted light is collected by a condenser with an NA of 0.9. Usage of objectives with large NA in both paths ensures efficient collection of the signal of dipole scattering, which is the dominant scattering mode of a small nanostructure [22], in the microscope system. The laser excitation beam is raster scanned in the lateral *x*- and *y*-directions using a pair of galvanometer mirrors, allowing for the observation of the PSF in both the forward and backward detection paths [23].

Figure 1b is a representative linear transmission profile of a single plasmonic nanostructure. The laser-scanning PSF is given as an inset in Figure 1b, having a bright background and a dark spot in the center where the nanostructure is located. The transmitted background represents the total excitation intensity (T_o), which is equal to the sum of the nanoparticle-induced attenuation (A_{NP}) and the transmission through the nanoparticle (T_{NP}), i.e., $T_o = A_{NP} + T_{NP}$. Note that forward scattering is included in the transmission signal T_{NP}. Thus, the attenuation signal A_{NP} only contains absorption and backscattering. The dark spot in the image, i.e., the Gaussian dip in the *x*-scan signal profile, quantifies the magnitude of attenuation.

Figure 1c is a representative profile of linear backscattering from a single plasmonic nanostructure at low excitation intensity, and the inset gives the laser-scanning PSF. A Gaussian peak is typically observed, and the peak height quantifies the intensity of the backscattering signal (R). Importantly, a confocal aperture in the backward detection path provides the capability of optical sectioning, and the nanostructure is typically immersed in oil to remove strong reflection signal from the glass slides (see Experimental section).

From the backscattering and attenuation profiles, the absorption of a single plasmonic nanostructure can be quantified as explained below. It is well known that the total attenuation contains the total absorption and the total scattering (forward and backward). Nevertheless, in our case, $A_{NP} = T_o - T_{NP}$, where the transmission through the nanoparticle T_{NP} already includes the forward scattering; thus, here the nanoparticle-induced attenuation A_{NP} is comprised of the absorption and "only" the backscattering R of the nanoparticle. As mentioned above, attenuation and backscattering are monitored in the forward and backward paths, respectively. By checking the linearity of the excitation and detection systems and calibrating the signal intensities with the aid of the glass reflections in the backward and forward paths (Experimental section), the pure
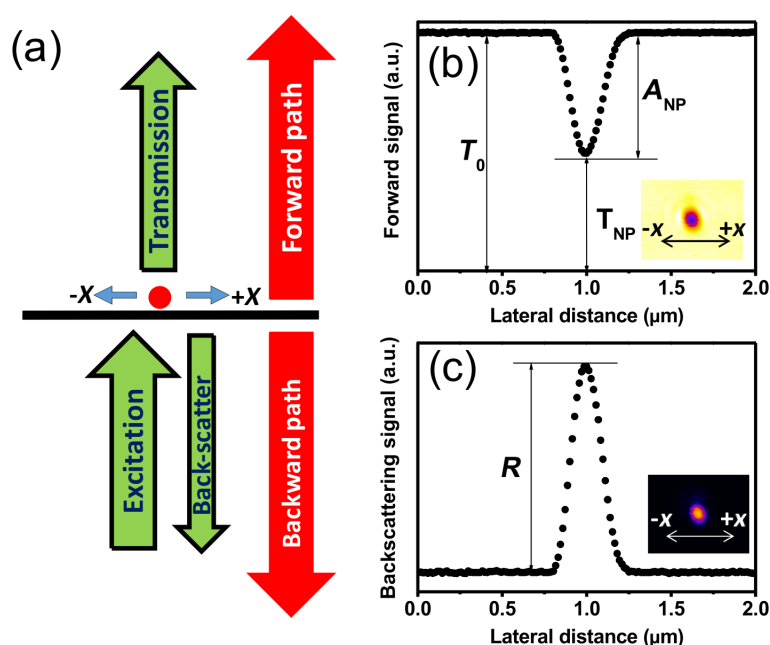

Figure 1: (a) Schematic principle of the *x*-scan method, the excitation focus is scanned in *x*-direction. The back-scattering and transmission of a single nanostructure are separately recorded in backward and forward direction. (b, c) Representative profiles corresponding to the two detection paths. (b) The dip value of the transmission profile gives the attenuation A_{NP} of the same single plasmonic nanostructure. T_0 and T_{NP} denote the initial laser intensity (no interaction with the nanostructures) and the transmission measured through the gold nanostructure, respectively. The peak value of (c) gives the backscattering intensity R.

absorption signal is obtained by subtracting the backscattering from the attenuation signal, i.e., $A_{NP} - R$.

In the following, we report how the attenuation and backscattering signals of a single spherical gold nanostructure with increasing excitation intensity develop from an initial linear Gaussian shape to the nonlinear profiles.
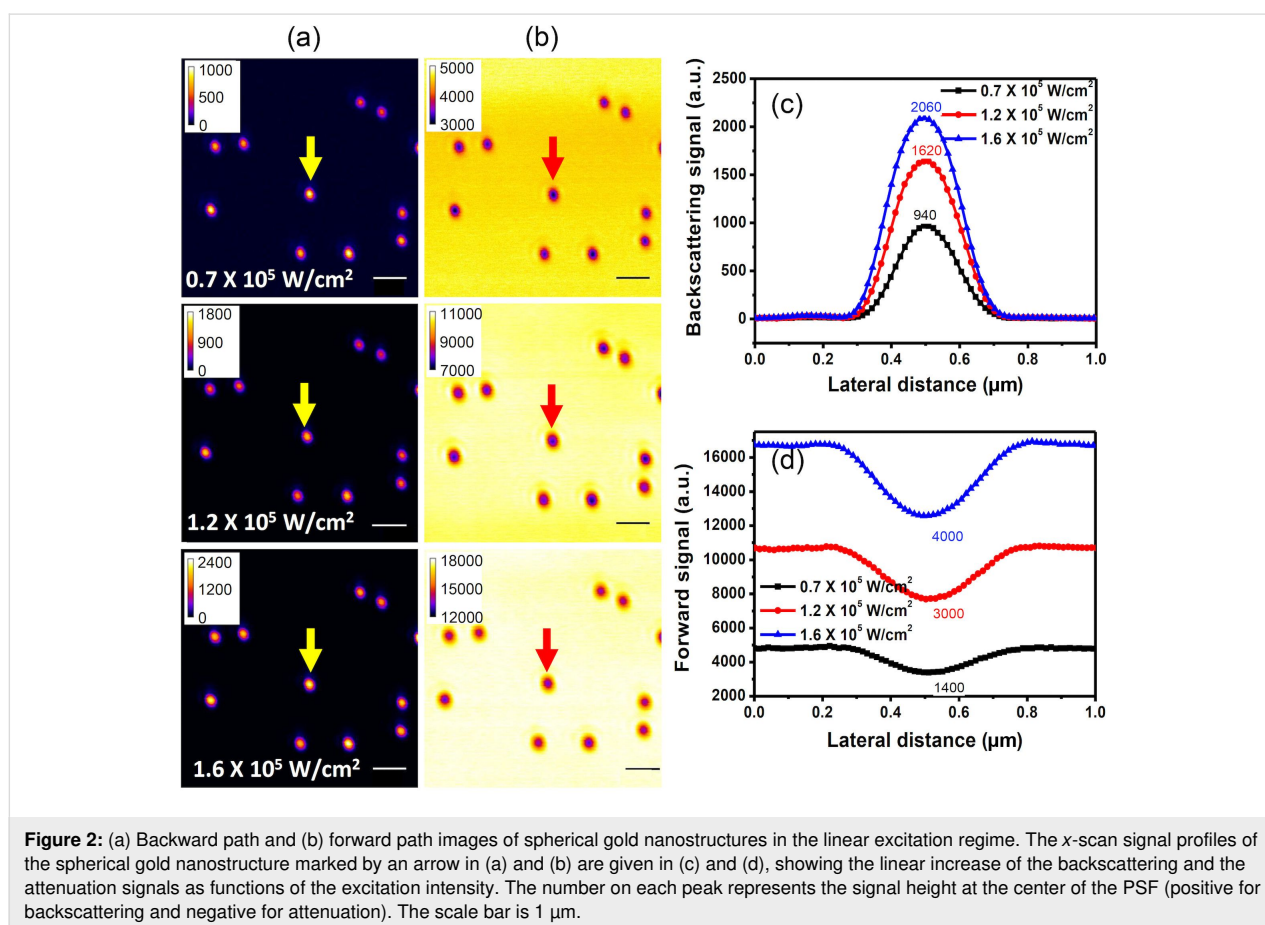
Linear response: Gaussian PSF

Spherical gold nanostructures dispersed on a glass surface are examined with the two-channel *x*-scan method. Figure 2 shows the power-dependent scattering images and the corresponding signal profiles in the low-power region, manifesting linear responses. Figure 2a and Figure 2b are images acquired in the backward and forward beam paths, respectively. The corresponding excitation intensities are given in each panel. Each image shows ten particles, most of which exhibit similar signal intensities, indicating that the nanoparticles are uniform in size.
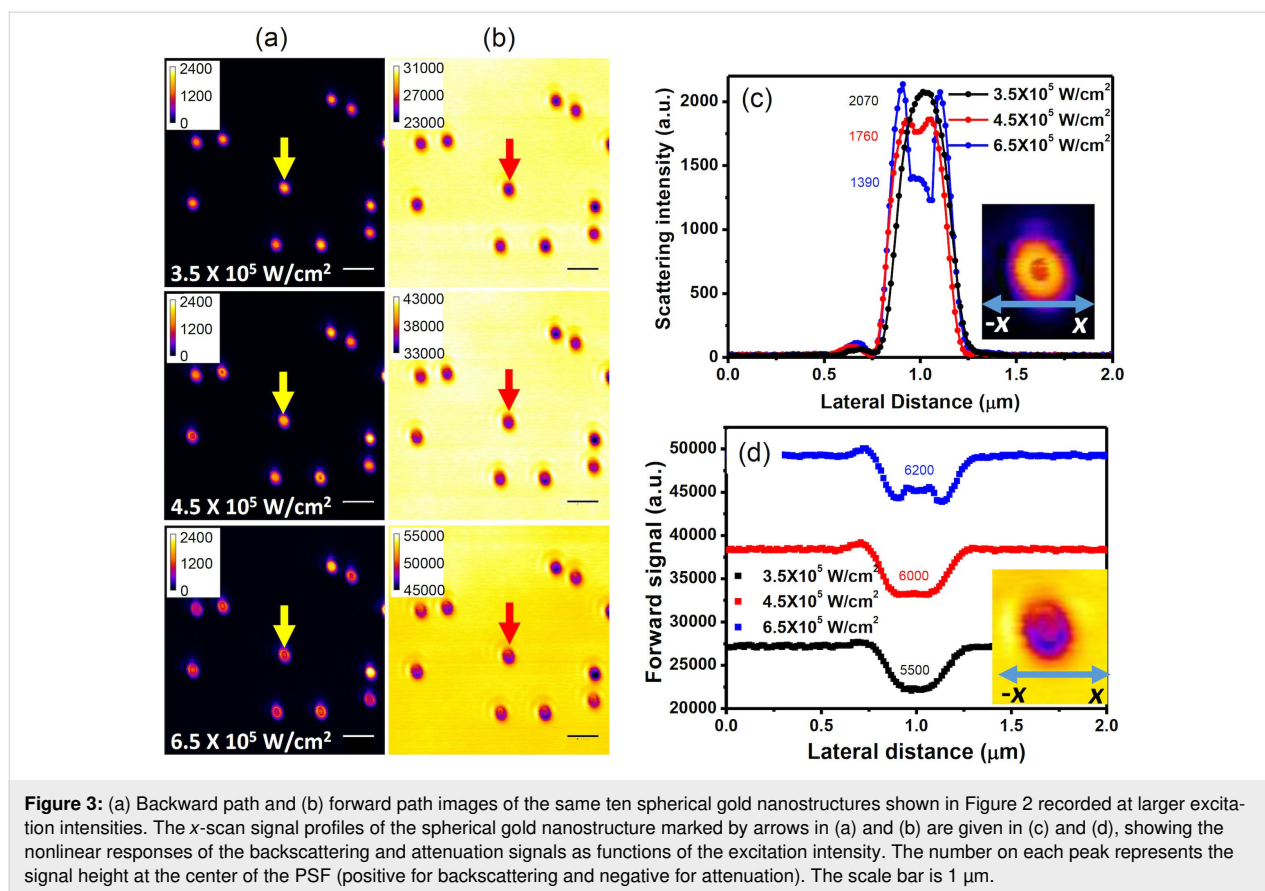
Figure 2c and Figure 2d show the respective backscattering and attenuation profiles of the randomly selected single gold nanostructure marked by an arrow in Figure 2a,b. Whether a single nanoparticle has been measured can be examined by inspection of the corresponding scattering spectrum and comparison of the resonance peak with the prediction by Mie theory. The scattering spectrum also helps to monitor changes of the particle size/shape while heating, as we have demonstrated in Figure 2a of [12]. Both the backscattering and the attenuation profiles show a nice Gaussian shape, suggesting that the optical responses are linear at low excitation intensities, as expected. The peak value and dip value (relative to the background) for each curve are given in the figures, showing that the backscattering and attenuation signal intensities indeed increase in proportion with the excitation intensity, further supporting the linear behavior in this excitation intensity range.

Nonlinear response I: saturation of the PSF

When we increase the excitation intensity, interesting changes in the shape of the PSF of the single spherical gold nanostructures are observed. Figure 3a and Figure 3b show the backward path and forward path images recorded at increasing excitation intensities. Figure 3c and Figure 3d give the corresponding scattering and attenuation profiles, respectively. The enlarged images of one randomly selected spherical nanostructure are shown as insets of Figure 3c and Figure 3d. The asymmetry in

Figure 2: (a) Backward path and (b) forward path images of spherical gold nanostructures in the linear excitation regime. The *x*-scan signal profiles of the spherical gold nanostructure marked by an arrow in (a) and (b) are given in (c) and (d), showing the linear increase of the backscattering and the attenuation signals as functions of the excitation intensity. The number on each peak represents the signal height at the center of the PSF (positive for backscattering and negative for attenuation). The scale bar is 1 μm.

Figure 3: (a) Backward path and (b) forward path images of the same ten spherical gold nanostructures shown in Figure 2 recorded at larger excitation intensities. The *x*-scan signal profiles of the spherical gold nanostructure marked by arrows in (a) and (b) are given in (c) and (d), showing the nonlinear responses of the backscattering and attenuation signals as functions of the excitation intensity. The number on each peak represents the signal height at the center of the PSF (positive for backscattering and negative for attenuation). The scale bar is 1 μm.

the enlarged forward path image might be due to the slight misalignment of the condenser in the forward collection path. There are several interesting observations to be made in these figures.

First, both the forward and the backward PSF profiles are no longer of Gaussian shape, indicating the existence of nonlinearities. At an excitation intensity of 4.5×10^5 W·cm^{-2} (red curves in Figure 3c and Figure 3d), nearly flattop PSFs are observed in both channels, manifesting the saturation behavior of both scattering and attenuation.

Second, dips in the intensity peaks are observed in both channels as the excitation intensity increases to 6.5×10^5 W·cm^{-2} (blue curves in Figure 3c and Figure 3d), leading to doughnut-like shapes, as shown in the insets. Since the excitation has a Gaussian profile, the intensity of which is highest in the center of the PSF, the doughnut-shaped responses indicate that the amplitude of the scattering and attenuation decreases with increasing excitation intensity. This is a counterintuitive result, but the doughnut-shaped PSF can indeed be observed for most of the particles shown in Figure 3a and Figure 3b. We will discuss the mechanism of this unexpected nonlinear response later.

Third, as obvious from the numbers on each peak in Figure 3c and Figure 3d, the backscattering signal decreases quickly while the attenuation signal increases slowly. As mentioned earlier, the attenuation intensity contains portions of absorption and backscattering signals, and with a proper calibration, we are able to quantify the percentage of absorption in the two-channel measurement. We derive the absorption as the difference in the scattering and attenuation signals. The results in Figure 3c and 3d indicate that the absorption nonlinearity might be different from the backscattering nonlinearity.

Nonlinear response II: reverse saturation of the PSF

Upon increasing the excitation intensity above 10^6 W·cm^{-2}, further interesting changes in the PSFs of individual gold nanostructures are observed in both detection paths. Figure 4a and Figure 4b show the backward and forward images of the nanoparticles, and Figure 4c and Figure 4d give the corresponding PSF profiles. Different from the saturation behavior described in the previous section, at excitation intensities of more than ca. 10^6 W·cm^{-2}, a new peak emerges at the center of the PSFs, manifesting a reverse saturation behavior. The phenomenon is more pronounced in the scattering curves depicted in Figure 4c than in the attenuation curves shown in Figure 4d. Yet, the
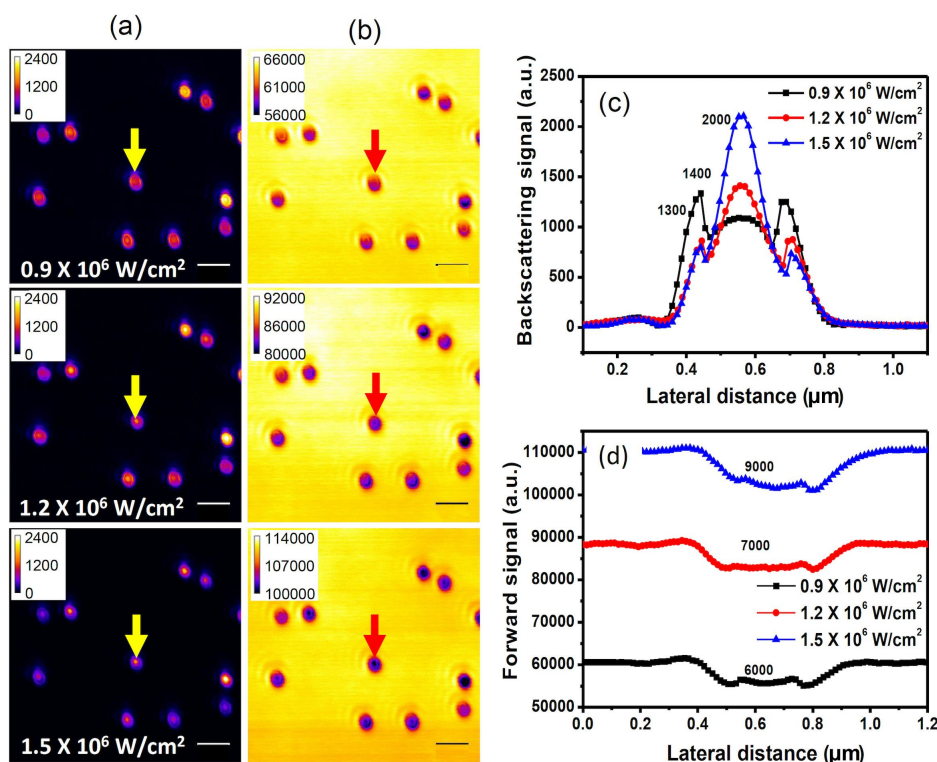
Figure 4: (a) Backward path and (b) forward path images of the same ten spherical gold nanostructures as in Figure 3 at excitation intensities above 10^6 W·cm^{-2}. The *x*-scan signal profiles of the spherical gold nanostructure marked by arrows in (a) and (b) are given in (c) and (d), showing strong nonlinear responses of the backscattering and the attenuation signals versus the excitation intensity. The number on each peak represents the signal quantity at the center of the PSF (positive for backscattering and negative for attenuation). The scale bar is 1 µm.

maximum signal values of each of the curves indicate that both scattering and attenuation enter the reverse saturation regime.

As the excitation intensity increases to 1.5×10^6 W·cm^{-2}, a new shape of the peaks emerges, which is most obvious in Figure 4c. Apparently, the new peak shape has a much smaller FWHM compared to the original diffraction-limited PSF (Figure 2). The small FWHM of the reverse saturation peak implies that the amplitude of the scattering and attenuation signals increases faster than the excitation intensity. This means that the power dependency in this region (slope of output versus input) exceeds linearity. Moreover, we did not observe any melting of the nanoparticles in the measurement range, thus, the *x*-scan measurement is fully reversible and repeatable even at the highest excitation intensity of 2×10^6 W·cm^{-2} employed in the measurement (see below in Figure 5). However, once the excitation intensity reaches 5×10^6 W·cm^{-2}, the *x*-scan process becomes nonreversible, possibly because the particles are melted or damaged.

Summarizing the nonlinear behavior

Figures 2–4 depict the backward and forward signals of ten plasmonic gold nanostructures at increasing excitation intensity.

Taking the maximum signal intensity values of the corresponding PSF profiles of the backward and forward signals, the excitation intensity dependent attenuation and scattering curves are derived (blue and red dots in Figure 5a). As described in Figure 1, the absorption ratio can be derived as $A_{NP} - R$ (green dots in Figure 5a). It is very interesting to see that the intensity dependence of the absorption differs strongly from that of the scattering. The latter significantly shows characteristics of saturation and reverse saturation, while the former shows signs of saturation.

Before we compare the nonlinear responses of scattering and absorption in more detail, first, we emphasize that the nonlinearity does not arise from second harmonic generation (SHG) or two-photon luminescence (TPL). Typically, laser intensities of gigawatts per square centimeter are necessary to induce SHG or TPL [24,25]. Yet, in our case, the excitation intensity is on the order of megawatts per square centimeter, hence, three orders of magnitude lower. In our earlier work, we suggested that the physical origin of the observed nonlinearity lies within photothermal plasmonic interactions [12]. Even though the narrow central peak shown in Figure 4c has a large slope when plotted on a double-logarithmic scale, as we have shown in
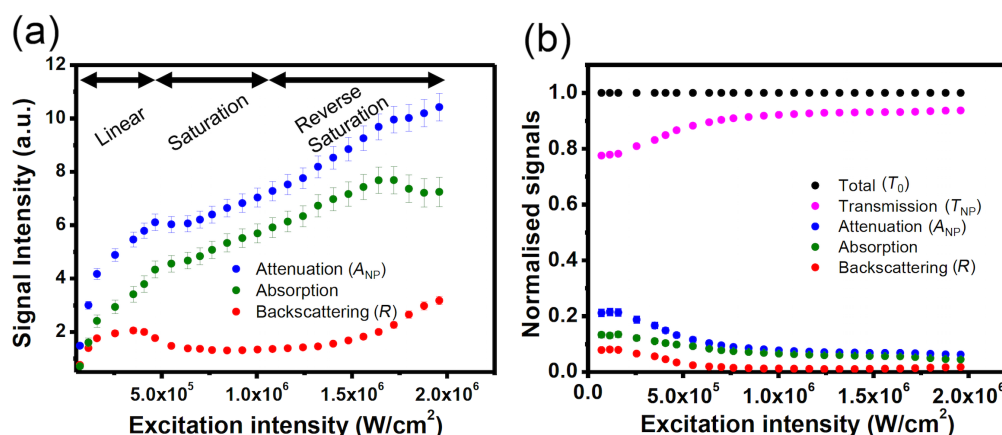
Figure 5: (a) Excitation intensity dependent attenuation (blue dots), absorption (green dots) and backscattering (red dots) signals. (b) Normalized signals (i.e., proportional to the corresponding cross sections) as functions of the excitation laser intensity.

[26], this behavior is different from conventional high-order nonlinearity.

In Figure 5b, we plot the normalized percentage of the different signals (total excitation intensity T_0, transmission T_{NP}, attenuation A_{NP}, absorption and backward scattering R). The different signals have been defined in Figure 1, and the absorption is given as $A_{NP} - R$. Since T_0 increases proportionally to the incident intensity, we normalized it to unity (black dots in Figure 5). All other signals were normalized accordingly. These normalized values can be viewed as the efficiency of the gold nanostructure interacting with light, that should be proportional to the corresponding cross sections. By definition T_{NP} (purple dots) + A_{NP} (blue dots) = T_0, which is true in the linear and in the nonlinear regime (Figure 5b).

In the linear regime, we find that the backward scattering efficiency is constant at a value of ca. 8% (red dots), which is about half of the efficiency of absorption (14%, green dots). This ratio is consistent with Mie theory, confirming the correctness of our signal calibration. According to Mie theory, the forward scattering ratio should be equal to the backward scattering ratio for this nanostructure. In our measurement, the transmission T_{NP} is 79% in the linear region, containing both forward scattering and photons that do not interact with nanostructures. Therefore, the true forward scattering contribution should be only ca. 8%, and about 71% should be due to transmission (no interaction with the nanoparticles). So, the derived ratios of scattering, absorption and transmission agree well with Mie theory.

In the nonlinear regime, i.e., at excitation intensities above 2×10^5 W·cm^{-2}, both attenuation and backscattering efficiencies decrease, but interestingly at different rates. Apparently,

the particles become more transparent at high excitation intensities, since the attenuation is significantly reduced. The corresponding absorption efficiency also decreases, which means that a saturation of the absorption is observed.

It is remarkable to see that the trends observed for attenuation and absorption in the nonlinear regime are quite different from that observed for backscattering. In the saturation regime (0.2–0.8 MW·cm^{-2}), the efficiencies of both absorption and backscattering are reduced by 7% (absorption 13.5% → 6.5%; backscattering 8% → 1%). However, the former changes only by a factor of two, while the latter by a factor of eight. Hence, the backscattering decay is by cubic order larger than the absorption decay.

One possible reason could be that scattering is proportional to the square of the variation of the dielectric constant, while absorption is linearly proportional to the dielectric constant. Within the dipole approximation, the absorption and scattering cross sections of a plasmonic nanosphere can be determined by classical Mie theory as:

$$c_{abs} = 4\pi k r^3 \, \mathrm{Im}\left(\frac{\varepsilon_p - \varepsilon_m}{\varepsilon_p + 2\varepsilon_m}\right) \qquad (1)$$

$$c_{sca} = 8\pi k^4 r^6 \left|\frac{\varepsilon_p - \varepsilon_m}{\varepsilon_p + 2\varepsilon_m}\right|^2 \qquad (2)$$

where, k is the wave vector, r is the radius of the particle, ε_p is the dielectric constant of the particle and ε_m is the dielectric

constant of the surrounding medium. Upon irradiation with high-intensity laser light, the photothermal effect induces a change of the particle permittivity leading to the nonlinearity. However, this equation only explains a square-order difference between scattering and absorption.

The above equation considers the total scattering cross section. Nevertheless, in our experiment, only backscattering is monitored. Therefore, another possible factor is asymmetric scattering due to the interference of high-order multipoles, which means that the efficiency of backscattering is no longer similar to that of forward scattering. Recently, there were many reports [27-29] on directional scattering effects due to multipole interferences in plasmonic nanostructures. However, most of them refer to specially designed structures for which the magnetic and the electric dipoles couple. More studies are necessary to prove the possibility of directional scattering in heated plasmonic nanostructures by simultaneously recording the efficiency of forward and backward scattering.

In addition to the interference of multipoles, in the forward direction, the light scattered in forward direction could also interfere with the transmitted light, such that the angular distribution might change. However, the forward scattered light is collected using a condenser of NA 0.9, hence, the collection angle is ±64°. Thus, most of the scattered light should be registered regardless of whether such interference occurs or not. Moreover, no interference patterns were observed in the forward image, and we have confirmed in the linear regime that the derived ratios of scattering, absorption and transmission agree well with Mie theory. Therefore, even if interference may occur in the forward direction, it does not influence the absorption efficiency in our case.

Another difference in the backscattering and absorption efficiencies shown in Figure 5 is that only the former exhibits a clear reverse saturation effect. This might be due to the additional thermal effect of the surrounding medium (immersion oil). Once again, further studies will be necessary to investigate the temperatures of the nanostructure and of the immersion medium, to provide a better explanation for the complicated photothermal nonlinearity.

Conclusion

In this report, we successfully demonstrate the simultaneous measurement of nonlinear attenuation, absorption and scattering in a single plasmonic nanostructure, for the first time using the two-path *x*-scan method. In contrast to the *z*-scan technique, the *x*-scan method, which is based on a laser scanning microscope, is capable to characterize and visualize the nonlinear responses from the PSF of a single nanostructure. With

the simultaneous measurement of forward and backward scattering, we could quantify the nonlinearity of absorption and scattering, which show surprisingly different behaviors. This may lead to the possibility of directional emission by a single heated nanostructure.

Experimental

The experimental setup, which is based on a modified confocal laser scanning microscope (IX71+FV300, Olympus, Japan) is shown in Figure 6a. A CW laser beam of wavelength 561 nm (Jive™ 561 nm, Cobolt, Sweden) was sent through a pair of built-in galvanometer (galvo) mirrors and then focused on plasmonic nanostructures by an objective (UPlanSApo 100x/NA1.4, Olympus, Japan) to form a two-dimensional raster scanning at its focal plane. The power of the excitation beam was fine-tuned through neutral density (ND) filters. The backscattered signals of the plasmonic nanostructures were collected through the same objective, separated from the incident beam with a 50/50 beam splitter, spatially filtered by a confocal aperture and finally detected by a backward photomultiplier tube (PMT) detector. On the other hand, the transmission signal was collected by a condenser (U-LTD/NA 0.9, Olympus, Japan) and was monitored by the forward PMT detector directly without confocal aperture. Both forward path and backward path images were formed on a computer by synchronizing the PMT signals and the scanner. Due to the different collection paths and PMT sensitivities in forward and backward directions, it is important to calibrate the signals in order to determine the absorption signal, as shown below.

Figure 6b shows the forward (transmission) and the backward (reflection) signals of a cover glass when gradually increasing the excitation intensity. Here, the backward signals came from the air–glass interface reflection at the top of the cover glass, while the transmitted photons make up the forward signal. The perfect linear dependency of both signals verifies that no nonlinearity is induced by the optical excitation and detection system. In addition, the air–glass reflection should be 4% and the transmittance 96%. This way, we made sure that the forward and backward signal were calibrated accurately (Figure 6c). The same calibration scheme was applied to yield Figures 2–5 in the main text, and to derive the ratio of scattering, absorption and transmission. Since the results agree well with the prediction of Mie theory, the reflectivity estimation should be reasonable.

Sample preparation

As samples, we used 80 nm diameter gold nanospheres commercially available from BBI Solutions, UK. Before use, the nanostructure solution was sonicated for 2 min to avoid particle aggregation. Then, one drop of the solution was placed
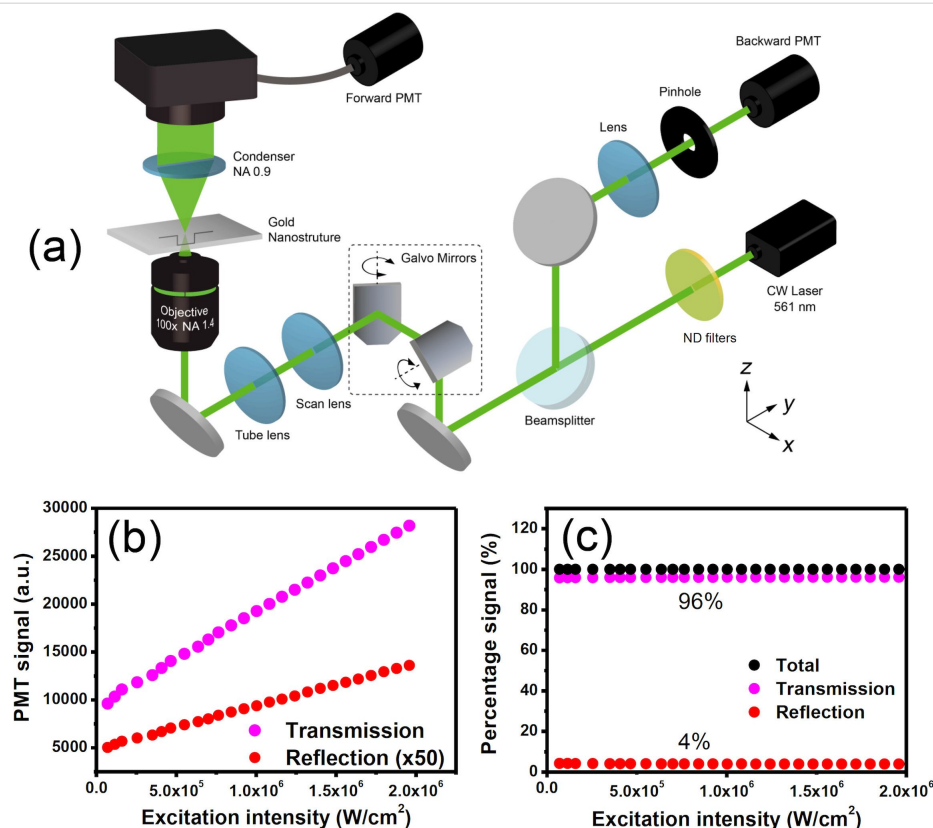
Figure 6: (a) Schematic of the experimental setup of the laser scanning system based on an inverted microscope. (b) Linearity test of the backward and forward signals from the partial reflection and transmission of a cover glass. It is obvious that no nonlinearity is induced by the microscope system. (c) The forward and backward signals are calibrated to correctly represent 4% reflection and 96% transmission from an air–glass interface. The same calibration applies to all signal processing in the main text.

on polysine slides (Thermo Fisher Scientifics, MA) for 20 s, which was subsequently gently rinsed with deionized water and dried in a nitrogen stream. The sample was immersed in index-matching oil to remove reflections by the glass.

Acknowledgements

ORCID® iDs

Shi-Wei Chu - https://orcid.org/0000-0001-7728-4329

Preprint

A non-peer-reviewed version of this article has been previously published as a preprint doi:10.3762/bxiv.2019.78.v1

References

1. Deka, G.; Sun, C.-K.; Fujita, K.; Chu, S.-W. *Nanophotonics* **2017,** *6,* 31–49. doi:10.1515/nanoph-2015-0149

2. Kauranen, M.; Zayats, A. V. *Nat. Photonics* **2012,** *6,* 737–748. doi:10.1038/nphoton.2012.244

3. Schuller, J. A.; Barnard, E. S.; Cai, W.; Jun, Y. C.; White, J. S.; Brongersma, M. L. *Nat. Mater.* **2010,** *9,* 193–204. doi:10.1038/nmat2630

4. Willets, K. A.; Wilson, A. J.; Sundaresan, V.; Joshi, P. B. *Chem. Rev.* **2017,** *117,* 7538–7582. doi:10.1021/acs.chemrev.6b00547

5. Stockman, M. I. *Opt. Express* **2011,** *19,* 22029–22106. doi:10.1364/oe.19.022029

6. Ogale, S. B.; Ahmad, A.; Pasricha, R.; Dhas, V. V.; Syed, A. *Appl. Phys. Lett.* **2006,** *89,* 263105. doi:10.1063/1.2424272

7. Oulton, R. F.; Sorger, V. J.; Zentgraf, T.; Ma, R.-M.; Gladden, C.; Dai, L.; Bartal, G.; Zhang, X. *Nature* **2009,** *461,* 629–632. doi:10.1038/nature08364

8. Kinkhabwala, A.; Yu, Z.; Fan, S.; Avlasevich, Y.; Müllen, K.; Moerner, W. E. *Nat. Photonics* **2009,** *3,* 654–657. doi:10.1038/nphoton.2009.187

9. Fang, Y.; Sun, M. *Light: Sci. Appl.* **2015,** *4,* e294. doi:10.1038/lsa.2015.67

10. Sun, Y.-P.; Riggs, J. E.; Henbest, K. B.; Martin, R. B. *J. Nonlinear Opt. Phys. Mater.* **2000,** *09,* 481–503. doi:10.1142/s0218863500000315

11. Chu, S.-W.; Su, T.-Y.; Oketani, R.; Huang, Y.-T.; Wu, H.-Y.; Yonemaru, Y.; Yamanaka, M.; Lee, H.; Zhuo, G.-Y.; Lee, M.-Y.; Kawata, S.; Fujita, K. *Phys. Rev. Lett.* **2014,** *112,* 017402. doi:10.1103/physrevlett.112.017402

12. Wu, H.-Y.; Huang, Y.-T.; Shen, P.-T.; Lee, H.; Oketani, R.; Yonemaru, Y.; Yamanaka, M.; Shoji, S.; Lin, K.-H.; Chang, C.-W.; Kawata, S.; Fujita, K.; Chu, S.-W. *Sci. Rep.* **2016,** *6,* 24293. doi:10.1038/srep24293

13. Fang, X.; MacDonald, K. F.; Zheludev, N. I. *Light: Sci. Appl.* **2015,** *4,* e292. doi:10.1038/lsa.2015.65

14. Kostritskii, S.; Aillerie, M.; Kokonyan, E.; Sevostyanov, O. *J. Phys.: Conf. Ser.* **2017,** *879,* 012003. doi:10.1088/1742-6596/879/1/012003

15. Munk, D.; Katzman, M.; Westreich, O.; Nun, M. B.; Lior, Y.; Sicron, N.; Paltiel, Y.; Zadok, A. *Opt. Mater. Express* **2018,** *8,* 66–72. doi:10.1364/ome.8.000066

16. Slabko, V. V.; Popov, A. K.; Tkachenko, V. A.; Myslivets, S. A. *Opt. Lett.* **2016,** *41,* 3976–3979. doi:10.1364/ol.41.003976

17. Sun, Q.; Liu, H.; Huang, N.; Wang, Z.; Li, S.; Han, J. *Laser Phys.* **2015,** *25,* 125403. doi:10.1088/1054-660x/25/12/125403

18. Liu, X.; Driscoll, J. B.; Dadap, J. I.; Osgood, R. M.; Assefa, S.; Vlasov, Y. A.; Green, W. M. J. *Opt. Express* **2011,** *19,* 7778–7789. doi:10.1364/oe.19.007778

19. Srivastava, A.; Medhekar, S. *Opt. Laser Technol.* **2011,** *43,* 1208–1211. doi:10.1016/j.optlastec.2011.03.010

20. Zakery, A.; Elliott, S. *Optical Nonlinearities in Chalcogenide Glasses and their Applications;* Springer Series in Optical Sciences; Springer: Berlin, Germany, 2007. doi:10.1007/978-3-540-71068-4

21. Sheik-bahae, M.; Said, A. A.; Van Stryland, E. W. *Opt. Lett.* **1989,** *14,* 955–957. doi:10.1364/ol.14.000955

22. Bohren, C. F.; Huffman, D. R. *Absorption and Scattering of Light by Small Particles;* Wiley: New York, NY, U.S.A., 1983. doi:10.1002/9783527618156

23. Chen, Y.-T.; Lee, P.-H.; Shen, P.-T.; Launer, J.; Oketani, R.; Li, K.-Y.; Huang, Y.-T.; Masui, K.; Shoji, S.; Fujita, K.; Chu, S.-W. *ACS Photonics* **2016,** *3,* 1432–1439. doi:10.1021/acsphotonics.6b00025

24. Chu, S.-W.; Wu, H.-Y.; Huang, Y.-T.; Su, T.-Y.; Lee, H.; Yonemaru, Y.; Yamanaka, M.; Oketani, R.; Kawata, S.; Shoji, S.; Fujita, K. *ACS Photonics* **2014,** *1,* 32–37. doi:10.1021/ph4000218

25. Molinaro, C.; El Harfouch, Y.; Palleau, E.; Eloi, F.; Marguet, S.; Douillard, L.; Charra, F.; Fiorini-Debuisschert, C. *J. Phys. Chem. C* **2016,** *120,* 23136–23143. doi:10.1021/acs.jpcc.6b07498

26. Butet, J.; Duboisset, J.; Bachelier, G.; Russier-Antoine, I.; Benichou, E.; Jonin, C.; Brevet, P.-F. *Nano Lett.* **2010,** *10,* 1717–1721. doi:10.1021/nl1000949

27. Mirin, N. A.; Halas, N. J. *Nano Lett.* **2009,** *9,* 1255–1259. doi:10.1021/nl900208z

28. Shegai, T.; Chen, S.; Miljković, V. D.; Zengin, G.; Johansson, P.; Käll, M. *Nat. Commun.* **2011,** *2,* 481. doi:10.1038/ncomms1490

29. Liu, W.; Miroshnichenko, A. E.; Neshev, D. N.; Kivshar, Y. S. *ACS Nano* **2012,** *6,* 5489–5497. doi:10.1021/nn301398a

Revealing the local crystallinity of single silicon core–shell nanowires using tip-enhanced Raman spectroscopy

Marius van den Berg[1,2], Ardeshir Moeinian[3], Arne Kobald[1,2], Yu-Ting Chen[1,2], Anke Horneber[1,2], Steffen Strehle[*4], Alfred J. Meixner[*1,2] and Dai Zhang[*1,2]

Full Research Paper

Address:
[1]Institute of Physical and Theoretical Chemistry, Eberhard Karls University of Tübingen, Auf der Morgenstelle 15, Tübingen, Germany, [2]Center for Light-Matter Interaction, Sensors & Analytics (LISA+), Eberhard Karls University of Tübingen, Auf der Morgenstelle 15, Tübingen, Germany, [3]Institute of Electronic Devices and Circuits, Ulm University, Albert-Einstein-Allee 45, Ulm, Germany and [4]Institute of Micro- and Nanotechnology, Technische Universität Ilmenau, Max-Planck-Ring 12, Ilmenau, Germany

Email:
Steffen Strehle[*] - steffen.strehle@tu-ilmenau.de; Alfred J. Meixner[*] - Alfred.meixner@uni-tuebingen.de; Dai Zhang[*] - dai.zhang@uni-tuebingen.de

* Corresponding author

Keywords:
core–shell nanowires; local crystallinity; polarization angle-resolved spectroscopy; silicon; tip-enhanced Raman spectroscopy

Abstract

Tip-enhanced Raman spectroscopy is combined with polarization angle-resolved spectroscopy to investigate the nanometer-scale structural properties of core–shell silicon nanowires (crystalline Si core and amorphous Si shell), which were synthesized by platinum-catalyzed vapor–liquid–solid growth and silicon overcoating by thermal chemical vapor deposition. Local changes in the fraction of crystallinity in these silicon nanowires are characterized at an optical resolution of about 300 nm. Furthermore, we are able to resolve the variations in the intensity ratios of the Raman peaks of crystalline Si and amorphous Si by applying tip-enhanced Raman spectroscopy, at sample positions being 8 nm apart. The local crystallinity revealed using confocal Raman spectroscopy and tip-enhanced Raman spectroscopy agrees well with the high-resolution transmission electron microscopy images. Additionally, the polarizations of Raman scattering and the photoluminescence signal from the tip–sample nanogap are explored by combining polarization angle-resolved emission spectroscopy with tip-enhanced optical spectroscopy. Our work demonstrates the significant potential of resolving local structural properties of Si nanomaterials at the sub-10 nanometer scale using tip-enhanced Raman techniques.

Introduction

The properties of silicon are long standing topics of various investigations because silicon is still the most widely used semiconductor material for a broad range of micro- and nano-electromechanical systems, microelectronics, and photovoltaics [1,2]. Silicon nanostructures, such as bottom-up-grown nanowires [3], were also synthesized serving as multifunctional plat-

forms for field-effect transistors [4-6], photovoltaic devices [7-10] and miniaturized chemical sensors [5,11,12]. A key element for many of those devices are high-quality nanometer-scale semiconductor junctions, such as pn-junctions that ensure the intended electronic functionality of such nanometer-scale building blocks. A rational and well-established synthesis strategy for the creation of complex silicon nanostructures is metal-catalyzed vapor–liquid–solid (VLS) nanowire growth [13]. VLS nanowire growth belongs to the gas-phase synthesis procedures, similar to chemical vapor deposition (CVD), and enables direct nanowire growth in a bottom-up manner. The nanowire composition, in particular the doping concentration, can be controlled by an adequate adjustment of the synthesis gas mixture, e.g., by setting the SiH_4/B_2H_6 ratio during the synthesis of boron-doped silicon nanowires (SiNWs). A rational strategy to obtain radial homo- and heterojunctions is to overcoat the as-grown nanowires within the same reaction chamber by implementing a conventional CVD process (e.g., thermal SiH_4-CVD) yielding core–shell nanowires [14]. Although ideal epitaxial growth is frequently assumed, the crystallinity of the shell is intimately linked to multiple process parameters and, thus, subject to local variations at the nanometer scale [15]. Control and knowledge of the crystal state of core–shell nanowires are important to rationally design, understand and control the optical and electronic behavior of nanowire building blocks. Hence, there is an inherent need for non-destructive characterization techniques that are able to elucidate the local crystallinity.

Raman spectroscopy is such a type of non-destructive characterization techniques and has become a popular method to investigate structural properties of silicon samples [16,17]. Mizoguchi et al. [18] and Hopkins et al. [19] utilized it to show the influence of stress on the crystal lattice orientation angles and to determine the degree of surface roughness. Kolb et al. measured the lattice orientational change due to laser-induced temperature variation [20]. Furthermore, crystalline (c-Si) and amorphous (a-Si) Si show different Raman peaks, which can be used to determine the fraction of crystallinity and bond-angle distortion [21,22]. For example, Nikolenko et al. [23] investigated the local structure and phases of silicon by measuring its Raman peaks along a silicon wire prepared under high pressure. They found a shift of the transverse optical (TO) phonon peak along the wire, which could be attributed to a non-uniform growth of the nanowire and different crystalline phases. Agbo et al. showed that polarized excitation Raman spectroscopy is useful to distinguish hydrogenated nano-crystalline silicon films (nc-Si) from a-Si and c-Si areas [24].

Although, Raman spectroscopy is an overall powerful tool to characterize the material properties of Si, this technique requires

still an improvement regarding the sensitivity and the diffraction-limited optical resolution. Thus, a high-resolution technique that reveals both, the structural and the optical properties at the nanometer scale is needed to study the fraction of crystalline phases and defects within the SiNWs. Tip-enhanced Raman spectroscopy (TERS) has distinguished itself as a powerful characterization technique, which allows to obtain both the morphology and the so-called chemical "finger print" information simultaneously with a resolution of a few nanometers. The key element of this technique is a sharp tip resembling a nanometer-scale antenna. This nanoantenna is typically made by chemical etching of a thin Ag or Au wire or by evaporating a Ag or Au thin film on AFM tips. The tip works like an optical antenna when it is brought as close as a few nanometers to the sample surface and when it is illuminated with a tightly focused laser beam. The near field localized at the tip apex enhances the optical field in the tip–sample gap by several orders of magnitude and simultaneously directs the emitted photons from the gap into the far field for detection. With recent demonstrations of a spatial resolution even at the angstrom level [25], TERS has made real chemical nanospectroscopy possible [26-28].

In this work, the structural properties of VLS-grown core–shell SiNWs are investigated using both confocal Raman spectroscopy and TERS. Notably, the silicon core is single crystalline while the shell should be amorphous to nanocrystalline, depending on the synthesis parameters. Hence, these nanowires resemble ideal objects to study local crystallinity variations at the sub-10 nanometer scale using TERS. Furthermore, polarization angle-resolved spectroscopy is for the first time combined with TERS, in order to reveal the different polarizations of Raman scattering and the photoluminescence from the tip–sample nanogap.

Results and Discussion
Silicon nanowire core–shell morphology
In accordance with the VLS synthesis method (see Experimental section), the utilized Pt catalyst, or finally Pt_xSi_y, remains at the tip of the nanowire during growth. However, it is worth mentioning that other mechanisms of Pt-catalyzed growth of nanowires were also previously observed [29]. The overall morphology of the SiNWs was investigated by transmission electron microscopy (TEM). The high-resolution TEM investigation of the core area indicates that the SiNWs are mainly single crystalline. However, in some areas along the nanowire axis defects are present as well (Figure 1a). The diffraction pattern of this part of the SiNW (Figure 1b) shows more than one reflection, which indicates that the structure of the SiNW consists presumably of segments or grains with different orientation. Furthermore, catalyst migration along the SiNW backbone was observed in some cases (Figure 1c). Although the
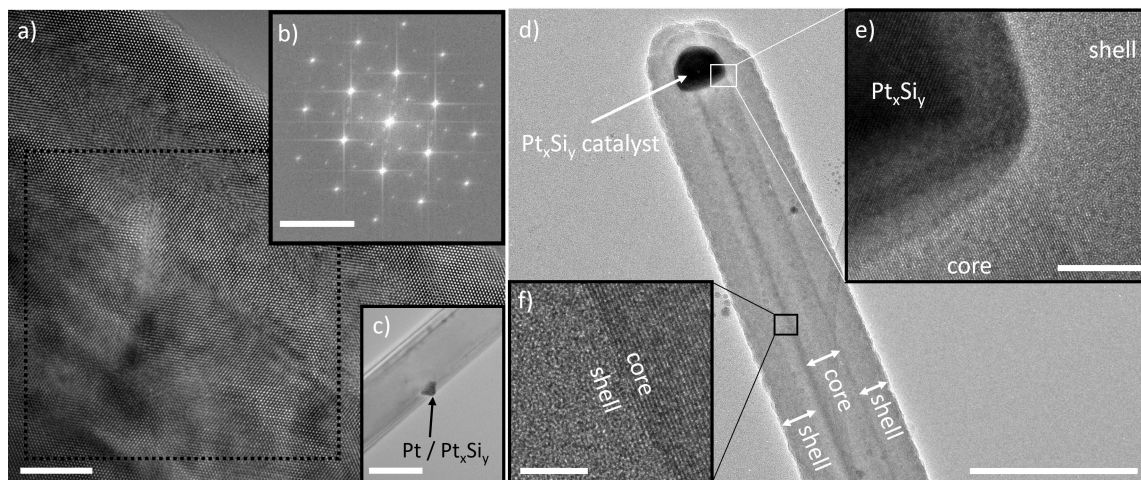
Figure 1: a) High-resolution TEM image of a segment of a SiNW obtained through Pt-catalyzed growth that exhibits several defects and differently oriented crystalline grains. b) The fast Fourier transformation image of the indicated area in panel a. c) TEM image showing a migrated metal particle on a SiNW. d) TEM image of a Pt-catalyzed core–shell SiNW showing the morphology of the junction between SiNW core and shell. e) Pt silicide catalyst and the shell region. f) Illustration of the interface between the SiNW core and the shell. Scale bars are for a) 5 nm, b) 5 nm^{-1}, c) 100 nm, d) 200 nm, e) 10 nm and f) 5 nm.

SiNWs grown by the VLS mechanism possess are crystalline, the silicon shells deposited onto the nanowires by thermal CVD (here using a temperature of 520 °C) can be amorphous [15]. Figure 1d illustrates such a core–shell SiNW with a distinct contrast in core–shell morphology. As it can be seen in Figure 1e and Figure 1f, the core region of the nanowire appears single crystalline and the crystal planes end abruptly at the core–shell interface. The shell region of the nanowire exhibits an amorphous morphology.

Confocal optical microscopy of silicon nanowires

As the first step, core–shell SiNWs grown with a platinum catalyst [29] are characterized using a custom-built confocal optical microscope. Figure 2a shows the representative geometry of these SiNWs, which were characterized using a helium ion microscope. In Figure 2b a hyper-spectral image composed of 32×24 spectra taken from an area of 20×20 μm^2 is shown, in which bundles of SiNWs can be seen. In Figure 2c two spectra taken from the positions marked with orange and blue points are given. The light blue and orange lines show the raw spectra, which are composed of a broad photoluminescence continuum emitted from the underlying Au thin film and sharp Raman peaks. For further analysis, these spectral features are fitted using Lorentzian functions for the Raman peaks and a Gaussian function for the photoluminescence peak. The first-order transverse optical mode of c-Si (F_{2g}) leads to a sharp Raman peak at 520 cm^{-1}; whilst a-Si is detected by a broad band centered at 495 cm^{-1} [28]. A thin oxide layer that covers the SiNWs, causes a broad Raman peak at 480 cm^{-1} and significantly influ-

ences the shape of the F_{2g} peak leading to a broadening and a stronger baseline of this peak [30,31]. In order to quantitatively evaluate the local structural composition, the a-Si and c-Si Raman peak intensities are therefore determined by integrating the total Raman intensities in the spectral ranges of 460–500 cm^{-1} for a-Si, and of 514–532 cm^{-1} for c-Si, after subtracting the PL background. To calculate the crystalline fraction (f_c) we use the model of Smit et al. [32] as shown in Equation 1. The areas of the Raman peaks of the c-Si and a-Si are used as the corresponding intensities (I_{c-Si} and I_{a-Si}) for the calculation of crystalline fraction (f_c).

$$f_c = \frac{I_{c-Si}}{\left(I_{c-Si} + 0.8 I_{a-Si}\right)}. \tag{1}$$

For the spots marked orange and blue Figure 2b, the corresponding spectra are shown in Figure 2c. Values of $f_c = 0.45$ and $f_c = 0.57$ were calculated, respectively. A further confirmation of the lower crystallinity in the spot marked by the orange dot comes from the full width at the half maximum (FWHM) of the Raman peaks. Both a-Si and c-Si peaks are significantly broader, 25% and 13%, respectively, at the location marked by the orange dot. These results agree well with the morphology revealed in the high-resolution TEM images (Figure 1c) since the sample position with the orange dot is located at the perimeter of the SiNW, where the a-Si shell dominates.

In order to obtain a detailed map of the crystalline fraction (f_c) along a single SiNW, 16×16 spectra are collected from a
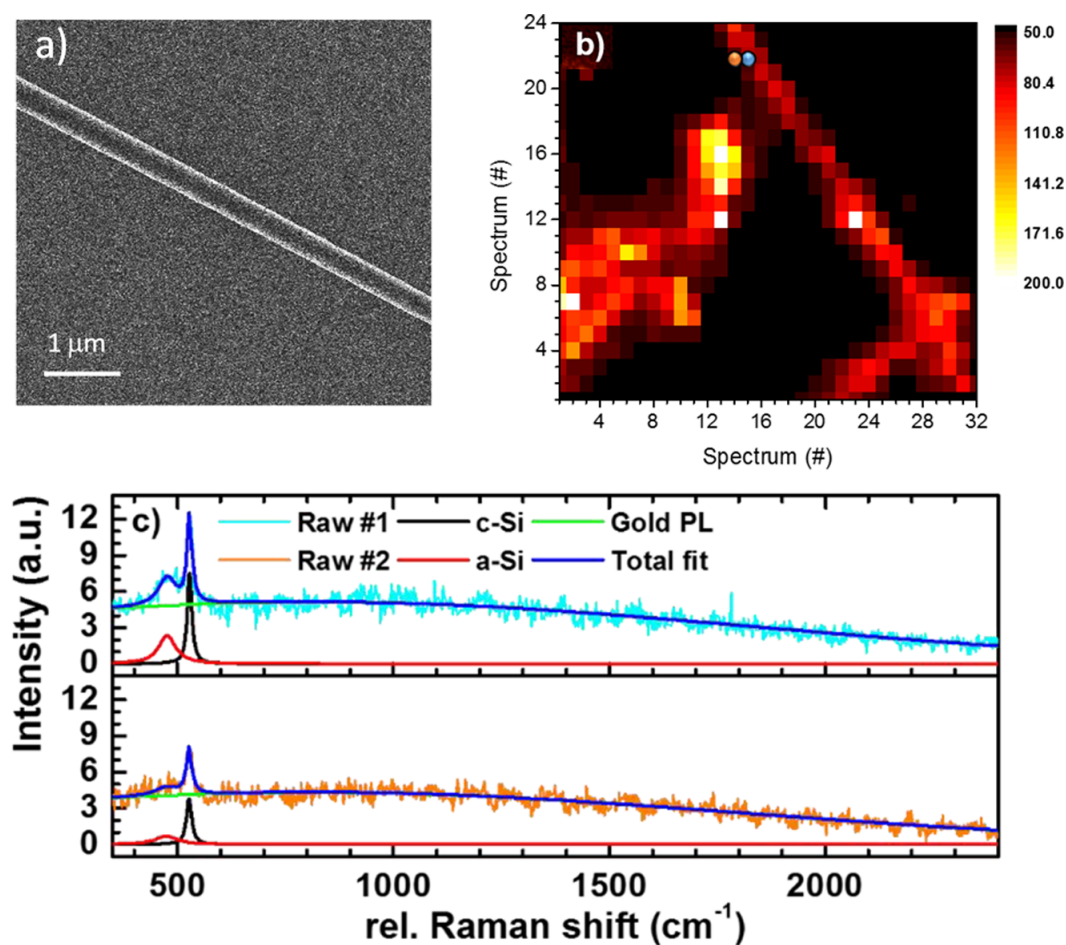
Figure 2: a) Representative helium ion microscopy image of a SiNW, which is supported on a Au-coated Si wafer. b) Hyperspectral image of the sample surface. 32 × 24 spectra are taken from a 20 × 20 µm² area. The color scale is based on the integrated intensity of each taken spectrum. c) Two example spectra taken from the positions marked by the orange and the blue dot in panel b. The original data is plotted in light-blue and orange. The Raman peaks of crystalline and amorphous silicon are fitted using Lorentzian functions, which are indicated by the black and the red line, respectively. The total fit for both spectra is indicated by the dark-blue line. Furthermore, the spectral background is fitted (green line) using a Gaussian function. The background results from photoluminescence of the Au film. Excitation source: 636.3 nm continuous-wave diode laser.

5 × 5 µm² area, which is marked by the yellow frame in Figure 3a. Each hyperspectral image consists of 16 × 16 spectra, resulting in a step size of 312.5 nm with a diffraction-limited laser focus of about 300 nm. In Figure 3b,c Raman spectra taken along the white arrow are shown. In Figure 3c, the Raman peaks of a-Si and c-Si were acquired with a better resolving grating with 600 lines/mm in contrast to the 150 lines/mm grating in panel b). The pink arrow in Figure 3c indicates the spectrum taken close to the ring-shaped pattern within the yellow frame in Figure 3a.

It can be clearly seen that the ratio between the intensities of a-Si and c-Si Raman peaks varies along the SiNW, mainly due to a change in the c-Si Raman intensity. To quantify this tendency, the 16 × 16 spectra are processed by peak fitting and integration as described above. The intensity distribution of the a-Si Raman peak is plotted in Figure 3d and appears to be rather constant along the silicon wire. It agrees with the TEM image in Figure 1c, where a homogenous presence of the amorphous component in the shell can be seen. In contrast, the intensity of the c-Si peak (Figure 3e) shows a clear decrease at the lower part of the SiNW. This could originate from a defect, visible as the ring-shaped pattern in Figure 3a, located at the bottom end of the yellow square. This observation is in line with the high-resolution TEM image in Figure 1c, where a migrated metal particle from the catalyst is shown. Inserting the intensity information from Figure 3d,e into Equation 1, a map of f_c along the SiNW is obtained. As shown in Figure 3f, the lowest crystalline fraction is about 0.45, and the highest is 0.70. Hence, an overview of the crystallinity of a single SiNW can be obtained at the diffraction-limited optical resolution of about 300 nm.
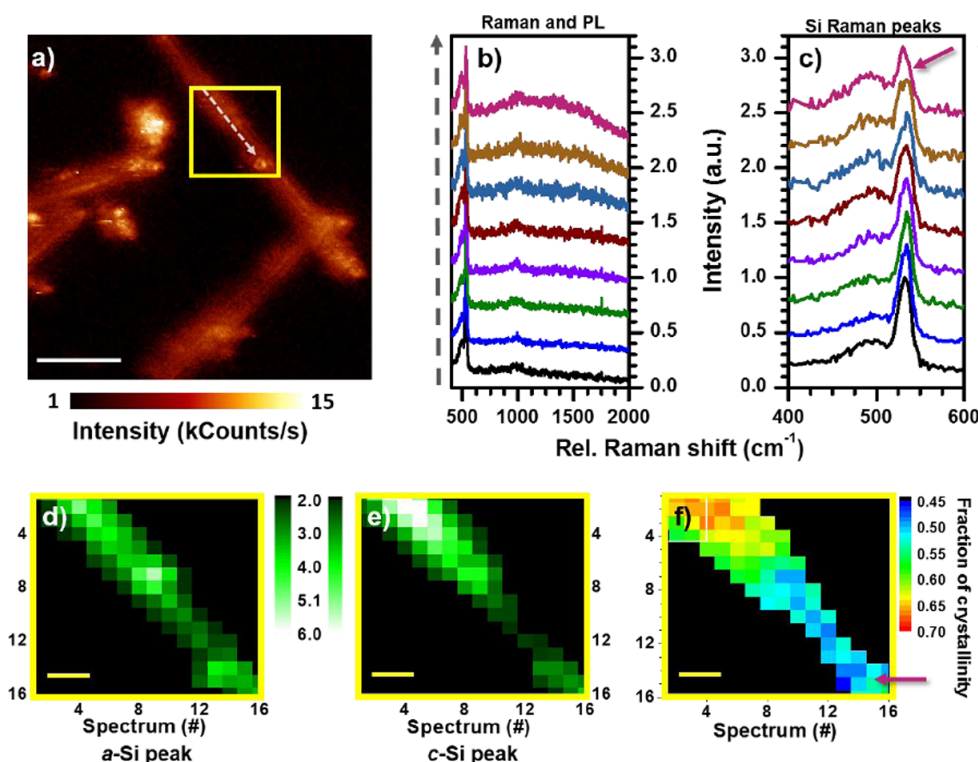
Figure 3: a) Confocal 20 × 20 μm² image of two intersecting SiNWs on a gold substrate. The yellow square marks the region where a hyperspectral image with16 × 16 spectra was recorded. b) Raman spectra with PL background were collected along the white arrow inside the yellow square in panel a. c) The evolution in a-Si and c-Si peak intensity along the scan direction shown in panel a. Spectra are vertically shifted for clarity. d) Integrated area of the a-Si peak. e) Integrated area of the c-Si peak. f) Calculated fraction of crystallinity. The drop in the fraction of crystallinity at the right bottom corner, corresponds to the ring-shaped pattern inside the yellow square in panel a. Its corresponding spectrum and position are indicated with a pink arrow in panels c and f, respectively. The white scale bar in panel a indicates 5 μm, and the yellow scale bars are 1 μm in panels d–f.

Tip-enhanced Raman spectroscopy of silicon nanowires

The evolution of c-Si and a-Si Raman peaks, and thus of the fraction of crystallinity of a single SiNW, is further studied using TERS, and the emitted optical signals are analyzed using polarization angle-resolved spectroscopy. Figure 4a shows a SEM image of the tip used for the TERS measurements. Scanning the tip across the laser focus gives an Airy disc-like pattern (Figure 4b), which is due to the photoluminescence emitted from the sharp tip apex. Irregularities can arise from the slight asymmetry of the tip apex. Figure 4c shows the polarization angle-resolved optical pattern of the photoluminescence of the gold tip. We positioned a Glan–Taylor polarizer in the beam in front of the entrance slit of the spectrometer and collected spec-
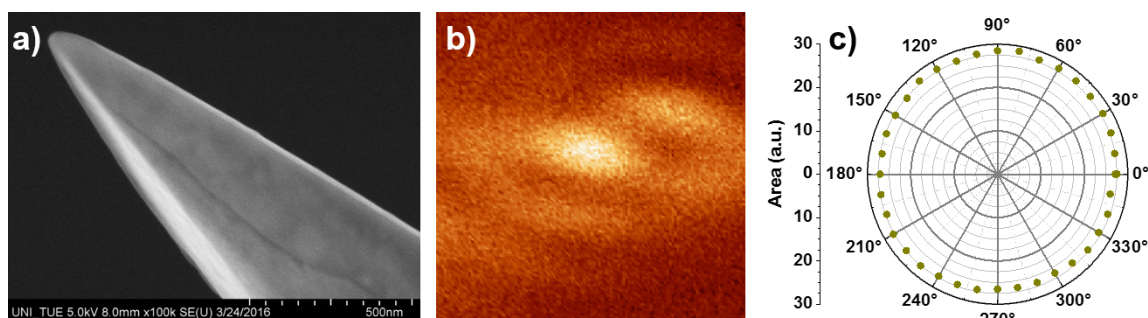

Figure 4: a) SEM image of the tip used. b) Optical image of the tip in focus. c) Polarization angle-resolved luminescence of the tip in focus without a sample; an almost perfectly circular emission pattern is observed.

tra while rotating the polarizer. The Glan–Taylor prism only transmits the optical signal along its fast axis. Therefore, the angle-resolved polarization of the emitted signal can be obtained by rotating the prism while collecting optical spectra. The circle pattern is originating from the emission of the plasmonic oscillation along the tip shaft. This is in good agreement with the electric field distribution in the focus of a radially polarized laser beam, where the dominant field component lays out-of-plane (parallel to the tip shaft). Figure 4b,c demonstrates that the tip apex can be easily excited, which is a precondition for producing a localized near field at the tip apex.

Next, we approached the sample to the tip and recorded the topography (size: 250×250 nm^2) along the perimeter of a SiNW. The tip–sample distance is controlled by a shear-force feedback. For this purpose, the tip is mounted on an oscillating tuning fork, which experiences a phase shift of the oscillation upon approach. This phase shift is recorded with a lock-in amplifier and fed to a feedback loop that maintains a constant distance to the sample. The scanned SiNW perimeter is indicated in Figure 5a. Along the white arrow, there is about 250 nm height difference between the SiNW and the underlying substrate. The white square shown in the optical image in Figure 5b highlights the SiNW measured using the shear-force scanning function of our custom-built TERS setup. Eight TERS spectra were taken along the white arrow in Figure 5a over a length of 64 nm. The dis-

tance between the two sequential spectra is 8 nm. The spectra were acquired from bottom to top, with the black spectrum on the SiNW and the yellow-green one on the underlying substrate. Notably, although a clear decrease in c-Si intensity is observed across the perimeter of the SiNW, the a-Si Raman peak intensity remains nearly constant and indicates the crystalline state of the SiNW shell. The Raman intensity evolutions of the c-Si and a-Si are shown in Figure S1a (Supporting Information File 1). We clearly show a decrease in the fraction of crystallinity from the center to the perimeter of the SiNW, which can be resolved with the optical resolution of 8 nm. These observations agree well with the morphology revealed by high-resolution TEM images in Figure 1c.

As a reference measurement, an equal number of far-field spectra (normal Raman spectra) are taken from the same sample positions (Figure 5d). Even between the SiNW and the underlying substrate, the decrease in the c-Si Raman peak is barely visible. This can be explained by the excitation area of the confocal laser focus, which is at least one order of magnitude larger than that in the TERS experiments. Therefore, only a marginal difference between two spectra of 8 nm apart is visible, even when the sampling point is not on the SiNW anymore ("off SiNW" spectrum, Figure 5d, and Figure S1b in Supporting Information File 1). Beeman et al. [22] suggested to use the root mean square bond-angle distortion $\Delta\Theta$ to evaluate the crys-
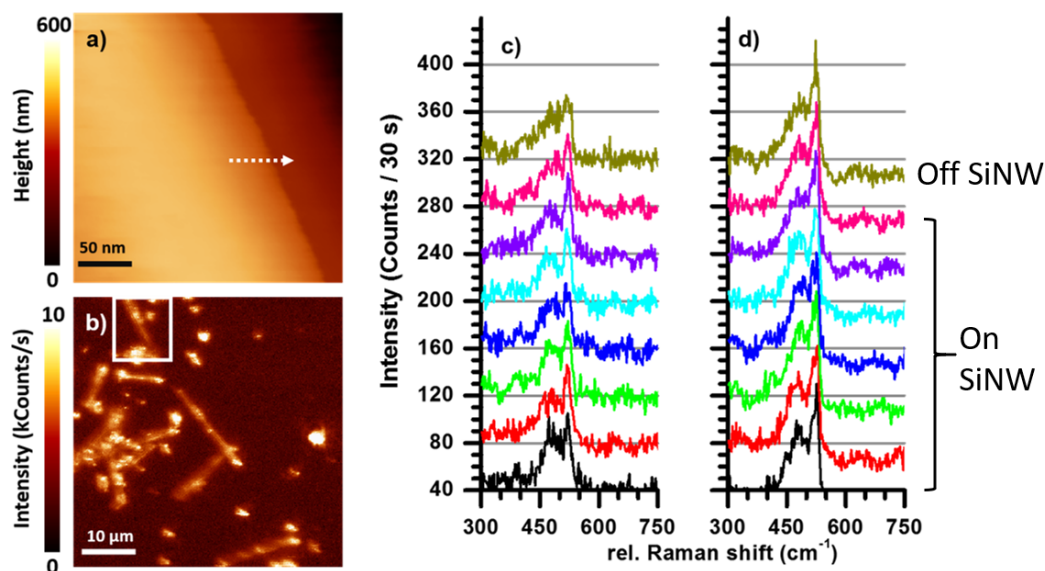

Figure 5: a) A shear-force scanning probe microscopy topography image (250×250 nm^2) of a silicon wire edge. The white arrow indicates the range and direction along which the Raman spectra in panels c and d were recorded. b) Location of the wire indicated on the 50×50 μm^2 optical image by a white square. c) TERS spectra recorded with a separation of 8 nm, vertically offset for clarity. A decreasing c-Si peak can be seeing when moving away from the edge along the arrow. d) Confocal spectra taken at exactly the same spots as the TERS spectra; the intensity ratios between the c-Si and a-Si show almost no variation. Both TERS and confocal spectra have been acquired with 170 μW excitation power and an integration time of 30 s per spectrum.

talline and amorphous fractions of Si, which can be calculated using the full width half maximum (FWHM, in cm^{-1}) of the one-phonon Raman peak of Si at about 520 cm^{-1} with the equation:

$$FWHM = \frac{(15 + 6\Delta\Theta)}{2}. \quad (2)$$

In c-Si with cubic diamond structure, $\Delta\Theta$ has a value of 0°, whereas in a-Si films $\Delta\Theta$ was experimentally determined to be in the range of 7.7° ≤ $\Delta\Theta$ ≤ 10.5°. In our experiments we calculated $\Delta\Theta_{avg,n\text{-}f} = 9.2°$ and $\Delta\Theta_{avg,conf} = 8.3°$ based on the near-field and confocal spectra, respectively. The slightly higher value of $\Delta\Theta$ determined with TERS could be due to the nanometer-sized penetration depth of the near field excited at the tip apex, in contrast to the far-field laser focus. Since the SiNWs contain a c-Si core and an a-Si shell (Figure 1), the shell can be excited stronger by the evanescent electromagnetic near field at the tip apex.

The highly improved optical resolution achieved with TERS depends strongly on the tip–sample interaction. When the sample is positioned within close proximity of the excited tip apex, the substrate material gains influence via the coupling between the oscillation field in the excited tip and its mirror image in the substrate. We have shown in a previous theoretical work that the permittivity of the tip and the substrate influences the near-field enhancement at the tip apex significantly [33]. In the next set of experiments, we combined angle-resolved polarization measurements with TERS to investigate the effects of tip–sample interactions on the optical signals. In Figure 6a the topography of a SiNW surface is shown. Along the dashed arrow, 32 spectra were recorded, and eight of them are plotted in Figure 6b. Although all spectra are taken on the surface of one SiNW, the intensity ratio differences between the c-Si and a-Si Raman peaks are clearly visible (Figure S2, Supporting Information File 1), which can be attributed to the variations of the local crystallinity within the SiNW. Furthermore, polarization angle-resolved emission measurements are performed at two
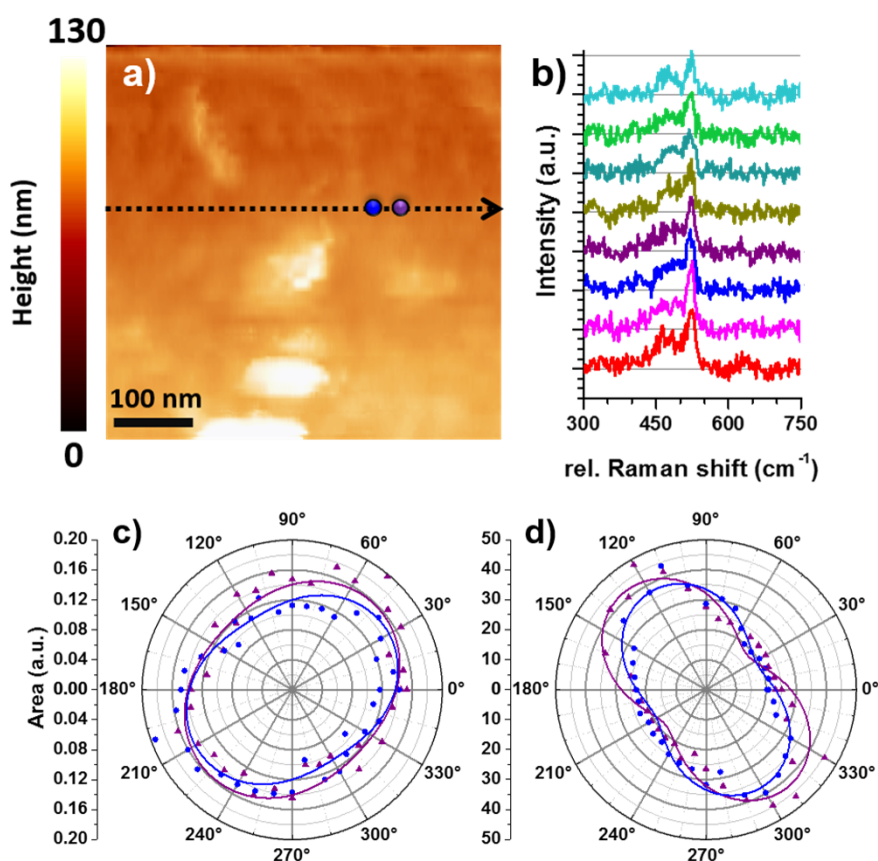

Figure 6: a) Topographical image of the top of a SiNW. The dashed arrow shows the region in which the 32 Raman spectra were recorded. The blue and the purple dot indicate the positions where the polarization angle-resolved measurements where performed. b) Eight of the collected Raman spectra along the white arrow in panel a showing varying c-Si Raman peak intensities. A detailed analysis about the intensity evolution of the a-Si and c-Si Raman peaks is shown in Figure S2 (Supporting Information File 1). c) Polarization angle-resolved Raman scattering of the c-Si Raman peak as a function of the rotation angle of the Glan–Taylor polarizer. The triangles and circles are the original data, whilst the closed lines are to guide the eyes. d) Polarization angle-resolved photoluminescence patterns collected from the same sample positions, indicated in panel a.

adjacent positions 30 nm apart, marked by the blue and the purple point in Figure 6a. The integrated area of the c-Si Raman peak is plotted as a function of the rotation angle of the fast axis of the Glan–Taylor polarizer. The measured polarization angle-resolved emission patterns from the two sample positions are rather similar, indicating similar polarization states of the Raman scatterings. Interestingly, when plotting the photoluminescence signal as a function of the rotation angle of the Glan–Taylor polarizer, as shown in Figure 6d, the patterns are distinctly different from those in Figure 6c. Note that the Raman intensity and the photoluminescence intensity used for the plots in Figure 6c and Figure 6d are derived from the same spectrum. Therefore, potential artefacts induced by any instrument operation errors can be excluded. Furthermore, upon approaching the gold tip to the SiNW, the angle-resolved polarization pattern changes from a circular pattern (Figure 4c) to a more structured shape in Figure 6d. It is likely that the high refractive index of the SiNW has a certain impact on the polarization of the photoluminescence emitted from the narrow gap between the gold tip and the SiNW. A more quantitative investigation of the polarization angle-resolved emission patterns in Figure 6 will be further pursued. The results shown in Figure 4 and Figure 6 demonstrate that it is possible to combine the polarization angle-resolved experiments with a TERS setup, which has been rarely pursued so far. The successful combination of both techniques is promising for developing new strategies to resolve the structural properties at the sub-10 nanometer scale, based on the polarization properties of the optical signals, demonstrated here for c-Si and a-Si using a core–shell SiNW.

Conclusion

Local structural properties, such as changes in the fraction of crystallinity of a c-Si/a-Si core–shell nanowire are characterized confocally at an optical resolution of about 300 nm. Applying tip-enhanced Raman spectroscopy, we show that variations of the intensity ratio between the crystalline Si and amorphous Si Raman peaks at sample positions as close as eight nanometers can be revealed. Furthermore, the polarizations of Raman scattering and photoluminescence signals locally emitted from a single SiNW are explored by combining polarization angle-resolved emission spectroscopy with tip-enhanced optical spectroscopy. Our work demonstrates the high potential of resolving local structural properties of nanomaterials, here demonstrated for silicon, at the sub-10 nanometer scale using tip-enhanced Raman techniques. TEM investigations are in line with TERS results, which supports the idea that TERS can be used as a micro/nano-structure characterization technique.

Experimental

Core–shell SiNWs were synthesized in two steps. At first, SiNWs were grown by utilizing the VLS growth mechanism [13] using dewetted Pt thin films as the growth catalyst [29] at a growth temperature of 720 °C, which yields a certain SiNW diameter distribution. VLS nanowire growth is carried out in a quartz tube furnace with a precursor gas mixture of H_2 (270 sccm) and SiH_4 (30 sccm), at a pressure of 100 mbar. Silicon shells are grown at a temperature of 520 °C with a gas mixture of H_2 (10 sccm) and SiH_4 (100 sccm), at a pressure of 100 mbar. The silicon shell growth rate under these conditions is in the range of 1 nm/min and yields a thickness of approximately 25 nm. To make confocal Raman and TERS investigations of individual nanowires, SiNWs are released from their original growth substrate by ultra-sonicating the growth substrate in purified water. For Raman and TERS investigations, nanowires are deposited on gold-coated silicon wafers as carrier substrates. For transmission electron microscopy (TEM), nanowires are deposited on copper TEM grids with lacey carbon meshes.

Using a custom-built setup with a parabolic mirror (NA: 0.998) [34], we achieve a diffraction-limited confocal resolution by illumination with a radially polarized laser beam [35]. With a 636.3 nm diode laser operating in continuous-wave mode we obtain a focus diameter of roughly 300 nm [36]. To further increase the resolution a chemically etched gold tip, attached to a tuning fork, is brought into the focus [37-41]. A plasmonic oscillation is generated at the tip apex by the excitation with a radially polarized laser beam along the tip axis. Here, the local field intensity is greatly increased leading to a strong local near field confined at the tip apex. This gives rise to the enhanced sensitivity of tip-enhanced Raman spectroscopy (TERS). TERS combined with scanning probe microscopy (SPM) also allows for the collection of correlated topography and optical images [42,43]. For polarization angle-resolved emission measurements, a Glan–Taylor prism as polarization filter is positioned in front of the entrance slit of the spectrometer.

Supporting Information

Supporting Information File 1

Additional experimental data.
[https://www.beilstein-journals.org/bjnano/content/supplementary/2190-4286-11-99-S1.pdf]

which is used for illustrating the optical and topography images [44].

ORCID® iDs

Steffen Strehle - https://orcid.org/0000-0002-1261-2894
Dai Zhang - https://orcid.org/0000-0001-8190-3030

Preprint

References

1. Tallur, S.; Bhave, S. A. *Nano Lett.* **2013,** *13,* 2760–2765. doi:10.1021/nl400980u
2. Dallas, W.; Polupan, O.; Ostapenko, S. *Meas. Sci. Technol.* **2007,** *18,* 852–858. doi:10.1088/0957-0233/18/3/038
3. Schmidt, V.; Wittemann, J. V.; Senz, S.; Gösele, U. *Adv. Mater. (Weinheim, Ger.)* **2009,** *21,* 2681–2702. doi:10.1002/adma.200803754
4. Guerfi, Y.; Larrieu, G. *Nanoscale Res. Lett.* **2016,** *11,* 210. doi:10.1186/s11671-016-1396-7
5. Zulfiqar, A.; Patou, F.; Pfreundt, A.; Papakonstantinopoulos, C.; Svendsen, W. E.; Dimaki, M. *Sens. Bio-Sens. Res.* **2017,** *13,* 88–95. doi:10.1016/j.sbsr.2016.09.001
6. Chen, K.-I.; Li, B.-R.; Chen, Y.-T. *Nano Today* **2011,** *6,* 131–154. doi:10.1016/j.nantod.2011.02.001
7. Garnett, E.; Yang, P. *Nano Lett.* **2010,** *10,* 1082–1087. doi:10.1021/nl100161z
8. Tsakalakos, L.; Balch, J.; Fronheiser, J.; Korevaar, B. A.; Sulima, O.; Rand, J. *Appl. Phys. Lett.* **2007,** *91,* 233117. doi:10.1063/1.2821113
9. Stelzner, T.; Pietsch, M.; Andrä, G.; Falk, F.; Ose, E.; Christiansen, S. *Nanotechnology* **2008,** *19,* 295203. doi:10.1088/0957-4484/19/29/295203
10. Adachi, M. M.; Anantram, M. P.; Karim, K. S. *Sci. Rep.* **2013,** *3,* 1546. doi:10.1038/srep01546
11. Crescentini, M.; Rossi, M.; Ashburn, P.; Lombardini, M.; Sangiorgi, E.; Morgan, H.; Tartagni, M. *Biosensors* **2016,** *6,* 15. doi:10.3390/bios6020015
12. Cao, A.; Sudhölter, E. J. R.; de Smet, L. C. P. M. *Sensors* **2014,** *14,* 245–271. doi:10.3390/s140100245
13. Wagner, R. S.; Ellis, W. C. *Appl. Phys. Lett.* **1964,** *4,* 89–90. doi:10.1063/1.1753975
14. Lauhon, L. J.; Gudiksen, M. S.; Wang, D.; Lieber, C. M. *Nature* **2002,** *420,* 57–61. doi:10.1038/nature01141
15. Moeinian, A.; Hibst, N.; Geiger, D.; Biskupek, J.; Strehle, S. *IEEE Trans. Nanotechnol.* **2017,** *16,* 736–740. doi:10.1109/tnano.2017.2692099
16. Piscanec, S.; Cantoro, M.; Ferrari, A. C.; Zapien, J. A.; Lifshitz, Y.; Lee, S. T.; Hofmann, S.; Robertson, J. *Phys. Rev. B* **2003,** *68,* 241312. doi:10.1103/physrevb.68.241312
17. De Wolf, I.; Maes, H. E.; Jones, S. K. *J. Appl. Phys.* **1996,** *79,* 7148–7156. doi:10.1063/1.361485
18. Mizoguchi, K.; Nakashima, S.-i. *J. Appl. Phys.* **1989,** *65,* 2583–2590. doi:10.1063/1.342787
19. Hopkins, J. B.; Farrow, L. A. *J. Appl. Phys.* **1986,** *59,* 1103–1110. doi:10.1063/1.336547

20. Kolb, G.; Salbert, T.; Abstreiter, G. *Fresenius' J. Anal. Chem.* **1991,** *341,* 166–170. doi:10.1007/bf00321541
21. Voutsas, A. T.; Hatalis, M. K.; Boyce, J.; Chiang, A. *J. Appl. Phys.* **1995,** *78,* 6999–7006. doi:10.1063/1.360468
22. Beeman, D.; Tsu, R.; Thorpe, M. F. *Phys. Rev. B* **1985,** *32,* 874–878. doi:10.1103/physrevb.32.874
23. Nikolenko, A.; Strelchuk, V.; Klimovskaya, A.; Lytvyn, P.; Valakh, M.; Pedchenko, Y.; Voroschenko, A.; Hourlier, D. *Phys. Status Solidi C* **2011,** *8,* 1012–1016. doi:10.1002/pssc.201000409
24. Agbo, S.; Sutta, P. *Dig. J. Nanomater. Biostruct.* **2013,** *8,* 111–116.
25. Zrimsek, A. B.; Chiang, N.; Mattei, M.; Zaleski, S.; McAnally, M. O.; Chapman, C. T.; Henry, A.-I.; Schatz, G. C.; Van Duyne, R. P. *Chem. Rev.* **2017,** *117,* 7583–7613. doi:10.1021/acs.chemrev.6b00552
26. Huang, T.-X.; Cong, X.; Wu, S.-S.; Lin, K.-Q.; Yao, X.; He, Y.-H.; Wu, J.-B.; Bao, Y.-F.; Huang, S.-C.; Wang, X.; Tan, P.-H.; Ren, B. *Nat. Commun.* **2019,** *10,* 5544. doi:10.1038/s41467-019-13486-7
27. Zhang, Y.; Yang, B.; Ghafoor, A.; Zhang, Y.; Zhang, Y.-F.; Wang, R.-P.; Yang, J.-L.; Luo, Y.; Dong, Z.-C.; Hou, J. G. *arXiv* **2019,** 1908.08720.
28. Lee, J.; Crampton, K. T.; Tallarida, N.; Apkarian, V. A. *Nature* **2019,** *568,* 78–82. doi:10.1038/s41586-019-1059-9
29. Hibst, N.; Knittel, P.; Biskupek, J.; Kranz, C.; Mizaikoff, B.; Strehle, S. *Semicond. Sci. Technol.* **2016,** *31,* 025005. doi:10.1088/0268-1242/31/2/025005
30. Qi, J.; White, J. M.; Belcher, A. M.; Masumoto, Y. *Chem. Phys. Lett.* **2003,** *372,* 763–766. doi:10.1016/s0009-2614(03)00504-9
31. Wang, R.-p.; Zhou, G.-w.; Liu, Y.-l.; Pan, S.-h.; Zhang, H.-z.; Yu, D.-p.; Zhang, Z. *Phys. Rev. B* **2000,** *61,* 16827–16832. doi:10.1103/physrevb.61.16827
32. Smit, C.; van Swaaij, R. A. C. M. M.; Donker, H.; Petit, A. M. H. N.; Kessels, W. M. M.; van de Sanden, M. C. M. *J. Appl. Phys.* **2003,** *94,* 3582–3588. doi:10.1063/1.1596364
33. Mihaljevic, J.; Hafner, C.; Meixner, A. J. *Opt. Express* **2013,** *21,* 25926–25943. doi:10.1364/oe.21.025926
34. Lieb, M. A.; Meixner, A. J. *Opt. Express* **2001,** *8,* 458–474. doi:10.1364/oe.8.000458
35. Fulmes, J.; Gollmer, D. A.; Jäger, S.; Schäfer, C.; Horrer, A.; Zhang, D.; Adam, P.-M.; Meixner, A. J.; Kern, D. P.; Fleischer, M. *Opt. Express* **2018,** *26,* 14982–14998. doi:10.1364/oe.26.014982
36. Stadler, J.; Stanciu, C.; Stupperich, C.; Meixner, A. J. *Opt. Lett.* **2008,** *33,* 681–683. doi:10.1364/ol.33.000681
37. Zhang, D.; Wang, X.; Braun, K.; Egelhaaf, H.-J.; Fleischer, M.; Hennemann, L.; Hintz, H.; Stanciu, C.; Brabec, C. J.; Kern, D. P.; Meixner, A. J. *J. Raman Spectrosc.* **2009,** *40,* 1371–1376. doi:10.1002/jrs.2411
38. Tang, X.; van den Berg, M.; Gu, E.; Horneber, A.; Matt, G. J.; Osvet, A.; Meixner, A. J.; Zhang, D.; Brabec, C. J. *Nano Lett.* **2018,** *18,* 2172–2178. doi:10.1021/acs.nanolett.8b00505
39. van den Berg, M.; Back, J.; Horneber, A.; Meixner, M.; Swider, K.; Ludwigs, S.; Zhang, D. *Macromolecules* **2016,** *49,* 8219–8227. doi:10.1021/acs.macromol.6b01671
40. Wang, X.; Broch, K.; Schreiber, F.; Meixner, A. J.; Zhang, D. *Phys. Chem. Chem. Phys.* **2016,** *18,* 15919–15926. doi:10.1039/c6cp01153e
41. Wang, X.; Braun, K.; Zhang, D.; Peisert, H.; Adler, H.; Chassé, T.; Meixner, A. J. *ACS Nano* **2015,** *9,* 8176–8183. doi:10.1021/acsnano.5b02361
42. Wang, X.; Broch, K.; Scholz, R.; Schreiber, F.; Meixner, A. J.; Zhang, D. *J. Phys. Chem. Lett.* **2014,** *5,* 1048–1054. doi:10.1021/jz500061y

43. Chen, Y.-T.; Pan, L.; Horneber, A.; van den Berg, M.; Miao, P.; Xu, P.; Adam, P.-M.; Meixner, A. J.; Zhang, D. *Nanophotonics* **2019,** *8,* 1533–1546. doi:10.1515/nanoph-2019-0100

44. Horcas, I.; Fernández, R.; Gómez-Rodríguez, J. M.; Colchero, J.; Gómez-Herrero, J.; Baro, A. M. *Rev. Sci. Instrum.* **2007,** *78,* 013705. doi:10.1063/1.2432410